

**Drug repurposing and remodeling: A study of the potential antitumorigenic activity of chemotherapeutic drugs against experimental murine lymphoma.**

Thesis submitted for the degree of Doctor of Philosophy (Science)

Department of Life Science and Biotechnology

Jadavpur University

Index No- 151/21/life Sc. /27

2024



By

**Debapriya Roymahapatra**

Department of Clinical and Translational Research

Chittaranjan National Cancer Institute, Kolkata



# CNCI

**Dr. Ugir Hossain Sk**  
**Clinical & Translational Research**  
**Chittaranjan National Cancer Institute**  
(An Autonomous Body under Ministry of Health & Family Welfare, Govt. of India)  
37, S. P. Mukherjee Road, Kolkata 700 026, INDIA  
Tel: 2476 5101/02/04/20/22 Mob: 91-8628800831  
E-mail: uhocju@gmail.com  
Web site: www.cnci.ac.in

## CERTIFICATE FROM THE SUPERVISORS

This is to certify that the thesis entitled “**Drug repurposing and remodeling: A study of the potential antitumorigenic activity of chemotherapeutic drugs against experimental murine lymphoma**” Submitted by Smt. **DEBAPRIYA ROYMAHAPATRA** who got her name registered on **13/12/2021** for the award of Ph. D. (Science) degree of Jadavpur University, is absolutely based upon his own work under the supervision of **Dr. Ugir Hossain Sk** and **Prof. Partha Pratim Manna** (Co-supervisor) that neither this thesis nor any part of it has been submitted for either any degree / diploma or any other academic award anywhere before.

  
Signature of Supervisor

**Dr. Ugir Hossain Sk, PhD**  
Senior Scientific Officer  
Department of Clinical & Translational Research  
Chittaranjan National Cancer Institute  
Govt. of India, Kolkata- 700 026



**Prof. Partha Pratim Manna**  
(Co-Supervisor)

**Prof. Partha Pratim Manna**  
Department of Zoology  
Banaras Hindu University  
Varanasi-221005

**Thesis**

**Dedicated**

**to**

**Baba and Maa**

**Thank you for your never-ending support and encouragement.**

## **Acknowledgement**

“Every work has got to pass through hundreds of difficulties before succeeding. Those that persevere will see the light, sooner or later”-  
Swami Vivekananda

I am thankful to Dr Ugir Hossain Sk for the guidance of my doctoral thesis. I also owe my deep gratitude towards my co-supervisor Professor Dr. Partha Pratim Manna, Banaras Hindu University for his novel research ideas and constant research assistance throughout my Ph.D. course work. Thank you, Sir, for being there even with me. I would like to thank Dr Ranjeet Singh, Banaras Hindu University for his valuable contribution to my biological part of work. I would also like to thank our reverent director Dr. Jayanta Chakraborty for providing me the institutional support and facilities. I am also thankful to the Institute and Indian Council of Medical Research, New Delhi (ICMR) for awarding me the fellowship throughout my Ph.D. course work.

I am also grateful to Dr Rathindranath Baral and Dr Saptak Banerjee for letting me use their instruments and Lab-space whenever I needed. I would also like to convey my deepest sense of gratitude to the members of CRIF facility.

I would also convey my heartfelt gratitude to Dr. Chinmay Kumar Panda for his expertise whenever I needed. I am thankful to Mohona Chakravorty and Jasmine Sultana for mentoring me in cell culture related techniques. Lastly, I am thankful to Saurav Bera, Jasmine Sultana, Juhina Das, Aishwarya Guha and Elijabeth Mahapatra for their immense mental and moral support in tough situation and also cherished time that we spent in CNCL.



I like to thank all of my teachers since nursery stage till today for uplifting my knowledge in education. I would also like to thank Dr Sulakshana Karmakar and Dr Sarmistha Ray Choudhury for their guidance during my graduation and post-graduation, especially Dr Abhay Chakraborty whose guidance and knowledge that I gathered.

Lastly but not the least, I would like to thank all the CNCI faculties for providing me a healthy working environment to pursue my doctoral thesis work smoothly.

I extend my deep sense of love and gratitude to my elder sister Tapapriya Panda for her tireless support and unconditional love. I am forever indebted to my parent's heavenly abode, Sures Raymahapatra my father and Kalpana Raymahapatra, my affectionate mother for their immense belief on me and giving me the liberty to explore and seek my own destiny. My heartfelt regards also go to my new family, my father-in-law, Dr Narayan Chandra Chatterjee, Retd. Professor of Botany, Burdwan University and my mother-in-law, Subhra Chatterjee for their unconditional love and cooperation to complete my Ph.D. thesis. I am indebted to my husband, Dr Anirban Chatterjee for his continuous inspiration, support, patience, companionship and understanding for completing my Ph.D. work. I would like to thank my niece Sreejata Panda, my grandmother Suhasini Mishra, my Heavenly abode, grandfather Kedar Mishra and my brother-in-law Dr Saurish Panda.

Last but not the least, I want acknowledge all the mice used in my Ph.D. course work study.

Debapriya Roymahapatra

## **Chapter Index**

Chapter No.	Chapter name	Page No.
Chapter 1	Literature review: Reintroduction of clinically relevant drugs for combating lymphoma	1-40
	1.1 Introduction:	2
	1.2 Advantage of drug repurposing over conventional drug discovery:	2-8
	1.3 Recent discovery of Drug repurposing against cancer:	8-16
	1.4 Why anti lymphoma drug discovery is important?	17-21
	1.5 Polymeric scaffold PAMAM Dendrimer in drug delivery against cancer:	21-26
	1.6 Repurposing of anti-glioma drug Temozolomide in oncology:	26-29
	1.7 Repurposing of antimalarial drug artesunate as chemotherapeutic drugs:	29-37
	1.8 DNA targeted drug development against lymphoma:	37-38
	1.9 Aims and scope of this thesis:	38-40
	1.10 Achievement of the thesis:	40
Chapter 2	Fabrication of dendronized system for the delivery of anti-glioma chemotherapeutic against experimental murine lymphoma	41-76
	2.1 Introduction:	42-43
	2.2 Material and methods:	43-54
	2.3 Results:	54-62
	2.4 Discussion & Conclusion:	62-63
	2.5 Characterization	64-76

Chapter 3	Design, synthesis and characterization of artesunate in conjugation with DNA-intercalator naphthalimide moieties: biophysical studies	77-110
	3.1 Introduction:	78-79
	3.2 Material and methods:	79-89
	3.3 Results:	89-97
	3.4 Discussion & Conclusion:	97-98
	3.5 Characterization	98-110
Chapter 4	Antitumor evaluation of artesunate-naphthalimide hybrid for multimodal therapy against experimental murine lymphoma	111-134
	4.1 Introduction:	112
	4.2 Material and methods:	112-118
	4.3 Results:	118-133
	4.4 Discussion & Conclusion:	133-134
	References	135-147
	Abbreviations	148
	Publications	149
	Patent	149

## **Preface**

The study majorly focuses on the establishment of novel therapeutic drug discovery for lymphoma management. Clinically, the systemic and combinatorial treatment, rituximab–cyclophosphamide-doxorubicin-vincristine and prednisone has become the standard therapy for newly diagnosed aggressive B-cell lymphoma patients. However, the treatment regimen in DLBCL only increases the overall 5-year survival rate associated with disease relapse and develops resistance to drugs. Therefore, the effort has been concentrated on alternatives developing an emergent need of small molecules-based drug discovery to ameliorate drug resistance along with poor prognosis rate in lymphoma. Also, to enhance the efficacy and circulation time of the synthesized drug, drug-polymer conjugation has been prepared to get more efficacious molecules. We have developed a drug delivery system by incorporating clinically relevant drug against new cancer type. The thesis focused with four chapters:

Chapter 1 deliberated about the prospect of present work and reported literature based on the previously induction of repurposing drug discovery system and their status in present scenario against cancer that also reflected the interest of our present aim.

Chapter 2 majorly focused on repurposed of anti-glioma temozolomide by developing drug delivery system via conjugating drug with the polymeric scaffold PAMAM dendrimer to get anti-lymphoma activity of temozolomide through sustained release of drug from the drug delivery nano-constructed device.

In chapter 3 effort has been made to repurpose non-oncogenic (artesanate) drug to oncogenic drug towards lymphoma by modifying the

parent drug with DNA targeted moiety. The synthesized drug-DNA interaction was further studied by different biophysical techniques.

The synthesized compounds mentioned in Chapter 3 were evaluated for *in vitro* and *in vivo* anti-lymphoma activity in Chapter 4. To determine the *in vitro* cellular uptake artesunate-naphthalimide conjugated drug was further conjugated with imaging agent FITC.

Successful synthesis, repurposing and modification of oncologic drug and non-oncologic drug against lymphoma were another achieved target of the thesis. However, the repurposing of oncologic and non-oncologic drug after remodeling showed better therapeutic effect against lymphoma.

All of the above four chapters together into consideration, reflected on effectiveness of repurposing of specific known anticancer drug towards other type of cancer by modifying the delivery method and also non-oncologic drug to oncologic drug.

The thesis is a record of original research work carried out by me under the supervision of Dr. Ugir Hossain Sk, Senior Scientific Officer, Department of Clinical and Translational Research, Chittaranjan National Cancer Institute. The work has not been submitted elsewhere for any other degree/diploma or any academic award.

Place: Kolkata

Date:

Debapriya Roymahapatra

**LITERATURE REVIEW**

**REINTRODUCTION OF CLINICALLY RELEVANT  
DRUGS FOR COMBATING LYMPHOMA**

**1.1 Introduction:** Enhancing clinical efficacy, improved prognosis rate and surveillance are the utmost challenge in Cancer drug discovery and drug development. The non oncology drugs can be utilized for repurposing in the area of cancer research which is less time consuming and pocket friendly compared to traditional drug discovery method. Moreover, in oncology only 5% drug compound entering in phase I clinical trial are approved by FDA [1]. Hence in cancer drug discovery repurposing of nononcologic drug is an alternative cost-effective approach. But design and synthesis of new drug molecule is a time consuming and cost-effective process. To solve this problem in 2004 Ashbern and Thor first introduced the term “repurposing” -means reusing of old drugs totally in a new direction [2]. As a result, for the prevention of wide spread cancer management required to rethink the cancer drug discovery by reusing old medicine in a new trick approach. The clinically relevant drugs which are utilized successfully to manage other disease may further reintroduced for the management of cancer. As well as reusing the oncologic drugs in other type of cancer treatment.

**1.2 Advantage of drug repurposing over conventional drug discovery:** Drug researchers discover the new chemical entity by doing so many tests of the molecular compound to find the most possible beneficial effects against the targeted disease as well as the current treatment which has severe toxicity related issues [3]. At this stage thousands of compounds having the potential for new drug discovery and development but only a few numbers of compounds go for further evaluation. In development stage the researchers conduct the experiment together for gathering the information on how the drug ADME properties, mechanism of action, safe dosage, route of administration, toxicity parameter, interaction with other drug and diseases, effectiveness as

compared with similar drugs and how it effects different groups of people (on the basis of gender, race, identity and origin) differently [4].For selecting a promising drug, a series of *in vitro* and *in vivo* experiment in preclinical research is important and inevitable because clinical trials are so expensive. It is the step between drug discovery and expensive clinical trial. Researchers design clinical trials for testing the safety and efficacy in humans as well as and to find the selection criteria (who qualities to participate in this trial), also the number of participants required for the study, duration, design a control group, dosage and how long the drug will give to the patient, procedure of data review and analysis. In general, before at the beginning clinical research, Investigational New Drug (IND)application was submitted to FDA by drug developers. In this application they must include the animal toxicity data, safe drug dose data, study plans, previous human research data. Clinical trials normally comprise four phases. In phase I study 20-100 healthy individuals or a small group of people with disease condition participate to evaluate safety and dosage determination for several months [U.S Food and drug administration]. Around 70% of drug move further to the next phase. Further evaluation of drug safety and determination of efficacy for several month to two-year time frame the larger group of participants required in phase II trial.



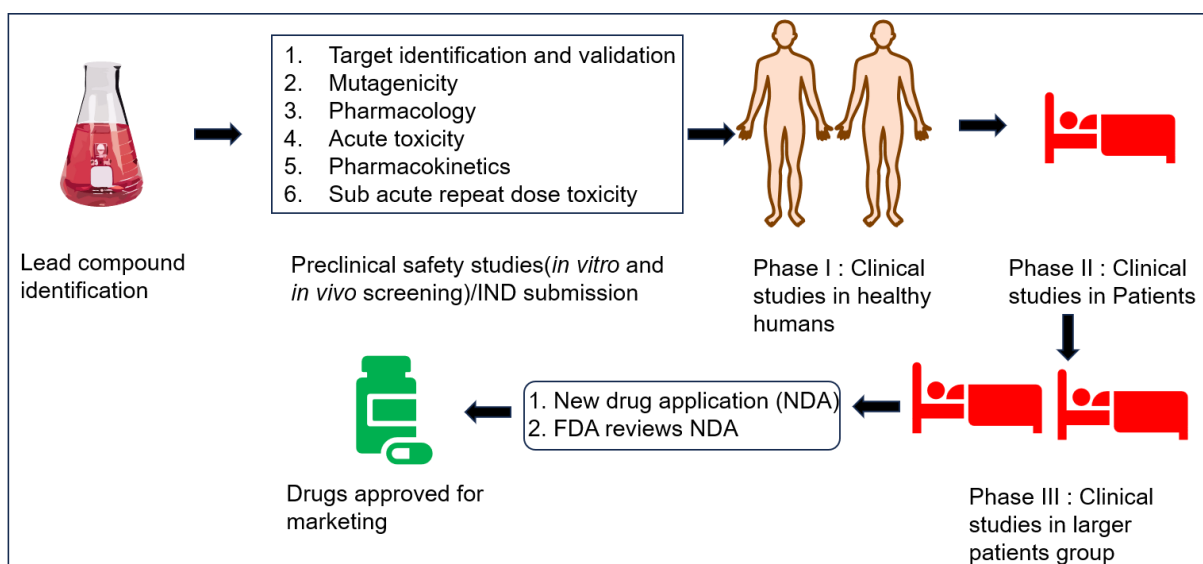


Figure 1: Traditional drug discovery and drug development method

Around 33% of drug move further to the next phase. In phase III clinical trial 300-3000 volunteers having disease or condition participate to evaluate efficacy and monitoring of adverse reaction for the time scale of 1-4 years. Only a 25-30% of drugs approved for the next phase. Phase IV clinical trials occur after marketing of the drug. These studies are come up with for monitoring the effectiveness of drug in population as well as the adverse effects associated with longer time period. The drug receives FDA approval when it is found to be safe and effective from phase III trials. New Drug Application (NDA) is enriched with full details of a drug. The role of NDA is to demonstrate the new discovered drug's safety and effectiveness for the intended study in population. A drug developer must include preclinical to phase III clinical trial data in the NDA. After this procedure the FDA review team has 6-10 month to make decision on the drug approval after conducting routine inspection and reviewing the clinical data, pharmacologist reviews from animal studies etc. For approval of a drug from FDA a manufacturing companies needs to meticulously follow the programmes as suggested by FDA adverse Event Reporting system (FAERS) database which includes reporting of problems with the drug

from health professionals, consumers and also from manufacturers [U.S Food and drug administration]. FAERS in turn help FDA to implement its post marketing safety of a drug. After entering the market, a new drug needs to go through by stringent regulations.

From a traditional drug discovery cycle repurposing approach can eliminate phase I clinical trial (for FDA approved drug) which is less time consuming, effort and cost friendly as compared to traditional drug discovery [5]. The pharmaceutical companies and drug researchers easily summarize the clinically relevant data for a new indication with rare disorders for management of poor prognosis and clinical outcomes due to severe side effects. In case of repurposed drug research pharmacokinetic, pharmacodynamics, toxicity, preclinical efficacy and safety data are readily available for a specific drug which reduces the development cost and saves the precious years. As a result, repositioned drug successfully marketed without investing time for phase I trial. The computational tools and off target databases help to determination of drug discovery with already approved drug totally in a new direction become an alternative and much affordable approach [6]. Based on this approach FDA approves 30% new drugs in recent year. For this reason, drug repurposing is an alternative approach as compared to conventional method of drug discovery.

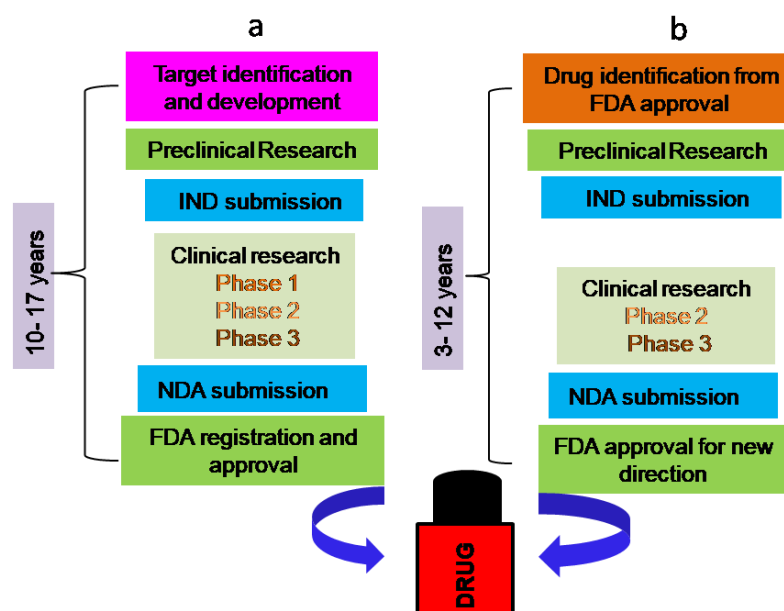


Figure 2: Repurposing drug development (b) is more superior than routine drug discovery (a)

The antibiotic actinomycin D was repurposed as a chemotherapeutic drug in the treatment of Wilms and Ewing tumours, testicular cancer, sarcomas, and choriocarcinoma successfully [7]. Thalidomide in oncology was the successful example of repurposing in oncology. Originally in 1957, German pharmaceutical company Grunenthal developed thalidomide as sedative and used for the treatment of morning sickness among the pregnant women [6]. Unfortunately, when it was introduced into the market it found to cause serious teratogenic birth defect, with malformation in limbs and other body extremities and having serious birth defects. After withdrawal of thalidomide from market several research groups reported its anticancer activity in 2006. In combination with dexamethasone, thalidomide successfully repurposed against multiple myeloma treatment approved by US-FDA [8].

Similarly, streptozotocin was originally identified as an antibiotic but it is in use to treat neuroendocrine tumours in combination with fluorouracil and

doxorubicin [9]. In another example tyrosine kinase inhibitor, Sunitinib is now approved by the FDA for the treatment of renal cell carcinoma as well as in imatinib-resistant gastrointestinal stromal tumours [10].

As the conventional approaches to drug discovery are a lengthy and expensive process as result the invention of a new drug quantity is not significantly increased. As an example, in worldwide (1975-2018) the total research and drug development cost for drug discovery was increased 10 times, followed by the number of new molecule entities approval has remain constant [11]. Chemotherapeutic drugs were reused in different type of cancer treatment other than its original invention purpose. As an example, Doxorubicin hydrochloride may be used to treat in ALL, AML, patients with metastatic, Hodgkin lymphoma, breast cancer, non-small cell lung cancer, non-Hodgkin lymphoma, Ovarian cancer, gastric cancer, bone sarcoma, thyroid cancer and Wilms metastatic tumour [12]. Cisplatin is used in bladder, testicular and ovarian cancer alone or along with combination drugs. Being an alkylating agent cyclophosphamide is used in ALL, AML, acute monocytic leukaemia, Breast cancer, stage III and stage IV Hodgkin lymphoma, multiple myeloma, neuro blastoma, non-Hodgkin lymphoma (nodular/diffuse lymphocytic lymphoma, mixed cell type lymphoma, histiocytic lymphoma and Burkitt lymphoma), ovarian cancer and retinoblastoma [13]. For the management of different brain tumor FDA approved temozolomide [14]. Temozolomide is also under studied in different type of cancer treatment.

The traditional drug discovery strategies usually have 5 stages- drug discovery, drug development, preclinical research, FDA review and finally the FDA-post market safety monitoring. The traditional drug development generally takes 10-15 years to develop a new drug. Hence it is urgent to find new alternative approach to discover drugs. Drug repurposing in

oncology and reusing chemotherapeutic drugs in a new treatment purpose is an alternative attractive approach to find new drugs at a pocket friendly, riskless and within a short time period.

Drug repurposing reduced the time limit as well as production and marketing cost. Moreover, in rare disease management, drug repurposing was beneficial as this alternative approach cut down the expensive clinical trials. Drug repurposing approach reduced the uncertainty raised during newly synthesized drug safety and pharmacokinetic properties.

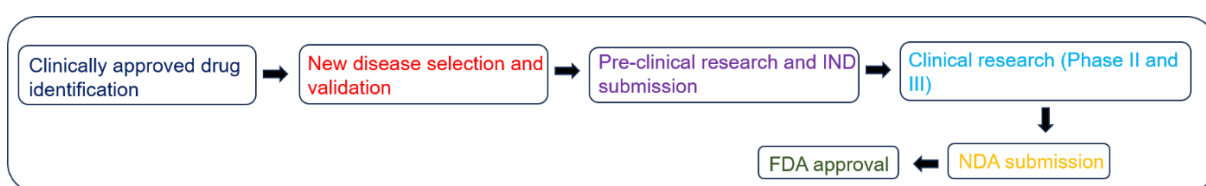


Figure 3 Steps involved in Drug development through drug repurposing before marketing.

### 1.3 Recent discovery of Drug repurposing against cancer:

Hippocrates, the father of medicine first provided the idea of cancer as a disease. Also, due to the similarity of cancer tissue growth with crabs he coined the term “carcinos”. Later Celsus replaced the term used by Hippocrates by latin word “Cancer”. The Greek physicians used the plant extract of Colchicum autumnale for the reduction of tumor mass. In 1930 Colchicine was purified and used in clinics for interference with microtubule assembly as a potential antitumor drug. The cellular origin of cancer was first credited by German Pathologist Rudolf Virchow in 1863 [15]. After that in 1889 the seed and soil hypothesis were given by Stephen Paget for understanding the metastatic disease. Consequently, Peyton Rous discovered that avian cancer caused by virus and hereafter in 1914 Theodor Boveri reported that chromosomal mutation was responsible for cancer occurrence [16]. Oswald Avery established that

from DNA the cellular information was stored and transmitted. Based on this study in 1953 Watson and Crick discovered the shape of DNA, which created a new horizon in science [17]. Further Temin, Mizutami and Baltimore determined Reverse transcriptase which has a significant impact on cancer medicine [18].

At that time Surgery was the first tool available in the treatment of Cancer [19]. After the discovery of anaesthesia and antisepsis, the affected area or organ by cancer only be dealt with surgically. The patient survival rate is decreased only by removal of their tumours alone. To resolve this problem medical science was introduced with radiation era with the discovery of X-rays by Roentgen (1895) [20] and the remarkable invention of Radium by Pierre and Marie Curie (1898) [21]

As a result, in 1928 by the fractionated radiation treatment successfully cured the Head and neck cancers. In 20<sup>th</sup> century after the discovery of Chemotherapy by Paul Ehrlich accelerated a new pathway for development of anticancer drug by the discovery of nitrogen mustard in lymphoma and Folic acid antagonists for induction of temporary remission in child leukaemia. Middle of 1960 combination chemotherapy was introduced for better treatment purpose in oncology.

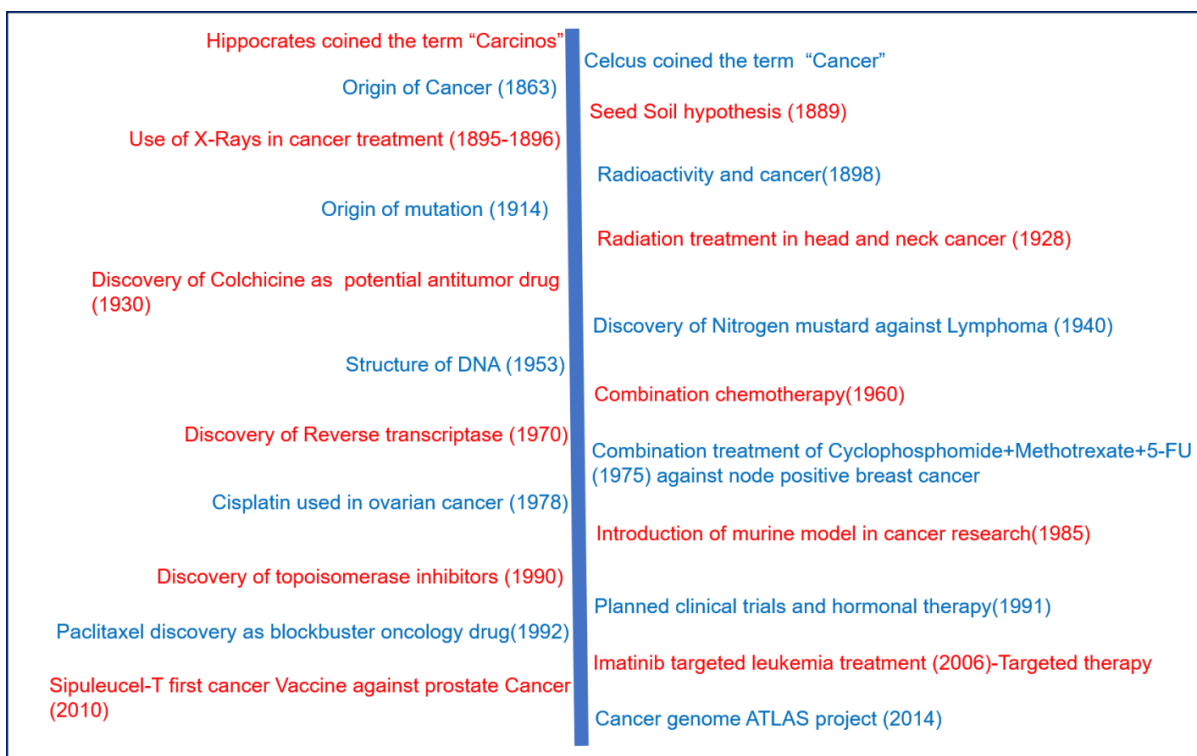


Figure 4: The History of chemotherapy

For the screening of Cancer cytotoxic drug, a great number of compounds required. Animal model played an important role in the evaluation of the drugs cytotoxicity. This process is quite lengthy and expensive process. Up to 1985 NCI followed the drug screening procedure by using the murine model with P388 tumours and three human tumour modules xenograft in nude mice model. This procedure is rejected due to its low predictive value and it also restricted to define a few new cancer drugs only. Cyclophosphamide, methotrexate and fluorouracil combined chemotherapeutic drug regimen used as an adjuvant in breast cancer treatment. In 1991 availability of effective chemotherapeutic agents, hormone treatment, early diagnosis tools, planned clinical trials decreased the rate of mortality in breast cancer. This drug regimen is used after post operative treatment. In chronic myeloid leukemia treatment, the efficacy of imatinib targeted molecular abnormality was exhibited by Druker et al. (2006).[22] As a result, the idea of targeted therapy was introduced. Thus,

cancer treatment started with surgery, radiation therapy and chemotherapy sequentially, later Immunotherapy was introduced for better treatment purpose.

Radiation therapy and chemotherapy cannot distinguish the normal cell and cancer cell also radiation therapy and chemotherapy destroy the localized tumor microenvironment and rapidly growing and dividing cells respectively. The Cancer cells which acquire resistance becomes more aggressive, are not treated by these two conventional methods. Due to lack of specificity of the two major weapon against cancer treatment resulted as the huge side effects like pain, nausea, cardiotoxicity, depression of immune system etc. Specifically, to target only cancer cells the idea of Targeted therapies has raised. Targeted therapies interfere with specific proteins involved in tumorigenesis, specifically designed for a particular type of cancer like lung, lymphoma, breast, leukemia etc. Targeted therapy minimized the off-target side-effects [23]. The conventional method of cancer drug discovery is limited with the association of surgical operation, radiotherapy, and biotherapy along with drug treatment. In chemotherapy the problem arises due its inability to distinguish between normal cells and cancer cells. Recently there is a drastic shift occurred after synthesis of cytotoxic drugs for increasing the specific potency towards cancer cell and to maintain a minimal effect on healthy cell. Targeted oncologic drugs are classified in two categories one is small molecule targeted drug and another one is macromolecules (polypeptide, monoclonal antibodies etc.). on the basis of pharmacokinetic properties, costs, patient compliance, storage, and transportation small molecule targeted drugs are more advantageous than macromolecules in cancer drug discovery. From literature it was evident that both in United states and China 89 small targeted molecules are approved for cancer



treatment. Kinases, regulatory proteins, DNA damage repair proteins, and proteasomes are the major target for the development of anticancer drug discovery. To solve this problem, we can reuse the clinically established small molecule totally in a new direction upon remodeling.

Table 1: Overview of clinically established non-oncologic and oncologic drugs fate and present status in cancer treatment

<b>SI no.</b>	<b>Drug</b>	<b>Use in Clinics</b>	<b>New indication in cancer treatment</b>	<b>Present status of the study</b>
1.	Aspirin	NSAID	newly diagnosed multiple myeloma [11], prostate Cancer [12], HER2 negative breast cancer	reduces recurrence rate (Phase3 (Completed))
2.	Mebendazole	Worm treatment	Temozolomide combined high-grade glioma treatment [24,25] (NCT01729260)	Determination of maximum tolerated dose of mebendazole in combination with temozolomide (Phase I Completed)
3.	Itraconazole	Antifungal	recurrent prostate carcinoma / stage I, II, III prostate adenocarcinoma [26,27,28]	50% decline in serum Prostate Specific Antigen (PSA) Phase II (completed)
4.	Thalidomide	Morning Sickness	multiple myeloma [29,30]	Approved
5.	Celebrex	Osteoarthritis	colon cancer and acute myeloid leukemia [31]	Approved

6.	Digoxin	Congestive heart failure	adenocarcinoma of the pancreas / malignant neoplasm of pancreas [32]	A phase II study of neoadjuvant chemotherapy in combination with Folinic acid, Irinotecan and Oxaliplatin against pancreatic cancer
7.	Riluzole	Amyotrophic lateral sclerosis	melanoma / advanced malignant solid neoplasm / metastatic colorectal carcinoma [33,34]	The safe dose determination and side effects of (phase1 study) riluzolein combination with sorafenib for treatment purpose.
8.	Raloxifene	Osteoporosis	breast cancer [35,36]	demonstrated for the reduction of the risk of breast cancer in phase III trials of older women with osteoporosis
9.	Fumagilin	Antiamebic	cancer [37,38]	Under preclinical study
10.	Nitroxoline	Urinary tract infection	cancer [39,40]	Under preclinical study

11.	Pioglitazone	Diabetes	chronic myeloid leukemia [41,42] (CML) , pancreatic cancer (phase II recruiting) (treatment) lung cancer [43]/ head and neck carcinoma and squamous cell carcinoma of the skin [44]	Phase II study completes for determination of improvement in the size of the tumor weight and reducing the side effects.
12.	All trans retinoic acid (ATRA)	Acne	advanced adenoid cystic carcinoma [45,46]	Phase II clinical studies complete for the purpose of determination of reduction of the size and slow down the growth of tumor.
13.	Pentostatin	T cell related leukemia	hairy cell leukemia [47,48]	Phase II trial of rituximab in combination with pentostatin or bendamustine for relapsed or refractory hairy cell leukemia
14.	Chloroquine	Malaria	glioblastoma multiforme [49,50]	Phase I clinical trial completes for the purpose of the determination of maximum tolerated dose (MTD) for chloroquine in combination with temozolomide

15.	Atrovastatin	HMG-CoA reductase inhibitor	estrogen receptor positive tumor [51] / malignant neoplasm of female breast [52]	The phase III clinical trial determined the efficacy of atorvastatin among breast cancer patients.
16.	Propanolol	non-selective beta-adrenergic antagonist	multiple myeloma [53,54]	From Phase II clinical trial (Active not recruiting) in hematopoietic stem cell transplant recipient's the gene expression of stress-mediated beta-adrenergic pathways observed
17.	Doxycycline	broad-spectrum antibiotic	resectable pancreatic cancer [55,56]	The objective of phase II clinical trial for studying the efficacy, pharmacokinetics of doxycycline in inducing metakaryotic cell death in primary pancreatic tumor.

18.	Niclosamide	Antihelminthic	metastatic hormone refractory prostate cancer [57,58] / recurrent prostate carcinoma / stage IV prostate cancer [59]	Phase II trial: abiraterone acetate, prednisone along with niclosamide combination treatment with hormone-resistant prostate cancer patients.
19.	Methadone	opioid analgesic	cancer of head and neck [60,61]	From phase IV studies it was evident that methadone improves the pain management in head-neck cancer patients
20.	Naltrexone	Narcotic antagonist used in opioid overdose	invasive breast cancer (stage I-III) [62,63,64]	After completion of Phase II clinical trial, it was suggested that naltrexone may help to reduce fatigue after receiving radiation therapy

In diffuse large B cell lymphoma management oncogenic drug dasatinib (originally used in B cell acute lymphoblastic leukemia and chronic myelogenous leukemia management) was repurposed. Aurorafin the drug used to treat rheumatoid arthritis was repurposed against lymphoma management as single or in combination (preclinical trial stage).

**1.4 Why anti lymphoma drug discovery is important?** Lymphoma, a solid tumour of lymphocyte origin is the most common among hematopoietic cancer. Lymphoma starts in white blood cells called lymphocytes, plays important role to maintain body's immune system and also fight against different infection and diseases. Mainly lymphomas are arising from the abnormalities of B and T lymphocytes and then travel to different parts of the body via lymph node, bone marrow, spleen, blood etc. Lymphomas are categorized into two groups a. Hodgkin lymphoma and b. non-Hodgkin lymphoma. In the nineteenth-century pathologist Thomas Hodgkin first coined the term Hodgkin lymphoma [65]. Hodgkin lymphoma mainly subdivided in two groups a. classical Hodgkin lymphoma (CHL) b. nodular lymphocyte-predominant Hodgkin lymphoma.

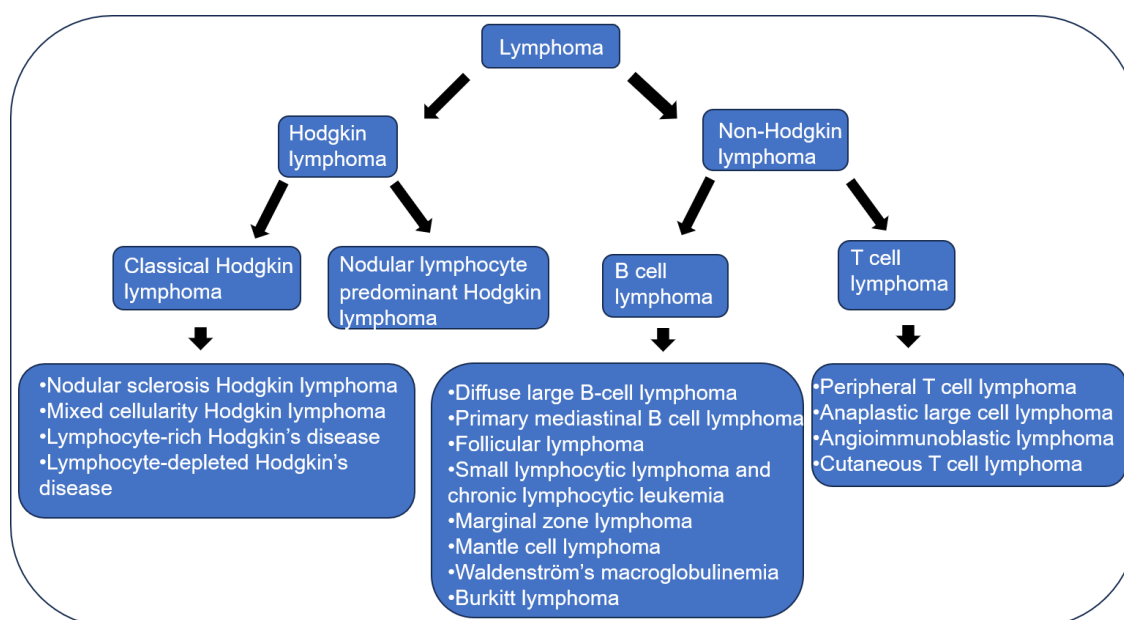


Figure 5: Categorization of lymphoma

cHL is clearly distinguished by the presence of large tumor cells called Reed-sternberg cells (mainly the abnormal B cells). Nodular sclerosis Hodgkin lymphoma, a subtype of Hodgkin lymphoma resulted as 7 out of 10 cases. It initiated from the lymph node of neck and chest.

The second most form of CHL (accounts 4 out of 10 cases) is mixed cellularity Hodgkin lymphoma occurred mostly in HIV infected patients and majorly occurred through the abnormalities in lymph nodes but stays in superior part of the body [American cancer society]. Being a rare subtype of CHL, Lymphocyte-rich Hodgkin lymphoma, usually restricted in the superior or cranial part of the body. Lymphocyte-depleted Hodgkin lymphoma is also a rare form of CHL mainly occurred mainly in older people with HIV infection. Among the subtypes of CHL this form is more aggressive and originate from the abdominal, spleen, liver and bone marrow lymph nodes.

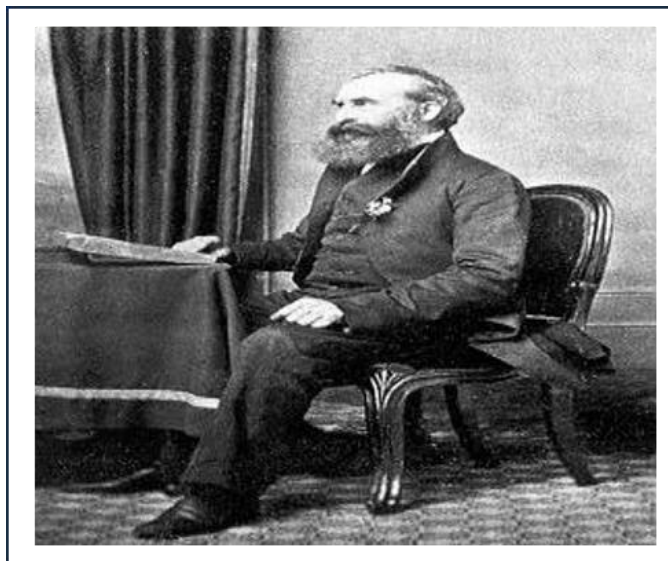


Figure 6: Thomas Hodgkin first described several cases of people with lymphoma patients (Picture Courtesy: Wikimedia)

Nodular lymphocyte-predominant Hodgkin lymphoma is another subtype of Hodgkin lymphoma looks like popcorn, termed as popcorn cells. Usually, they originate from the neck and under the arm's the lymph nodes **[American cancer society]**. The occurrence of Nodular lymphocyte-predominant Hodgkin lymphoma is unrestricted to any age group but more in males as compared to females.

Diffuse Large B-cell lymphoma (DLBCL) is a heterogeneous aggressive tumor from the subtype of non-Hodgkin lymphoma is primarily originates from lymph nodes and migrates very quickly to another part of the body. DLBCL classified into three groups a. germinal centre B-cell-like DLBCL b. activated B-cell-like DLBCL and c. unclassified DLBCL. Follicular lymphoma (FL), mantle cell lymphoma (MCL), and marginal zone lymphoma (MZL) are the other subtypes of non-Hodgkin lymphoma **[American cancer society]**.

FL is the second most common indolent subtype of non-Hodgkin lymphoma. Burkitt lymphoma is one of the fastest growing forms of non-Hodgkin lymphoma but it has high rates of remission and cure possibilities after intensive chemotherapy. Cell surface proteins like CD-19, CD 22, and CD20 are highly expressed in B-cell lymphoma and are the potential key target in targeted therapy. As Rituximab can efficiently recognize and bind with B cell antigens, CD-20 is mostly used as an immunotherapeutic agent in NHL treatment. Rituximab diminishes B cells by direct antibody-dependent cellular cytotoxicity (ADCC), complement-mediated cell death, and signalling apoptosis mechanism. From the literature, it was evident that immunotherapy in combination with a chemotherapeutic regimen significantly improved the survival rate of NHL patients. Chemotherapeutic drug combinations CHOP (cyclophosphamide, doxorubicin, vincristine, and prednisone) has been used more than 40 years. For increasing the prognosis rate US Food and Drug Administration (FDA) in 2006 approved rituximab as first-line treatment of patients with DLBCL in combination with CHOP [58]. Rituximab was introduced with the CHOP regimen for increasing target specificity as lymphoma cells expressed with CD 20, and being monoclonal antibody rituximab recognizes and sticks to CD20. Based on these studies currently, the systemic and combinatorial



treatment R-CHOP has become the accepted treatment for newly diagnosed aggressive B-cell lymphoma patients. From NHL, DLBCL is a heterogeneous group of lymphomas.

Diffuse large B cell lymphoma (DLBCL) is a heterogeneous group of NHL. However, the treatment regimen of DLBCL with R-CHOP resulted as five year increment of survival rate (among 58%), but in 30% patients the disease relapses and develops resistance toward the treatment regimen [59]. The major drawback of this chemotherapeutic regimen against lymphoma is the primary refractory disease (20%) and disease relapsing after complete remission (30%). Most of the refractory patients exhibit MYC-BCL2 rearrangement or MYC-BCL2 hyperexpression [66]. Currently, there is no good definition enabling us to identify these two groups upon diagnosis. Several randomized clinical trials have been conducted for better remission and fewer relapse rates in DLBCL patients, by using multiple targeted agents in combination with CHOP, like bortezomib, ibrutinib, and lenalidomide. However, none of these combinatorial trials are successful. Also, the dose-mediated etoposide, prednisone, vincristine, cyclophosphamide, and doxorubicin along with rituximab showed survival improvement among DLBCL patients (phase III randomized study CALGB 50303). Combination treatments are more advantageous than single drugs because it has different mode of action to inhibit cancer cells. As an example, Cyclophosphamide, vincristine sulfate, procarbazine hydrochloride and prednisone chemotherapeutic drug combination were used as against lymphoma treatment [67]. Another Chemotherapeutic drug combination used in lymphoma treatment is etoposide phosphate, vincristine sulfate (Oncovin), cyclophosphamide, and doxorubicin hydrochloride (hydroxy daunomycin) and the steroid hormone prednisone. Cyclophosphamide, vincristine sulfate, doxorubicin

hydrochloride (Adriamycin), methotrexate, and cytarabine along with dexamethasone drug regimen is also used against lymphoma. In lymphoma treatment targeted therapeutic drug rituximab is combined along with chemotherapeutic drugs ifosfamide, carboplatin, and etoposide phosphate etc. Two-thirds DLBCL patients are able to take CHOP regimen and the problem arises due to the great heterogeneity of DLBCL and the absence of response occurring because of resistance as a result disease relapsed. To overcome this problem more repurposed drug and novel synthesized drugs are required in therapeutics, which may have less cytotoxicity towards normal cell and thus minimizing the side effects and increases prognosis rate along with the survivability in lymphoma patients.

**1.5 Polymeric scaffold PAMAM Dendrimer in drug delivery against cancer:** The synthetic nanocarrier in chemotherapy was required as the chemotherapeutic drugs were degraded before reaching the target site. At the winter polymer Gordon conference (1983) Donald A Tomalia first describe the synthesis of PAMAM dendrimer. PAMAM dendrimers are highly branched and monodispersed structure, having ethylene diamine (EDTA) at the core. Repeated unit of Methyl acrylate and EDTA were added to get the desired number of dendrimer generation. The terminal end of PAMAM dendrimer was conjugated with different functional group including -NH<sub>2</sub>, -OH, -COOH, -COONa etc. Moreover, PAMAM dendrimer gained attention as a drug delivery carrier due to its spherical structure, non-immunogenic nature, increment of water solubility, sustained release of drug from the PAMAM dendrimer. The PAMAM dendrimer with terminal -NH<sub>2</sub> group mainly used to deliver drug inside the cells. It is due to the variation of the terminal group PAMAM dendrimer non-covalently conjugated with different chemotherapeutic drugs along with imaging molecules, as a result non-specific toxicity and drug degradation was

minimized (Duncan et al. European J. Cancer,1999). The noncovalent conjugation of PAMAM dendrimer and drug helped to increase the circulation time in blood, the renal clearance rate was also reduced along with permeability and retention effect in leaky tumors was incremented.

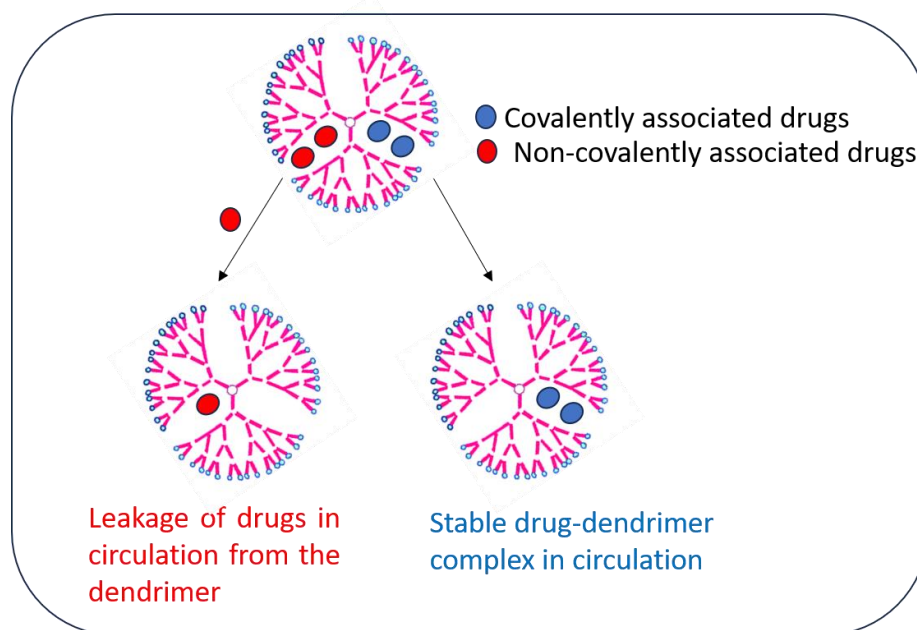


Figure 7: Covalent drug conjugation versus non-covalent drug association. The non-covalent drug association increased the rate of drug delivery through leakage of drug in circulation. (Only the Dendrimer structure is adopted from Rengaraj, A., et.al., PAMAM/5-fluorouracil drug conjugate for targeting E6 and E7 oncoproteins in cervical cancer: a combined experimental/in silico approach. RSC Advances, 7(9), 5046–5054.2017)

Some chemotherapeutic drugs including doxorubicin, methotrexate, paclitaxel, cisplatin etc. were conjugated with PAMAM dendrimer for decreasing the systemic toxicity as well as increasing bio-availability. Through cathepsin B-cleavable tetrapeptide Gly-Phe-Leu-Gly linkages paclitaxel was conjugated with PAMAM dendrimer (Satsangi A, et al, Molecular Pharmaceutics, 2014). This novel conjugate has cytotoxic as

well cytostatic effect by reducing the tumor volume in MDA-MB-231 tumor xenograft model (figure 8a).

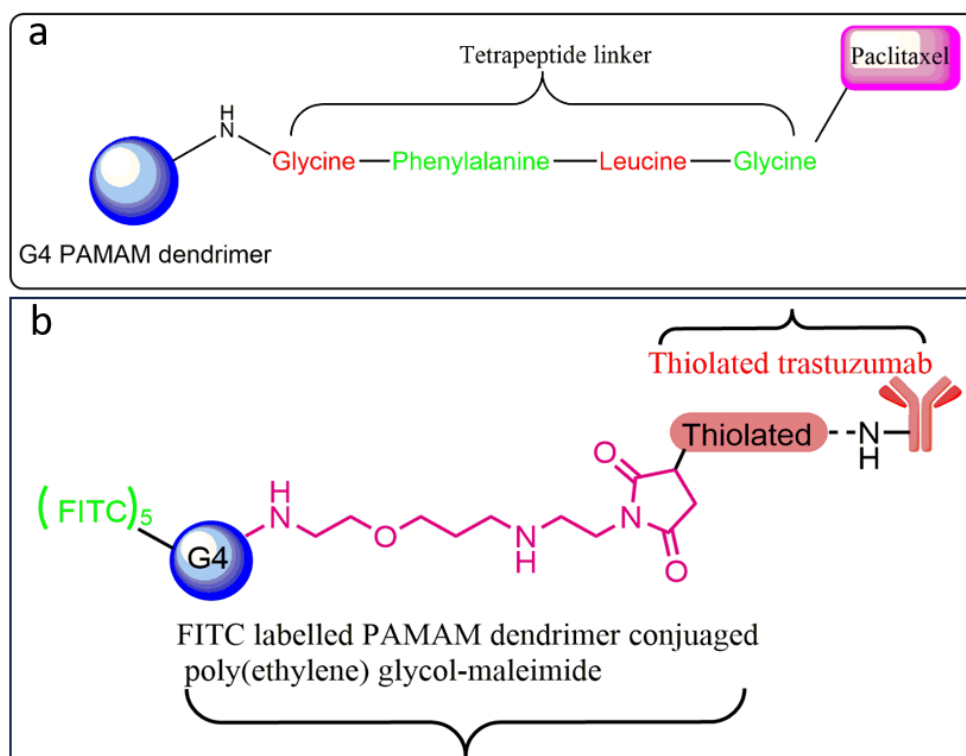


Figure 8: (a) Paclitaxel conjugated with PAMAM dendrimer by cathepsin B-cleavable tetrapeptide Gly-Phe-Leu-Gly linkages. (b) theranostic FITC labelled PAMAM dendrimer conjugated with trastuzumab.

Trastuzumab conjugated with G<sub>4</sub>-PAMAM dendrimer (Kulhari, H, et al, Sci Rep, 2016) due to the presence amine and carboxyl group which may be beneficial for imaging and delivery of drugs to HER-2 positive breast cancer cells (figure 8b).

PAMAM dendrimer conjugated with 5-FU for targeting E6 and E7 oncoprotein in HPV mediated cervical cancer (A Rengaraj, et al, RSC Adv., 2017). PEGylated -PAMAM dendrimer- doxorubicin conjugate is effective against solid tumor treatment (figure 9).

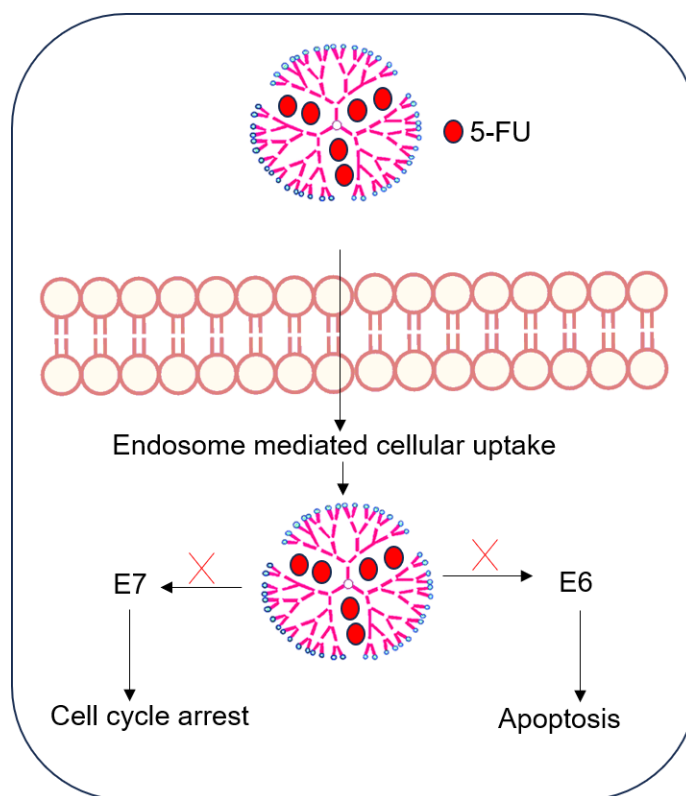


Figure 9: Encapsulation of 5-FU in PAMAM dendrimer to target the HPV mediated cervical cancer oncoprotein.

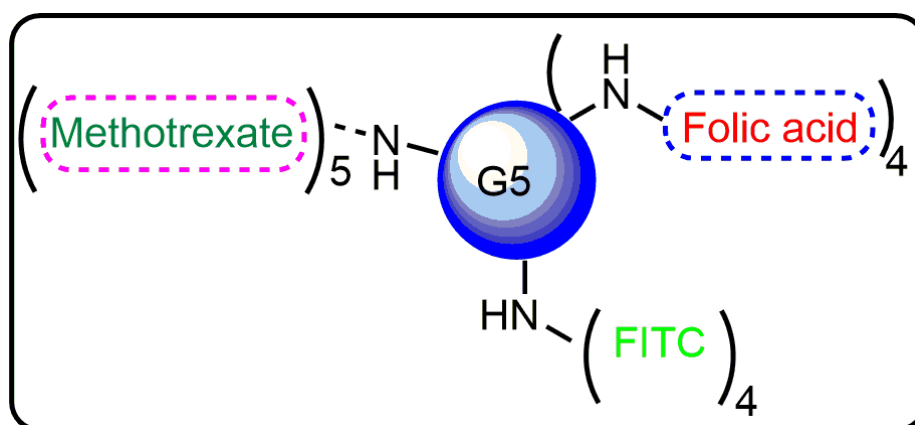


Figure10: PAMAM dendrimer (G5) conjugation with chemotherapeutic drug (MTX), targeting ligand (FA) and imaging agent (FITC).

The multiple functional dendritic was used against targeted drug delivery along with imaging. As the multifunctional nano device was conjugated with a ligand (Folic acid, over expressed in different cancer) along with chemotherapeutic drug (MTX) (Majoros et al, Journal of Medicinal

Chemistry, 2005) also reduced the nonspecific toxicity and the drug circulation time was also increased (figure 10).

The hydroxy terminated G<sub>4</sub>-PAMAM dendrimer can cross the blood brain barrier (BBB) successfully. The brain delivery of donepezil was increased after conjugation with PAMAM dendrimer (Singh A.k, et al, ACS Omega, 2019). The cellular internalization of the drug donepezil was increased after the conjugation along with better pharmacokinetic stability of the drug (figure 11).

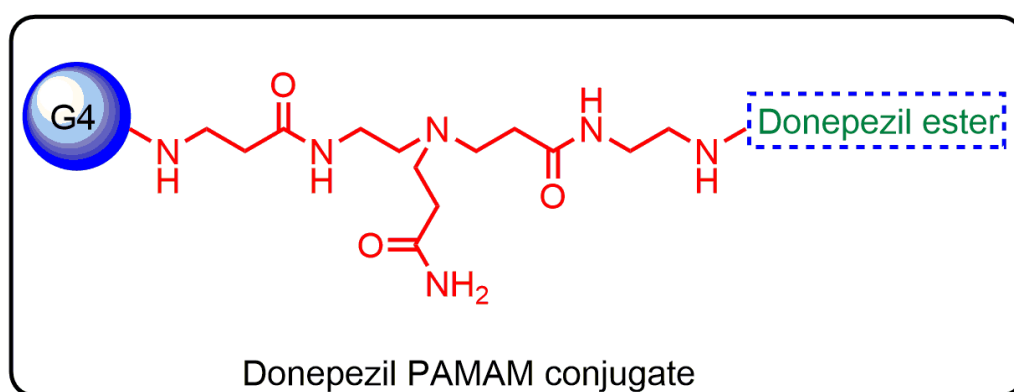


Figure 11: Synthesis scheme of Donepezil conjugated PAMAM dendrimer for better delivery across BBB.

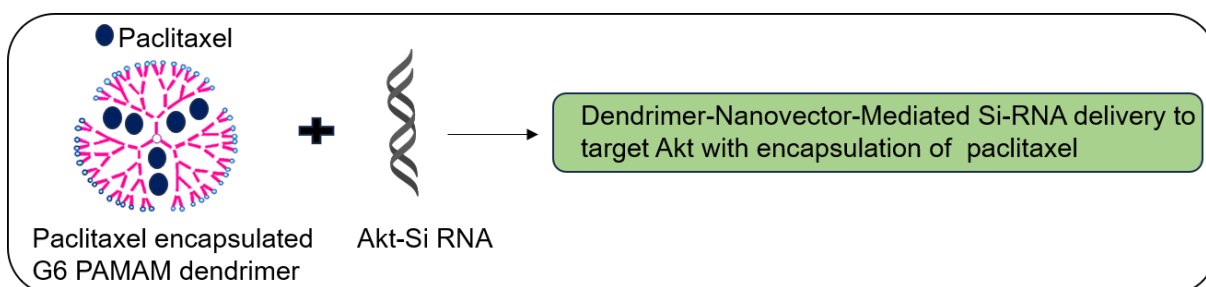


Figure12: PAMAM dendrimer conjugated with siRNA and chemotherapeutic drug paclitaxel (PTX) against ovarian cancer.

PAMAM dendrimer conjugated with Akt-si RNA (Kala. S, et al, Journal of medicinal chemistry, 2014) along with paclitaxel drug showed potent therapeutic efficacy against ovarian cancer (figure 12). PAMAM

Dendrimers could be successfully used as a drug delivery nanodevice as the circulation time of drug and stability of the drug was increased thereby increased the bio-availability of the drug and sustained release of the drug from the nano construct, thereby minimized the non-specific toxicity.

### **1.6 Repurposing of anti-glioma drug temozolomide in oncology:**

Temozolomide is a lipophilic prodrug provided the methyl group to the purine bases of DNA. At the end of 1980 Professor Malcolm Stevens discovered the dacarbazine analog TMZ. Due to its small (molecular weight 194.154 gm/mol) lipophilic structure TMZ can cross the BBB easily. In 1999 it was first marketed as the second line treatment against glioblastoma (GBM). TMZ drew the limelight over the previously used drug carmustine and lomustine, due to their poor survival benefit and toxicity related issues. The survival rate of GBM patients was increased after the TMZ usage. As a result, in combination with radiotherapy TMZ was used as first line drug GBM treatment and second line treatment of different malignant gliomas. At physiologic and basic pH the water molecule interacts with the C-4 atom of TMZ, as a result the active metabolite MTIC was produced. TMZ exerts cytotoxicity as MTIC is responsible for the methylation of adenine and guanine bases. DNA mismatch repair system recognises this error as a result the cells stopped in G1/S and G2/M for longer period and finally apoptosis was induced. TMZ shown a positive effect on previous treatment with capecitabine in neuroendocrine tumor due to depletion of MGMT enzyme levels. [68]

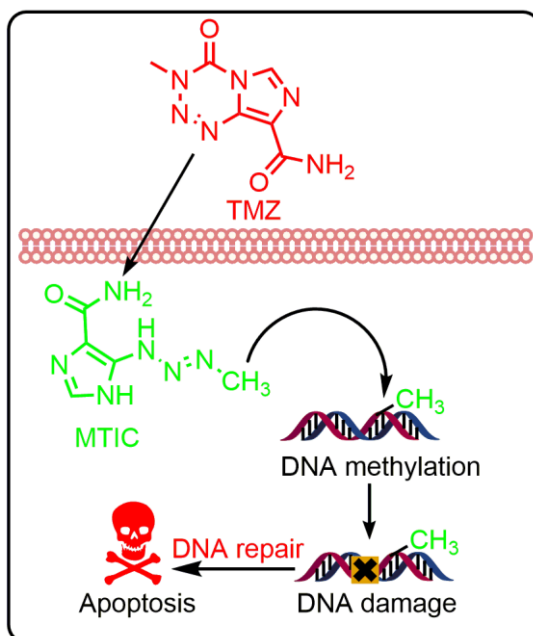


Figure 13: The mechanism of action of TMZ prodrug. TMZ hydrolyses to MTIC, as a result the DNA methylation occurred and finally apoptosis occurred.

However different nano formulation of TMZ made it more target specific, lower the cytotoxicity, improvement of drug stability. Temozolomide conjugated doxorubicin increased the binding capability with DNA though intercalative mode of interaction (Figure 14). Even at higher concentration doxorubicin alone unable to kill the U87MG cells. The doxorubicin conjugated temozolomide (DuK., et al, *Applied Materials & Interfaces*. 2020) successfully kill the U87MG cells at lower concentrations.



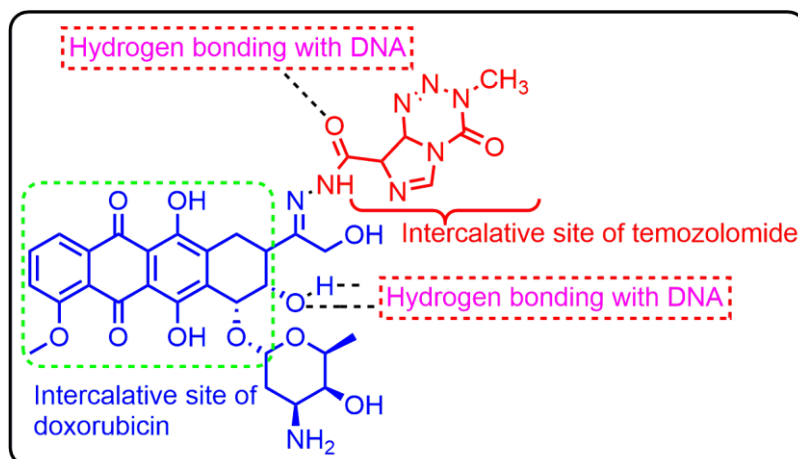


Figure 14: Synthesis scheme of TMZ conjugated doxorubicin and their interaction with DNA by intercalation.

As compared to TMZ alone, TMZ loaded albumin nanoparticles and chondroitin sulphate conjugated with TMZ loaded albumin nanoparticles increased the therapeutic efficacy against brain tumor (Kudarha R. R, et al, Drug Delivery and Translational Research,2020). Chondroitin sulphate conjugated with TMZ loaded albumin nanoparticles also increased the uptake of TMZ through CD 44 receptor mediated targeting (Figure 15).

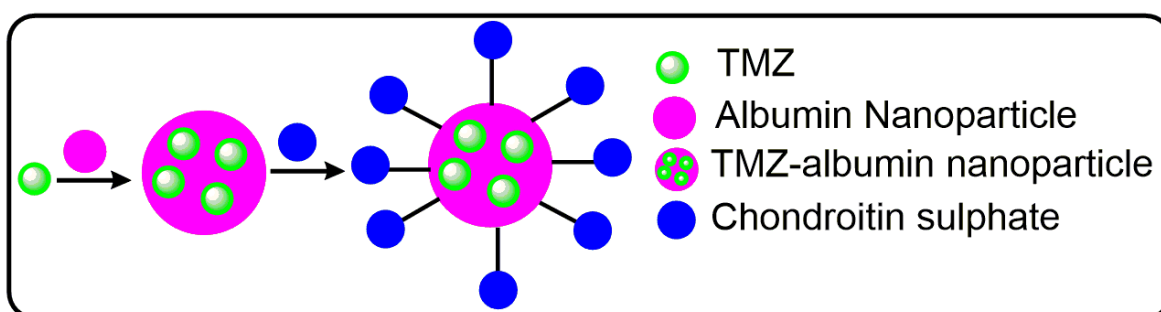


Figure 15: Chondroitin sulphate conjugated with TMZ loaded albumin nanoparticles.

TMZ conjugated poly (2-methacryloyloxyethyl phosphorylcholine) increased the overall stability of TMZ and responsible sustained release of TMZ from the synthesized drug-polymer conjugate (Sarah M. Ward, et al, ACS Molecular Pharmaceutics ,2018). The synthesized drug polymer

conjugate was effective against chemo-sensitive as well as chemo resistance glioblastoma cell lines. For increasing the accumulation at tumor site TMZ was incorporated into a protein nanocage, apoferritin. By endocytosis apoferritin encapsulated TMZ was internalized at the specific tumor site and the apoptosis was initiated. In vitro studies of TMZ-apoferritin nanoconstruct against glioblastoma cell lines showed enhanced cytotoxicity than TMZ only [69]. TMZ embedded nanoconstruction enhanced the circulation time, tissue specificity and sustained release of TMZ from the nano-construction. TMZ showed better prognosis and survival rate in the patients of non-small cell lung carcinoma with brain metastasis. TMZ along with fotemustine has been come up with the alternative treatment in melanoma patients, when immunotherapy was failed. In small cell lung cancer TMZ is used in combination with veliparib (NCT01638546) [70]. TMZ was encapsulated with different nanocarriers for increasing the half-life, circulation time and tumor specificity in glioblastoma multiform management and also can be repurposed in different type of cancer.

### **1.7 Repurposing of antimalarial drug artesunate as chemotherapeutic drugs:**

Artemisinin is derived from *Artemisia annua* L. (sweet wormwood) having a active 1, 2, 4-trioxane ring (endoperoxide bridge) associated with a lactone moiety. Professor Youyou Tu was awarded to Nobel prize in 2015 for the remarkable discovery of artemisinin. For better antimalarial activity and pharmacokinetic properties, several semisynthetic derivatives of artemisinin, dihydroartemisinin, artesunate, artemether have and been developed. Discovery of artemisinin and other derivative of artemisinin reduced the rate of malaria related mortality. For the successful and stable antimalarial extraction from the sweet wormwood plant professor

Tu replaced the extraction solution with ether from ethanol. As a result, the active antimalarial components stability was increased. For increasing water solubility and drug efficacy further Professor Tu discovered dihydroartemisinin. Artemisinin first concentrated in erythrocyte and then rapidly hydrolysed to dihydroartemisinin. The derivatives of dihydroartemisinin were artesunate, artemether and arteether. For the treatment of multidrug resistant malaria artesunate and artemether the derivative of artemisinin was used. The presence of a hydrophilic group in artesunate makes it more potent than derivatives of artemisinin. Artesunate derives from natural resources and is effective alone or in combination with oral administration.

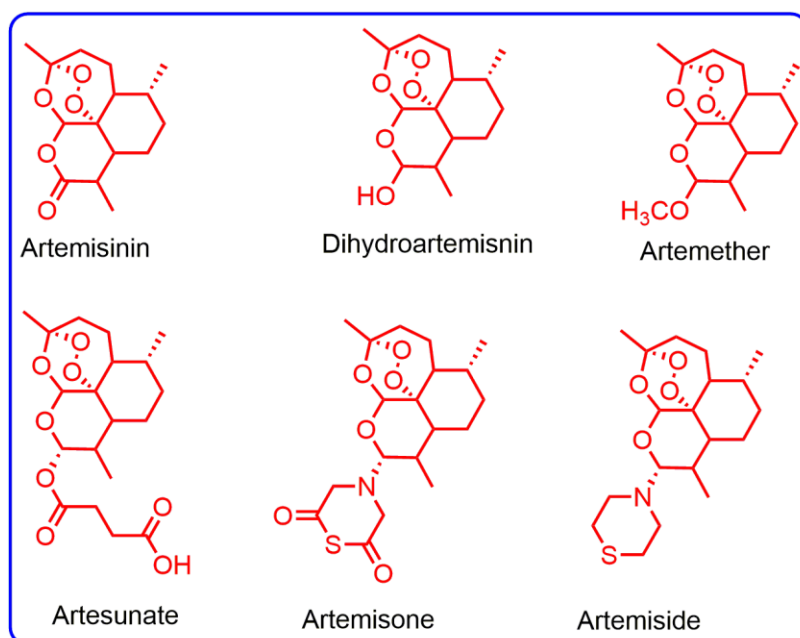


Figure 16: Derivatives of artemisinin

It is used as standard treatment for cerebral malaria along with other malaria. Several research reports indicate cytotoxicity properties of artesunate in different lymphoma cell lines [71].

Also, artesunate is efficient in stimulating cell differentiation, arresting the cell cycle in the G1 and G2/M phases, inhibiting cell proliferation, and

inducing apoptosis through mitochondrial and caspase signalling pathways. The antimalarial mechanism of artesunate differs from the cytotoxic property. To understand the better pharmacokinetics of ADMET (absorption, distribution, metabolism, and excretion) information is essential to focus on how physiological condition interferes with the drug or vice-versa.

Also, the metabolism of the drug information and its excreted product further help to modify the existing drug toward the clinical implication. From literature review indicated the half-life time of artesunate was less than 15 minutes through intravenous administration. The active metabolite of artesunate, DHA indicated the highest concentration 25 minutes post-dose and excreted from the human body with a half-life of 30 - 60 minutes. However, the best route through oral administration associated with the high bioavailability of DHA (dihydroartemisinin) is more than 80% [72]. Anticancer activity of the artesunate was involving several clinical investigations.

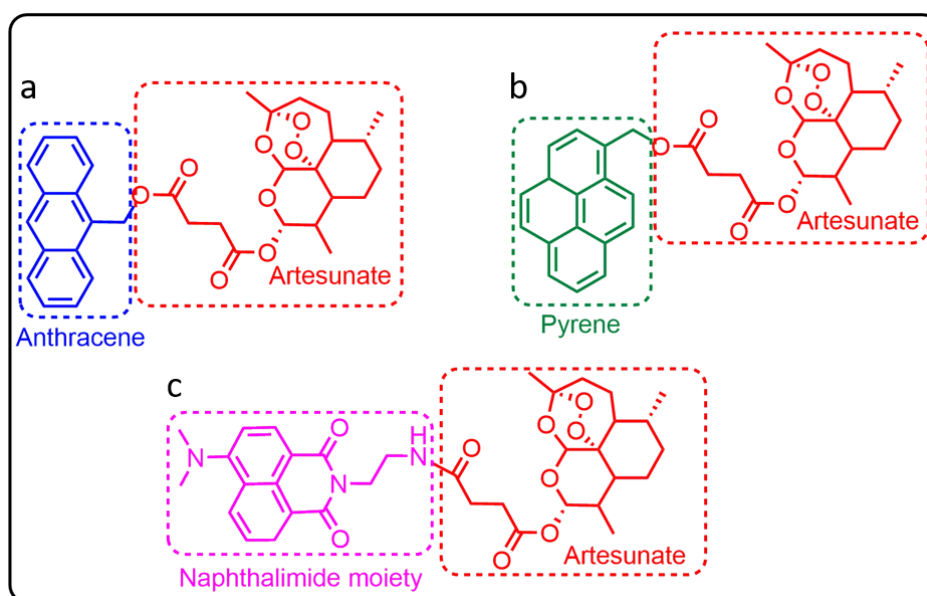


Figure 17: Artesunate in conjugation with anthracene (a), pyrene (b) and naphthalimide (c) moiety.

Zihao Yang et. al modified the artesunate derivatives in conjugation with different planar molecules like anthracene, pyrene and naphthalimide moiety for the treatment against breast cancer (Yang Z, et al, Dyes and Pigments,2017). The result indicated low cytotoxicity for the artesunate derivatized molecules as compared to artesunate against MCF-7 ( figure 17).

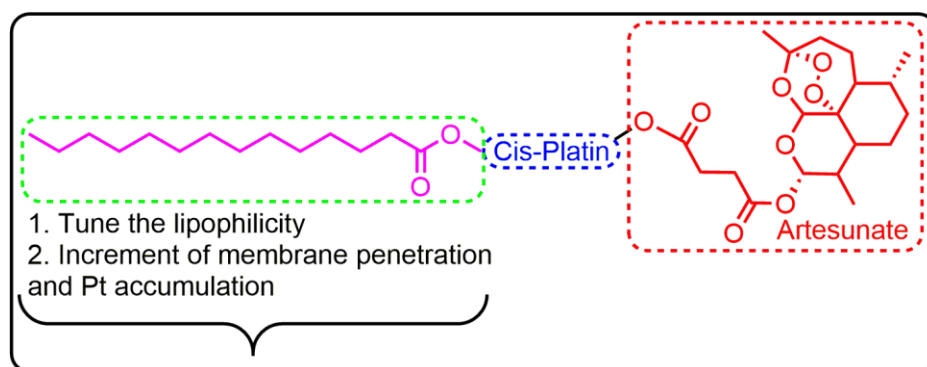


Figure 18: Potent antitumor efficacy study of artesunate derivatized with platinum ( $\text{Pt}^{\text{IV}}$ ).

Artesunate conjugated with platinum drugs against different cancer cell lines. The synthesized platinum conjugated artesunate derivative inhibited metastasis (Wei L, et al, ACS journal of medicinal chemistry, 2023). The synthesized compound-initiated cell cycle arrest as a result apoptosis occurred (figure 18).

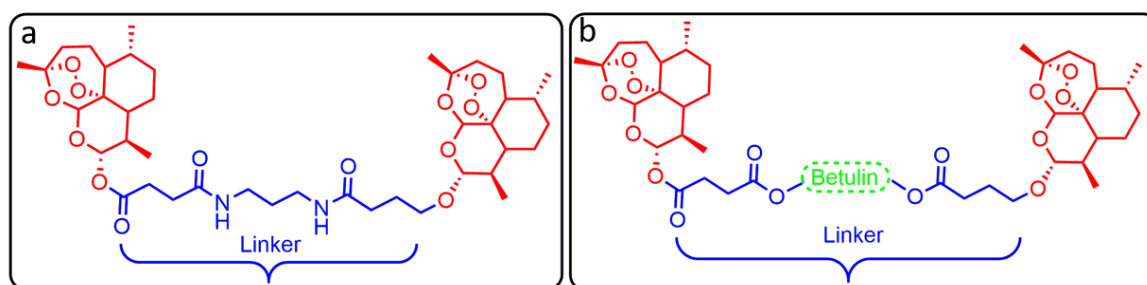


Figure 19: Synthesis of (a) homodimer of artesunic acid and the (b) betulin conjugated artesunic acid against human leukemia cell lines. (adopted from: Horwedel, C, et al, *Journal of Medicinal Chemistry*,2010)

Synthesis of homodimer of artesunic acid and the betulin conjugated artesunic acid was effective against leukemia cell lines and the subline of multidrug resistant cell lines. (Figure 19)

The side effects and safe drug dose selection of artesunate were determined in patients with high-grade anal intraepithelial neoplasia. Artesunate may kill the cells infected with HPV. Artesunate completes phase I clinical trial for treatment purpose of cervical grade 2/3 intraepithelial neoplasia , locally advanced breast cancer, metastatic breast cancer high-risk HPV, and hepatocellular carcinoma. In a study of artesunate in metastatic Breast cancer (ARTIC-M33/2) involving patients to validate the tolerability of add-on therapy with a duration of 4 weeks (NCT00764036). The trial of artesunate in ointment form for treating patients with high-grade vulvar intraepithelial neoplasia are caused by HPV. As a result, the high-grade vulvar intraepithelial neoplasia caused by HPV is reduced.

In cancer cell in presence of iron the endoperoxide bridge of artesunate cleaves as a result apoptosis occur by oxidative DNA damage. The induction of Iron-dependent oxidative stress by artesunate is also responsible for the loss of mitochondrial outer membrane integrity as a result the mitochondrial permeability transition pore (mPTP) opens followed by initiation of apoptosis.

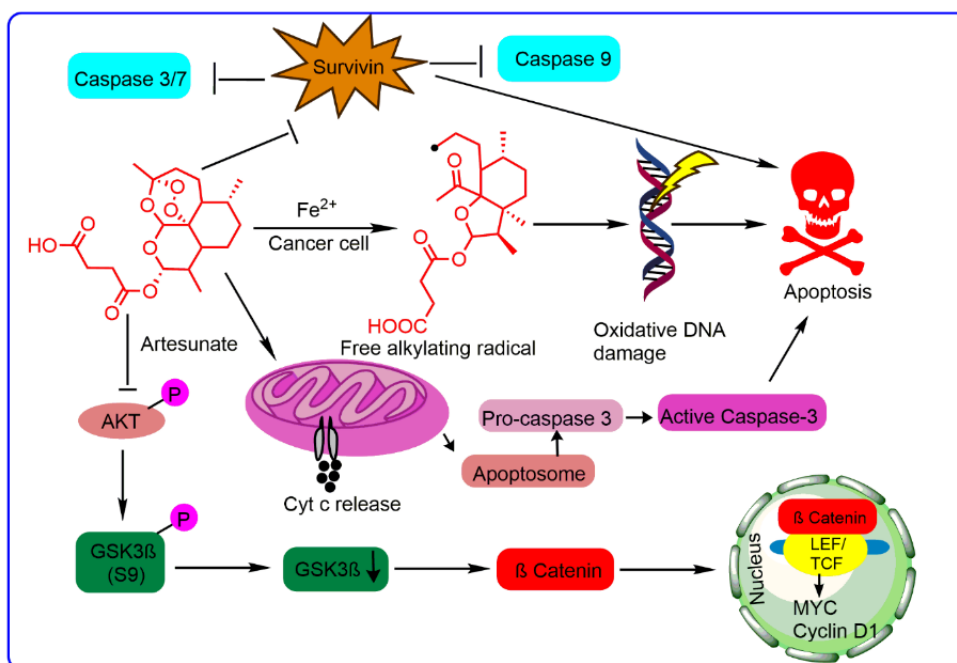


Figure 20: The probable mechanism of artesunate in cancer cell

Artesunate downregulates the surviving expression and initiates apoptosis by activating effective caspase-3 and 7. Artesunate suppresses the GSK3 beta phosphorylation resulted with the downregulation of downstream targets (c-myc) and beta-catenin. Artesunate has been used for the sensitization of radiotherapy along with cisplatin, carboplatin, and doxorubicin combined drug regimen [73]. Artesunate exerts its antimalarial activity by the interaction with the endo-peroxide bridge which interacts with heme liberated from parasite-infected red blood cells [74]. As a result, the reactive oxygen species ( $R^*$ ) and carbon-centered radical formed, which have been shown to damage and kill parasitic organisms by alkylating and poisoning the essential malarial membrane proteins [75]. The antimalarial activity of artesunate is associated with protein damage; this raises the question of whether it may target specific proteins in lymphoma [76]. Moreover, additionally, artesunate reported with cytotoxic effect makes it a promising target as a chemotherapeutic agent. Ferrous iron is necessary for the activation of artesunate via the cleavage of its

endo-peroxide bridge as a result of ROS (Reactive oxygen species) produced [77], [78]. As compared to normal cells cancer cells have higher iron concentration [79], [80]. This may be the reason for artesunate cytotoxicity towards tumour cells.

In mammals, lysosomes are analogous to food vacuoles, contain high levels of redox active iron, resulted with stimulation of mitochondrial apoptosis [81]. Iron-dependent oxidative stress induced by artesunate is also responsible for the loss of mitochondrial outer membrane integrity in cancer drug discovery one of the major targets is the opening of a mitochondrial permeability transition pore (mPTP), and as a result bioenergetic collapse and apoptosis initiates. However, clinical studies have so far been disappointing [82]. The known anticancer chemotherapeutics target mitochondria thereby activating anticancer mechanistic pathways. Lysosomal iron is the lethal source of ROS generation by ART, which is mainly responsible for ART-triggered cell death by inhibiting several parameters associated with mitochondrial outer membrane permeability, releasing of Cyt c, and induction of intrinsic pathway of apoptosis leading towards cell death by upregulated Bax expression, downregulated Bcl-2 expression, and activated caspase-9 and caspase-3 expression [83]. Thus, the intrinsic apoptotic pathway may be involved in ART-induced apoptosis. In current cancer research survivin the inhibitor of apoptosis protein family is one of the prominent targets for novel drug discovery [84]. Survivin highly expressed in cancer cells, including some types of lymphoma also. In half of the Anaplastic large cell lymphoma (ALCL) tumor survivin is expressed. Survivin expression modulation may provide a novel target for experimental therapy in patients with ALCL. Survivin controls apoptosis rate and regulates cell division. In a dose-dependent treatment, schedule artesunate downregulates



surviving expression and initiates apoptosis by activating effective caspase-3 and 7 [85]. Therefore, we assumed that artesunate has a future prospect alone or in combination against lymphoma. Cyclophosphamide was quickly dispersed in the body after intravenous or oral administration. After entering in liver cyclophosphamide converted to 4-hydroxycyclophosphamide stays in equilibrium with aldophosphamide [86]. Through passive diffusion aldophosphamide readily cross the cell membrane of lymphocytes and liberates propenal (acrolein) and active phosphoramidate mustard [83]. As a result, majorly at the guanine sites interstrand DNA crosslinks was formed from the active phosphoramidate mustard. In artesunate in presence of ferrous iron the active endoperoxide bridge is cleaved followed by the generation of ROS and carbon-centered free radicals. Artesunate-induced ROS and carbon-centered free radicals' generation may lead to oxidative DNA damage, which ultimately accounts for the cytotoxic activity against cancer cells.

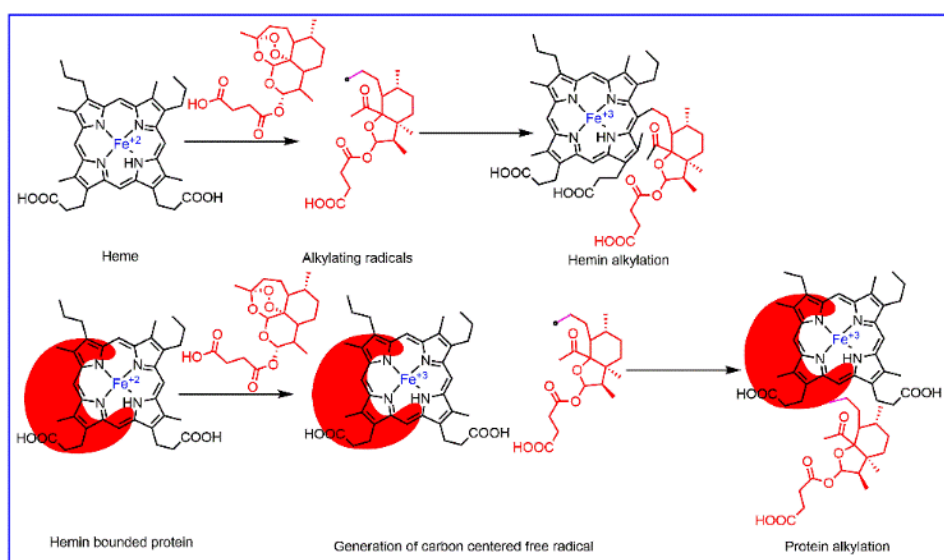


Figure 21: Heme and Hemin bounded protein alkylation by artesunate

Artesunate downregulates C-Myc and other antiapoptotic members of Bcl-2. Artesunate suppressed the GSK3 beta phosphorylation [100] and as a

result, the protein level of beta-catenin is lowered and its downstream targets (c-myc). Due to rapid uptake and high concentration of iron in cancer cells the anticancer mechanism of artesunate is similar to antimalarial mode of action. Artesunate exhibited the anti-lymphoma activity by alkylating of multiple key proteins associated with cellular viability under an iron-rich environment. From the literature, it is evident that lymphoma patients, co-expressed with both C-Myc and Bcl-2 have poor prognosis rates [87,88]. The antimalarial drug artesunate downregulates C-Myc and other antiapoptotic members of Bcl-2. So, from the literature review it was evident that artesunate can replace cyclophosphamide in R-CHOP drug resume for the management of lymphoma as it has the same type of DNA alkylating mechanism resulting in oxidative damage in cancer cell.

### **1.8 DNA targeted drug development against lymphoma:**

The binding of small molecules to DNA can alternate the structure of nucleic acid as a result the DNA replication and transcription was hampered. During DNA duplication helicase unwinds the double stranded DNA to single stranded DNA. As a consequence, the nucleus became fragile as the exposure time is longer in case of single stranded DNA. Hence the nucleus is an important target for the chemotherapeutic drugs to induce apoptosis of tumor cells. Therefore, so many nuclei targeting nanocarriers have been developed for improving the target efficacy within the nucleus.

Small molecules able to bind with DNA by covalent (alkylation, inter and intra strand cross linking) and non-covalent binding mode (intercalation, major and minor groove binding through van der wall forces and

electrostatic interaction between small molecules and phosphate backbone of DNA).

Being a highly electrophilic compounds the alkylating drugs and their derivatives formed a strong covalent bond with the nucleophilic groups of DNA, resulted with the transfer of alkyl group to the nitrogen bases of nucleic acid causes DNA damage. Alkylating drugs (cisplatin, mitomycin) and their derivatives(cyclophosphamide) used as chemotherapeutics against leukaemia, lymphoma, ovarian cancer and testicular cancer etc.

The DNA targeted drug cyclophosphamide cross linked with guanine bases of double stranded DNA as a result cells are unable to uncoil and replication inhibited. Another DNA targeting drug doxorubicin efficiently damage DNA upon intercalation in activated B cell like- DLBCL (diffuse large B cell lymphoma). The natural product derived drug Etoposide efficiently inhibited replication by forming a complex with topoisomerase II as a result formation of this complex induces the double stranded break in DNA and inhibit the repair by topoisomerase II. The combination treatment of etoposide, methylprednisolone, high-dose cytarabine, and oxaliplatin can be an alternative option for patients with aggressive non-Hodgkin lymphoma (NHL) (Phase II clinical trial).

For increasing survival and prognosis rate in lymphoma drug discovery, DNA targeted drug (Covalent and non-covalent binding mode) was the one of the important targets.

**1.9 Aims and scope of the thesis:** For the development of new chemotherapeutic drug DNA is considered as one of the major targets. In lymphoma treatment the current drug regimen only increases the five-year survival rate. As an example, cyclophosphamide used in lymphoma treatment is an DNA targeted drug. So, the design, synthesis and

development of new chemotherapeutic DNA-intercalating drug is an emergent need in lymphoma management. Several biophysical studies are usually performed to understand the binding characteristics of synthesized drug and DNA. Different research group successfully synthesized the DNA intercalated naphthalimide conjugated planar molecules (amonafile and mitonafile) to target DNA. The naphthalimide analog are out of clinical trial due to the toxicity related issues. Upon introduction of different functionating group to naphthalimide moiety is an alternative approach to reduce toxicity. Moreover, the introduction of novel chemotherapeutic drug to clinics is a time consuming, lengthy and costly approach. As an alternative the concept of repurposing is an innovative approach towards chemotherapeutic drug development. Repurposing approach is beneficial over conventional drug discovery method by reducing the time frame and cost. Herein, the thesis work includes drug repurposing in the form of small molecules modification by conjugating DNA targeting moieties with non-oncogenic drug to have more potent anti lymphoma drug. Within the scope in drug discovery further the drug was delivery through a polymeric scaffold and function considered Therefore, the first objective of this thesis is to repurposing a chemotherapeutic drug (temozolomide) by conjugating with a PAMAM dendrimer for the sustained release against DL induced solid murine lymphoma. Another objective of the thesis is to repurposed the non-oncologic drug (artesunate) by remodeling with various substituted naphthalimide moieties to target DNA against DL induced solid murine lymphoma. The thesis work covers mainly on the following:

1. The design, synthesis and development of temozolomide-conjugated PAMAM dendrimer against lymphoma.

2. Repurposing and remodeling of non-oncologic drug artesunate in conjugation with naphthalimide moieties to target DNA and its implication in lymphoma. Further artesunate-naphthalimide moiety is conjugated with imaging agent FITC for studying the *in vitro* cellular internalization and apoptosis against lymphoma.

### **1.10 Achievement of the thesis:**

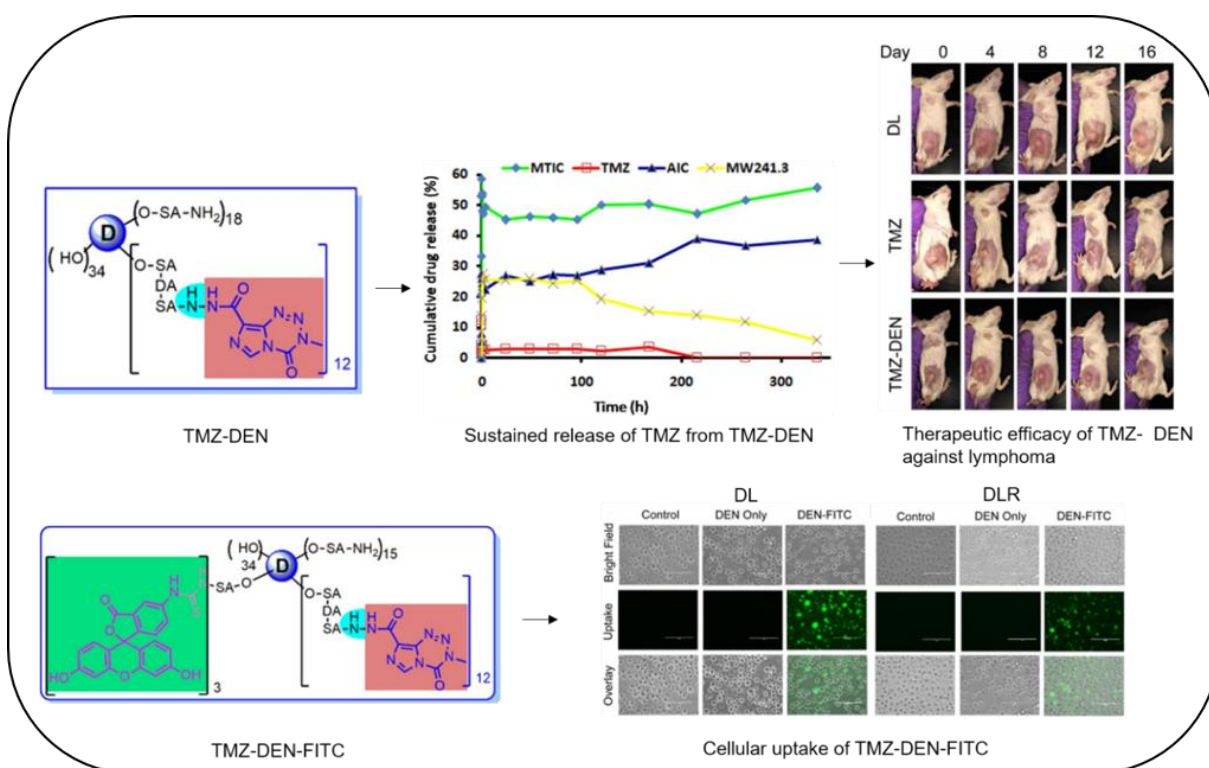
This thesis majorly covered the developing of a drug delivery system by incorporating clinically relevant drug against new disease target. Repurposing of anti-glioma drug temozolomide in lymphoma with remodeling after conjugation with PAMAM dendrimer for the sustained release of drug. This drug delivery approach of TMZ was innovative against lymphoma, increased the TMZ release from the novel nano-construct for prolong time. Imaging agent FITC was further conjugated with the novel nano-construct for studying the *in vitro* cellular uptake against lymphoma.

Successfully repurposing and modification of non-oncologic drug against lymphoma was the another achieved main target of the thesis work. The antimalarial drug artesunate was repurposed after remodeling with DNA intercalating naphthalimide moiety via different linker against lymphoma.

The current drug regimen against lymphoma only increased the five-year survival rate among the patients. However, the repurposing of oncologic and non-oncologic drug after remodeling showed better therapeutic effect against lymphoma.

## Chapter 2

# FABRICATION OF DENDRONIZED SYSTEM FOR THE DELIVERY OF ANTI-GLIOMA CHEMOTHERAPEUTIC AGAINST EXPERIMENTAL MURINE LYMPHOMA.



**2.1 Introduction:** Engineered nanosized polymeric scaffolds hold a significant promise to improve the disease condition along with treatment specific. Dendrimers used as prodrug or a vehicle for solubilization, encapsulation and site-specific targeting of small molecule drugs. The commercially available and widely used PAMAM (polyamidoamine) dendrimers played a major role in drug delivery arena due to less toxicity along with biocompatibility and increasing solubility of lipophilic drugs in aqueous media. The PAMAM dendrimers are nontoxic and have low immunogenicity. Trastuzumab conjugated with G<sub>4</sub>-PAMAM dendrimer due to the presence amine and carboxyl group which may be beneficial for imaging and delivery of drugs to HER-2 positive breast cancer cells. PAMAM dendrimer conjugated with 5-FU for targeting oncoproteins in HPV mediated cervical cancer. PEGylated -PAMAM dendrimer-doxorubicin conjugate is effective against solid tumor treatment. The hydroxy terminated G<sub>4</sub>-PAMAM dendrimer can cross the blood brain barrier (BBB) successfully. The brain delivery of donepezil was increased after conjugation with PAMAM dendrimer. The cellular internalization of the drug donepezil was increased after the conjugation along with better pharmacokinetic stability of the drug. Temozolomide is a DNA methylating acid stable lipophilic prodrug. TMZ is used to treat glioblastoma multiforme, anaplastic astrocytoma and pediatric solid tumor treatment. TMZ was also used for the treatment of B-cell and CNS lymphomas. Upon oral administration TMZ is able to cross BBB. At physiologic pH TMZ hydrolyses methyl diazonium cation. TMZ exhibited antineoplastic properties by methylation of adenine and guanine bases. As a result, TMZ gradually converted with the active metabolite MTIC (3-methyl-(1H-1,2,4-triazen-1-yl) imidazole-4-carboxamide) and the inactive 5-aminoimidazole-4-carboxamide (AIC). Sustained release of MTIC from TMZ is important for the successful drug delivery system along with the

avoidance of repeated dose of TMZ for effective antitumor activity. In glioblastoma treatment chitosan conjugated TMZ showed two to six-fold increment in cellular uptake and seven-fold increment of stability. Our objective is to conjugate PAMAM dendrimer with TMZ linked by a hydrazide bond for stabilizing and sustaining the release of active part MTIC for prolong time in tumor microenvironment against DL induced solid lymphoma model.

## **2.2 Materials and methods**

### **2.2.1 Materials**

Generation -four PAMAM dendrimer (hydroxyl terminated) was purchased from Dendritech Inc. (USA). 4-dimethylamino pyridine (DMAP), PyBOP, triethylamine (TEA), succinic anhydride, dimethylformamide (DMF), diisopropylethylamine (DIEA),  $\text{CDCl}_3$ , DMSO- $d_6$  were purchased from Sigma-Aldrich. From Acros Organics N-(tert-butoxy carbonyl)-1,2 diamino-ethane, trifluoroacetic acid (TFA), temozolomide (TMZ) were purchased. 3500 Da (molecular weight cut off) snake skin dialysis tube was purchased from Thermo Scientific. For purification and separation TLC silica gel 60 F254 plates (Merck, Germany, aluminum sheets) was used. Other solvents used in separation and purification were purchased from Merck, India. On Bruker Avance-III 400 spectrometer NMR spectroscopy was performed and as an internal standard tetramethylsilane (TMS) was used. Proton chemical shifts and coupling constants (J) were reported in ppm ( $\delta$ ) and hertz respectively.

### **2.2.2 Synthesis of the temozolomide linker**

**2.2.2.1 Compound 2:** Temozolomide (**1**) (1.8 g, 9.27 mmol) was suspended in 12 ml cold concentrated  $\text{H}_2\text{SO}_4$  and stirred for one hour at room temperature. sodium nitrite (1.9 g) in 8 mL water was added drop



wise for one hour with continuous stirring below at 4°C. The stirring will continue for overnight. Chilled ice water was poured in to the reaction mixture with continuous stirring forming solid precipitate (ppt) which was separated out, washed with cold water and filtered. A white colored product (1.5 g) was procured.  $^1\text{H}$  NMR (600 MHz, DMSO- $d_6$ )  $\delta$  8.76 (s, 1H), 3.87 (s, 3H). (Figure 3A)  $^{13}\text{C}$  NMR (150 MHz, DMSO- $d_6$ )  $\delta$  162.18, 139.49, 136.85, 129.47, 128.42, and 36.70 (Figure 3B). ESI-MS Calculated for  $\text{C}_6\text{H}_5\text{N}_5\text{O}_3$ , 195.0392; measured,  $\text{C}_6\text{H}_5\text{N}_5\text{O}_3\text{Na}$  218.0183 (Figure 3C).



Figure 1: Synthesis of temozolomide linked succinic anhydride (TMZ-SA) (Compound 5)

**2.2.2.2 Compound 3:** tButylcarbazate (0.373 g, 2.81 mmol) along with compound 2 (0.5, 2.56 mmol) were treated with 4.0 ml dry DMF and 10 ml dry  $\text{CHCl}_3$ , followed by the dropwise addition of TEA (340  $\mu\text{L}$ , 2.56 mmol) at 0°C. Finally, TBTU (0.91 g, 2.81 mmol) was given and continued the reaction for 5 minutes at 0°C and finally at 5 hours at RT. The reaction mixture was diluted by the addition of 30 ml dichloromethane and finally washed with saturated brine solution. A crude brown-orange colored product was purified through column chromatography by eluent 95: 5 ( $\text{CH}_2\text{Cl}_2$ : MeOH). The pure product (3) of 0.6 g was isolated.  $^1\text{H}$  NMR (600 MHz,  $\text{CDCl}_3$ )  $\delta$  8.95 (s, 1H-NH, b), 8.38 (1H, s), 6.85 (1H-NH, s, b), 4.00 (s, 3H), 1.44 (9H, S) (Figure 4A).  $^{13}\text{C}$  NMR (150 MHz,  $\text{CDCl}_3$ ): 158.67, 155.05, 138.54, 134.46, 129.64, 128.17, 82.01, 36.64 and 28.08 (Figure 4B). ESI-

MS Calculated for  $C_{11}H_{15}N_7O_4$ , 309.1186; measured,  $C_{11}H_{16}N_7O_4$ , 310.1233 (Figure 4C).

**2.2.2.3 Compound 4:** The compound **3** (0.95 g) was dissolved in 20 ml 1,4-dioxane and dry HCl (g) was passed slowly at  $>15^{\circ}C$  for half an hour. The reaction was continued for another twelve hours at room temperature. After decanting the solvent, the solid white solid product was isolated and successively washed with dry diethyl ether and dry acetone and finally dried under reduced pressure. The pure white product (**4**) (0.73 g) was isolated.  $^1H$  NMR (400MHz, DMSO- $d_6$   $D_2O$  exchange):  $\delta$  8.85 (1H, s), 3.85 (3H, s) (Figure 5A).  $^{13}C$  (100 MHz, DMSO- $d_6$ ): 158.88, 138.91, 135.66, 129.15, 126.70, 36.36 (Figure 5B). ESI-MS Calculated for  $C_6H_7N_7O_2$ , 209.0661; measured,  $C_6H_8N_7O_2$ , 210.1203 (Figure 5C).

**2.2.2.4 Compound 5:** The Compound **4**, temozolomide hydrazide (0.1 g, 0.408 mmol) was taken in 5 ml dry DMF along with DIEA (52.7 mg, 71  $\mu L$ , and 0.408 mmol) and stirred for 10 minutes at RT. In the reaction mixture solid succinic anhydride (49 mg, 0.49 mmol) was added. After completion of the reaction, an excess of dry ether was added to separate the solid precipitated and the solid was treated with a mixture of solvent ( $CHCl_3$ ,  $Et_2O$ , and MeOH) to get the desired purified product. The product (**5**) (110 mg) was isolated as the pure and confirmed through several characterizations.  $^1H$  NMR (DMSO-  $d_6$ , 600MHz)  $\delta$  12.10 (1H, s), 10.18 (1H, s), 8.85 (1H, s), 3.86 (3H, s), 2.46-2.47 (4H, m) (Figure 6A).  $^{13}C$  (DMSO- $d_6$ , 150 MHz):  $\delta$  174.60, 170.65, 159.04, 139.61, 135.57, 129.18, 36.69, 40.35, 29.29 (Figure 6B), ESI-MS Calculated for  $C_{10}H_{11}N_7O_5$ , 309.0822; measured,  $C_{10}H_{11}N_7O_5Na$ , 332.1129 (Figure 6D).

## Dendrimer conjugated TMZ

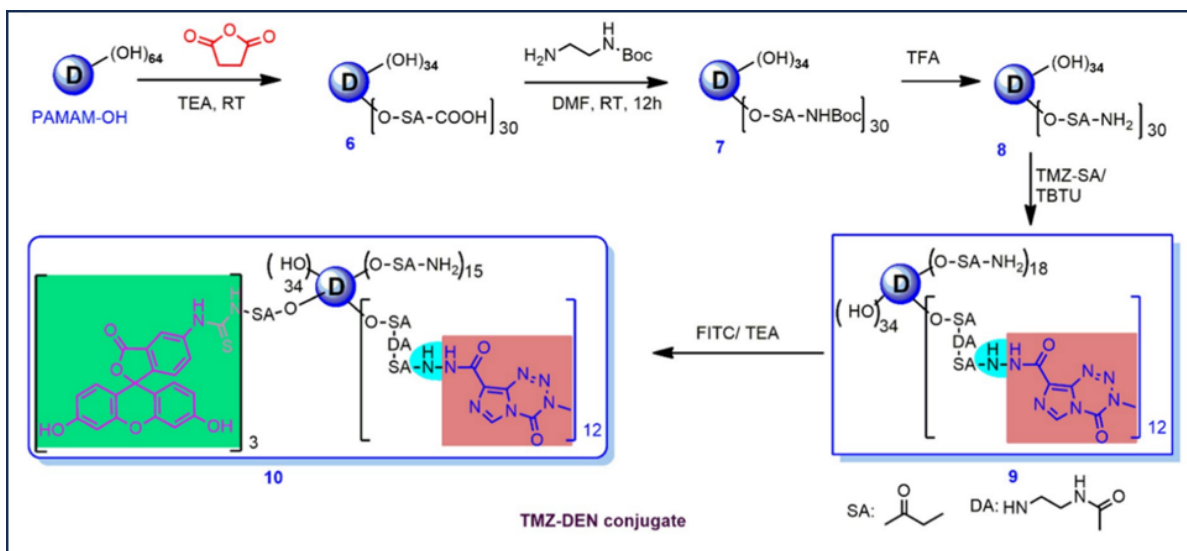


Figure 2: Synthesis of TMZ-DEN construct linked by hydrazide bond. TMZ-DEN conjugate synthesis linked by hydrazide bond (Compound 9), and synthesis of TMZ-DEN conjugated FITC (TMZ-DEN-FITC) (compound 10)

**2.2.2.5 Compound 6 (D-SA):** The mixture of G4-dendrimer (1.5 g, 0.10 mmol) in TEA (0.67 mL, 5.04 mmol) and DMAP (0.256 g, 2.1 mmol) were taken in 20 ml dry DMF addition of followed by the succinic acid (0.5g, 5.04 mmol) and continuously stirred for overnight and finally purified through dialysis membrane against DMF solvent. After purification, volatiles were evaporated to get the solid amorphous product. Through NMR and MALDI-TOF characterization it was established that the 30 succinic acid linking (D-SA) takes place. <sup>1</sup>H NMR (DMSO-d<sub>6</sub>, 600MHz): δ 8.18-7.71, 4.07- 3.92, 3.58, 3.44-3.34, 3.35-3.20, 3.18-2.97, 2.70-2.56, 2.55-2.32, 2.32-1.90 (Figure 7A). MALDI-TOF: m/z 16564.409 (Figure 7B)

**2.2.2.6 Compound 7 (D-NH-Boc):** In the suspension of D-SA conjugate (1.5 g, 0.0834 mmol) in dry DMF (10 mL), N-hydroxy succinimide (NHS; 0.46 g, 4.0 mmol), 4- dimethyl aminopyridine (DMAP; 0.204 g, 1.7 mmol),

N, N-Diisopropylethylamine and O- (Benzotriazol-1-yl)-N, N, N', N'-tetramethyl uranium tetra fluoroborate (TBTU; 1.28 g, 4.0 mmol) added sequentially in a stirring condition. At RT, in an inert environment the reaction mixture was stirred for one hour. Dropwise *N*-(*tert*-Butoxycarbonyl)-1,2-diaminoethane (0.642 g, 4.0 mmol) was added and continued the reaction for 12 hours. Finally, under reduced pressure the resultant reaction mixture was concentrated, and in 10 ml DMF the solid part was re-dissolved. The solution was poured into a membrane dialysis bag (MWCO 3kDa) and dialyzed against DMF and deionized water over a period of 24 hours. <sup>1</sup>H NMR (DMSO-d<sub>6</sub>, 600MHz): δ 8.12-7.71, 6.83-6.73, 4.03-3.94, 3.46-3.35, 3.33-3.23, 3.2-2.93, 2.78-2.6, 2.56-2.44, 2.42-2.31, 2.29- 2.15, 1.44-1.31(Figure 8A). MALDI-TOF: m/z 21844.11(Figure 8B).

**2.2.2.7 Compound 8 (D-SA-NH<sub>2</sub>):** The D-NH-Boc (1.8 g, 0.08 mmol) dissolved in anhydrous 15 ml DMF along with 15 ml TFA. After stirring for 12 hours at RT, volatiles were evaporated. The final product was re-dissolved in 10 ml DMF and dialyzed in a dialysis membrane (CO: 3kD) to get the pure product D-SA-NH<sub>2</sub> (1.5 g). <sup>1</sup>H NMR (DMSO-d<sub>6</sub>, 600MHz): δ 8.69-8.1, 8.1-7.8, 7.80-7.62, 4.13-3.9, 3.69-3.31, 3.31-3.21, 3.21-2.98, 2.93-2.76, 2.76-2.71, 2.68-2.51, 2.44-2.21(Figure 9A). MALDI-TOF: m/z 17355.438(Figure 9B)

**2.2.2.8 Compound 9 (TMZ-DEN):** Temozolomide succinic acid (TMZ-SA; 0.213 g, 0.692 mmol) was suspended in a mixture 3 ml DMF. N, N-diisopropylethylamine (0.148 mL, 0.922 mmol), N-hydroxy succinimide (NHS, 0.106 g, 0.92 mmol), and then O-(Benzotriazol-1-yl)-N, N, N', N'-tetra methyl uranium tetra fluoroborate (TBTU; 0.223 g, 0.692 mmol) was added to reaction mixture sequentially. After stirring for 6 hours at RT, the D-SA-NH<sub>2</sub> (0.3 g, 0.0154 mmol) was dissolved in 1ml of DMF for successful conjugation. For the purification of the crude product, dialysis

was performed by following standard protocol against DMF solvent using snake-skin dialysis membrane cutoff 3.0 kD. Under vacuum environment the resulting evaporated reaction mixture was re-dissolved in 2 ml distilled water and dried to get the pale yellowish-white product (D-TMZ). <sup>1</sup>H NMR (DMSO-d<sub>6</sub>, 600MHz): δ12.23, 10.03, 8.88, 8.59-8.06, 8.01-7.83, 4.04, 3.89, 3.61-3.36, 3.19-3.11, 3.11-2.95, 2.87, 2.69-2.54, 2.50-2.18(Figure 10A). MALDI-TOF: m/z 20604.656 (Figure 10B)

**2.2.2.9 Compound 10 (TMZ-DEN-FITC):** The TMZ-DEN (**9**) (0.2, 0.009 mmol), was dissolved in 5 ml DMSO and TEA (0.005g, 0.057 mmol). At RT FITC (0.015 g, 0.038 mmol) was given to the reaction mixture for 12 hours. After that, in 10 ml anhydrous DMSO the resulting reaction mixture was re-dissolved and finally dialyzed against dialysis membrane(CO: 3kD) to get the desired product TMZ-DEN-FITC (0.15 g). <sup>1</sup>H NMR (DMSO-d<sub>6</sub>, 600MHz): δ10.20, 10.14, 10.01, 8.87, 8.30-7.71, 7.61, 7.30-7.14, 6.69, 6.57, 3.99, 3.87, 3.66-3.35, 3.34-3.2, 3.2-2.97, 2.95-2.63, 2.42-2.06(Figure 11A). MALDI-TOF: m/z 21.988.819(Figure 11B).

#### **2.2.2.10 Ultra-Performance Liquid Chromatography (UPLC) Analysis:**

The synthesized drug conjugates were scanned by Waters UPLC instrument attached with an PDA detector, binary pump and auto sampler interfaced with Masslynk software. The chromatogram was monitored at 328 nm. As a mobile phase 0.1 % formic acid enriched water/acetonitrile was freshly prepared and degassed. The ACQUITY UPLC BEH C18, 1.7 μm, 2.1x100 mm column was used for this analysis. Initial condition 95:5 the flow was used for first 2.5 minutes and then 50:50 gradient flow used for 3 minutes and finally 95:5 gradient flow used for another 4 minutes, with a constant rate of flow maintained at 0.3 ml/min. 1 mg/ml TMZ-DEN conjugate solution was prepared in acetonitrile for UPLC analysis.

(Figure 12).

#### **2.2.2.11 Matrix-assisted laser desorption ionization-time of flight (MALDI-TOF) and Electrospray ionization (ESI) mass spectra**

Mass spectrum was obtained from Waters QToF Micromass electrospray ionization (ESI) were recorded). In AXIMA-CFR Plus spectrometer system associated with a pulsed nitrogen laser (Shimadzu- Kratos, UK) the MALDI-TOF mass spectra were recorded and operated in a linear mode using a matrix of 2,5-dihydroxybenzoic acid. As an external standard 12300 Da cytochrome c was used. The solution of 2 mg of dendrimer conjugates were dissolved in 1 ml of ACN: H<sub>2</sub>O (1:1) mixture. In 500 ml water/ACN (1:1) mixture (0.14% TFA vol/vol), 10 mg of matrix was added and dissolved. The analytical samples were prepared by dissolving two ml of dendrimer solution in 20 ml of matrix solution. By using over layer method, the MALDI-TOF samples were prepared. At first only 1 ml of matrix solution was deposited onto the stainless-steel plate. Dendrimer-matrix solution was allowed to deposited on the solid matrix and dried at 22-25°C.

#### **2.2.2.12 Measurement of hydrodynamic diameter and zeta potential**

By using a Zetasizer Nano ZS (Malvern Instrument Ltd., MAL1049758, Worcester, U.K) associated with a 50 m WHe-Ne laser (633 nm) the particle size and zeta potential of TMZ-DEN was determined by dynamic light scattering (DLS). The 0.5 mg/ml TMZ-DEN conjugate solution was prepared in HPLC water. Through a 0.45-micron Millipore filter (Millex-HN) the solution was filtered and the DLS measurement were performed at 25 °C with a 173° scattering detector angle.

### **2.2.2.13 HR-TEM analysis**

To study the shape, size and dot's structure the TEM-images of TMZ-DEN conjugates were captured in HR-TEM (FEI Tecnai G2 F 20, Netherlands). In ethanol the TMZ-DEN conjugate was dispersed. A drop of dispersed particle was placed and dried on a 300-mesh carbon-coated Cu grid.

### **2.2.2.14 *In vitro* drug release study:**

The sustained liberation of metabolites from TMZ-DEN was observed at 37°C in 0.1 M, PBS buffer (pH 7.4). In a water bath-maintained temperature at 37°C, TMZ-DEN (2 mg/ml) and TMZ-SA solution(1mg/ml) were kept with continuous stirring. At different time interval the samples (500 µl) were taken from the water bath and scanned by quattro micro-API 4000 mass spectrometer (Waters). BEH C18 1.7 µm column (2.1×100 mm) was used for peak separation. With a constant rate of flow maintained at 0.3 ml/min, Water and acetonitrile (95:5, v/v) mixture was used as mobile phase system. Initially with a gradient flow 95:5 (3 minutes),50:50 (4 minutes),95:5 (6 minutes) used. One µl of sample solution collected at various time points were injected for the drug release study at 20°C.

### **2.2.2.15 Mice**

The female 6–8-week-old CD-1 mice were procured from the Hylasco Bio-Technology Pvt. Ltd, Hyderabad. All the animals were housed under clean and germ-free environment in the animal house of the department in compliance with the CPSEA guidelines.

### **2.2.2.16 Cell lines and DL induced murine lymphoma model**

Raji cell was obtained from ATCC, Manassas, USA. Highly metastatic murine lymphoma cell line DL and doxorubicin resistant DL (DLR) cells

were cultured and maintained in complete RPMI-1640 media supplemented with 10% FBS and antibiotics. DL induced solid murine lymphoma and maintained in the peritoneum of female CD-1 mice. Into the right flank of female CD-1 mice the solid tumor was induced by injecting  $10^6$  DL tumor cells (in 100  $\mu$ L HBSS) [89]. On day eight, the average tumor volume was reached to  $151.5 \pm 1.18 \text{ mm}^3$ , as a result the drug treatment was initiated. Thrice a week the tumor volume ( $\text{cm}^3$ ) was measured by a caliper using the formula: tumor Volume ( $\text{mm}^3$ ) =  $1/2 [\text{length} \times (\text{width})^2]$

Animals were sacrificed when the tumor width was more than 25 mm and without any distress condition raised in mice. Survival of the animals were recorded for treated and untreated groups after the induction of tumor inoculation.

#### **2.2.2.17 Cell viability assay**

Cell viability of tumor cells and normal human cells of the novel synthesized TMZ-DEN, dendrimer and free TMZ was evaluated by a colorimetric XTT assay (Roche, Indianapolis, IN). In a 96 well plate  $5 \times 10^3$  cells/well tumor cells, normal human peripheral blood mononuclear cells (PBMC), NIH/3T3 cells were cultured and incubated at  $37^\circ\text{C}$ , 5%  $\text{CO}_2$  for 18 hours in a concentration dependent manner of the dendrimer, TMZ and TMZ-DEN construct. In a Synergy HT, BioTek, USA, plate reader the OD was taken at 450 nm. The percent of live cells were calculated by using the formula [103].

$$\% \text{ Cell Viability} = \frac{\text{Experimental OD}_{450}}{\text{Control OD}_{450}} \times 100$$

#### **2.2.2.18 Cell growth inhibition assay**

Through MTT assay the growth inhibition potential of dendrimer, TMZ only and TMZ-DEN construct against DL, doxorubicin resistant DL and Raji



was studied. In a 96 well plate  $5 \times 10^3$  cells/well tumor cells were cultured and incubated at 37°C ,5% CO<sub>2</sub> for 48 hours of the dendrimer, TMZ and TMZ-DEN construct. In a Synergy HT, BioTek, USA plate reader, the OD was taken at 570 nm [103]. The cell growth inhibition percentage was calculated by using the formula mentioned below.

$$\% \text{ Growth Inhibition} = [1 - \frac{\text{Experimental OD}_{570}}{\text{Target OD}_{570}}] \times 100$$

### **2.2.2.19 Cytotoxicity assay**

Through cytotoxicity assay (CytoTox 96 Cytotoxicity assay kit from Promega, USA), the cytotoxic activity of dendrimer, TMZ and TMZ-DEN against tumor cells was measured. For 18 hours, in a 96 well plate  $5 \times 10^3$  tumor cells/well were cultured and incubated at 37°C in a concentration dependent manner of the dendrimer, TMZ and TMZ-DEN construct. Percent-specific lysis was determined from the formula mentioned below [103].

$$\% \text{ Cytotoxicity} = \frac{(\text{Experimental} - \text{Effector Spontaneous} - \text{Target Spontaneous})}{(\text{Target Maximum} - \text{Target Spontaneous})} \times 100$$

### **2.2.2.20 Apoptosis & cellular internalization assay**

The Initiation of apoptosis by free TMZ and TMZ-DEN was treated for 12 hours against parental DL and DLR (doxorubicin resistant DL) cells. Use of dendrimer only act as positive control group along with the untreated cells. After washing with PBS, the cells were stained with FITC-conjugated Annexin V for half an hour and finally staining with PI for 5 minutes. After incubation the cells were treated with Annexin V buffer. Under fluorescence microscope (EVOS FL Cell Imaging System equipped with Plan Fluor, 40X, NA 0.75 objective, Life Technologies, USA) FITC-conjugated Annexin V positive cells were visualized. The

cellular uptake was studied by the treatment of TMZ-DEN-FITC in parental DL and doxorubicin resistant DL cells, with an intracellular green fluorescence inside the cells.

#### **2.2.2.21 Hemolysis assay**

The blood samples were incubated for 4 hours with a concentration (10-250  $\mu$ M) dependent manner of dendrimer, free TMZ and TMZ-DEN. The aliquot of the blood samples was centrifuges for 5 minutes. In a 96 well plate 25  $\mu$ l of blood plasma along with 225  $\mu$ l of Drabkin's reagent was added and properly mixed along with 300 rpm lateral agitation and the OD was measured at 540 nm by using Synergy HT Multi- Mode Microplate Reader BioTek, USA [104].

The lysis of hemoglobin was studied by the dilution (100-fold) of whole blood in Drabkin's reagent. The OD was measured at 540 nm. The PBS and saponin (2 mg/ml final blood concentration) were used as negative and positive control respectively. The plasma samples without any additives were considered as basal conditions. For standard calibration curve the bovine hemoglobin (Sigma) solution (0.07–3.9 mg/mL) treated with Drabkin's reagent. The hemolysis percentage was calculated by dividing the free plasma hemoglobin (mg/ml) by total hemoglobin (mg/ml) multiplied by 100. Experiment was repeated three times [104].

#### **2.2.2.22 Statistical analysis**

For each experimental group ( $n = 3$  to  $5$ ) the mean  $\pm$  standard deviation (SD) value was calculated. Differences among as well as between the groups were quantified by ANOVA and Holm-Sidak post hoc multiple comparison tests by using the (GraphPad) PRISM statistical analysis software. By using GraphPad Prism software (GraphPad) the Survival plots (Kaplan-Meier analysis) were generated, and statistical significance

between the groups was analyzed by means of the log-rank (Mantel-Cox) test.  $p < 0.05$  was considered as statistically significant. \*0.05, \*\*0.01, \*\*\*0.001, \*\*\*\*0.0001.

## **2.3 Results:**

### **2.3.1 Chemistry:**

The presence of three NMR peaks at  $\delta$  10.18, 8.85 and 3.86 and disappearance of  $\delta$  12.12 confirmed the conjugation of succinic anhydride linked TMZ with PAMAM dendrimer (Figure 13A). NMR data suggested that twelve molecules of TMZ-SA conjugated with the PAMAM dendrimer. For the cellular internalization study FITC was tagged with TMZ-DEN, confirmed by the presence of the characteristic peaks at  $\delta$  7.61, 7.3, 6.69 and 6.57 (Figure 13A). MALDI-TOF data confirmed the attachment of 12 molecules of TMZ-SA resulted with the increased molecular weight of DEN-SA-NH-TMZ than DEN-SA-NH<sub>2</sub> (Figure 13B). The observed hydrodynamic diameter of TMZ-DEN construct was  $239 \pm 33.9$  nm (Figure 13C) and the zeta potential was  $37.6 \pm 3.3$  mv (Figure 13D). Presence of free amine and amide group on the dendrimer carrier was the reason behind positive zeta potential. The TMZ-DEN construct was positively charge due to the presence of amine and nitrogen group on TMZ surface. From DLS study it was evident that the positive charge assisted to aggregate in aqueous solution resulted in larger particle size. The 7-9 nm particle along with crystalline fringes was studied by TEM (Figure 13E).

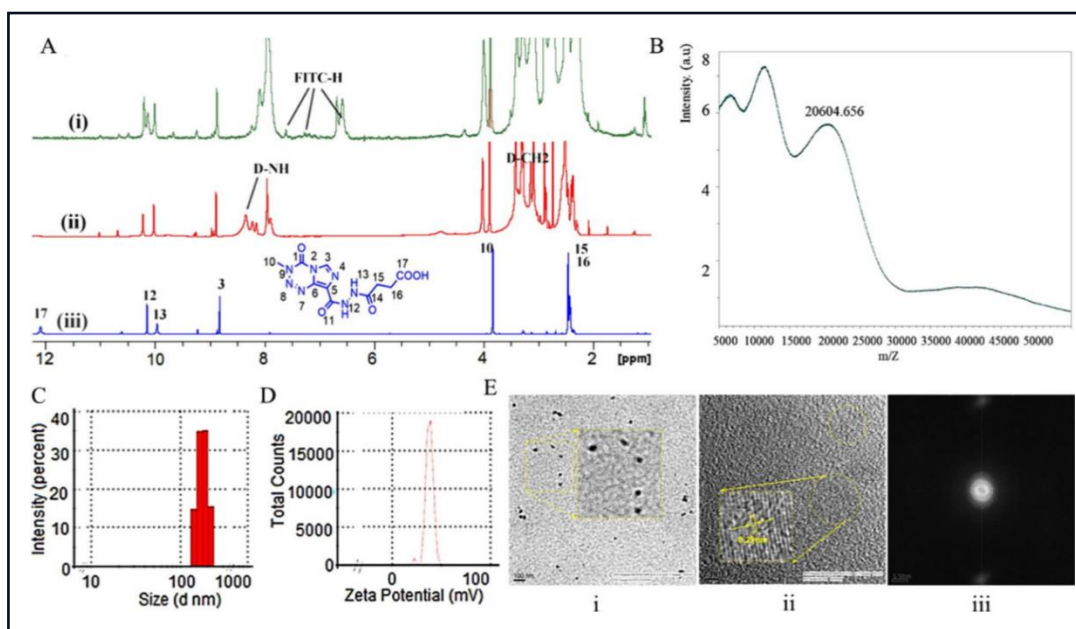


Figure 13: TMZ-DEN conjugate characterization (A) comparison of NMR (<sup>1</sup>H) spectrum (i) TMZ-DEN-FITC conjugate, (ii) TMZ-DEN nano-construct, and (iii) TMZ-SA (B) MALDI-TOF spectra of TMZ-DEN (C) Size distribution of TMZ-DEN conjugates (nm) (D) Zeta-Potential (mV) of the TMZ-DEN conjugate E. TEM images of TMZ-DEN conjugate i. particle size of TMZ-DEN ii. The crystalline fringes of the novel construct iii. SAED pattern of crystalline characters.

**2.3.2 Drug release study:** Release study of different degraded molecules was monitored by mass and percentage of relative intensity m/z (AIC+NH<sub>4</sub>) =146, MTIC=168, TMZ=194, TMZ-SA+ Na= 332 and m/z=241 (Figure 14 E). In PBS (Ph=7.0) from TMZ-DEN the MTIC, AIC, TMZ and m/z 241.3 were released. From the drug release study, it was clear that the TMZ concentration decreased gradually and the active metabolite's concentration (MTIC) was increased for 4 hours (Figure 14A). In PBS (pH=7.0) the TMZ-SA release study indicated that the decreased TMZ concentration along with increased inactive AIC metabolite concentration (Figure 13B). In citrate buffer (pH =5.4) the release of active metabolite MTIC increased gradually from TMZ-DEN with time (Figure

14C). Release kinetics of TMZ-DEN from PBS (pH =7) indicated the higher stability of active metabolite MTIC than the inactive metabolite AIC (Figure 14D).

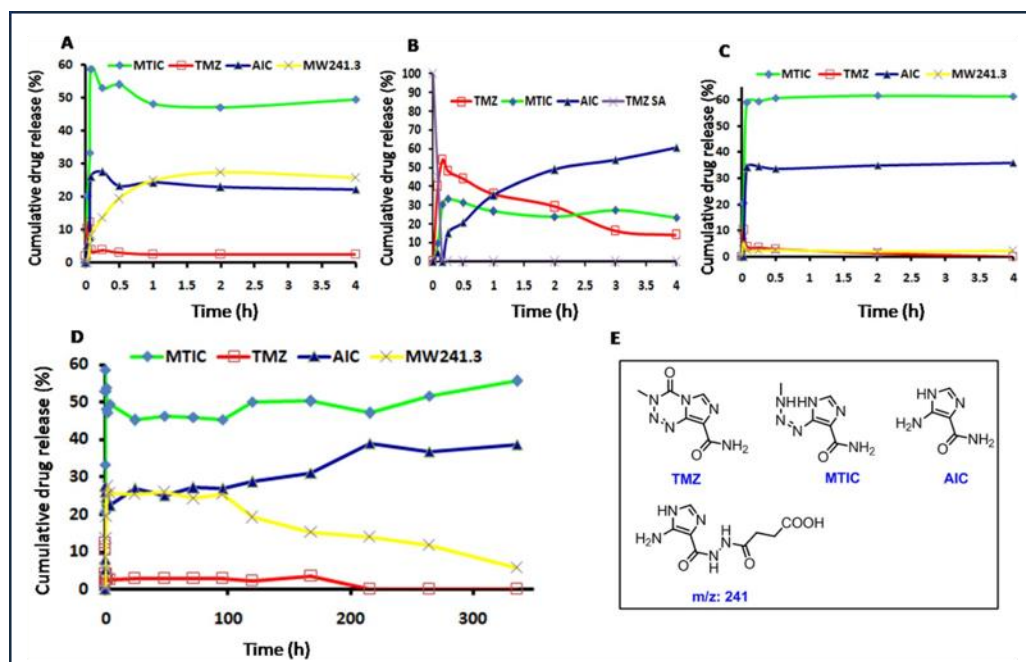


Figure 14: Sustained drug release study from TMZ-DEN construct by LC/MS (A) Release kinetics of TMZ and metabolites in PBS (pH 7.0) (B) *In vitro* release of TMZ and metabolites from TMZ-SA in PBS (pH 7.0) (C) In citrate buffer (pH 5.4) from TMZ-DEN, TMZ and metabolites released (D) Release kinetics TMZ and metabolites in PBS buffer (pH 7.0) for 14 days (E) Structures of TMZ and TMZ metabolites detected during the release study by LC/MS.

**2.3.3 In vitro tumoricidal activity:** Tumoricidal activity of TMZ-DEN conjugates was studied against DL and DLR cells in concentration dependent manner. At highest concentration (250  $\mu$ M) of TMZ-DEN the percent viability was reduced to <60% compared to free drug (Figure 15A). The percent cellular viability was reduced as compared to free drug in DL resistant cell-line. This data suggests that the synthesized construct was effective in reducing the cell viability against drug resistant cell line.

The novel synthesized construct showed significant growth inhibition in all the TMZ-DEN concentration. At highest concentration the 100% growth inhibition was observed in TMZ-DEN conjugate, indicated the highest efficacy of the conjugate. Whereas the dendrimer alone has no impact as such on the growth inhibition. At highest concentration TMZ-DEN showed 60% growth inhibition on resistant DL cell line. TMZ-DEN showed significant cytotoxicity as compared to concentration dependent free drug alone in both DL and DLR cell lines. IC 50 values of the conjugate TMZ-DEN was higher both in DL and DLR cell line as compared to free TMZ.

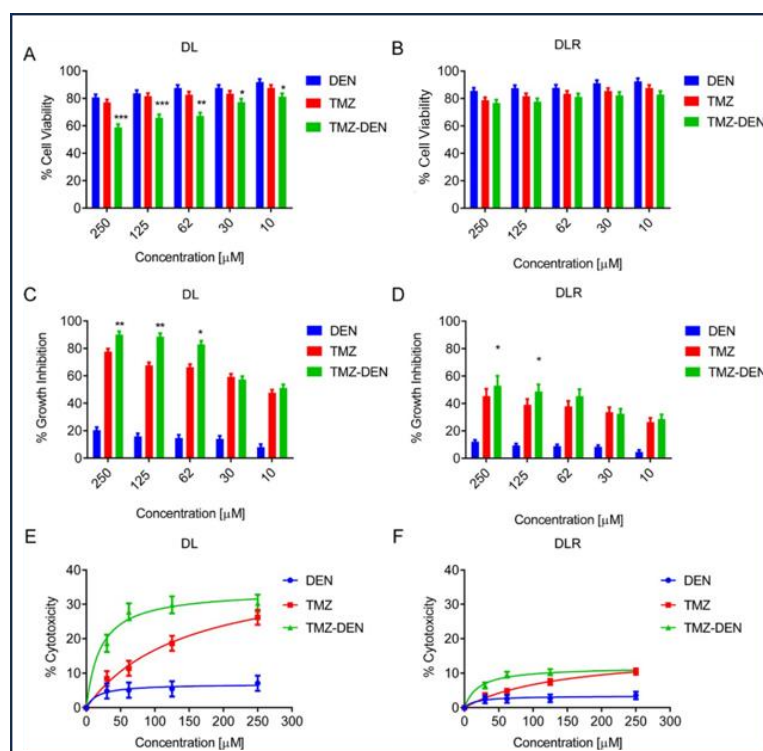


Figure 15 *In vitro* anti-tumor activity of TMZ-DEN against DL and DLR cells. Percentage of Cell viability for 18 hours studied by the XTT assay against (A) parental DL and (B) DLR cells. Percentage of growth inhibition by MTT assay (48 hour) of (C) DL and (D) DLR cells. Percentage of cell cytotoxicity by LDH assay (18 hour) of (E) DL and (F) DLR cells.

**2.3.4 Biocompatibility study of TMZ-DEN:** As compared to free TMZ (250 $\mu$ M) showed significantly higher reduction in viability as compared to

TMZ-DEN conjugate against NIH3T3 cells (Figure 16A). Free TMZ showed more susceptibility as compared to free dendrimer and TMZ-DEN against human peripheral blood mononuclear cells (PBMC) (Figure 16B). At 250 $\mu$ M concentration free TMZ showed 25% hemolysis, while free dendrimer and TMZ-DEN was well tolerated to ward RBC (less than 5% lysis). Also, at lowest concentration (10-30  $\mu$ M) only TMZ demonstrated significant lytic activity as compared to free dendrimer and TMZ-DEN construct (Figure 16C).

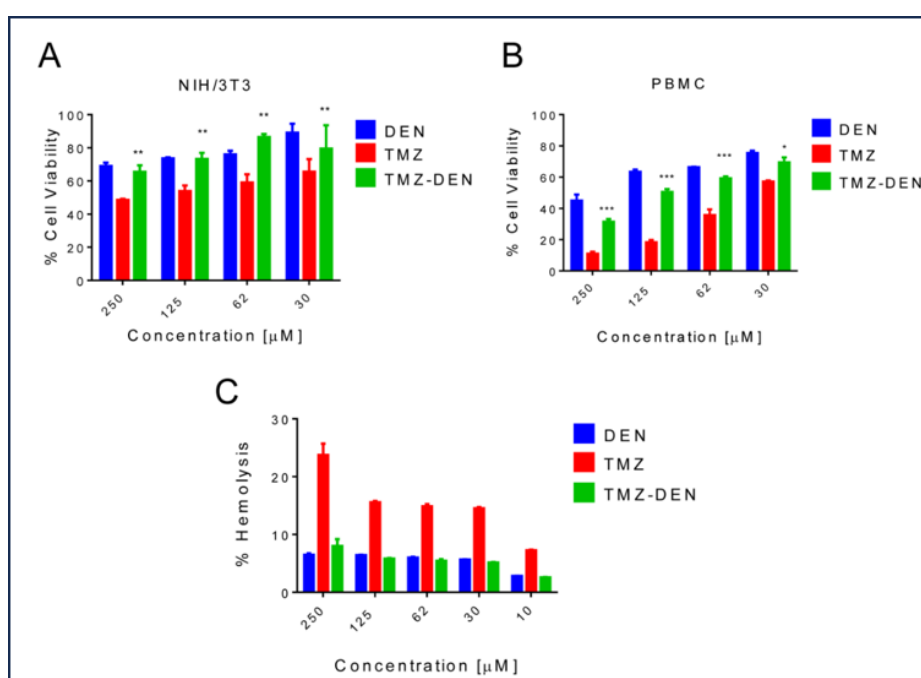


Figure 16 Biocompatibility study of TMZ-DEN. Effects of free dendrimer (DEN), free drug (TMZ) and TMZ loaded dendrimer (TMZ-DEN) on the viability of (A) NIH/3T3 mouse fibroblast and (B) human PBMC. (C) Hemolysis of red blood cells in the presence of indicated formulations. Data presented as Mean $\pm$  SD with triplicate measurements.

**2.3.5 Induction of apoptosis and cellular uptake by TMZ-DEN conjugate:** The damage to DL cells caused by TMZ-DEN construct via apoptosis, as a result propidium iodide uptake was facilitated. The DNA damage in DL cells caused by TMZ-DEN (Figure 17A). In doxorubicin



resistant DL cells TMZ-DEN conjugate also showed the uptake of propidium iodide due to the induction of apoptosis (Figure 17B). was increased the cellular internalization in DL cells (Figure 17C). DLR cells exhibited lesser TMZ-DEN-FITC uptake than DL cells. From the comparison study it was clear that the DLR cells are also susceptible to novel synthesized nano construct (Figure 17D).

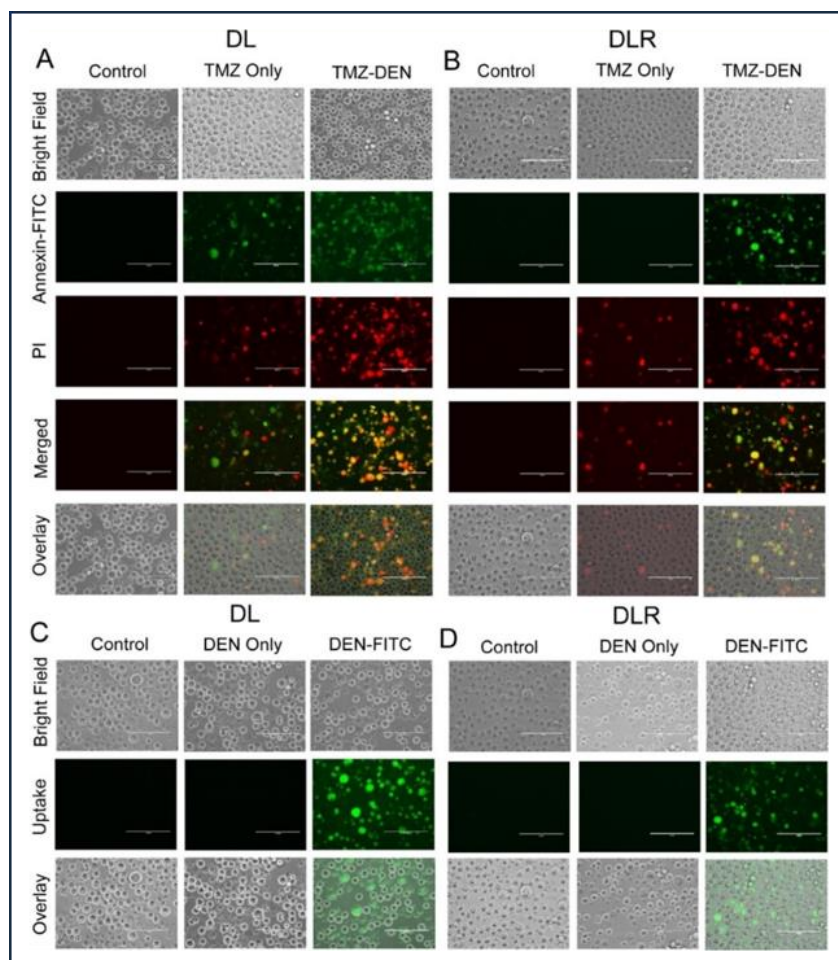


Figure 17 Induction of apoptosis by TMZ (50  $\mu$ M drug treatment for 8 hour) and TMZ-DEN conjugate (50  $\mu$ M drug treatment for 8 hour) against (A) parental DL (B) doxorubicin resistant DL cells, control (no drug treatment). Induction of cellular internalization by TMZ-DEN-FITC and dendrimer only against (C)parental DL (D) doxorubicin resistant DL cells, incubated for 8 hours. Control (no drug treatment). Images were taken from an inverted microscope.



### **2.3.6 *In vivo* therapeutic efficacy and inhibition of metastasis:**

DL induced a solid highly metastatic murine lymphoma model was used to study the *in vivo* therapeutic efficacy of TMZ-DEN nano construct. The DL cells ( $5 \times 10^6$ ) were inoculated in the right flank of 6–8 week-old female CD-1 mice. After 8-10 days a palpable tumor was formed and was continued to grow up to a sizeable tumor mass. A treatment schedule was formulated by using the TMZ-DEN construct (10 mg/kg body weight). TMZ-DEN was given altogether in two batches (five doses each), with seven days of interval between two batches. At day 16 the tumor volume was reduced significantly in TMZ-DEN treated group as compared to untreated group (Figure 17B). On day 30 the tumor volume was significantly reduced in TMZ-DEN treated group as compared to the untreated DL group, where the tumor growth increases (Figure 18 C-E). The weight of the animal having DL tumor was increased from  $17.35 \pm 1.34$  to  $31.45 \pm 0.83$  in untreated DL group. The weight of the animal having DL tumor after treatment with TMZ and TMZ-DEN was reduced to  $23.82 \pm 1.20$  and  $22.85 \pm 2.86$  respectively. After tumor inoculation tumor volume was reduced in TMZ-DEN group as compared to TMZ treated group and untreated group at day 30. The weight of the tumor volume of DL induced untreated group and TMZ-DEN treated group were  $6.88 \pm 0.22$  and  $0.12 \pm 0.002$  respectively. It was also evidenced from the animal study that the TMZ-DEN treated group was able to inhibit metastasis by reducing the vascularized organs weight than the untreated DL group. Kaplan Meier survival analysis study indicated that TMZ-DEN showed 70% survival up to day 60 and beyond whereas DL untreated group and TMZ showed survival only day 35 and 55.

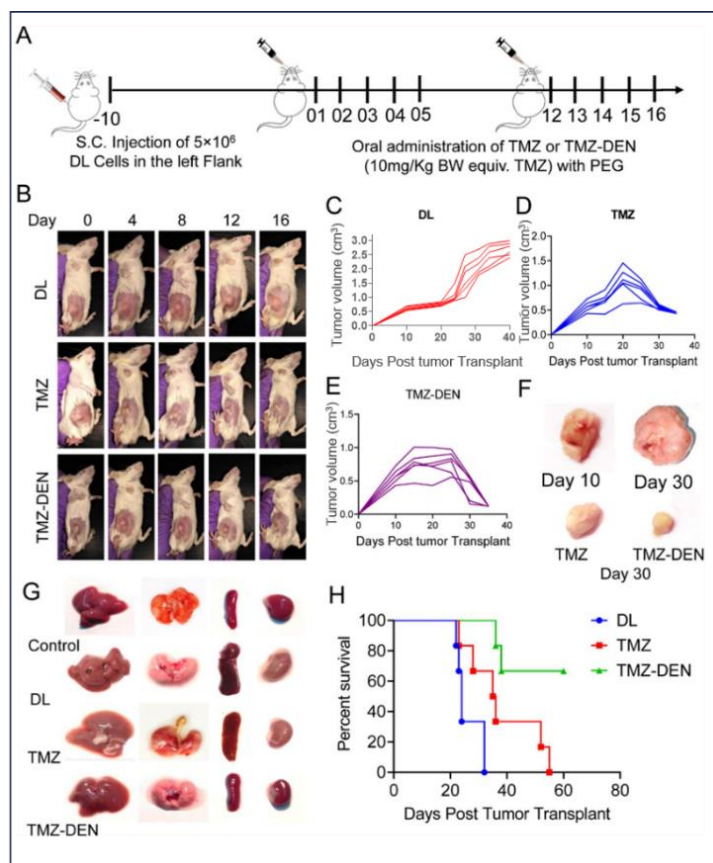


Figure 18: In vivo therapeutic efficacy of TMZ-DEN conjugate against highly metastatic murine solid lymphoma. (A) Treatment schedule starting from induction of DL tumor cells. After induction of solid tumor, 10 mg/kg TMZ and TMZ-DEN was administered orally in two batches (seven days interval after five doses) (B) In DL control group, TMZ and TMZ-DEN treated group tumor volume was measured at four-day interval. (C-E) The tumor was grown up to day 40 in untreated (C), TMZ treated(D) and TMZ-DEN treated (E) group (F) Tumor size of untreated, TMZ and TMZ-DEN treated group after sacrificed the mice at day 30. (G) Pictorial images of different vascularized organs (liver, lung, spleen and kidney) of control (normal mice), DL (untreated group), TMZ and TMZ-DEN treated group on day 30. (H) After tumor transplantation the survival analysis of untreated, TMZ and TMZ-Den treated group.

From the histopathology of liver and spleen the TMZ-DEN treated group showed the areas closely resembled with the normal tissue architecture and

removal of tumor infiltrated cell, whereas in DL untreated group extensive metastasis occurred with the infiltration of tumor cells. Treatment with TMZ only in liver partially restricted tumor metastasis by preventing the tumor infiltration as compared to untreated control group.

In untreated DL group the extensive metastasis occurred in spleens cortex and medulla region. The lost splenic architecture was restored by the use of TMZ-DEN conjugate. Significant differences in the number of metastatic tumor foci observed between untreated and treated group (Figure 19B).

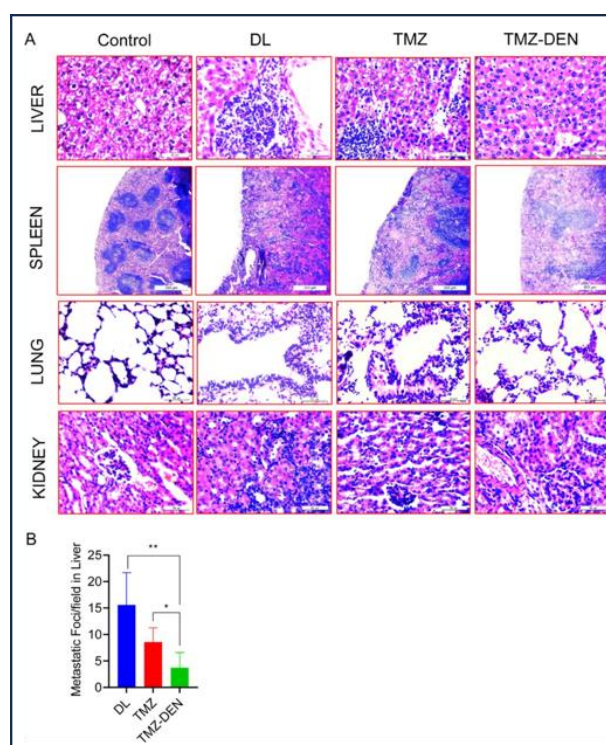


Figure 19: The novel construct TMZ–DEN inhibits metastasis of vascularized organs like liver, spleen, lung and kidney. (A) Histopathology study of the vascularized organs of healthy control, untreated, and treated groups. (B) Estimation of liver metastatic foci untreated and treated group quantitatively.

## 2.4 Discussion & Conclusion:

The mechanism of action of temozolomide associated with the methyl guanine DNA-methyl transferase (MGMT), plays a major role in

temozolomide induced resistance. Our result indicates that TMZ-DEN restricts uncontrolled growth of lymphoma and has potential as an alternative drug against lymphoma and doxorubicin resistant lymphoma cells. TMZ-DEN exhibited significant *in vitro* cytotoxicity as compared to free TMZ Against DL and doxorubicin resistant DL cells. The cellular uptake was increased in FITC conjugated TMZ-DEN as compared to free TMZ and PAMAM dendrimer in DL cells. The novel nano construct has a profound and significant effect on better therapeutic efficacy in DL induced murine lymphoma model. The novel PAMAM dendrimer conjugated TMZ has associated with significant advancement of lymphoma and doxorubicin-resistant lymphoma.

## 2.5 Characterization of Temozolomide conjugates (Synthesis of TMZ linked succinic anhydride (TMZ-SA), temozolomide-dendrimer (TMZ-DEN) conjugated by hydrazide bond and FITC conjugated with temozolomide-dendrimer)

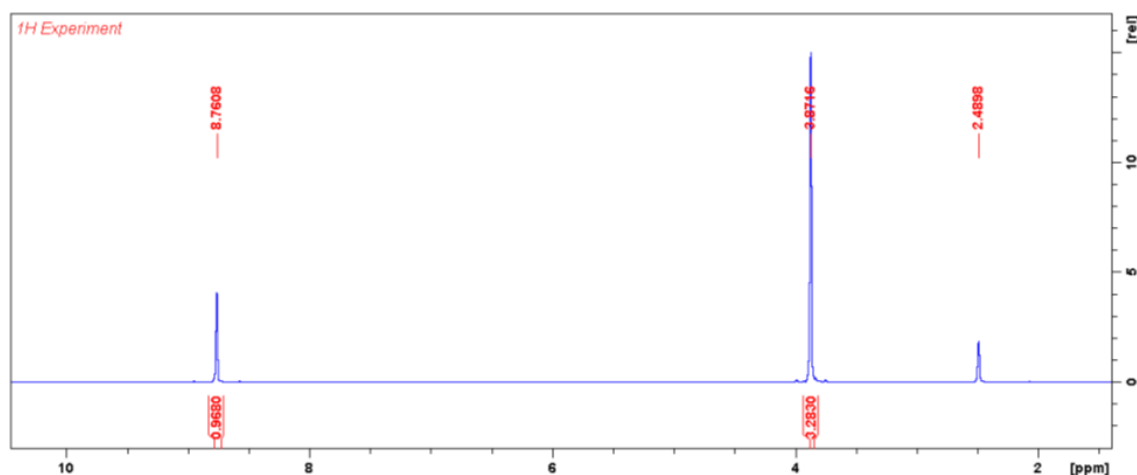


Figure 3A:  $^1\text{H}$ -NMR (600 MHz, DMSO- $d_6$ ) of compound **2**.  $^1\text{H}$ -N- $\text{CH}_3$  and  $\text{H}_3$  proton appears at  $\delta$  3.87 and 8.76, respectively.

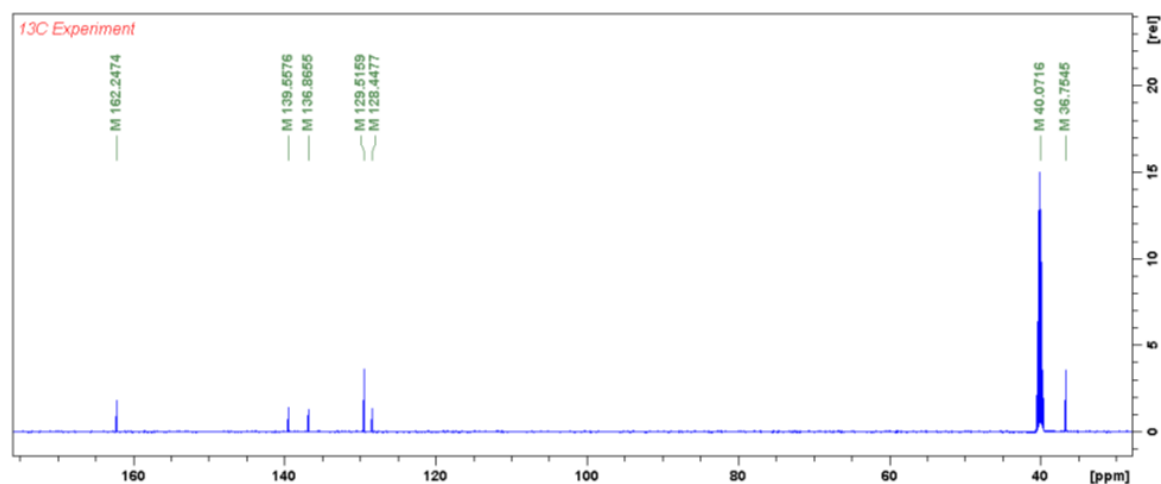


Figure 3B:  $^{13}\text{C}$ -NMR (150 MHz, DMSO- $d_6$ ) of compound **2** showing the peak of  $^{13}\text{C}$  -N- $\text{CH}_3$  and -COOH at 36.75 and 162.24 ppm respectively.

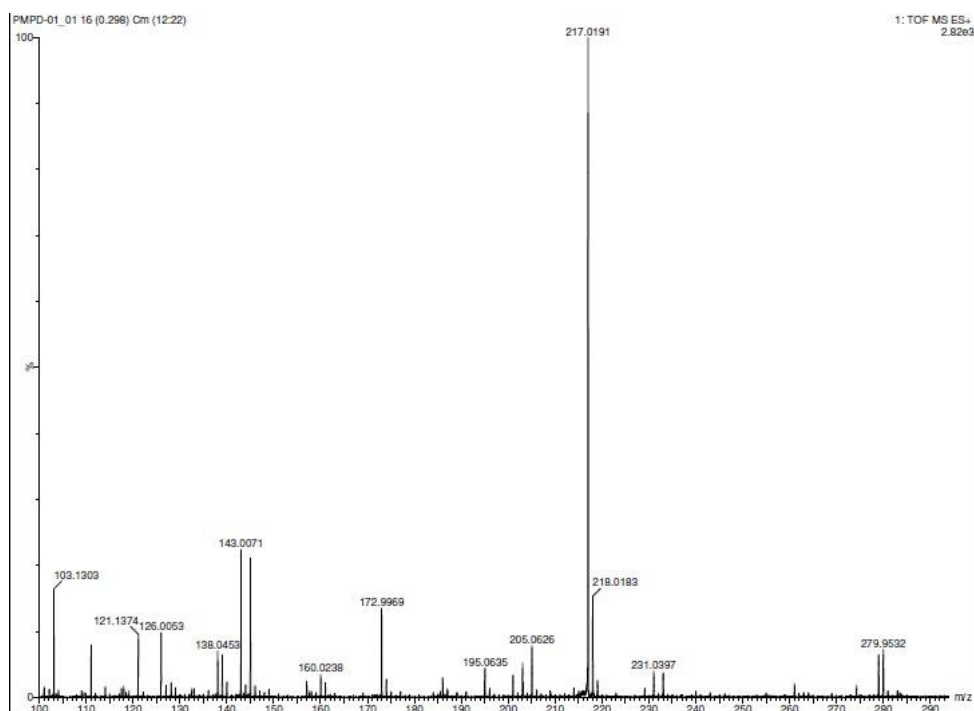


Figure 3C: EIMS of (compound **2** +Na) is appeared with m/z at 218.0183.

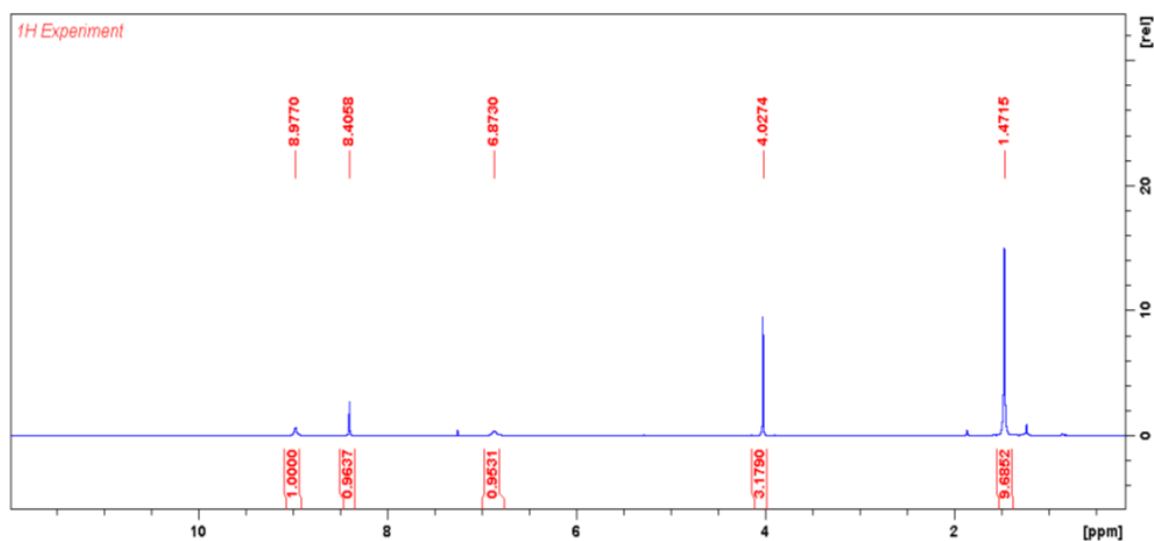


Figure 4A: <sup>1</sup>H-NMR (600 MHz, CDCl<sub>3</sub>) of compound **3**. Characteristic additional peak of 09 protons appears at δ 1.47 in comparison to compound **2**.

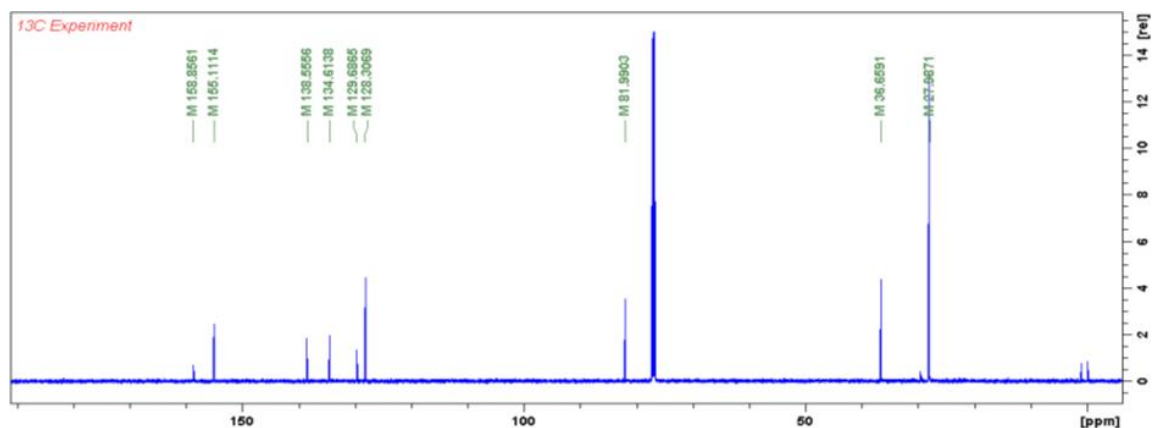


Figure 4B:  $^{13}\text{C}$ -NMR (150 MHz,  $\text{CDCl}_3$ ) of compound **3**. Appearance of peak at 27.98, 158.85 and 155.11 ppm (from Boc group) indicate the product formation.

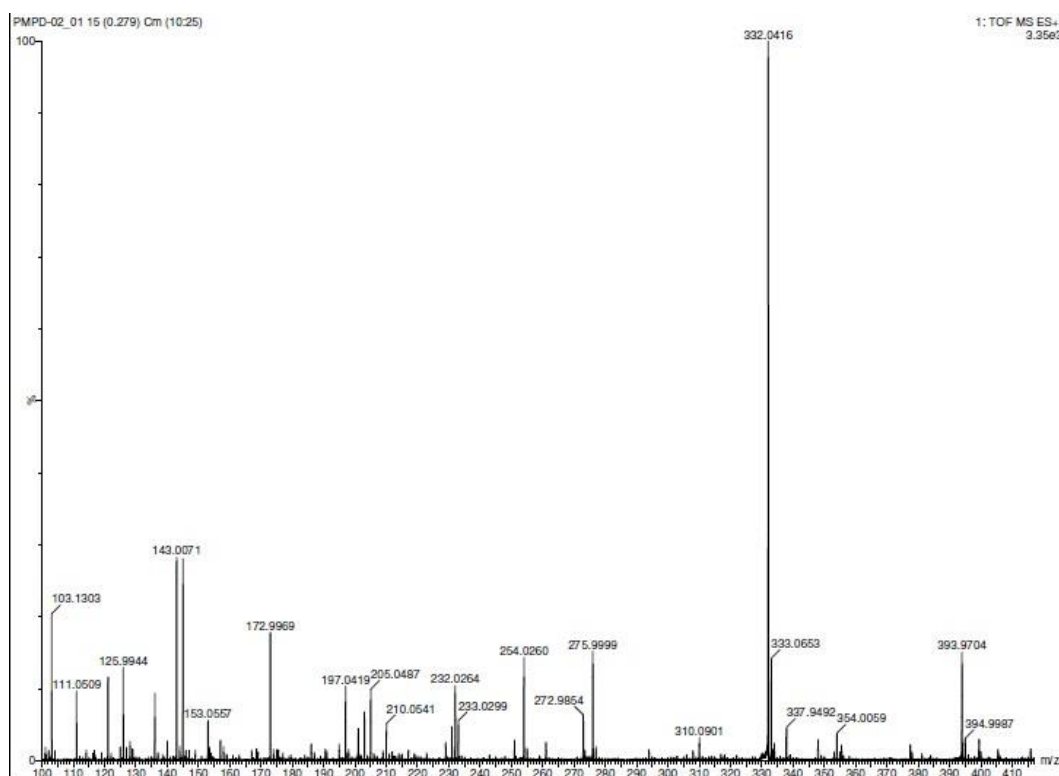


Figure 4C: EIMS of (compound **3**+H)  $\text{C}_{11}\text{H}_{16}\text{N}_7\text{O}_4$ ,  $m/z$  is 310.1233.

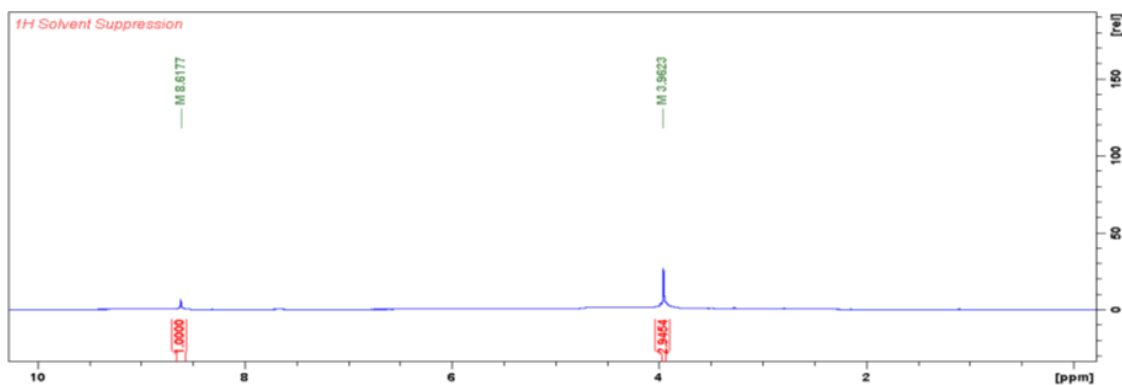


Figure 5A:  $^1\text{H}$ -NMR (600 MHz, DMSO- $d_6$ ) of compound **4**. Boc-group is deprotected as confirmed by the disappearance of peak  $\delta$  1.47 from previous compound **3**.

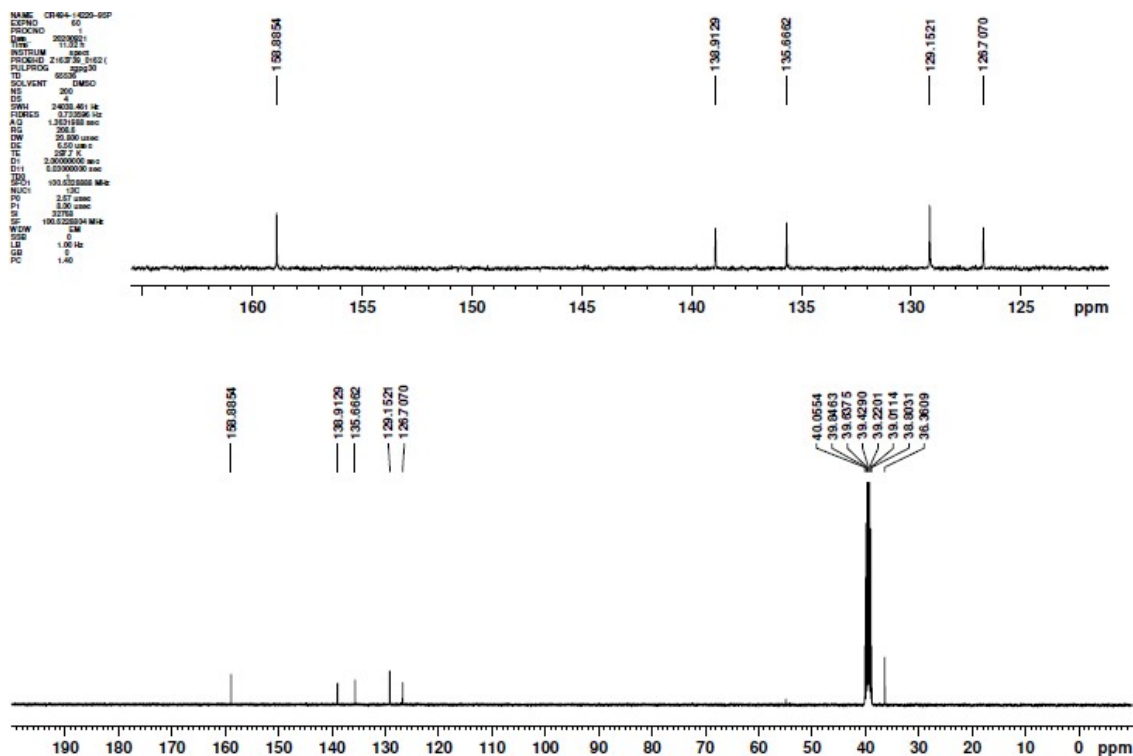


Figure 5B:  $^{13}\text{C}$ -NMR (400 MHz, DMSO- $d_6$ ) of compound **4**. Disappearance of peak at 27.98 ppm from previous compound **3** is confirmed.





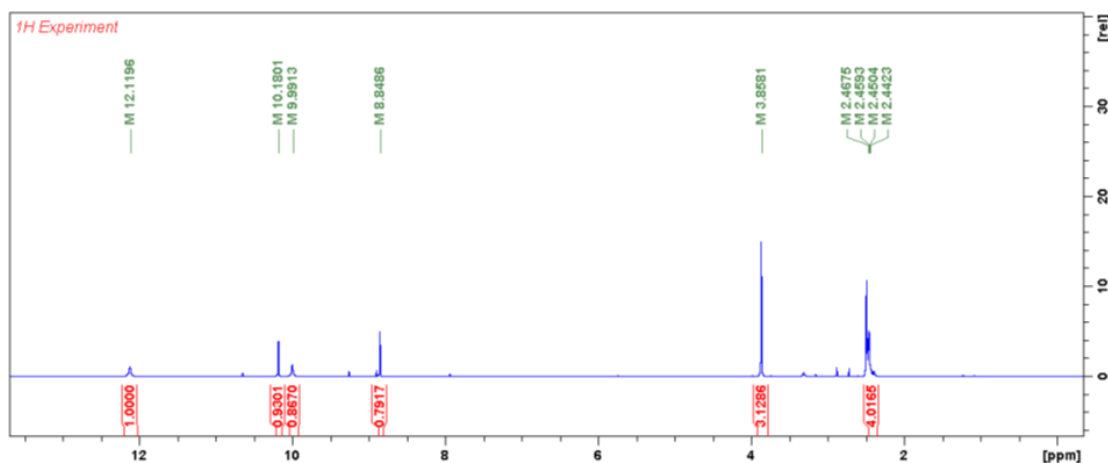


Figure 6A: <sup>1</sup>H-NMR of compound **5**. Additional peak of **4** proton was appeared at  $\delta$  2.46- 2.44 and acid peak at  $\delta$  12.11 is confirmed.

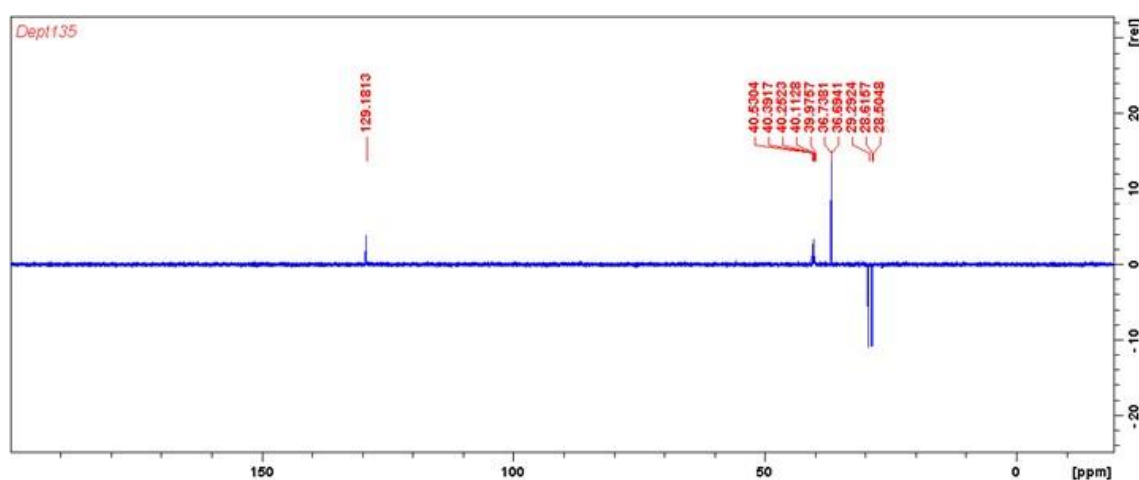


Figure 6B: <sup>13</sup>C-NMR of compound **5**. Additional methylene peaks at 28.63, 29.32 ppm followed by two carbonyl carbon at 170.64 and 174.03 ppm are confirmed.

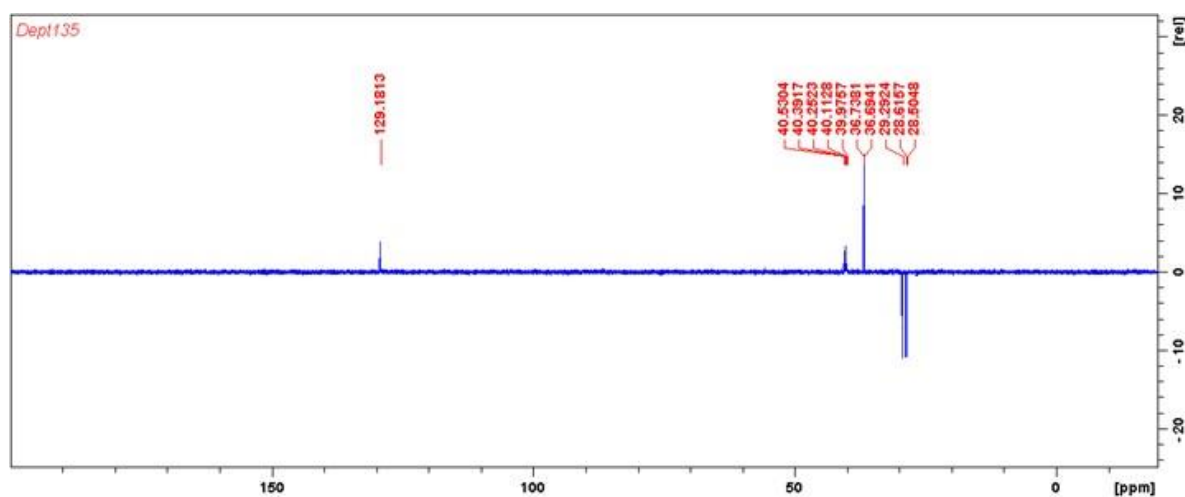


Figure 6C: DEPT of compound **5**. Two  $-\text{CH}_2$  carbon at 29.29 and 28.61 are confirmed and indicates acylated product.

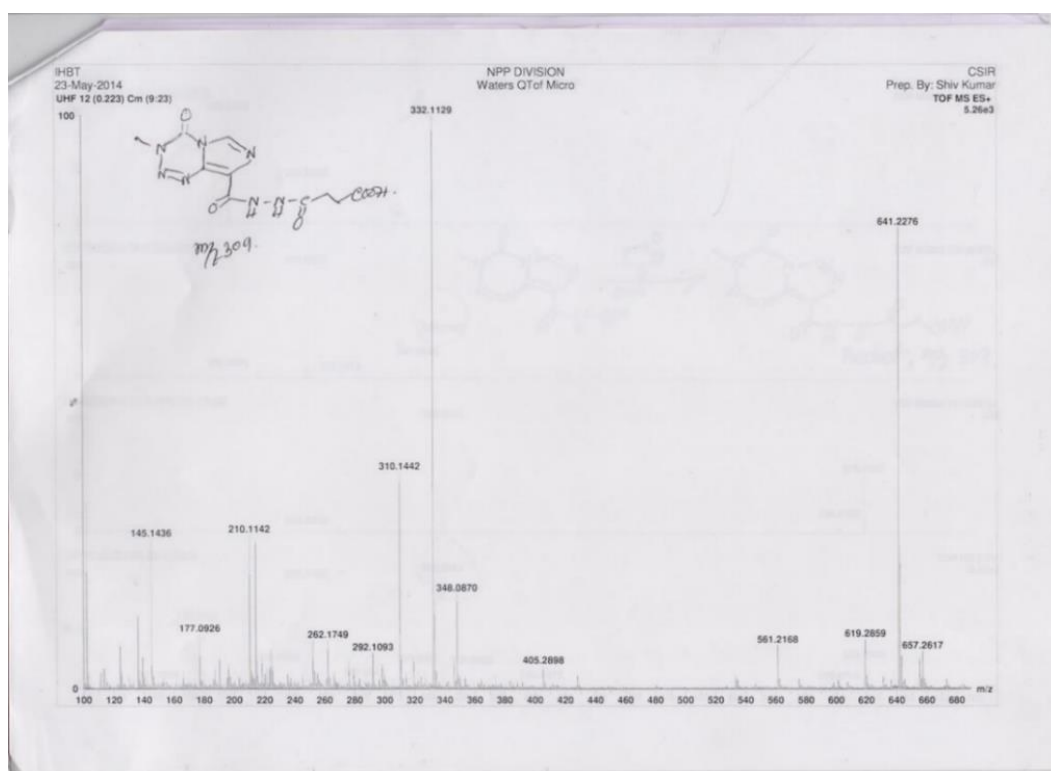


Figure 6D: EIMS of (compound **5**+Na), with  $\text{C}_{10}\text{H}_{11}\text{N}_7\text{O}_5\text{Na}$ ,  $m/z$  value is 332.1129.

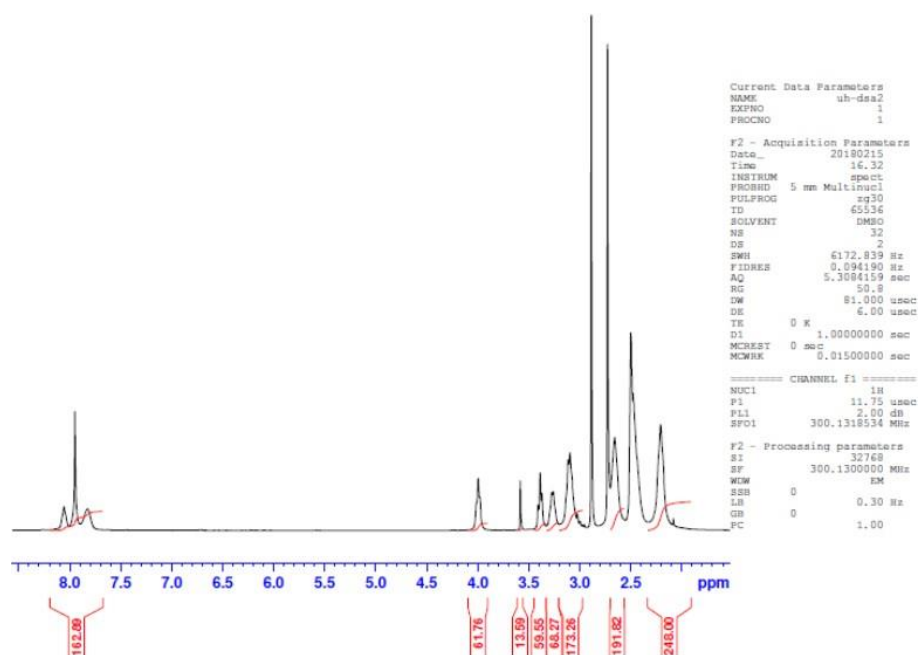


Figure 7A: In compound **6**, additional peak at  $\delta$  3.27 and 3.39 of  $^1\text{H}$ -NMR in comparison to PAMAM-dendrimer. Also  $-\text{CH}_2\text{-OH}$  (in PAMAM) is shifted towards de-shielded region at  $\delta$  4.007

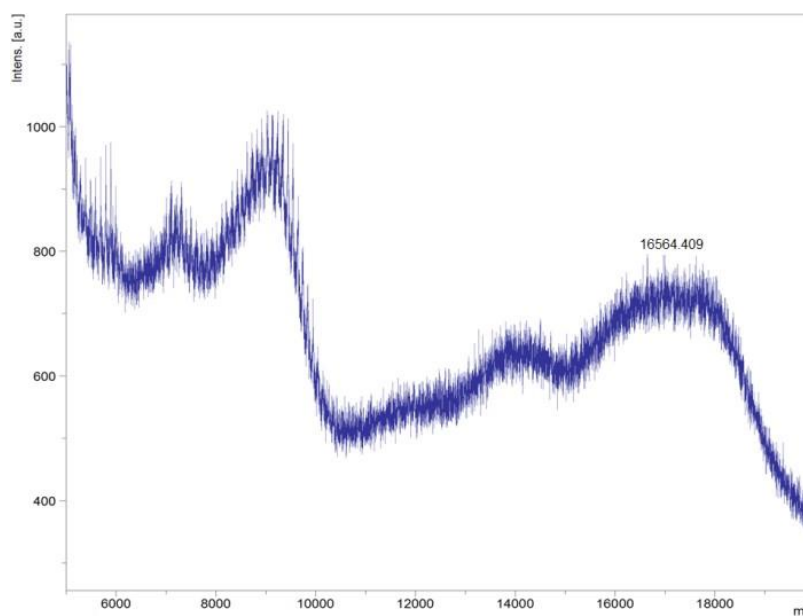


Figure 7B: MALDI-TOF data of compound **6** (DEN-SA) with  $m/z$  16564.409

Dr Ujir MLP066  
 PROTON DMSO (D:\IHBT\data\2017) nmrsu 14

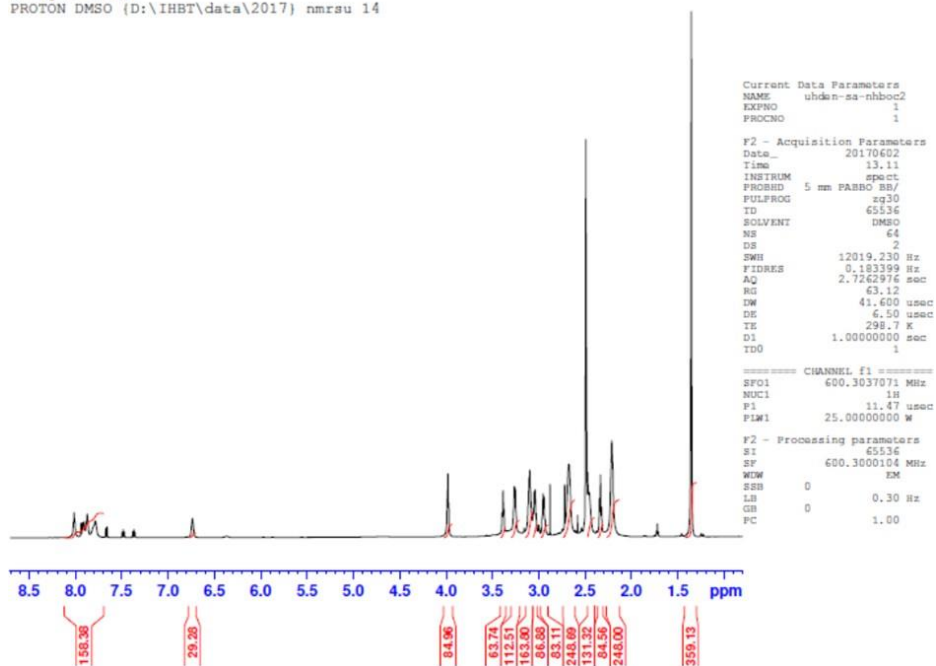


Figure 8A: In compound **7** ( $^1\text{H}$ -NMR), appearance of additional peak at  $\delta$  2.96, 3.056 and 1.44 confirmed the Boc protected conjugate.

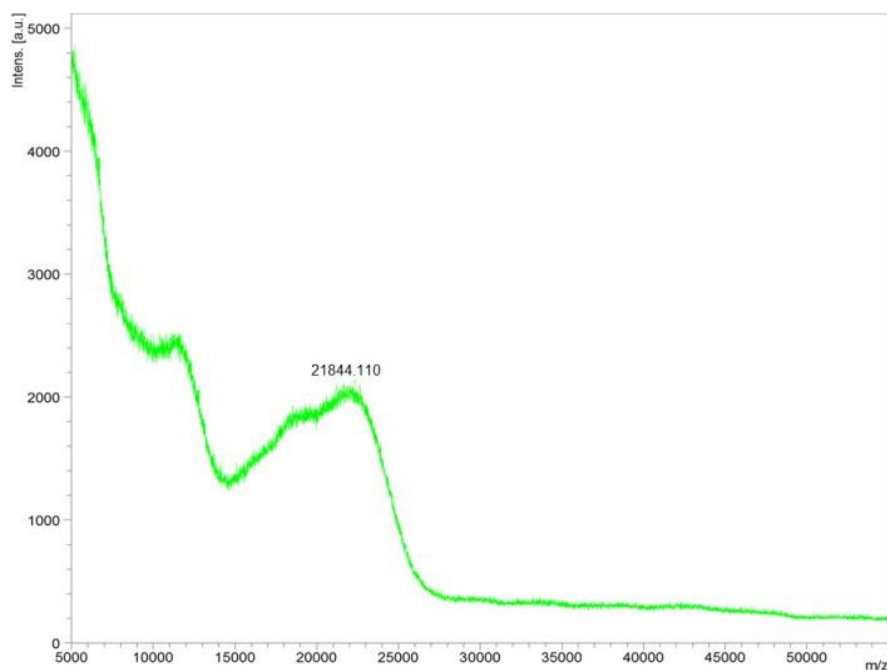


Figure 8B: MALDI-TOF analysis of DEN-SA-NH-BOC with m/z 21844.11

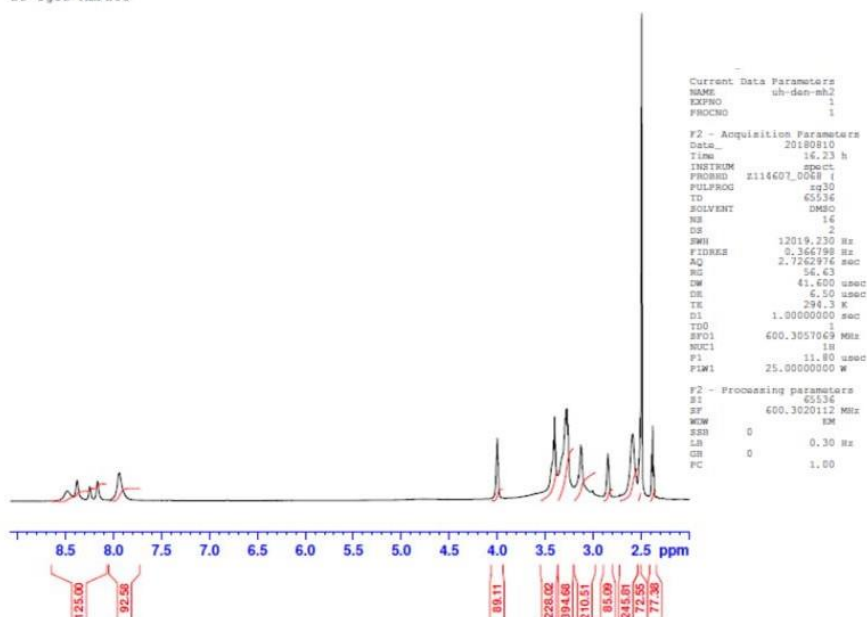


Figure 9A: In comparison to the previous  $^1\text{H}$ -NMR (S7A), upon treatment with  $\text{TFA-CH}_2\text{Cl}_2$ , Boc group was de-protected.

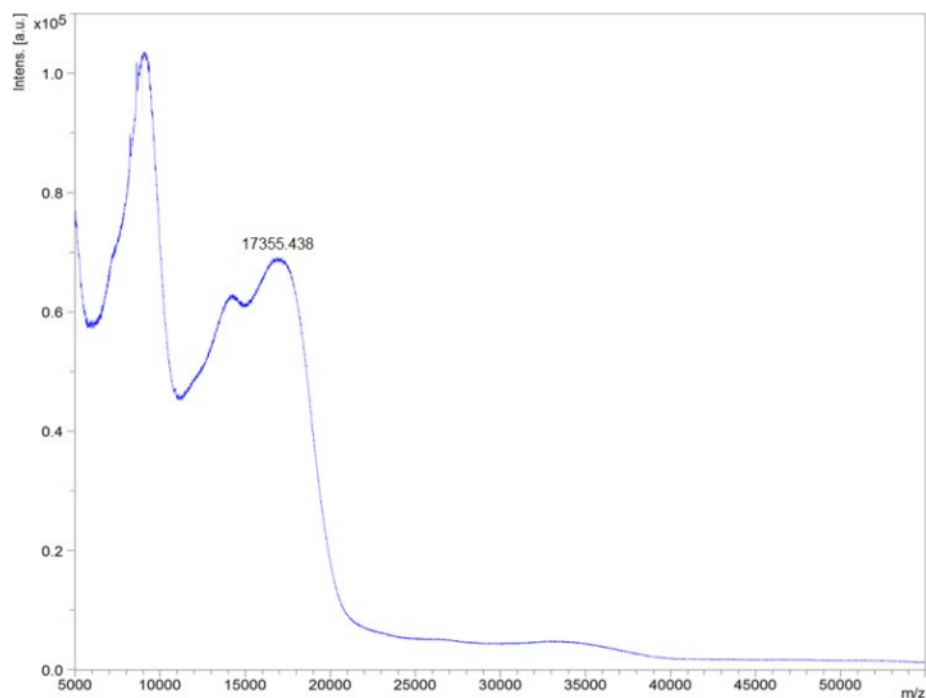


Figure 9B: MALDI-TOF analysis of  $\text{DEN-SA-NH}_2$ , showing lowering of the molecular weight to  $m/z$  17355.438, confirming Boc-deprotection.

74

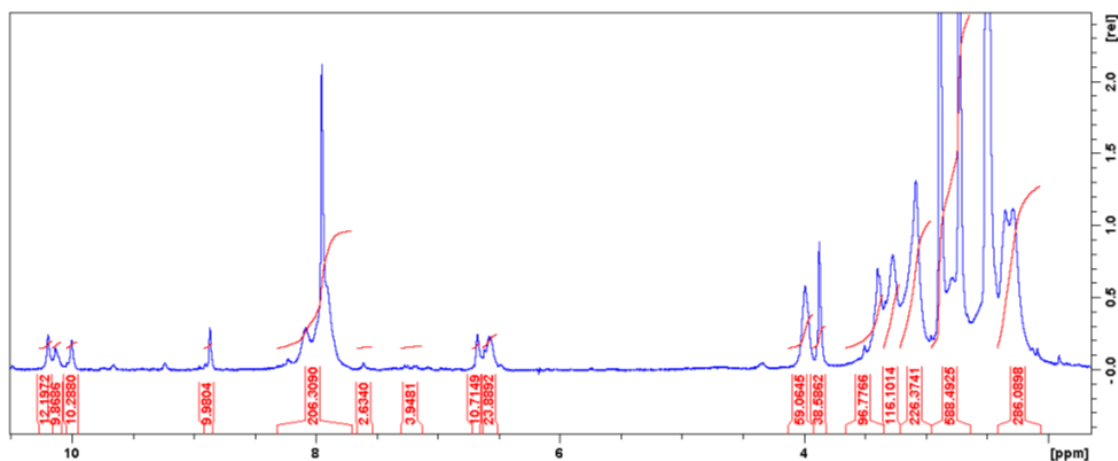


Figure 11A: The peak appeared on compound **10** showed the conjugates at  $\delta$  7.61, 7.30-7.14, 6.69 and 6.57 indicating FITC-conjugation.

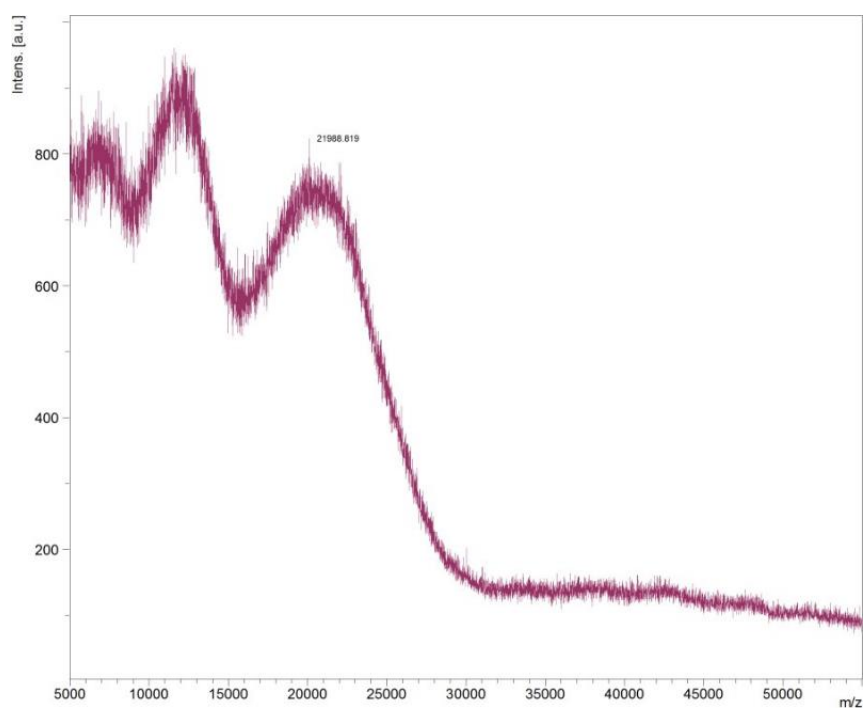


Figure 11B: MALDI-TOF analysis of TMZ-DEN-FITC conjugation confirmed the increased molecular weight of FITC by approximately 3 times.



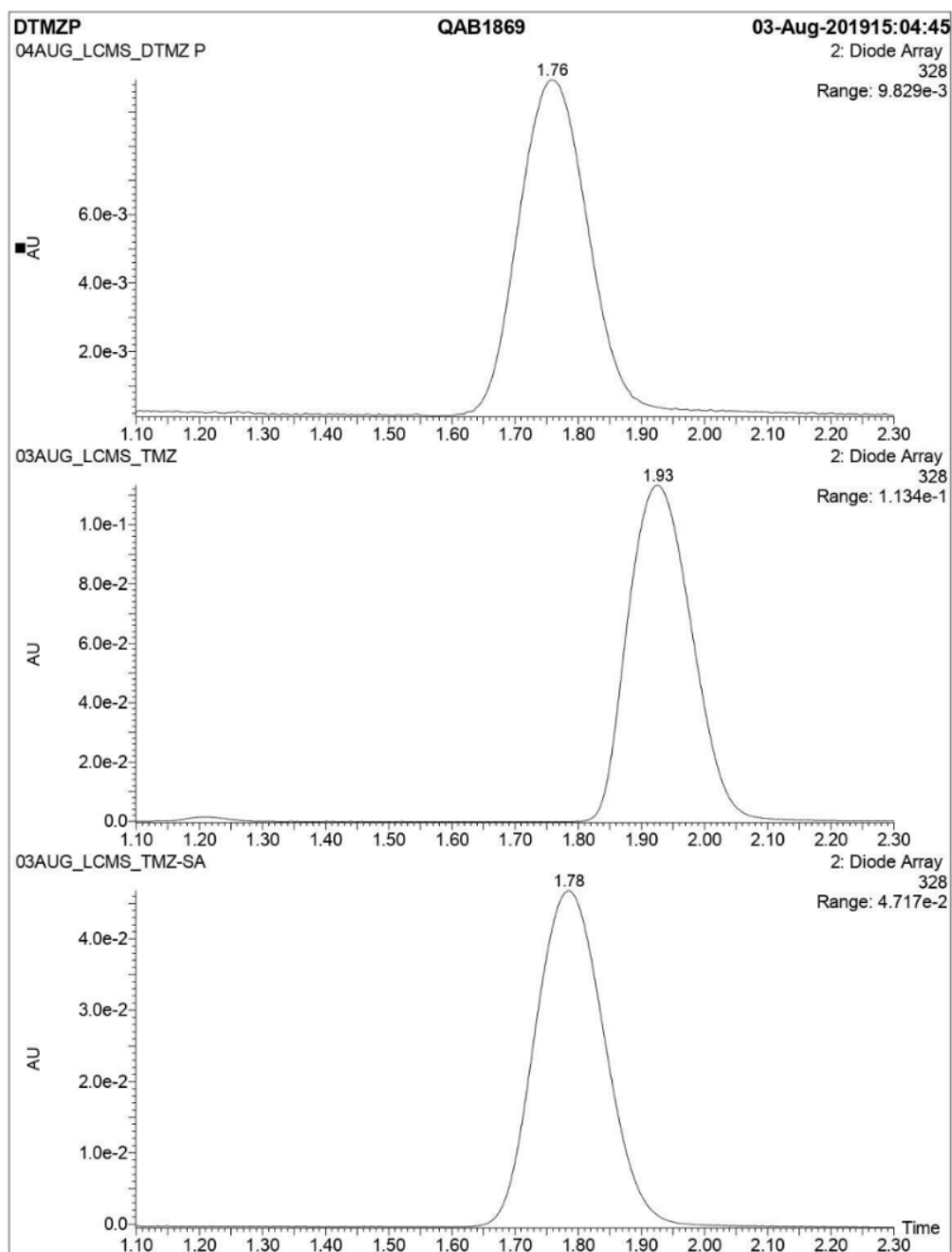
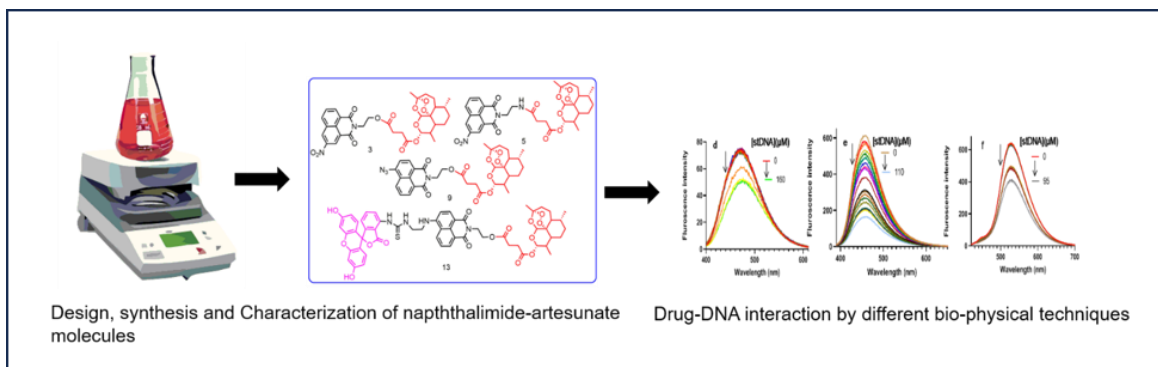


Figure 12: Elution of the compounds in UPLC-MS chromatogram. TMZ-DEN (top), TMZ (middle) and TMZ-SA (bottom) with their respective retention time 1.76, 1.93 and 1.78, respectively. These molecules retention time are different from each other and monitored at 328 nm.

## Chapter 3

# DESIGN, SYNTHESIS AND CHARACTERIZATION OF ARTESUNATE IN CONJUGATION WITH DNA- INTERCALATOR NAPHTHALIMIDE MOIETIES: BIOPHYSICAL STUDIES



**3.1 Introduction:** Traditional drug discovery in cancer treatment have limitation due to toxicity, off targeted to the cancer tissues, increasing drug resistance. Synthesis and development of target based small molecules may solve the traditional therapies limitation in oncologic drug discovery. To keep eye on the limitations the scientific community are hunting to find better ways to deliver selective targeted therapy, which would abrogate resistance and enhance the therapeutic efficacy for cancer treatment. The target of a drug can be a protein, DNA, or RNA that contributes to disease. For the development of new chemotherapeutic drugs, DNA is considered to be one of the most important targets. The novel antitumor drug having DNA intercalating moiety like naphthalimide can change DNA conformation upon intercalation and inhibit duplication, transcription, and cancer cell growth. DNA intercalating moieties are getting more attention due to their  $\pi$  deficient aromatic planar moieties can easily insert between the base pair of DNA. Upon intercalation the sugar phosphate backbone was distorted and as a result the degree of rotation in successive base pair was changed as a result DNA backbone structure was altered and DNA-protein interaction was hampered. Naphthalimides inhibited topoisomerase II by forming the ternary drug -DNA topoisomerase forming complex. In early seventies Brana first reported a series of 1,8 naphthalimide compounds showed cytotoxicity against Hela and KB cell lines. The naphthalimide derivatives like amonafide, mitonafide showed significant cytotoxicity but they are out of clinical trial due to their toxicity related issue. By keeping the naphthalimide moiety intact appropriate functional groups are added to reduce the toxicity related issues. Moreover, in oncology the number of FDA approved drug is limited. So, repurposing of clinically relevant drug in a new direction is always is an alternative approach. Repurposing of antimalarial drug artesunate by

remodeling with different substituted naphthalimide moiety to target DNA against lymphoma.

## **3.2 Materials and methods**

### **3.2.1 Materials**

4-(dimethylamino) pyridine (DMAP), 1-(3-Dimethylaminopropyl)-3-ethylcarbodiimide hydrochloride (EDC.HCl), triethylamine (TEA), dimethylformamide (DMF), DMSO-d<sub>6</sub>, CDCl<sub>3</sub>, DMSO, DMF, ethidium bromide (EtBr), acridine orange (AO) and deoxyribonucleic acid (DNA) sodium salt from Salmon Testes were purchased from Sigma–Aldrich. Hoechst-33342 was purchased from Thermo Fisher, and artesunate was purchased from TCI Chemicals. From Acros Organics N-(tert-butoxycarbonyl)-1,2- diaminoethane was purchased. From Merck, India other required solvents and chemicals were purchased. The reactions were carried out under a nitrogen environment. For isolation and separation of the desired components, thin-layer chromatography (TLC) were performed on TLC Silica gel 60 F254 plates (aluminium sheets) (Merck, Germany), and the UV active spots were visualized with 254 nm light. NMR spectroscopy was performed on a Bruker Avance-III 400 spectrometer using CDCl<sub>3</sub> and DMSO-d<sub>6</sub> solvents. As an internal standard tetramethylsilane (TMS) was used. Proton chemical shifts are reported in ppm ( $\delta$ ) and coupling constants (J) are reported in hertz (Hz). The final compounds (**3**, **5**, **9** and **13**) were analysed through UPLC and reported >95% pure (indicated by chromatograms).

### **3.2.2 Ultra-performance liquid chromatography (UPLC) analysis:**

Synthesized compounds **3**, **5**, **9** and **13** were analysed by a Waters UPLC instrument associated with a binary pump, PDA-detector, and auto sampler interfaced with Masslynk software. The UPLC chromatograms

were monitored at 254 nm simultaneously using a dual PDA absorbance detector (200-800 nm). Freshly prepared Water (H<sub>2</sub>O)/acetonitrile (ACN) (in 0.1% formic acid) was filtered, degassed, and used as the mobile phase. An ACQUITY UPLC BEH C18, 1.7  $\mu$ m, 2.1x100 mm column was used. A gradient flow was used with an initial condition of 5:95, continued for 0.50 minutes, then 25:75 (ACN/H<sub>2</sub>O) in 3 minutes and returned to 80:20 (ACN/H<sub>2</sub>O) in 3.50 minutes, 90:10 for 4.00 minutes, and 25:75 for 5 minutes with a flow rate of 0.3 mL/min. Compounds **3**, **5**, **9** and **13** were solubilized in ACN for injection.

### 3.2.3 Synthesis of compounds **3**, **5** and **9**:

M03.03.01 Synthesis of compound (**3**): In 20 ml ethanol, 3-nitro-1,8-naphthalic anhydride **1** (2.0 g, 0.0082 mol) along with ethanolamine (1.50 g, 0.0247 mol) was heated under reflux condition for 1.5 hr. Under reduced pressure the resulting mixture was concentrated upon evaporating ethanol and then cooled the mixture at 4°C. The mixture was filtered and washed with cold ethanol and finally dried to afford **2** (1.8 g, 76%). <sup>1</sup>H-NMR (DMSO-d<sub>6</sub>, 400 MHz):  $\delta$  9.45 (1H, Ar-H, s), 8.92 (1H, Ar-H, s), 8.76 (1H, Ar-H, d, *J* = 8.2 Hz), 8.66 (1H, Ar-H, d, *J* = 7.2 Hz), 8.04 (1H, Ar-H, t, *J* = 7.7 Hz), 4.81 (1H, t, *J* = 5.8 Hz), 4.16 (2H, t, *J* = 6.3 Hz), 3.64 (2H, t, *J* = 6.0 Hz) (**Figure 2**).

As the compound **2** was pure as result it was directly used for the preparation of compound **3**. Artesunate (1.61 g, 4.1 mmol) was placed in a round bottom flask in anhydrous DMSO (8.0 ml). Then, the coupling agent EDC·HCl (1.34 g, 6.9 mmol) and DMAP (0.42 g, 3.4 mmol) were added and stirred to solubilize in an inert gas environment. Finally, for 12 h at R.T compound **2** (1 g, 3.4 mmol) was added to the reaction mixture. The obtained product (**3**) was treated with ethyl acetate and water. Finally,

for the removal of water the obtained product **3** was dried over magnesium sulfate.

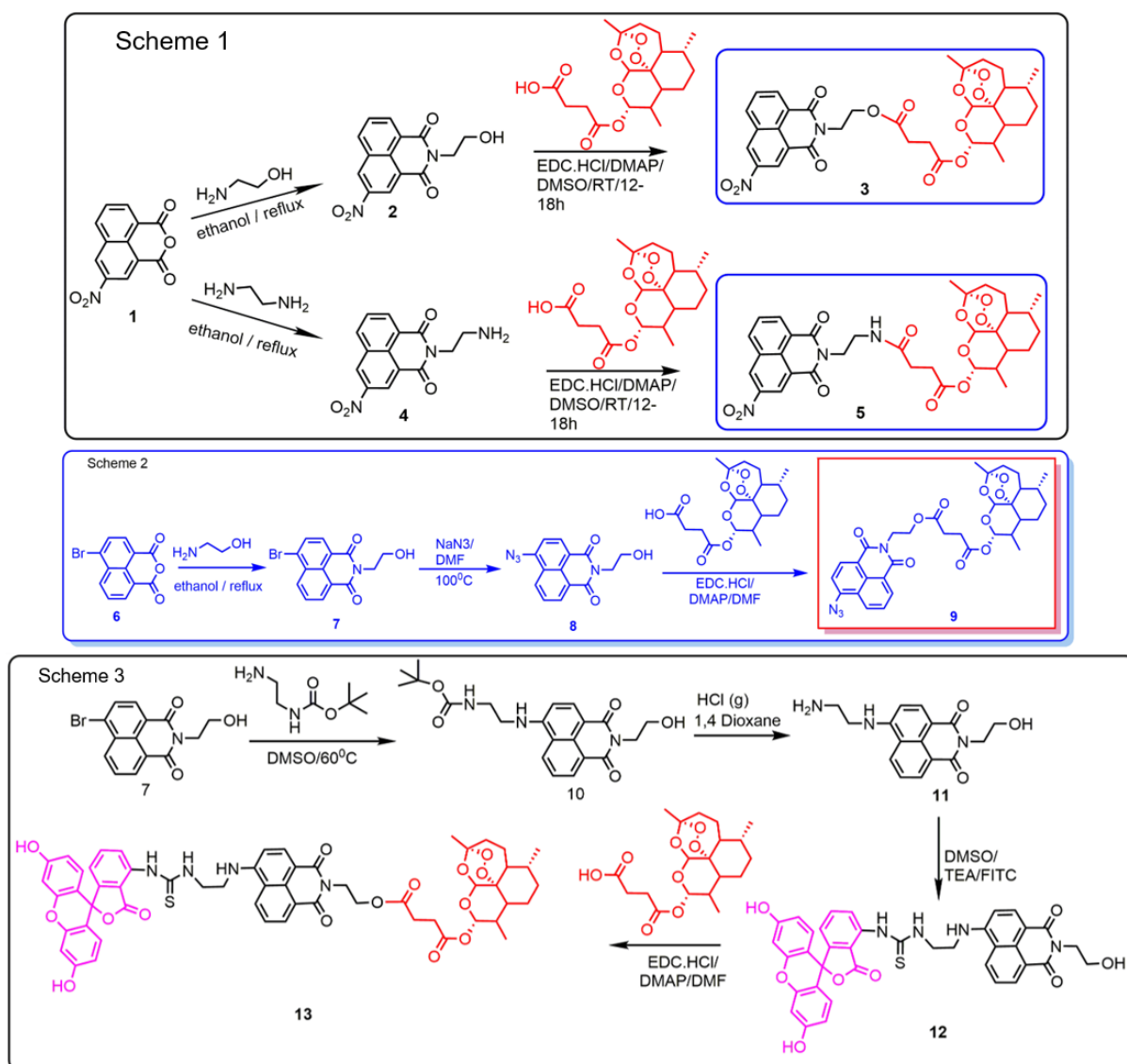


Figure 1: Synthesis scheme of naphthalimide-artesunate molecules by ester (**3,9**) and amide (**5**) linkage and further conjugated with FITC (**13**)

Upon evaporation, the oily crude product was recovered, and the final white colored product (**3**) (1.18 g, 51%) was purified through column chromatography over silica-gel (100-200 mesh) in  $\text{CH}_2\text{Cl}_2$ : MeOH (99:01). In LCMS, the retention time was 4.05 mins (**Figure 3**). Compound **3** showed EI-MS ( $\text{M}^+ + \text{Na}$ ):  $m/z$  670.6,  $^1\text{H-NMR}$  (DMSO- $d_6$ , 400 MHz):  $\delta$  9.49 (1H, Ar-H, s), 8.98 (1H, Ar-H, s), 8.79 (1H, Ar-H, d,  $J = 7.84$  Hz), 8.70

(1H, Ar-H, d,  $J$  = 7.2 Hz), 8.06 (1H, Ar-H, t,  $J$  = 7.8 Hz), 5.49 – 5.44 (2H, m,  $J$  = 9.8, 13.92 Hz), 2.58 (2 H, d,  $J$  = 5.64 Hz), 2.53 (1H, s), 2.18 – 2.12 (2H, m,  $J$  = 10.16, 12.4 Hz), 1.98 – 1.95 (1H, m,  $J$  = 10.84 Hz), 1.78 (1H, s), 1.61-1.53 (2H, m,  $J$  = 7.28, 13.32 Hz), 1.46-1.28 (4H, m,  $J$  = 13.64 Hz), 1.25 (3H, s), 1.19-1.09 (1H, m,  $J$  = 11.12 Hz), 0.95 (1H, s), 0.89 (2H, d,  $J$  = 6.2 Hz), 0.63 (3H, d,  $J$  = 7.1 Hz) (**Figure 4A**).  $^{13}\text{C}$  NMR (100 MHz, DMSO- $d_6$ , ppm):  $\delta$  171.70, 170.55, 162.72, 162.21, 145.61, 136.28, 133.91, 130.71, 129.67, 129.35, 129.14, 123.61, 122.78, 122.20, 103.47, 91.58, 90.52, 79.60, 61.05, 51.05, 44.44, 35.95, 35.79, 33.58, 31.40, 28.43, 28.28, 25.38, 24.06, 20.94, 19.9432, 14.11, 11.45 (**Figure 4B**). HR-MS Calculated for  $\text{C}_{33}\text{H}_{36}\text{N}_2\text{O}_{12}$ , 652.2268; measured,  $\text{C}_{33}\text{H}_{36}\text{N}_2\text{O}_{12}\text{Na}$  675.2166 (**Figure 4C**)

### 3.2.4 Synthesis of compound 5:

Compound **1** (2 g, 0.0082 mol) was dissolved in 10 ml ethanolamine and ethylenediamine (1.48 g, 0.025 mol) was added into the reaction mixture and heated under reflux condition for 2.0 h (**Figure1**, **Scheme1**). Upon evaporating ethanol, the resulting mixture was concentrated under reduced pressure and then cooled to 4°C. The solid material was filtered, washed with cold ethanol and dried to afford **4** (2.0 g, 78%).  $^1\text{H}$ -NMR (DMSO- $d_6$ , 400 MHz):  $\delta$  9.45 (1H, Ar-H, s), 8.93 (1H, Ar-H, s), 8.75 (1H, Ar-H, d,  $J$  = 8.2 Hz), 8.66 (1H, Ar-H, d,  $J$  = 7.2 Hz), 8.04 (1H, Ar-H, t,  $J$  = 7.7 Hz), 4.08 (2H, t,  $J$  = 6.6 Hz), 2.90 (2H, t,  $J$  = 6.6 Hz), 2.07 (2H, -NH<sub>2</sub>, broad peak) (**Figure 5**).

At room temperature a magnetically stirred solution of compound **4** (0.74 g, 0.0019 mol) was dissolved in 5.0 ml anhydrous DMSO. Finally, artesunate (1 g, 0.0026 mol) was added in the presence of the coupling agent EDC·HCl (0.99 g, 0.0026 mol) and a catalytic amount of DMAP

(0.32 g, 0.00083 mol) for 12 hrs at room temperature. The obtained product was treated with ethyl acetate and water. Upon evaporation, the oily crude product was recovered, and the product was further purified through column chromatography over silica gel in CH<sub>2</sub>Cl<sub>2</sub>: MeOH (99:01). For further purification, the compound was treated simultaneously with a 50:50 hexane-chloroform mixture, ether-hexane mixture (40:10) and acetone. The pure compound was yellow compound **5** (1.15 g, 68%). The LCMS retention time was 3.75 mins (**Figure 3**). Compound **5** showed EIMS (M<sup>+</sup> + NH<sub>4</sub><sup>+</sup>): m/z 669.1. <sup>1</sup>H-NMR (DMSO-d<sub>6</sub>, 400 MHz): δ 9.48 (1H, Ar-H, s), 8.96 (1H, Ar-H, s), 8.78 (1H, Ar-H, d, J= 8.2 Hz), 8.69 (1H, Ar-H, d, J= 7.2 Hz), 8.06 (1H, Ar-H, t, J= 7.7 Hz), 8.01 (2H, s), 5.56 (1H, d, J= 9.8 Hz), 5.5 (1H, s), 4.15 (2H, t, J= 5.7 Hz), 3.41 (2H, d, J= 5.8 Hz), 2.27 (2H, t, J= 6.84 Hz), 2.25-2.13 (2H, m, J= 14.2 Hz), 2.11-2.08 (1H, m, J= 12.48 Hz), 2.00-1.96 (1H, m, J= 14.32 Hz), 1.80 (1H, d, J= 3.32 Hz), 1.62-1.59 (2H, m, J= 11.56 Hz), 1.52-1.49 (1H, m, J= 13.36 Hz), 1.44-1.38 (2H, m, J= 10.32, 11.84 Hz), 1.33 (1H, s), 1.2 (3H, s), 1.23-1.14 (4H, m, J= 11.24, 4.64, 6.68 Hz), 0.95 (1H, s), 0.89 (3H, d, J= 6.16 Hz), 0.69 (3H, d, J= 7.04 Hz) (**Figure 6A**). <sup>13</sup>C NMR (100 MHz, DMSO-d<sub>6</sub>, ppm): δ 170.96, 170.70, 162.82, 162.32, 145.64, 136.05, 133.71, 130.69, 129.45, 129.11, 124.00, 122.56, 103.51, 91.50, 90.46, 79.69, 68.40, 55.71, 54.81, 51.05, 44.54, 36.26, 35.95, 35.82, 33.63, 34.51, 29.55, 28.81, 25.40, 24.11, 20.92, 19.93, 11.58 (**Figure 6B**). HR-MS Calculated for C<sub>33</sub>H<sub>37</sub>N<sub>3</sub>O<sub>11</sub>, 651.2428; measured, C<sub>33</sub>H<sub>37</sub>N<sub>3</sub>O<sub>11</sub>Na 674.1628 (**Figure 6C**)

### 3.2.5 Synthesis of compound 9:

To a solution of 4-bromo-1,8-naphthalic anhydride **6** (1.0 g, 0.0036 mol) in dry ethanol (6 mL) and 2-aminoethanol (0.44 g, 0.0072 mol) were added dropwise to the reaction mixture dissolved in dry ethanol (5 mL). The mixture was stirred, heated to reflux and continued for 4 h. The resulting



mixture was allowed to cool at ice temperature and filtered. Cold ethanol was used to wash the resultant solid residue. A white solid product **7** was obtained after purification (0.85 g, yield 73.91%). <sup>1</sup>H-NMR (CDCl<sub>3</sub>, 400 MHz): δ 8.67 (1H, Ar-H, d, *J*=7.3 Hz), 8.59 (1H, Ar-H, d, *J*=8.6 Hz), 8.43 (1H, Ar-H, d, *J*=7.9 Hz), 8.05 (1H, Ar-H, d, *J*=7.8 Hz), 7.86 (1H, Ar-H, t, *J*=8.3 Hz), 4.45 (2H, t, *J*= 5.2 Hz), 3.98 (2H, t, *J*= 5.2 Hz) (**Figure 7**).

**3.2.6 Compound 7:** Compound **6** (1.0 g, 0.0031 mol) was added to 6 ml of DMF and stirred for 0.5 hour to make a solution. Then, NaN<sub>3</sub> (0.40 g, 0.0062 mol) in water (1 ml) was added to the mixture. The reaction mixture was heated to 95°C, and then the colour changed from white turbid to brown clear solution. The reaction was terminated by the addition of water. The reaction mixture containing yellow precipitate was filtered and washed with cold ethanol to get the desired yellow coloured compound **8** (0.70 g, yield 55.0%). <sup>1</sup>H-NMR (CDCl<sub>3</sub>, 400 MHz): δ 8.64 (1H, Ar-H, d, *J*=7.16 Hz), 8.59 (1H, Ar-H, d, *J*=7.92 Hz), 8.46 (1H, Ar-H, d, *J*=8.2 Hz), 7.75 (1H, Ar-H, t, *J*= 7.8 Hz), 7.62 (1H, Ar-H, d, *J*=7.96 Hz), 4.44 (2H, d, *J*= 5.2 Hz), 3.97 (2H, d, *J*= 5.1 Hz) (**Figure 8**)

Artesunate (0.50 g, 0.0017 moles) was placed in an RB flask in anhydrous DMSO (6.0 ml). Then, the coupling agents EDC and HCl (0.67 g, 0.0034 mol) and a catalytic amount of DMAP (0.108 g, 0.00085 mol) were added and stirred to solubilize in an inert gas environment until the solution became clear. After half an hour, compound **8** (0.50 g, 0.0017 mol) was added and the reaction was continued at R. T for 12 h, the color changed to brown. The obtained crude product was successively washed with ethyl acetate and water. Upon evaporation, the crude product was recovered. The crude product was purified through column chromatography over silica gel (100-200 mesh) in EtOAc: hexane (20:80) to obtain desired compound **9** (0.97 g, 84%). In LCMS, the retention time was 4.37 min

(**Figure 3**).  $m/z$  calculated for  $C_{33}H_{36}N_4O_{10}$  (**9**), 648.65; and corresponding EIMS found ( $M^+ + NH_4^+$ ): 666.4  $^1H$ -NMR (DMSO- $d_6$ , 400 MHz):  $\delta$  8.57 (1H, Ar-H, d,  $J=7.00$  Hz), 8.52 (1H, Ar-H, d,  $J=8.00$  Hz), 8.46 (1H, Ar-H, d,  $J=8.4$  Hz), 7.89 (1H, Ar-H, t), 7.78 (1H, Ar-H, d,  $J=8.1$  Hz), 5.52-5.46 (2H, m,  $J=7.9, 11.72$  Hz), 4.32 (4H, s), 2.57 (2H, d,  $J=5.84$  Hz), 2.16-2.14 (2H, m,  $J=11.84$  Hz), 2.00 (1H, s), 1.57 (1H, s), 1.61-1.53 (2H, m,  $J=13.96$  Hz), 1.44-1.32 (4H, m,  $J=11.88, 13.32$  Hz), 1.26 (3H, s), 1.14 (1H, d,  $J=6.28$  Hz), 1.08 (1H, s), 0.88 (3H, d,  $J=6.0$  Hz), 0.62 (3H, d,  $J=7.0$ ) (**Figure 9A**)  $^{13}C$  NMR (150 MHz, DMSO- $d_6$ , ppm):  $\delta$  171.69, 170.58, 163.21, 162.80, 142.77, 131.57, 128.33, 128.21, 127.13, 123.38, 121.84, 117.84, 115.79, 103.46, 91.59, 90.61, 79.72, 61.23, 50.99, 44.36, 44.38, 38.44, 35.93, 35.82, 33.61, 31.44, 28.46, 28.33, 25.42, 24.07, 20.95, 19.94, 11.46 (**Figure 9B**). HR-MS calculated for  $C_{33}H_{36}N_4O_{10}$ , 648.2431; measured,  $C_{33}H_{36}N_4O_{10} + H_2O$  666.2192 (**Figure 9C**).

### 3.2.7 Synthesis of compound 13:

Boc-protected compound **10** was obtained in quantitative yield by reaction of compound **7** (1.0 g, 0.0031 mol) and N-tert-butoxy carbonyl 1,3-diamino ethane (1.0 g, 0.0062 mol) in anhydrous DMSO (8.0 ml) at 70°C for 16 hrs. The yellowish mixture was washed with ethyl acetate and water, followed by dried over sodium sulfate. The oily crude product was further purified by column chromatography over silica gel (100-200 mesh) in  $CH_2Cl_2$ : MeOH (99:1) to produce a red product (**10**) (680 mg, 54.4%).  $^1H$ -NMR (DMSO- $d_6$ , 600 MHz):  $\delta$  8.72 (1H, Ar-H, d,  $J=8.34$  Hz), 8.42 (1H, Ar-H, d,  $J=7.56$  Hz), 8.24 (1H, Ar-H, d,  $J=9.18$  Hz), 7.68 (1H, Ar-H, t,  $J=6.66$  Hz), 6.81 (1H, Ar-H, d,  $J=9.24$  Hz), 7.72 (2H, t,  $J=6.66$  Hz), 7.07 (2H, t,  $J=6.72$  Hz), 5.57 (1H, s), 4.79 (2H, t,  $J=5.04$  Hz), 4.11 (2H, t,  $J=7.56$  Hz), 3.57 (1H, m,  $J=6.78$  Hz), 3.43 (1H, m,  $J=5.82$  Hz), 3.27 (1H, m,  $J=5.88$  Hz), 1.3

(9H, s) (**Figure 10A**). HR-MS Calculated for  $C_{21}H_{25}N_3O_5$ , 399.1794; measured  $[C_{33}H_{36}N_4O_{10}+H]^+$  400.1859 (**Figure 10B**)

Dry HCl (g) was passed through a mixture of compound **10** (995 mg; 0.0025 mol) in 1,4-dioxane (10.0 mL) to afford the chloride salt of compound **11** (0.50 g, 60%).  $^1H$ -NMR (DMSO- $d_6$ , 600 MHz):  $\delta$  8.86 (1H, Ar-H, d,  $J=9.42$  Hz), 8.42 (1H, Ar-H, d,  $J=7.14$  Hz), 8.27 (1H, Ar-H, d,  $J=7.62$  Hz), 7.68 (1H, Ar-H, t,  $J=7.98$  Hz), 6.85 (1H, Ar-H, d,  $J=9.54$  Hz), 8.31 (2H, s),  $\delta$  4.13 (2H, t,  $J=5.32$  Hz), 3.82 (1H, s), 3.68 (2H, t,  $J=5.46$  Hz), 3.39 (1H, s), and 3.18 (2H, m, 6.36 Hz) (**Figure 11A**).  $^{13}C$  NMR (100 MHz, DMSO- $d_6$ , ppm):  $\delta$  164.50, 163.70, 150.68, 134.49, 131.31, 129.78, 129.64, 124.84, 122.42, 120.83, 109.08, 104.48, 58.44, 41.94, 40.93, 37.82 (**Figure 11B**). HR-MS calculated for  $C_{16}H_{17}N_3O_3$ , 299.1270; measured,  $[C_{16}H_{17}N_3O_3+H]^+$  300.1336 (**Figure 11C**)

A solution of compound **11** (0.20 g; 0.0006 mol) in DMSO (8 mL) was further treated with fluorescein isothiocyanate (FITC) (0.27 g; 0.0007 mol) followed by TEA (0.120 g; 0.0012 mol). The resulting reaction medium was stirred overnight at room temperature under inert conditions. The desired orange colored compound **12** (200 mg, 48%) was purified through column chromatography over silica gel (100-200 mesh) in  $CH_2Cl_2$ : MeOH (90:10).  $^1H$ -NMR (DMSO- $d_6$ , 600 MHz):  $\delta$  8.70 (1H, Ar-H, d,  $J=8.64$  Hz), 8.44 (1H, Ar-H, d,  $J=6.84$  Hz), 8.28 (1H, Ar-H, d,  $J=9.36$  Hz), 7.73 (1H, Ar-H, d,  $J=7.8$  Hz), 7.69 (1H, Ar-H, t,  $J=7.86$  Hz), 10.14 (3H, s), 8.29 (1H, s), 8.17 (1H, s), 7.90 (1H, s), 7.18 (1H, d, 8.28 Hz), 6.99 (2H, d, 8.52 Hz), 6.68 (5H, d, 2.22 Hz), 6.61-6.56 (2H, m,  $J=8.76$  Hz) 4.80 (1H, t, 5.94 Hz), 4.12 (2H, t, 6.9 Hz), 4.89 (2H, q, 6.0 Hz), 4.78 (2H, m, 6.6 Hz, 6.24 Hz) (**Figure 12A**).  $^{13}C$  NMR (150 MHz, DMSO- $d_6$ , ppm):  $\delta$  168.91, 164.36, 163.53, 159.97, 152.35, 151.08, 141.53, 134.57, 131.16, 129.92, 129.47, 129.03, 127.09, 124.85, 122.45, 120.66, 113.06, 110.16, 108.61, 104.48, 102.72,

66.82, 65.38, 58.44, 46.21, 42.75, 42.50, 41.88, 40.53, 40.41, 40.28, 40.14, 39.99, 39.86, 39.72, 39.58, 15.63 (**Figure 12B**). HR-MS Calculated for  $C_{37}H_{28}N_4O_8S$ , 688.1628; measured,  $[C_{37}H_{28}N_4O_8S + H]^+$  689.1689 (**Figure 12C**).

The magnetically stirred solution of compound **12** (0.175 g, 0.0003 mol) in DMF (6.0 mL) was treated with artesunate (117.0 mg, 0.0003 mol) in the presence of the coupling agent EDC·HCl (73.0 mg, 0.0004 mol), with a catalytic amount of DMAP (31.0 mg, 0.0003 mol) and with TEA (0.030 mg; 0.0003 mol) for 12 h at R.T. Through column chromatography,  $CH_2Cl_2$ : MeOH (80:20) the concentrated reaction mixture was purified to produce pure orange-colored product **13** (82.0 mg; 30%). In LCMS, the retention time was 4.28 mins (**Figure 13**).  $^1H$ -NMR (DMSO- $d_6$ , 400 MHz):  $\delta$  8.70 (1H, s), 6.87 (1H, s), 8.44 (2H, d, Ar-H,  $J=6.60$  Hz), 8.29 (1H, t, Ar-H,  $J=6.00$  Hz), 7.72 (1H, s, Ar-H), 7.69 (1H, s, Ar-H), 7.31-6.87 (5H, m), 6.81 (1H, s), 6.61 (1H, s), 5.68 (1H, s), 4.29 (1H, s), 4.11 (1H, t,  $J=6.64$  Hz), 3.90 (1H, s), 3.66 (1H, s), 3.57 (1H, d,  $J=5.76$  Hz), 3.40-3.32 (1H, m,  $J=7.04$  Hz), 2.90 (2H, s), 2.80 (2H, s), 2.59 (1H, d,  $J=3.88$  Hz), 2.31 (1H, d,  $J=10.4$  Hz), 2.19-2.13 (2H, m,  $J=13.48$  Hz), 1.98-1.96 (2H, m,  $J=10.8$  Hz), 1.78 (1H, s), 1.60-1.23 (12H, m,  $J=9.56$  Hz), 1.19-1.07 (2H, m,  $J=4.36$  Hz), 1.05-0.87 (4H, m), 0.86-0.77 (4H, m) (**Figure 13A**). HR-MS calculated for  $C_{57}H_{56}N_4O_{15}S$ , 1068.3463; measured,  $[C_{57}H_{56}N_4O_{15}S + H]^+$  1069.3542 (**Figure 13B**).

### 3.2.8 Synthesized drug DNA interaction by bio-physical techniques:

#### 3.2.8.1 DNA binding study of the synthesized compounds (3, 5 and 9):

Ultraviolet–visible spectroscopy titrations: Novel compounds with st-DNA were studied at 25°C using a 1 cm path length quartz cuvette. Stock

solutions of 1 mM concentrations of compounds **3**, **5**, and **9** were prepared in a mixture of MeOH-H<sub>2</sub>O solvent. Additionally, st-DNA stock solution was prepared by dissolving st-DNA (1.0 mg) in HPLC grade water (1.0 mL). From the absorbance ratio at 260 and 280 nm, the purity of st-DNA was monitored. The ratio of A<sub>260</sub>/A<sub>280</sub> was found to be 1.91, indicated no such protein contamination. The concentration of st-DNA solution was spectrophotometrically determined to be  $4.84 \times 10^2 \mu\text{M}$  using its known molar absorption coefficient at 260 nm, which is  $6600 \text{ M}^{-1} \text{ cm}^{-1}$ . All stock solutions were stored at 0–4°C [90]. st DNA and the complexes were prepared freshly. UV–visible absorption titrations were performed by adding St-DNA to a quartz cuvette containing approximately 1.0 mM hybrid solution.

#### **3.2.8.2 Fluorescence spectroscopy titrations:**

Fluorescence emission spectra were measured at 25°C using a 1 cm path length quartz cuvette. The compound concentration (1 mM) was kept constant and titrated with increasing amounts of st-DNA. Fluorescence spectra were recorded after addition of st-DNA to the cuvette [106]. The binding constant ( $K_b$ ) of a small molecule with DNA can be determined by following the equation  $\log[1/c] + \log [(F_0 - F)/F] = \log K_b$  equation 1, where  $K_b$  is the binding constant for the interaction of naphthalimide-DNA, and  $F_0$  and  $F$  denote the steady-state fluorescence intensities in the presence and absence of DNA, respectively. The binding constant ( $K_b$ ) could be determined from the intercept and slope by plotting  $\log [1/c]$  against  $\log [F / (F_0 - F)]$  where, ( $\log K_b = \text{intercept}$ ) according to equation 1.

**3.2.8.3 Competitive displacement assay:** Competitive displacement was studied for determining the ability of the synthesized drugs displacement of dye from the dye-DNA complex [91]. Ethidium bromide

(EB) and acridine orange (AO) were used as intercalating dyes, whereas Hoechst 33342 dye was used as a minor groove binder to validate the binding mode between the drugs and DNA. EB-DNA complexes were excited at 301 nm, and the emission spectra were recorded in the presence of increasing concentrations of drug solution. Similarly, the AO-DNA complex was excited at 490 nm, and emission spectra were recorded from 500 to 750 nm in the presence of increased drug solution. The DNA-Hoechst 33342 complex was excited at 343 nm in the presence of increasing concentrations of drug solution, and the emission spectra were recorded from 400-700 nm.

**3.2.8.4 Thermal denaturation studies:** Compounds **3**, **5** and **9** were subjected to thermal denaturation studies with st-DNA solution [92]. Fifty micromolar DNA and 1 mM solutions of compounds **3**, **5** and **9** were prepared in a methanol-water mixture. The thermal denaturation study of compounds **3**, **5** and **9** was prepared by using a 1:1 ratio of DNA to compound. The prepared drug-DNA complexes were then monitored at 260 nm using a Cary 100 Bio UV–Visible spectrophotometer fitted with a high-performance temperature controller, and heating was applied from 20°-100°C. The midpoint of the resultant melting temperature ( $T_m$ ) curve represents the point where half of the DNA melts. Thus, the thermal denaturation of DNA in the presence of synthesized naphthalimide-artesunate derivatives (compounds **3**, **5** and **9**) provides useful information on the conformational changes of DNA-drug binding.

### **3.3 Results:**

#### **3.3.1 Results and discussion:**

We designed, synthesized and characterized a series of DNA intercalative molecules containing a naphthalimide moiety conjugated with the

antimalarial drug artesunate through a suitable linker via ester (**3**, **9** and **13**) and amide (**5**) bonds by a multistep synthetic procedure. The products were obtained in a multistep synthetic procedure followed by detailed characterizations. First, commercially available 3-nitro-1,8-naphthalic anhydride was reacted with ethanol amine to obtain compound **2** under refluxing conditions in ethanol. Compound **2** was further reacted with artesunate by utilizing a coupling reagent to afford final product **3**. The artesunate naphthalimide conjugate **3** was confirmed by  $^1\text{H}$ -NMR spectroscopy data with  $\delta$  9.49- 8.06, the presence of the five aromatic protons (**Figure 4A**) was further confirmed by  $^{13}\text{C}$  NMR (**Figure 4B**) and HR-MS (**Figure 4C**). Nitro-substituted naphthalimide was introduced to further estimate the impact on anti-lymphoma validation. Therefore, commercially available 3-nitro 1,8-naphthalic anhydride **1** was considered and reacted with 1,2-ethylenediamine to obtain intermediate product **4** under refluxing conditions in an inert atmosphere. Compound **4** was further reacted with artesunate in the presence of a coupling agent to obtain the desired product compound **5**, which was further confirmed by  $^1\text{H}$ -NMR spectroscopy data with the presence of five aromatic protons with  $\delta$  9.48- 8.08 (**Figure 6A**) and further confirmed by  $^{13}\text{C}$  NMR (**Figure 6B**) and HR-MS (**Figure 6C**). The starting material 4-bromo-1,8-naphthalic anhydride **6** was reacted with 2-aminoethanol to obtain the desired product **7** under refluxing conditions in dry ethanol. Compound **7** was further converted to azide derivative **8**. The newly formed precursor compound **8** was further reacted with artesunate in the presence of a coupling agent to obtain the desired product **9**. Compound **9** is further confirmed by  $^1\text{H}$ -NMR spectroscopy data with the presence of five aromatic protons with  $\delta$  8.57- 7.78 (**Figure 9A**) and further confirmed by  $^{13}\text{C}$  NMR (**Figure 9B**) and HR-MS (**Figure 9C**). For the synthesis of the theranostic lymphoma drug, the amino-terminal naphthalimide moiety (**11**)

was conjugated with FITC for the validation of cellular bioavailability, and artesunate was attached to the naphthalimide moiety via an ester link (**13**), which was also characterized through  $^1\text{H}$  NMR and  $^{13}\text{C}$  NMR.

**3.3.2 DNA binding study of synthesized compounds (3,5 and 9) UV–visible spectroscopy:** Compounds **3**, **5** and **9** were analyzed by UV–visible spectroscopy. This study primarily monitored the changes in st-DNA topology upon incremental addition of DNA to the solution of compounds **3**, **5** and **9**. Compound **3** in the solution phase exhibited a prominent absorption band at 331 nm. In addition, DNA showed hypochromicity with a slight bathochromic shift from 331 nm to 333 nm (indicated by a 2 nm redshift) (**Figure 14**), indicating DNA intercalation with compound **3**. Similarly, compound **5** showed a prominent absorption band at 331 nm. The addition of st-DNA showed hypochromicity at 331 nm and a redshift from 331 nm to 334 nm, indicating an interaction between DNA and compound **5** (**Figure 14**). Compound **9**, upon the addition of st-DNA, showed a prominent absorption band at 367 nm, which resulted in hypochromicity at 367 nm along with a redshift to 376 nm (9 nm redshift) with the interaction of DNA (**Figure 14**). Ultimately, the results indicate that compounds **3**, **5** and **9** resulted in DNA intercalation between the two strands of St-DNA.

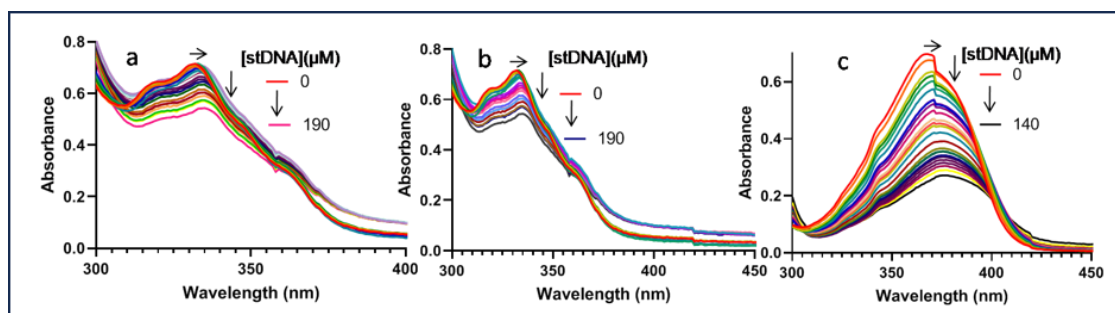


Figure 14. Effect on compounds **3**, **5** and **9** in a methanol-water mixture followed by incremental addition of DNA: (a) st-DNA addition (0 to 190



$\mu\text{M}$ ) on the absorption spectra of compound **3** (1 mM) in solution. The arrows indicate the hypochromicity at 331 nm, and a and 2 nm redshift from 331 nm to 333 nm; (b) st-DNA (0- 190  $\mu\text{M}$ ) on absorption spectra of compound **5** (1 mM), the arrows indicate the hypochromicity at 331 nm and redshift from 331 nm to 334 nm. (c) st-DNA (0-140  $\mu\text{M}$ ) on the absorption spectra of compound **9** (1 mM). The arrows indicate the hypochromicity at 367 nm and redshift from 367 nm to 376 nm.

**3.3.2 Fluorescence spectroscopy:** Fluorescence spectroscopy was performed to understand the mode of interaction between all three compounds (**3**, **5**, and **9**) and st-DNA to assess the electronic environment around the drug-DNA complex. The interaction of compound **3** with the DNA showed a prominent peak at 470.00 nm, scan condition:  $\lambda_{\text{ex}}$  400 nm,  $\lambda_{\text{emi}}$  410 – 680 nm (**Figure 16**). Following the addition of increasing concentrations of DNA, the fluorescence intensity gradually decreases. From equation 1 (mentioned in methodology section), the binding constant of compound **3** with DNA was ( $K_b = 5.3 \times 10^2 \text{ M}^{-1}$ ) at 470 nm (**Figure 15**). Similarly, compound **5** showed a prominent peak at 453.03 nm, scan condition:  $\lambda_{\text{ex}}$  380 nm,  $\lambda_{\text{emi}}$  390 – 680 nm (**Figure 16**).

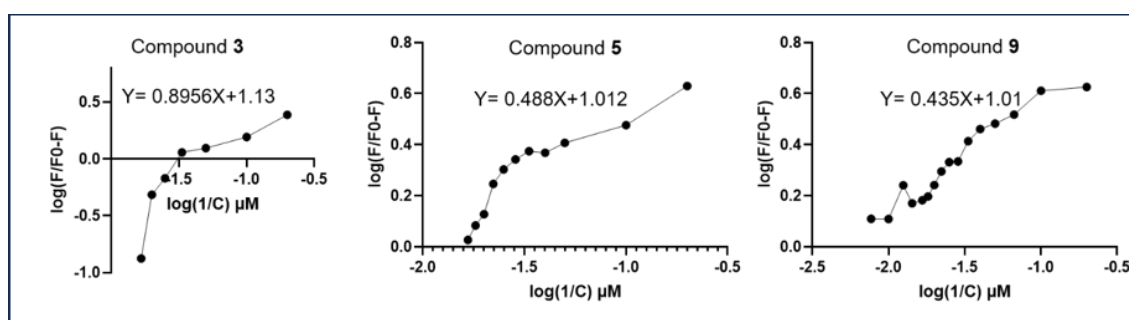


Figure 15: Plot to calculate the Binding constant of synthesized drugs (**3**, **5** and **9**) to st-DNA

Upon incremental addition of DNA to the compound solution **5**, the emission peak intensity decreased gradually at 453.03 nm as the DNA

seemed to lose its structural advances due to intercalation. From equation 1, the binding constant of compound 5 and DNA was ( $K_b = 5.3 \times 10^3 \text{ M}^{-1}$ ) at 453.03 nm (**Figure 15**). Compound 9 showed a prominent peak at 525.00 nm, scan condition:  $\lambda_{\text{ex}}$  410 nm,  $\lambda_{\text{emi}}$  420 – 700 nm (**Figure 16**). With the incremental addition of DNA to the compound solution 9, the emission peak intensity decreased gradually at 525.00 nm. From equation 1, the binding constant of compound 9 and DNA was ( $K_b = 4.00 \times 10^3 \text{ M}^{-1}$ ) at 525 nm (**Figure 15**). The result indicates that upon binding with DNA the fluorophore lost its structural advances upon interaction with DNA as a result the emission from the free drug (compounds 3, 5 and 9) decreases significantly.

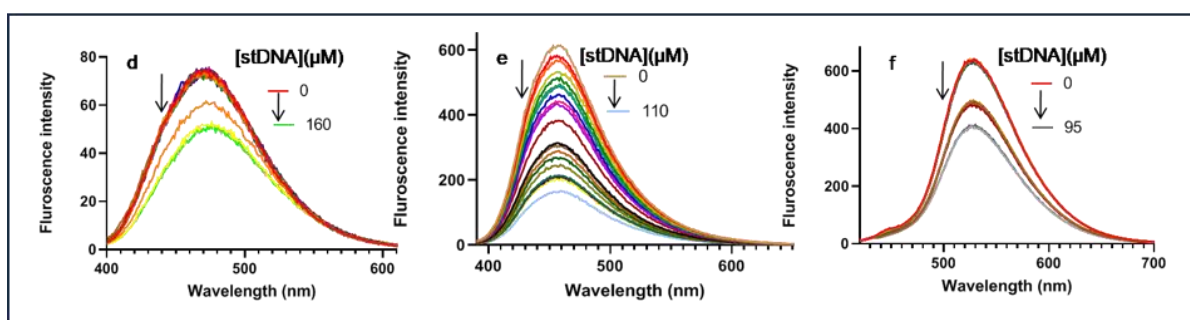


Figure 16. Effect of incremental addition of st-DNA (0-160 μM) to compound 3 (1 mM) in a methanol-water mixture; (e). Effect of incremental addition of st-DNA (0-110 μM) to Compound 5 (1 mM) in a methanol-water mixture. The arrows indicate the decrease in fluorescence intensity upon incremental addition of DNA; (f). Effect of incremental addition of st-DNA (0-95 μM) to compound 9 (1 mM) in a methanol-water mixture. The arrows indicate the decrease upon incremental addition of DNA.

### 3.3.3 Competitive displacement assay of compounds 3, 5 and 9:

The ethidium bromide (EB) displacement assay is usually performed to study the DNA binding mode. The incremental addition of compound 3 to the EB-DNA complex was able to displace EB from the complex as the

emission intensity gradually decreased upon excitation at 510.00 nm (**g**). The results indicate that compound **3** binds with DNA by a mechanism similar to that of intercalator EB and replaces EB from the DNA helix; as a result, the fluorescence emission intensity gradually decreases (15  $\mu$ M-100  $\mu$ M) with the addition of compound **3** (**Figure 17**). Compound **5** binds with DNA by a similar mechanism; as a result, it replaced EB from DNA, followed by a gradual decrease in the emission intensity upon  $\lambda_{\text{ex}}$  510.00 nm(**j**). Similarly, the incremental addition of compound **9** also replaced EB from the EB-DNA complex ( $\lambda_{\text{ex}}$  510.00 nm) (**m**), indicating the intercalative binding mode between compound **9** and DNA (**Figure 17**). The acridine orange (AO) displacement assay is useful to determine the DNA intercalative binding mode, and the Hoechst-33342 displacement assay is used to study the drug binding ability in the minor groove of DNA. Fluorescence intensity decreases in the presence of the incremental addition of compounds **3,5** and **9** in acridine orange (**h, k** and **n**) excited at 480 nm and Hoechst 33342 (**i, l** and **o**) excited at 343 nm with the st-DNA complex (**Figure 17**). The AO-DNA complex was excited at 480 nm, and the emission spectra were recorded from 450-700 nm. The Hoechst-DNA complex was excited at 343 nm, and the emission spectra were recorded from 400 to 700 nm. **Compounds 3, 5 and 9** bind with DNA by a mechanism similar to that of the intercalator AO and replace AO from the DNA helix; as a result, the fluorescence emission intensity decreases gradually (**h, k** and **n**) (**Figure 17**). The incremental addition of compound **3** (10  $\mu$ M -100  $\mu$ M) to the Hoechst-33342- DNA complex was able to displace Hoechst-33342 from the complex as the emission intensity gradually decreased (**i**). **Compounds 3, 5 and 9** bind with DNA by a similar mechanism to Hoechst-33342 and replace Hoechst-33342 from the DNA helix; as a result, the fluorescence emission intensity decreases gradually (**i, l** and **o**) (**Figure 17**). The result obtained from the

displacement assays indicates intercalative binding along with minor groove binding interaction of the synthesized compound (**3**, **5** and **9**) with DNA. This result indicates that the part of the compounds (**3**, **5** and **9**) with a naphthalimide moiety intercalates with st-DNA and that the part containing artesunate is a minor groove binder, as it can replace hoechst-33342.

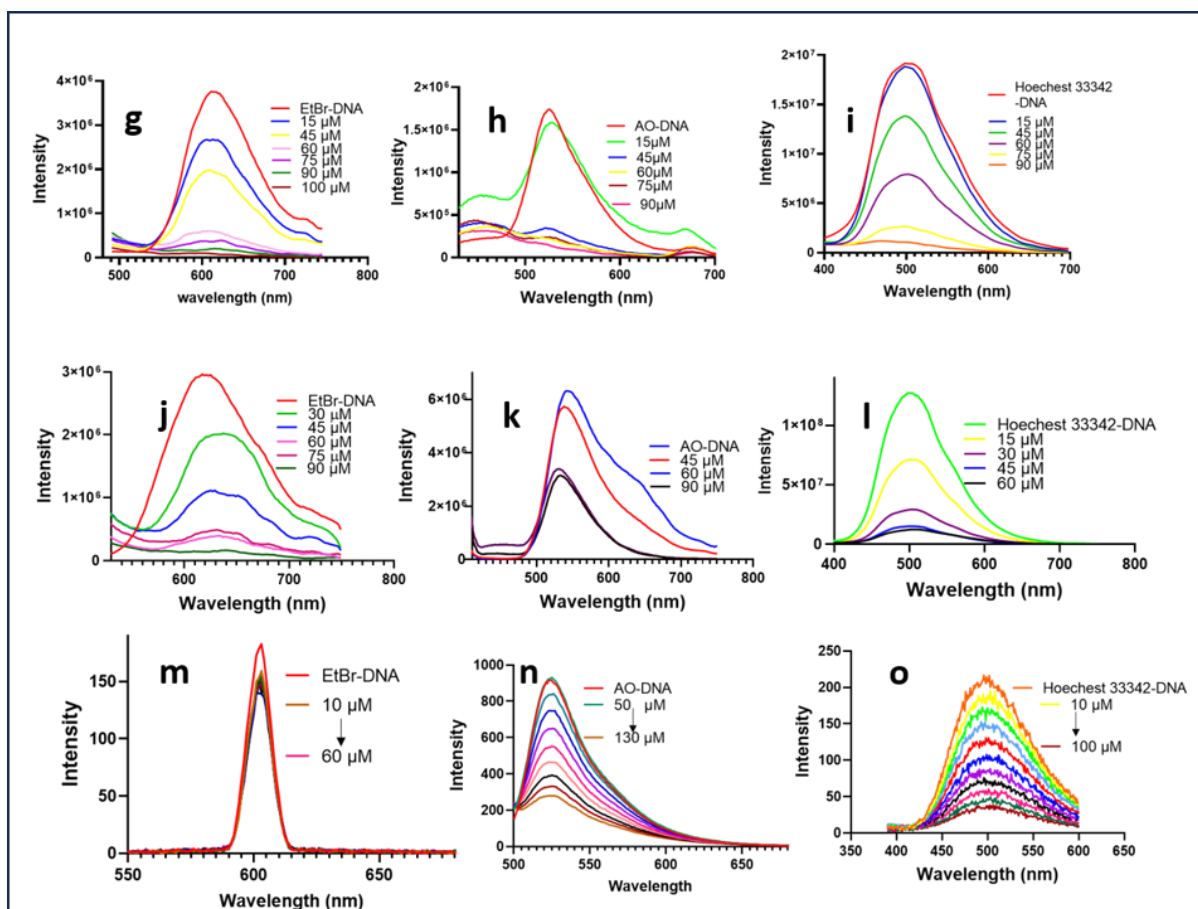


Figure 17. The St-DNA and EB complex was excited in the presence of increasing concentrations of compound **3**. The fluorescence emission intensity decreased with incremental addition of compound **3**, suggesting an intercalative mode of interaction with the DNA helix. Scan conditions:  $\lambda_{\text{ex}} = 510 \text{ nm}$ ,  $\lambda_{\text{emi}} = 520 - 800 \text{ nm}$  (g). The AO-DNA complex was excited at 480 nm, and the emission spectra recorded from 500-800 nm (h) with incremental addition of compound **3**. The Hoechst-DNA complex was

excited at 343 nm, and the emission spectra recorded from 350 to 650 nm with incremental addition of compound **3**(i). The St-DNA and EB complex was excited in the presence of incremental addition of compound **5**. The fluorescence emission intensity decreased with incremental addition of Compound **5**, suggesting an intercalative mode of interaction between compound **5** and DNA. Scan conditions:  $\lambda_{\text{ex}} = 510 \text{ nm}$ ,  $\lambda_{\text{emi}} = 520 - 800 \text{ nm}$  (j). The AO-DNA complex was excited at 480 nm, and the emission spectra recorded from 500-800 nm (k) with incremental addition of compound **5**. The Hoechst-DNA complex was excited at 343 nm, and the emission spectra recorded from 400 to 800 nm (l) with incremental addition of compound **5**. The St-DNA and EB complex was excited in the presence of incremental addition of compound **9**. The fluorescence emission intensity decreases with incremental addition of Compound **9**, suggesting an intercalative mode of interaction between compound **9** and DNA. Scan conditions:  $\lambda_{\text{ex}} = 510 \text{ nm}$ ,  $\lambda_{\text{emi}} = 520 - 700 \text{ nm}$  (m). At 480 nm the AO-DNA complex was excited, and the emission spectra were recorded from 500-800 nm with incremental addition of drug (n). The Hoechst-DNA complex was excited at 343 nm, and the emission spectra were recorded from 350 to 650 nm with incremental addition of drug (o).

### **3.3.4 Thermal denaturation study:**

Drug-DNA intercalation was studied from the thermal denaturation studies. The structure of DNA was stable due to hydrogen bonding and base stacking interactions. With rising temperature, the hydrogen bond and base stacking interactions were hampered as a result the double helix dissociated into single strands. At melting temperature ( $T_m$ ) half of the DNA sample melts. If a molecule intercalated with DNA a change in  $T_m$  may be observed. The  $T_m$  value of free st-DNA is 88°C. The melting temperatures ( $T_m$ ) of DNA-compound **3**, DNA-compound **5** and DNA-

compound **9** were 92°C, 94°C, and 94°C, respectively (**Figure 18**), indicating that compounds **5** and **9** possessed higher DNA melting temperatures than compound **3**.

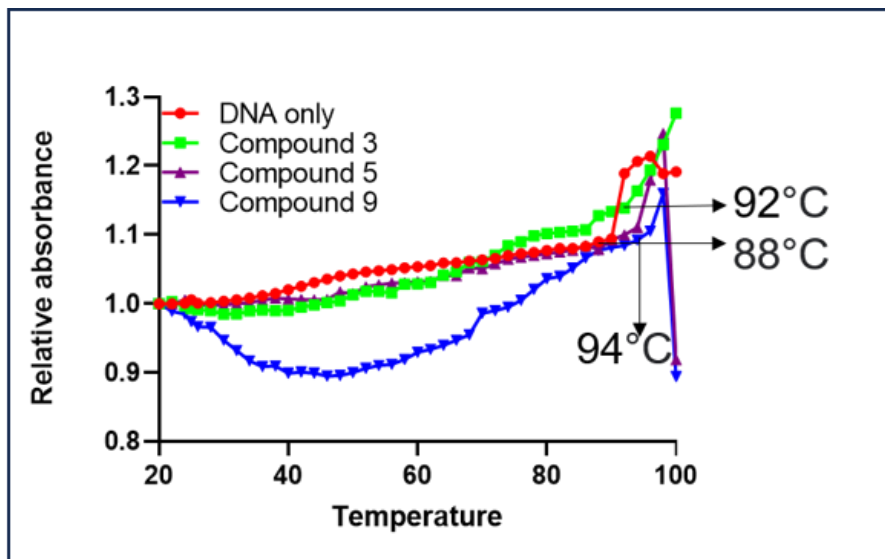


Figure 18. Thermal denaturation studies of compounds **3**, **5** and **9** and st-DNA only. The  $T_m$  value of free st-DNA is 88°C. The melting temperatures ( $T_m$ ) of DNA-compound **3**, DNA-compound **5** and DNA-compound **9** were 92°C, 94°C and 94°C, respectively.

### 3.4 Discussion & Conclusion:

All three compounds (**3**, **5** and **9**) differ with respect to the substituent on the naphthalimide moiety and the presence of a linker between artesunate and naphthalimide. Compound **5** contains an amide linker between artesunate and naphthalimide. The linker consists of an amide bond, which is considered stronger than the ester bond. In in vitro drug and DNA interactions, the results of different binding constants ( $K_b$ ) indicate that compound **5** has higher values, suggesting stable intercalation properties in comparison to the other two compounds (**3** and **9**). The stable interaction may also demonstrate the stability of the molecules (**5**), which consist of an amide linker between artesunate and 1,8- naphthalimide.

From the biophysical data it was evident that the naphthalimide moiety intercalate with DNA due to its planar structure followed by hypochromic red shift along with fluorescence intensity decreases. From the competitive displacement assay, it was clear that the naphthalimide moiety clearly displaced the intercalating dye AO and EtBr from The Dye-DNA complex but its counterpart artesunate is responsible for the displacement of Hoechst-33342 displacement which is a minor groove binder. So, the synthesized compounds intercalate with DNA with its naphthalimide moiety and the counter-part artesunate is responsible for binding with minor groove of the DNA.

### 3.5 Characterization of novel naphthalimide-artesunate compounds (3, 5 and 9) and FITC-conjugated naphthalimide-artesunate compound (13):

$^1\text{H}$  spectra of compounds **2**, **3**, **4**, **5**, **7**, **8**, **9**, **10**, **11**, **12**, and **13** and  $^{13}\text{C}$ -NMR spectra of compounds **3**, **5**, **9**, **12**, and **13**

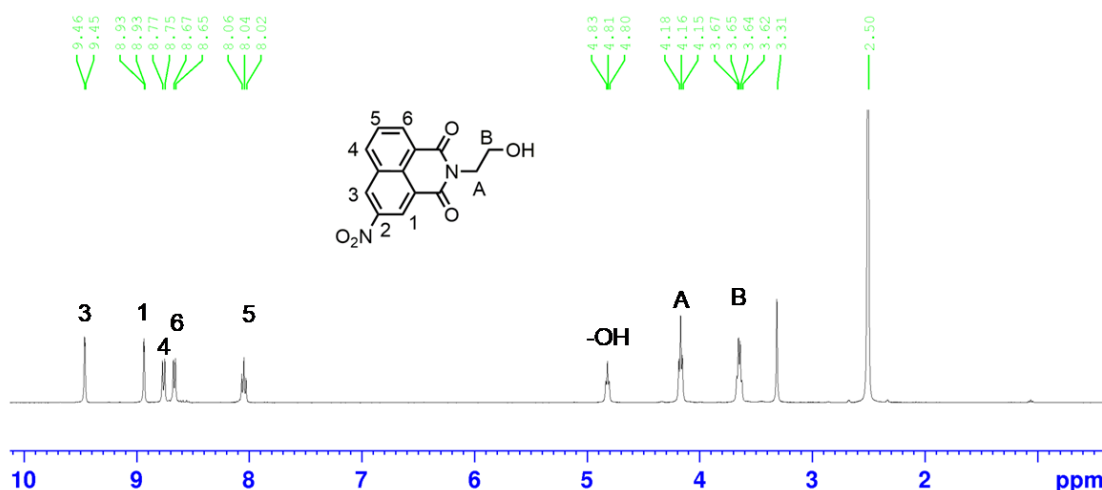
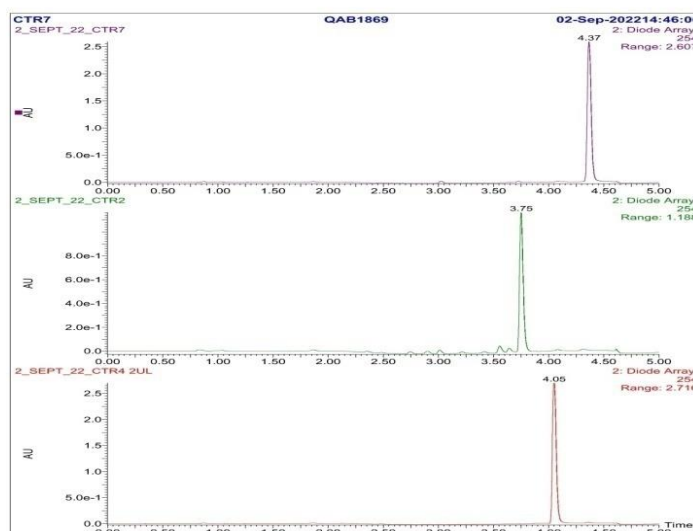
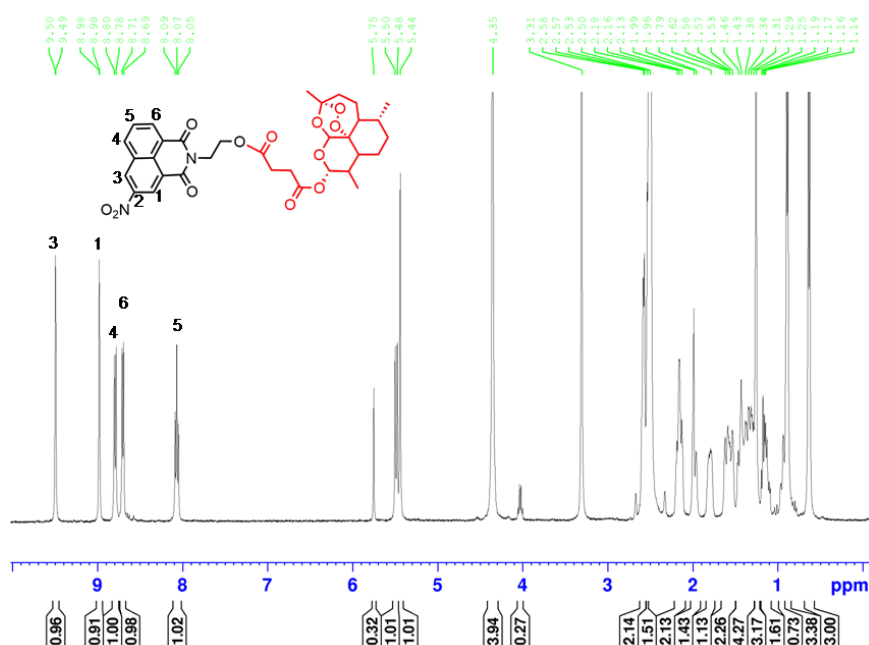


Figure 2.  $^1\text{H}$ -NMR (DMSO- $d_6$ , 400 MHz) of compound **2**, with the presence of five aromatic protons at  $\delta$  9.45-8.04, two  $-\text{CH}_2$  carbons at  $\delta$  3.64 and 4.1



**Figure 3.** The elution chromatogram of the compounds in UPLC–MS was presented on the basis of the UV spectrum. The UV spectra of compound **3** (bottom), compound **5** (middle) and compound **9** (top) are presented with retention times of 4.37, 3.75 and 4.05 minutes, respectively. The UV spectra were recorded at 254 nm.



**Figure 4A.**  $^1\text{H}$ -NMR (DMSO- $d_6$ , 400 MHz) of compound **3** with  $\delta$ 9.49-8.06, the presence of the five aromatic protons, and  $\delta$ 2.15 -0.6219 indicates the presence of an artesunate moiety.



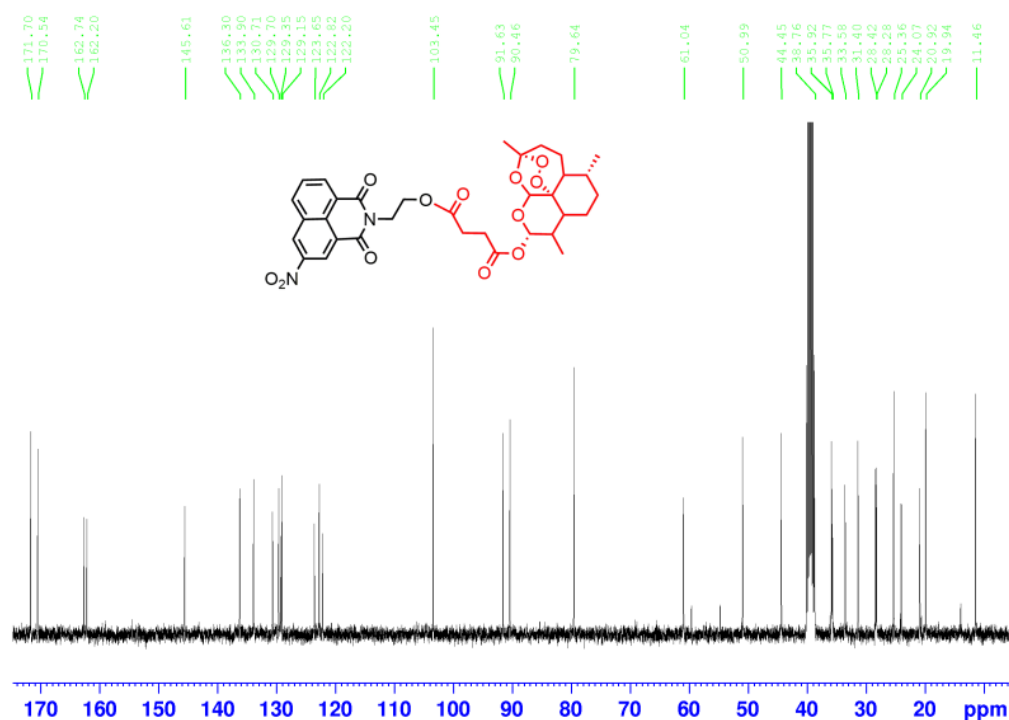


Figure 4B. <sup>13</sup>C-NMR (150 MHz, DMSO-d<sub>6</sub>) of compound **3**

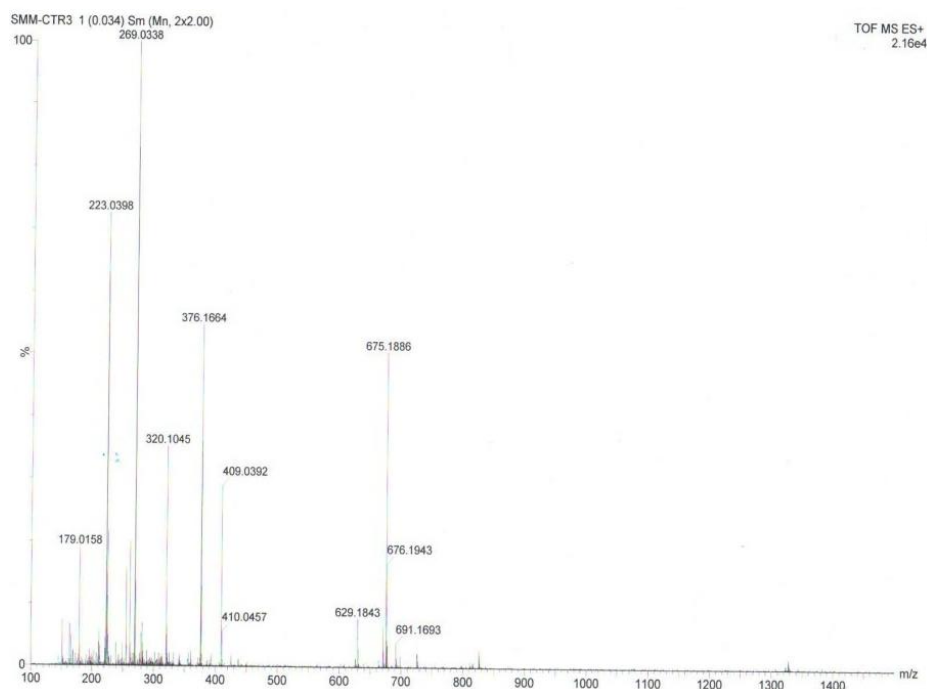


Figure 4C. HR-MS Calculated for C<sub>33</sub>H<sub>36</sub>N<sub>2</sub>O<sub>12</sub>, 652.2268; measured, C<sub>33</sub>H<sub>36</sub>N<sub>2</sub>O<sub>12</sub>Na 675.2166 Compound **3**

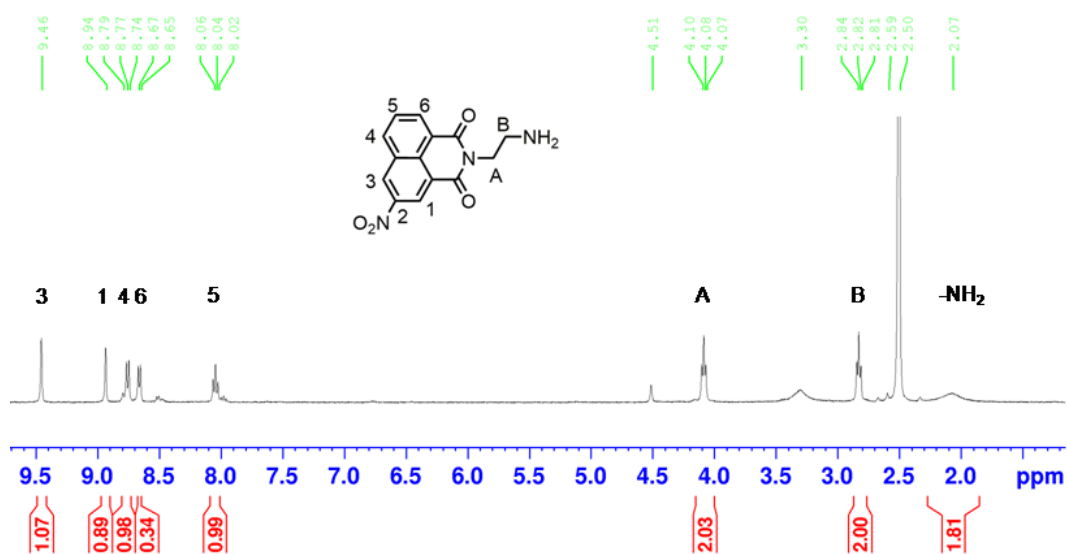


Figure 5. <sup>1</sup>H-NMR (DMSO-d<sub>6</sub>, 400 MHz) of compound **4** with  $\delta$  9.46-8.04, the presence of the five aromatic protons and two –CH<sub>2</sub> peaks at  $\delta$  4.08 and 2.82

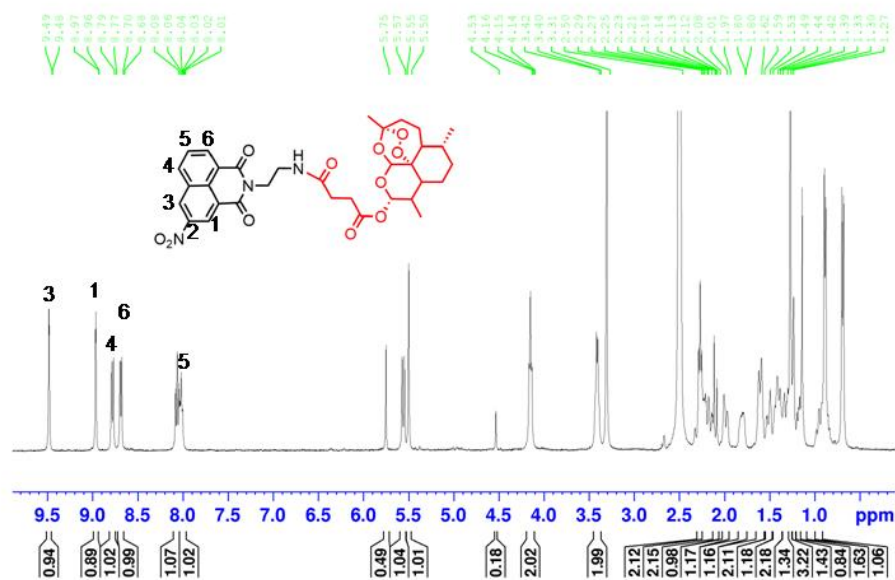


Figure 6A. <sup>1</sup>H-NMR (DMSO-d<sub>6</sub>, 400 MHz) of compound **5** with the presence of the five aromatic protons with  $\delta$  9.48- 8.06 and  $\delta$  2.28-0.6817 indicates the presence of an artesunate moiety

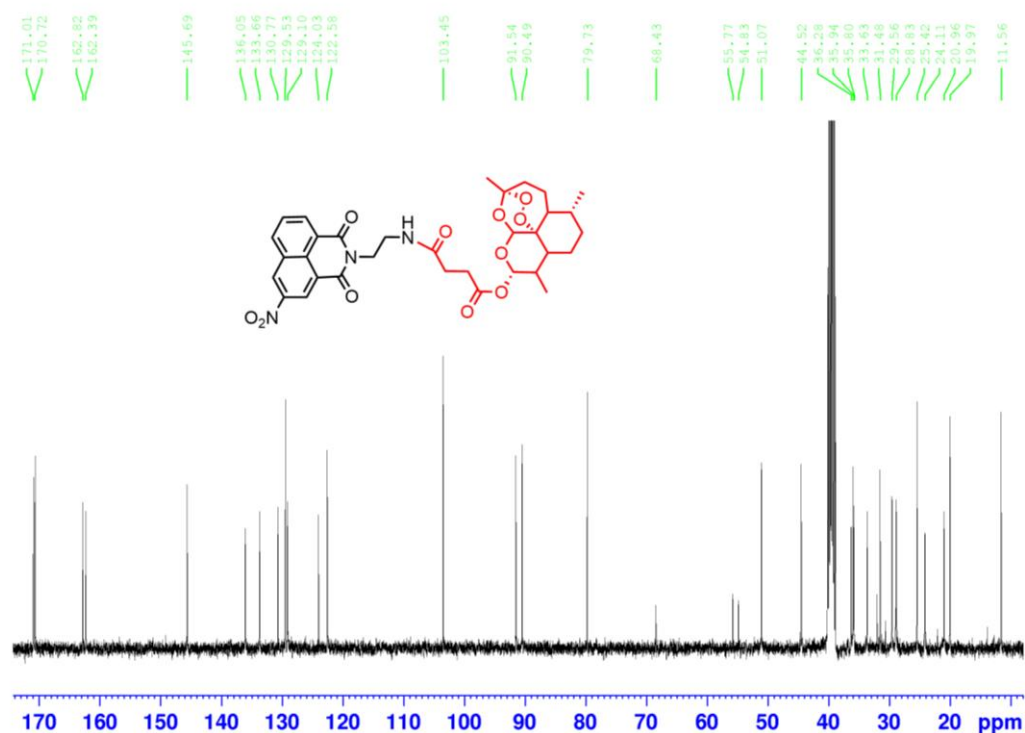


Figure 6B. <sup>13</sup>C-NMR (150 MHz, DMSO-d<sub>6</sub>) of compound **5**

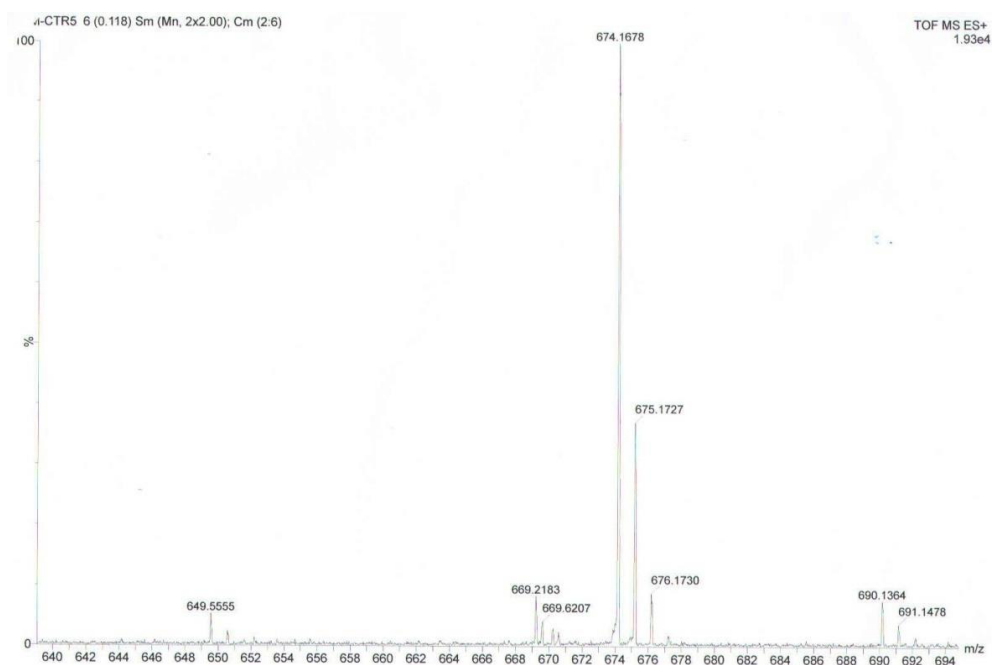


Figure 6C. HR-MS Calculated for C<sub>33</sub>H<sub>37</sub>N<sub>3</sub>O<sub>11</sub>, 651.2428; measured, C<sub>33</sub>H<sub>37</sub>N<sub>3</sub>O<sub>11</sub>Na 674.1628 Compound **5**

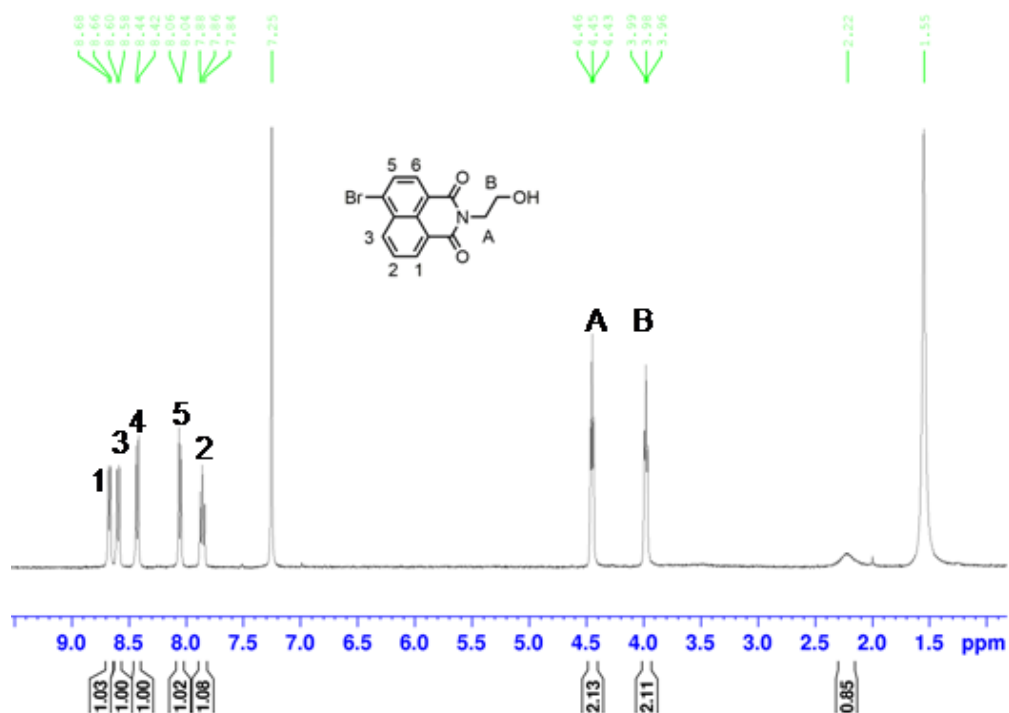


Figure 7. <sup>1</sup>H-NMR (CDCl<sub>3</sub>, 400 MHz) spectrum of compound **7** with the presence of five aromatic protons at δ 8.67–7.86 and two –CH<sub>2</sub> peaks at 4.45 and 3.98

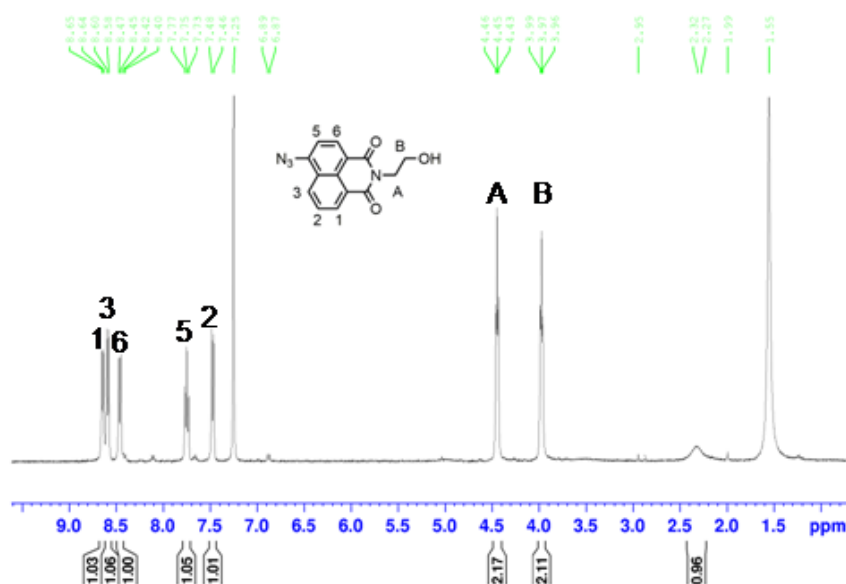


Figure 8. <sup>1</sup>H-NMR (CDCl<sub>3</sub>, 400 MHz) of compound **8**, with the presence of five aromatic protons with δ 8.64–7.62 and two –CH<sub>2</sub> peaks at 4.44 and 3.97

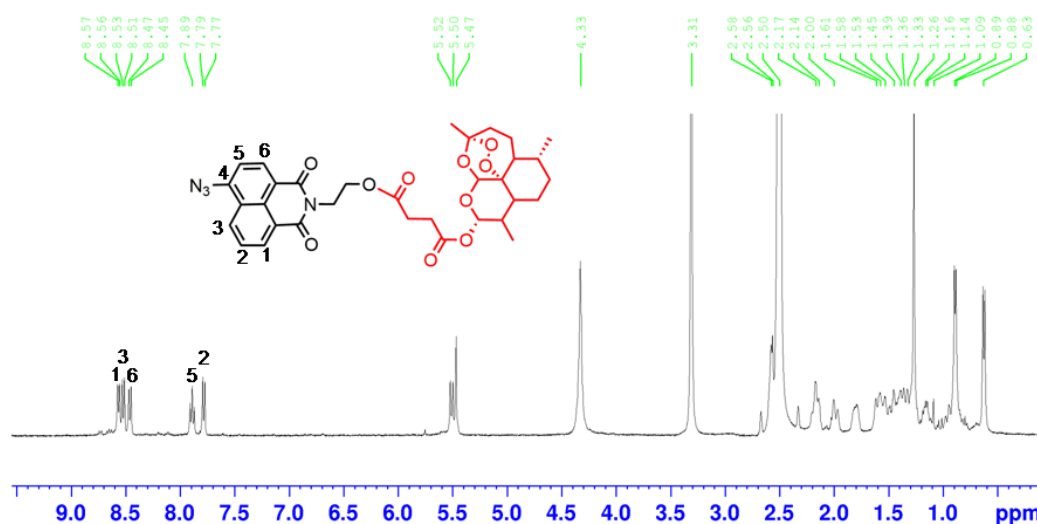


Figure 9A.  $^1\text{H}$ -NMR: (DMSO- $d_6$ , 400 MHz) of compound **9** with the presence of the five aromatic protons with  $\delta$  8.57- 7.78 and  $\delta$ 2.16-0.61 indicates the presence of an artesunate moiety

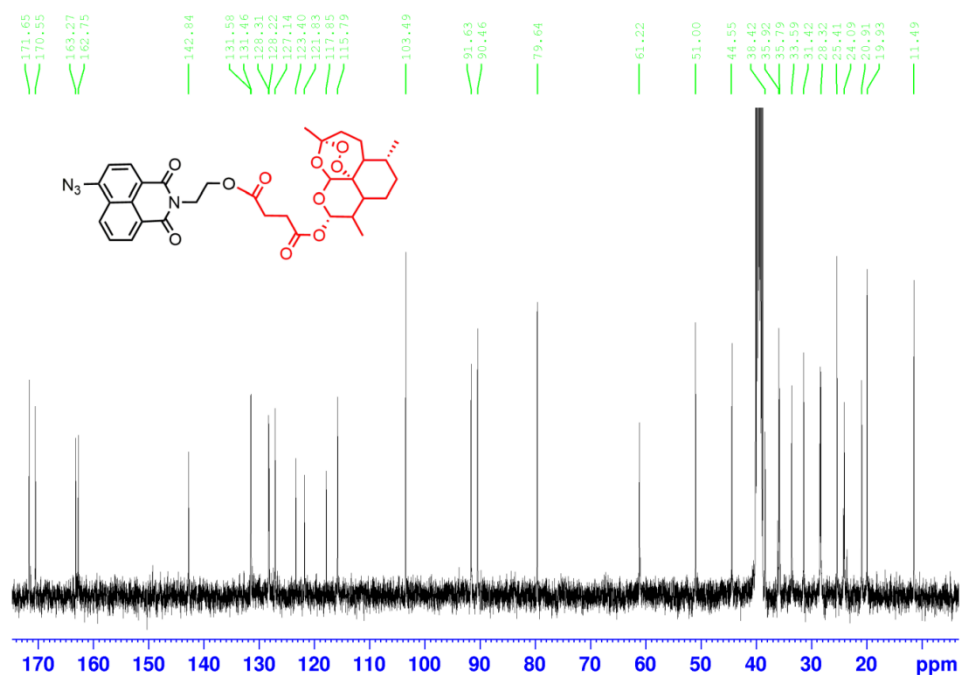


Figure 9B.  $^{13}\text{C}$ -NMR (150 MHz, DMSO- $d_6$ ) of compound **9**

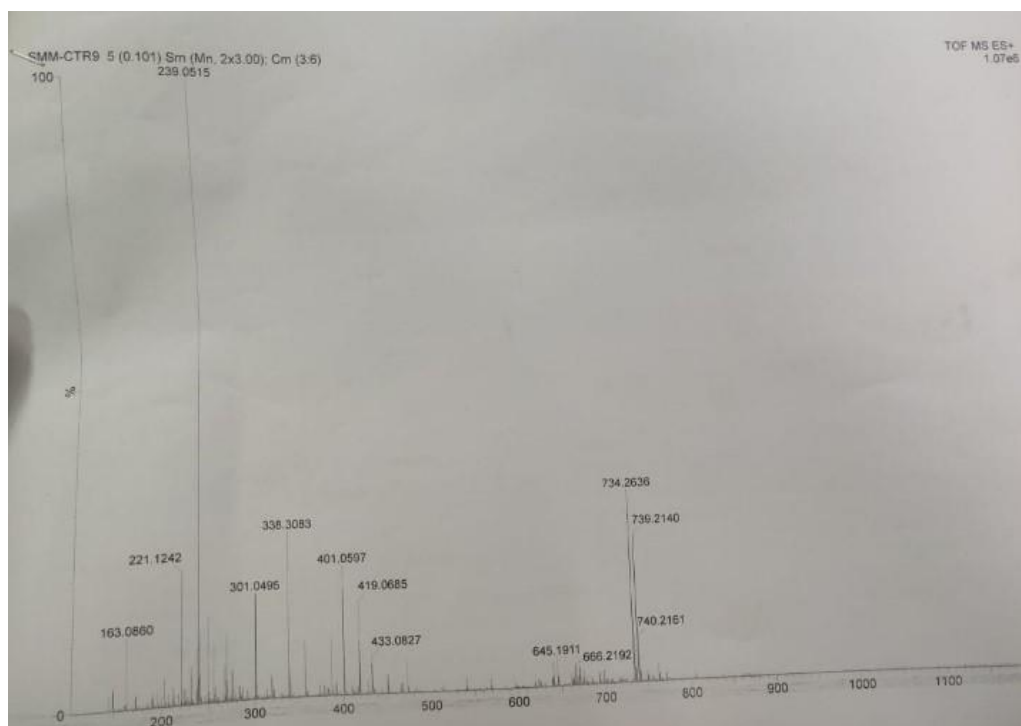


Figure 9C HR-MS Calculated for  $C_{33}H_{36}N_4O_{10}$ , 648.2431; measured,  $C_{33}H_{36}N_4O_{10}+H_2O$  666.2192 Compound **9**.

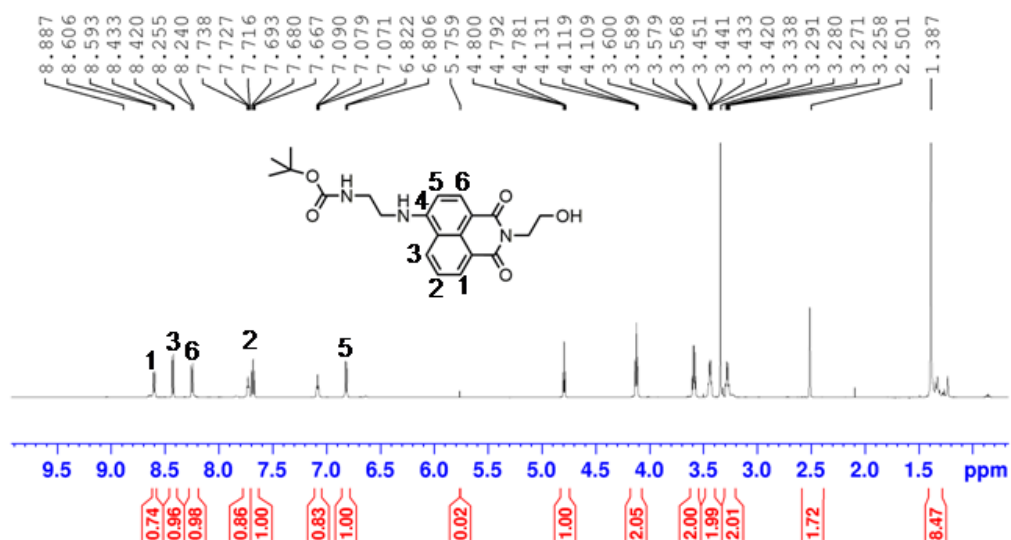


Figure 10A.  $^1H$ -NMR (DMSO, 400 MHz) of compound **10** with the presence of the five aromatic protons with  $\delta$  8.72- 6.81 and  $\delta$  1.38 indicate the presence of a methyl group

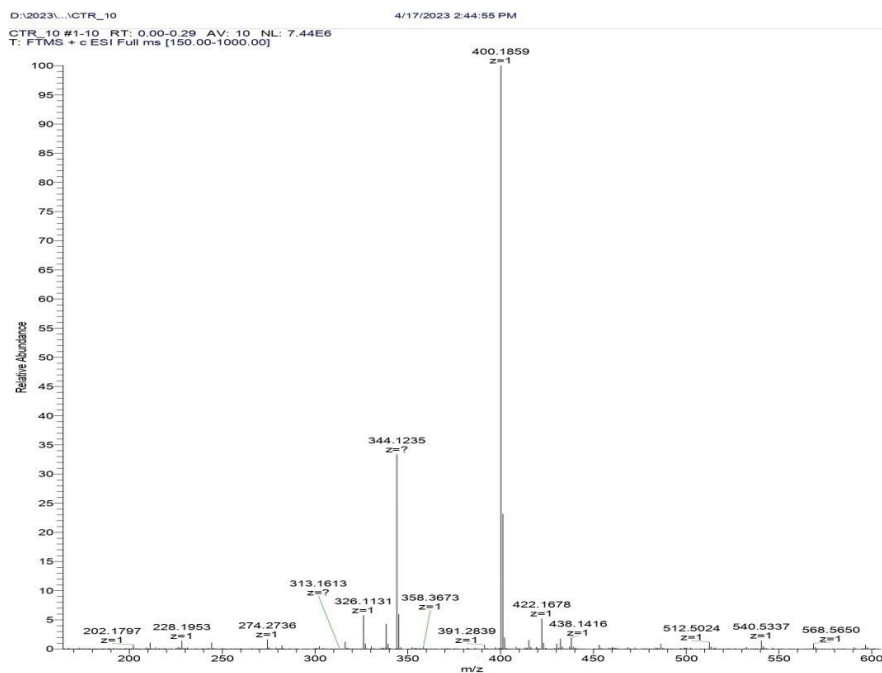


Figure 10B. HR-MS Calculated for  $C_{21}H_{25}N_3O_5$ , 399.1794; measured  $[C_{33}H_{36}N_4O_{10}+H]^+$  400.1859 Compound **10**

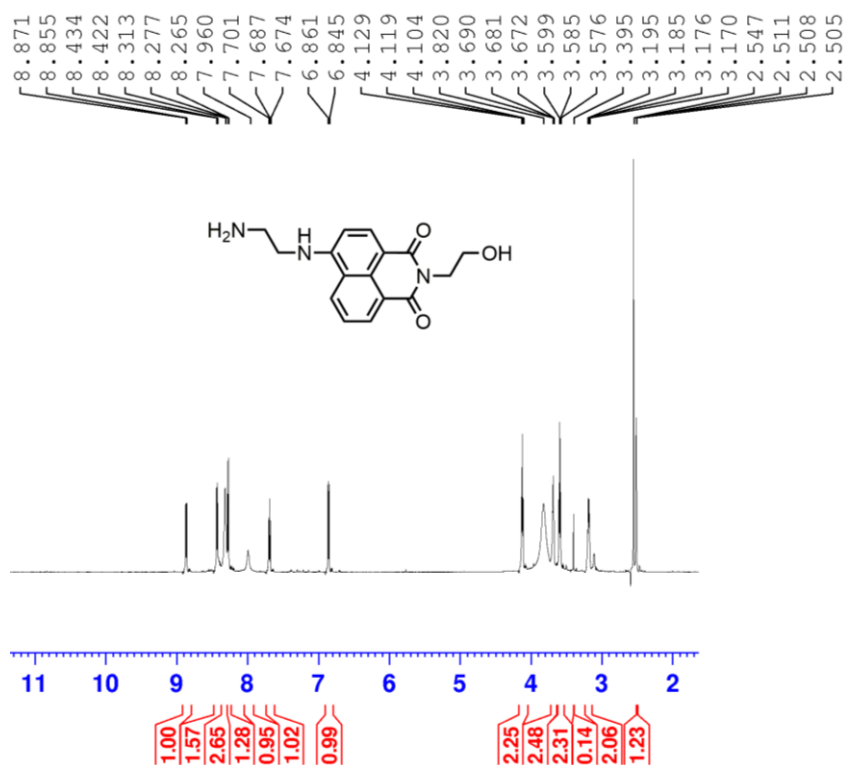


Figure 11A.  $^1H$ -NMR (DMSO, 600 MHz) of compound **11** with the presence of the five aromatic protons with  $\delta$  8.86- 6.85, the absence of a peak at  $\delta$  1.38 indicates Boc deprotection.

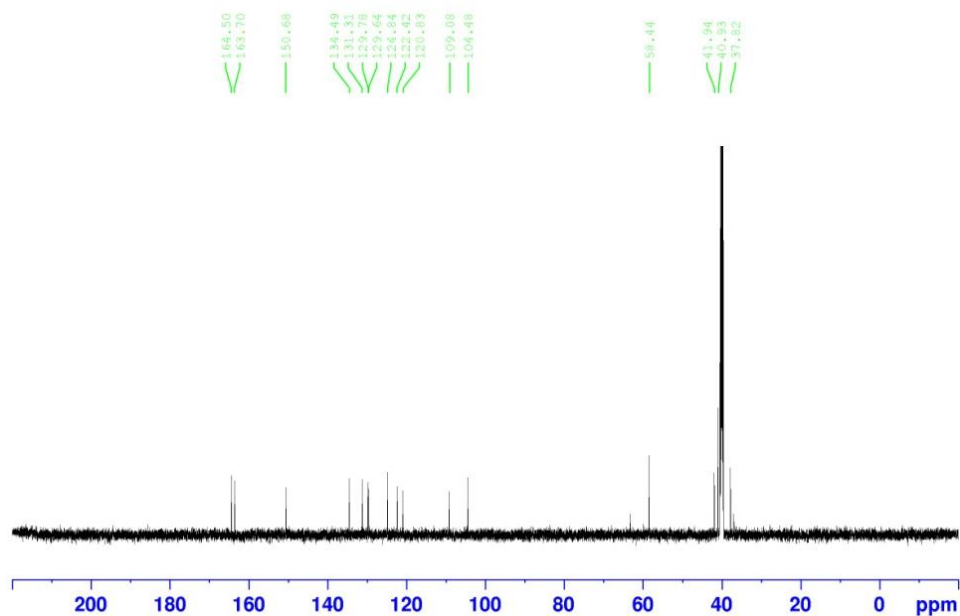


Figure 11B.  $^{13}\text{C}$ -NMR (150 MHz,  $\text{DMSO-d}_6$ ) of compound **11**

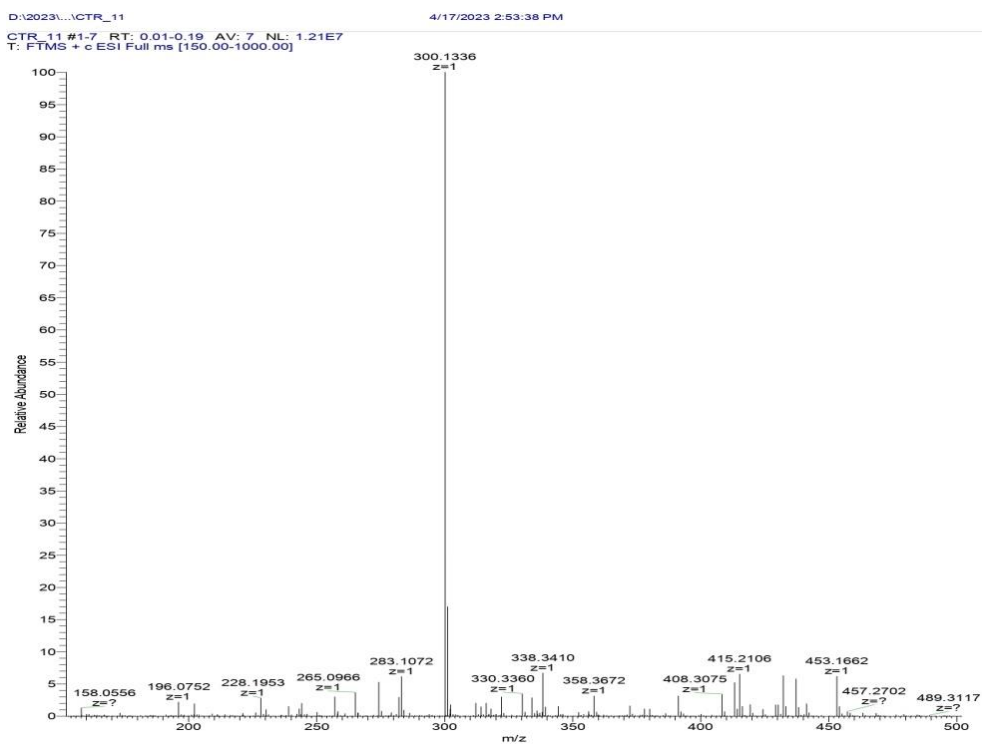


Figure 11C. HR-MS Calculated for  $\text{C}_{16}\text{H}_{17}\text{N}_3\text{O}_3$ , 299.1270; measured,  $[\text{C}_{16}\text{H}_{17}\text{N}_3\text{O}_3+\text{H}]^+$  300.1336 Compound **11**



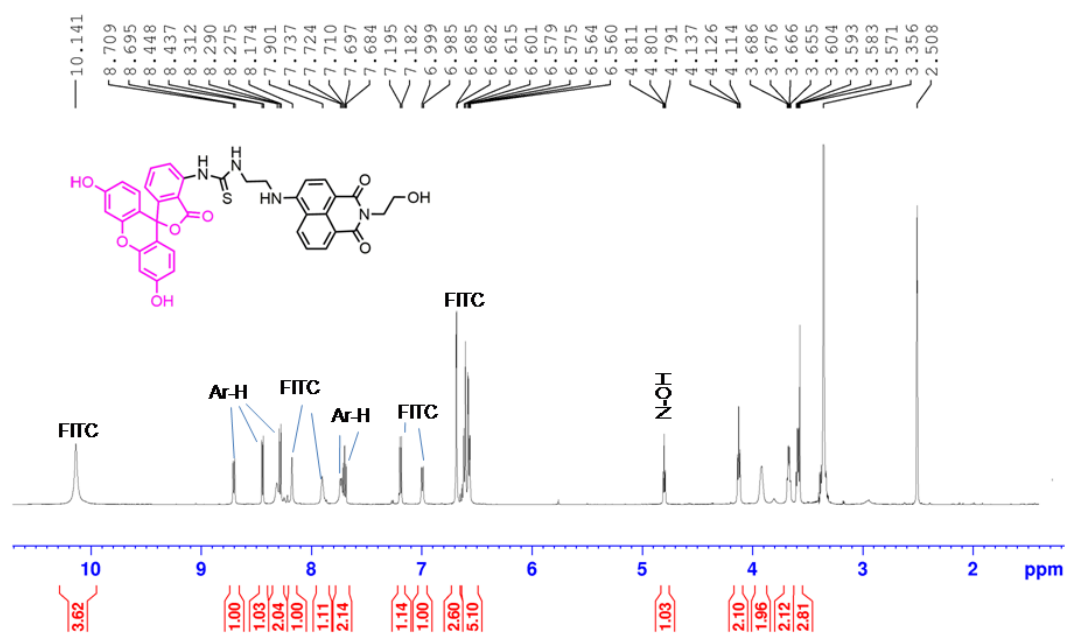


Figure 12A. <sup>1</sup>H-NMR (DMSO-d<sub>6</sub>, 600 MHz) of compound **12**.

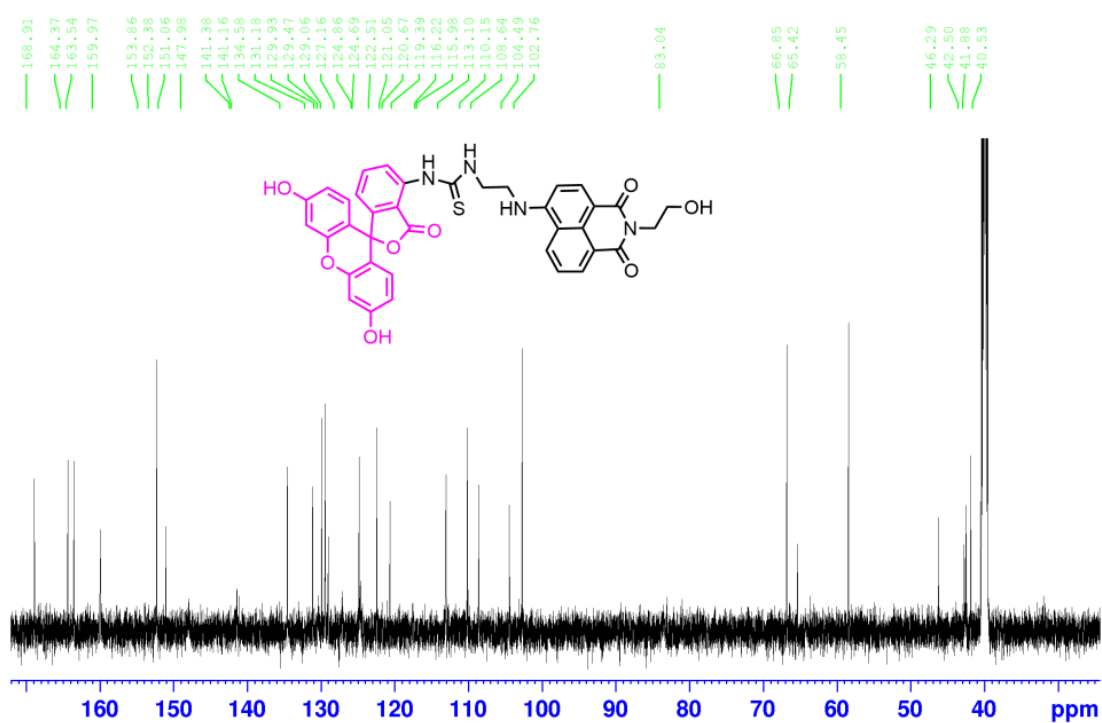


Figure 12B. <sup>13</sup>C-NMR (150 MHz, DMSO-d<sub>6</sub>) of compound **12**

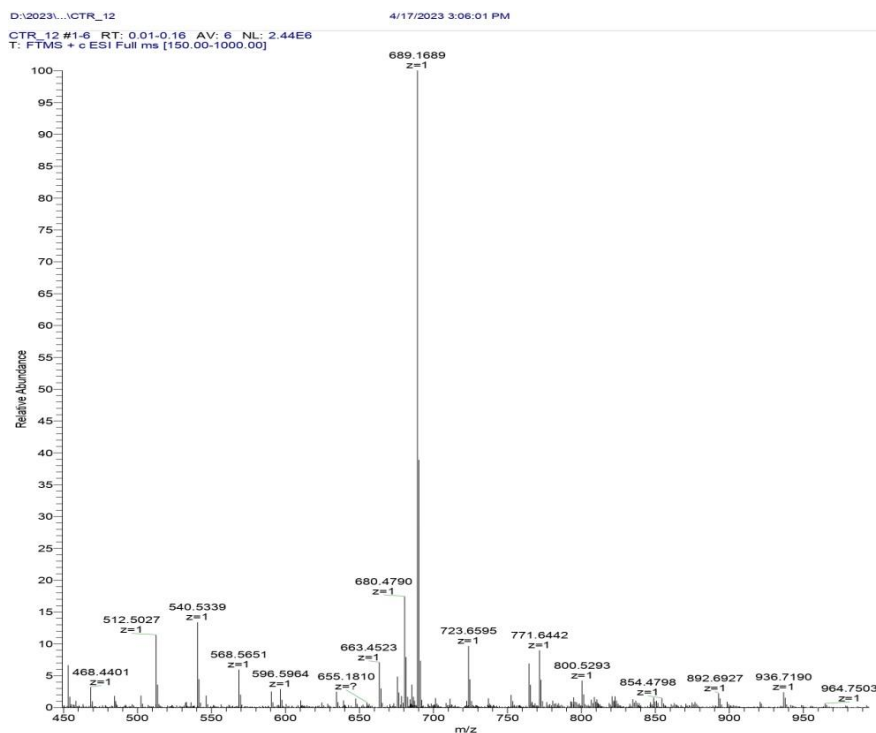


Figure 12C. HR-MS Calculated for  $C_{37}H_{28}N_4O_8S$ , 688.1628; measured,  $[C_{37}H_{28}N_4O_8S + H]^+$  689.1689 Compound **12**

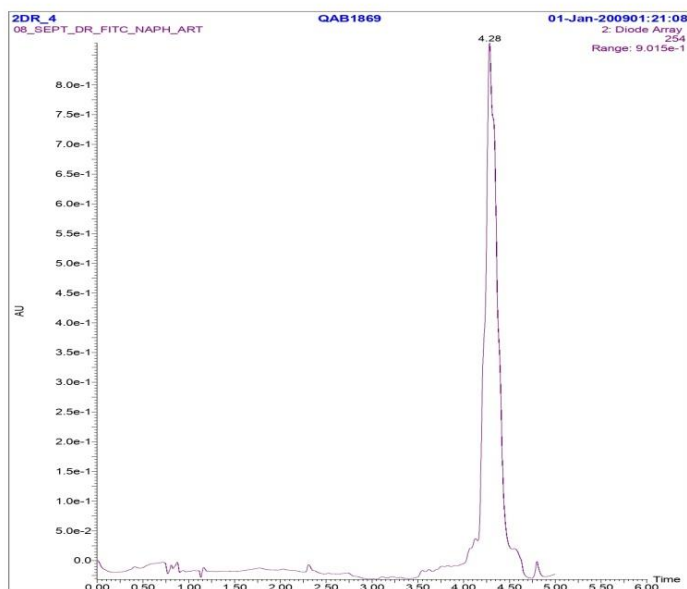


Figure 13. Elution of the compound in the UPLC–MS chromatogram, compound **13**, with a retention time of 4.28 min, monitored at 254 nm

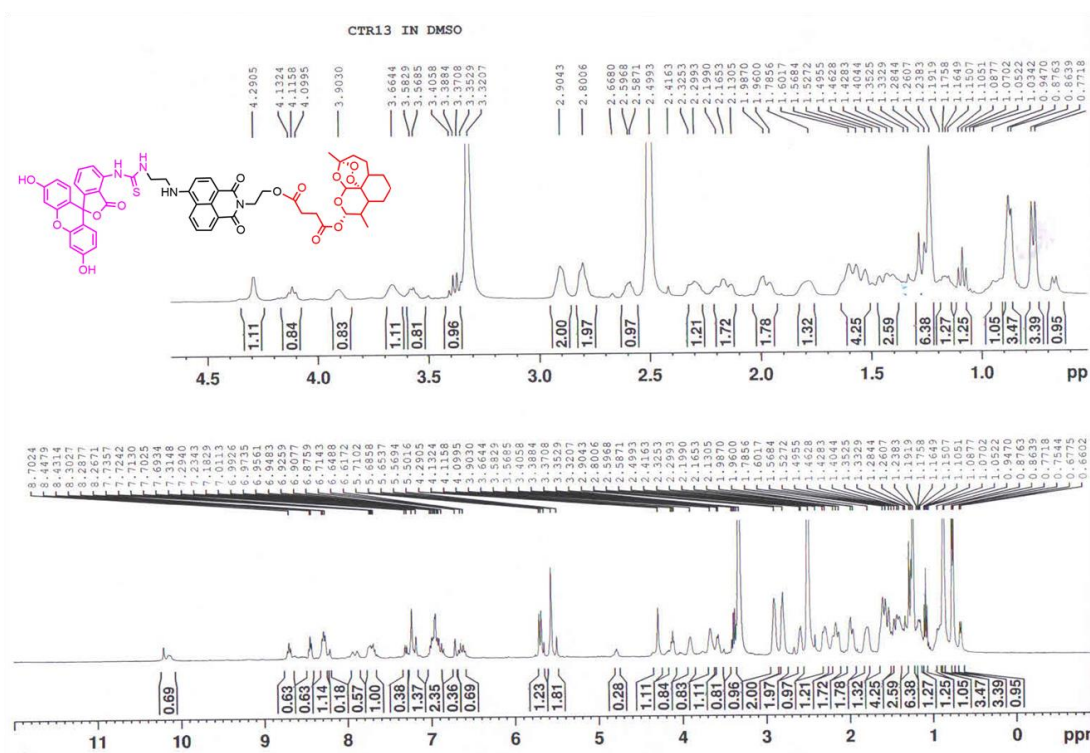


Figure 13A. <sup>1</sup>H-NMR (DMSO-d<sub>6</sub>, 400 MHz) of compound **13**.

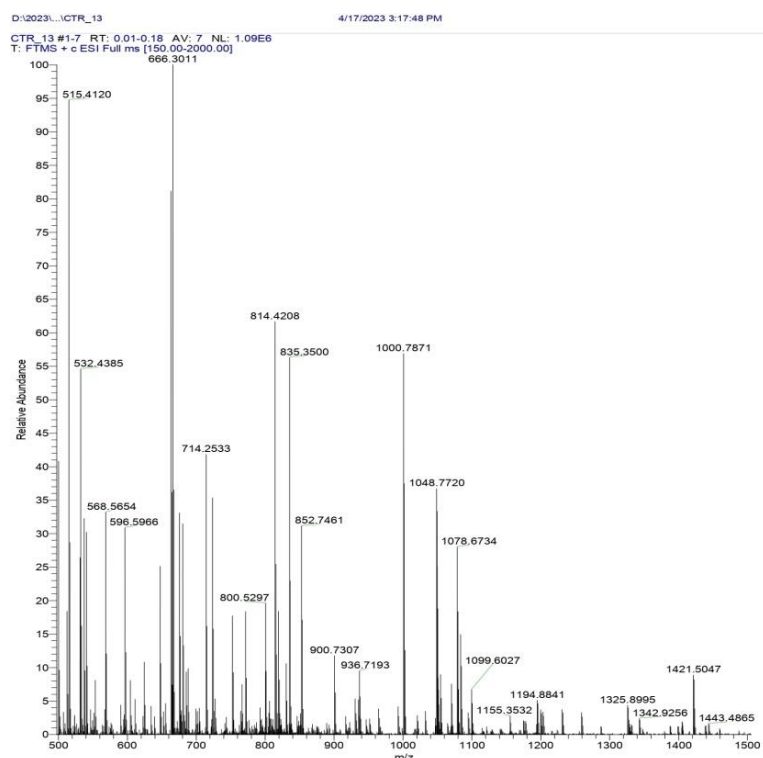
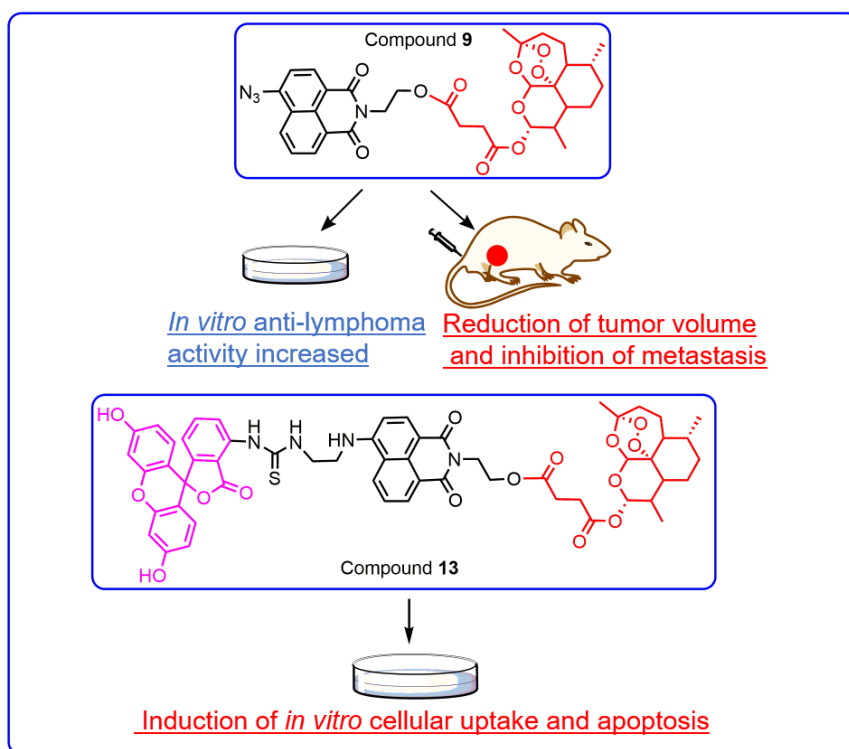


Figure 13B. HR-MS Calculated for C<sub>56</sub>H<sub>54</sub>N<sub>4</sub>O<sub>15</sub>S, 1055.1210; measured, C<sub>56</sub>H<sub>54</sub>N<sub>4</sub>O<sub>15</sub>S Na 1078.6734 Compound **13**

## Chapter 4

### **ANTITUMOR EVALUATION OF ARTESUNATE-NAPHTHALIMIDE HYBRID FOR MULTIMODAL THERAPY AGAINST EXPERIMENTAL MURINE LYMPHOMA.**



**4.1 Introduction:** Current drug treatment regimen in lymphoma only increases five-year survival of patients. Emergent need of novel molecule in lymphoma management is always welcome. Most of the successful drugs used in lymphoma target DNA. Naphthalimide in conjugation with artesunate via different linker may target DNA by intercalation. Amonafide and mitonafide are out of clinical trial due to the toxicity related issues. After modification in different substitution attached to the planar moiety the toxicity may change.

Cancer cells has more intracellular iron concentration than normal cells. In presence of intracellular iron, the endoperoxide bridge of artesunate cleaved as a result carbon centered free radical was generated. The reactive oxygen species (ROS) generation by artesunate is the lethal source of apoptosis by losing the mitochondrial outer membrane integrity followed by opening of a mitochondrial permeability transition pore (mPTP) followed by the liberation of Cyt c and upregulation of Bax expression, downregulation of Bcl-2 expression, and activation caspase-9 and caspase-3. Repositioning of clinically relevant drug artesunate by remodeling with a DNA intercalating moiety naphthalimide by different linkages for targeting DNA against lymphoma.

## **4.2 Materials and methods:**

**4.2.1 Materials:** RPMI 1640 (Invitrogen, USA), Fetal bovine serum (HyClone, Logan, UT, USA), Penicillin, Streptomycin (Invitrogen), colorimetric XTT assay (Roche, Indianapolis, IN), MTT assay CellTiter 96 kit (Promega, USA), CytoTox 96 Cytotoxicity assay kit from Promega, USA,

#### 4.2.2 Ethics statement:

This study was carried out under the rules and regulations of Committee for the purpose of control and supervision of Experiments on Animals (CPSEA). According to the AVMA guidelines the mice were euthanized by cervical dislocation.

#### 4.2.3 Mice, cell lines, and cell culture:

6-8 week old female germ free BALB/c mice were used for the *in vivo* study. DL cells were inoculated intraperitoneally into BALB/c (H2<sup>d</sup>) mice. The cells were maintained in RPMI 1640 media along with 10% fetal bovine serum and antibiotics. From ATCC RAJI and MCF-7 cells were purchased.

#### 4.2.4 Cell viability assay:

The effect of artesunate (ARTN), 4-azide naphthalimide-ethanol (**8**), 3-nitro naphthalimide-ethanoamine (**4**), 3-nitro-naphthalimide-ethanol (**2**), 4-azide-naphthalimide-artesunate (**9**), 3-nitro naphthalimide artesunate-amide (**5**), and 3-nitro naphthalimide-artesunate-ester (**3**) on the viability of tumor cells was evaluated by a colorimetric XTT assay [106]. In a 96 well plate  $5 \times 10^3$  cells/well tumor cells were inoculated. The above-mentioned compounds were incubated for 18 hours at 37°C with concentration dependent manner. In a plate reader (Synergy HT, BioTek, USA) at 450 nm the absorbance was measured. The percentage of cellular viability was calculated by the formula mentioned below.

$$\% \text{ Cell Viability} = \frac{\text{Experimental OD}_{450}}{\text{Control OD}_{450}} \times 100$$

#### 4.2.5 Cell growth inhibition assay:

Against DL and RAJI tumor cells the growth inhibition of above-mentioned compounds was studied by MTT assay. In a 96 well plate  $5 \times 10^3$  cells/well tumor cells were inoculated. The above-mentioned compounds were incubated for 48 hours at  $37^\circ\text{C}$  with concentration dependent manner [108]. In a plate reader (BioTek, USA) the absorbance was measured at 570 nm. The percentage of growth inhibition was calculated by the formula mentioned below.

$$\% \text{ Growth Inhibition} = \left[ 1 - \frac{\text{Experimental OD}_{570}}{\text{Target OD}_{570}} \right] \times 100$$

#### 4.2.6 Cytotoxicity assay:

The cytotoxic activity of the above-mentioned formulations against the tumor cells ( $5 \times 10^3$ ) was measured by cytotoxicity assay. In a 96 well plate  $5 \times 10^3$  cells/well tumor cells were inoculated. The above-mentioned compounds were incubated for 18 hours at  $37^\circ\text{C}$  with concentration dependent manner [103]. The percentage of cytotoxicity was calculated by the formula mentioned below.

$$\% \text{ Cytotoxicity} = \frac{(\text{Experimental} - \text{Effector Spontaneous} - \text{Target Spontaneous})}{(\text{Target Maximum} - \text{Target Spontaneous})} \times 100$$

#### 4.2.7 *In vitro* wound healing assay:

*In vitro* scratch-wound healing assay was performed on serum starved MCF-7 cells [95]. The wound was created by scratching the confluent layer of MCF-7 cells with a sterile microtips. The image was captured immediately after scratching. The cells were grown in presence of two different concentration of compound **9** (150  $\mu\text{M}$ , 250  $\mu\text{M}$ ) at different time (16, 24 and 48 hour) interval. The wound area was calculated by using

ImageJ by calculating the distance between the edge. The wound closure percentage was calculated.

$$\text{Wound closure (\%)} = [A(t=0h) - A(t=\Delta h) / A(t=0h)] \times 100$$

Wound area at measured 0 h ( $A(t=0h)$ ) and wound area measured after different time interval ( $A(t=\Delta h)$ ).

#### **4.2.7 Apoptosis and cellular internalization study:**

The induction of cellular apoptosis was studied in DL, RAJI and MCF-7 tumor cells following treatment with the indicated formulations (50, 25 and 12.5  $\mu\text{M}$ ) for eight hours. Untreated cells were used as a positive control. After eight-hour incubation the cells were treated in cold PBS and finally stained with PE-conjugated Annexin V for half an hour. Again, the cells were washed in annexin V buffer. Under a fluorescence microscope (EVOS FL Cell Imaging System equipped with Plan Fluor, 40X, NA 0.75 objective, Life Technologies, USA) the PE-conjugated Annexin V positive cells were visualized. Temporal uptake of substituted naphthalimide-FITC (**12**) or substituted naphthalimide-artesunate-FITC (**13**) in DL, RAJI and MCF-7 cells was assessed, followed by observation of intracellular green fluorescence in the cells.

#### **4.2.8 *In vitro* cellular uptake study by Fluorescence spectroscopy:**

The number of *in vitro* cellular internalization in DL cells of compound **12** and **13** were calculated by using a standard curve of different concentrations (10.0, 5.0, 2.5 and 1.0  $\mu\text{M}$ ) of compound **12** and **13** in PBS [94]. DL cells ( $5 \times 10^3$ ) were seeded into the 96-well black plates and incubated to form a confluent monolayer. From the stock solution of 50.0, 35.0, 25.0, 15.0 and 12.5  $\mu\text{M}$  concentration of compound **12** and **13** were treated followed by incubation for eight-hours at 37°C in 10% FBS and 1% penicillin-streptomycin supplemented RPMI media. After eight-hour



incubation it was centrifuged and washed by using PBS (pH 7.4) and RIPA lysis buffer was added to lyse the cells. After cell lysis the cell associated FITC conjugated compound **12** and **13** were quantified by analyzing the lysate in a fluorescence plate reader instrument SpectraMax i3x ( $\lambda_{ex}$  488 nm,  $\lambda_{em}$  515 nm). Fluorescent intensity of the supernatant was also measured [96]. Cellular uptake efficiency percentage was calculated by the formula mentioned below.

Cellular uptake efficiency (%) = (Cell uptake FITC/amount of fluorescence present in the medium+ Cell uptake FITC)  $\times$  100

#### **4.2.9 Cellular Uptake study by FACS:**

In a six well plate the DL cells were seeded ( $5 \times 10^5$ ) and cultured for 24 h in 10% FBS and 1% penicillin-streptomycin supplemented RPMI media. 12.5  $\mu$ M FITC-labelled drug conjugate Compound **12** and **13** was added and incubated for 1,2,4,6 and 8 hours respectively. The treated cells were taken in a falcon tube and given a spin at 1650 RPM; the supernatant was discarded. The pellet was washed twice with 2% FBS enriched PBS (pH 7.4). The pellet was dissolved in 600 $\mu$ l sheath fluid and analysed using a FACS Calibur flow cytometer and ModFit software (BD Biosciences). DL cells ( $5 \times 10^5$ ) were seeded in six well plate and cultured for 24 hours in RPMI media supplemented with 10% FBS and 1% penicillin-streptomycin. 100.0, 50.0 and 12.5  $\mu$ M FITC-labelled drug conjugate Compound **12** and **13** were added and incubated for 8 hours. The treated cells were taken in a falcon tube and given a spin at 1650 RPM; the supernatant was discarded. The pellet was washed twice with 2% FBS enriched PBS (pH 7.4). The pellet was dissolved in 600 $\mu$ l sheath fluid and analysed using a FACS Calibur flow cytometer and ModFit software (BD Biosciences). For each sample a total of 50,000 events were collected and analysed [97].

#### **4.2.9 Tissue processing and histopathological assays:**

Vascularized organs were collected from healthy control, DL tumor-bearing mice. The organs were fixed in normal buffered formalin and processed further. The tissue sections were embedded in paraffin. Finally stained with hematoxylin and eosin (H&E) and for scrutinized the regions of tumor metastasis. In a Nikon 80i research microscope ( $\times 400$ ) the images were captured.

#### **4.2.10 *In vivo* studies: Induction of solid murine lymphoma and treatment experiments:**

The DL tumors were maintained (*in vitro*) in 10% FBS supplemented RPMI 1640 media. *In vivo* the DL tumor cells were mentioned in the peritoneal cavity of female BALB/c mice. The DL tumor cells ( $3 \times 10^4$ ) were inoculated intradermally in the left flank of 18-20 g ( $n=6/\text{group}$ ) female BALB/c mice. At day 10, the treatment schedule was started, and altogether, 5 injections were given at an interval of 5 days. Tumor volume and weight were calculated using digital slide calipers. Using a slide caliper, the tumor volume ( $\text{mm}^3$ ) was measured by using the formula mentioned below: tumor volume ( $\text{mm}^3$ ) =  $1/2$  [length $\times$ (width)  $\times$  height]. Control animals received PBS only. Mice were observed until day 50, for survival analysis.

#### **4.2.11 Statistical analysis:**

For each experimental group ( $n = 3$  to  $5$ ) the mean  $\pm$  standard deviation (SD) value was calculated. Differences among as well as between the groups were quantified by ANOVA and Holm-Sidak post hoc multiple comparison tests by using the (GraphPad) PRISM statistical analysis software. By using GraphPad Prism software (GraphPad) the Survival plots (Kaplan-Meier analysis) were generated, and statistical significance

between the groups was analyzed by means of the log-rank (Mantel-Cox) test. \*0.05, \*\*0.01, \*\*\*0.001, \*\*\*\*0.0001.

### 4.3 Results:

**4.3.1 Compound 3,5 and 9 reduces tumor cell growth (*in vitro*):** The tumoricidal potential of compound **3**, **5**, **9** and artesunate was studied in DL tumor cells and RAJI cell line. With the treatment of compound **9** in the above-mentioned lymphoma cell line the viability was significantly reduced as compared to other synthesized compounds (**3,5,2,4** and **8**) and artesunate in a concentration dependent manner. At the highest concentration the viability upon compound **9** treatment was reduced to <30%, compared to 60% when treated with artesunate or 80% in the presence of compound **8** ( $p<0.0001$ ). Compound **9** showed similar type of pattern at lower concentration than other derivatives and artesunate. Result indicates compound **9** showed significant reduction of viability as compared to other derivatives.

Compound **9** exhibited significant cytotoxicity upon releasing LDH as compared to other synthesized derivatives and artesunate. Compound **9** showed significant increment of cytotoxicity (73%) at highest concentration as compared to artesunate (40%) and compound **8** (20%) ( $p<0.0001$ ).

In DL cells compound **9** showed 87% growth inhibition, where the only artesunate treatment group showed 71% growth inhibition ( $p<0.01$ ). Synthesized compound **3** and **5** also showed significant inhibition as compared to artesunate only treatment group. Compound **2,4** and **8** were significantly less potent as compared to compound **3,5** and **9**. Result indicates that artesunate conjugated azide decorated naphthalimide

moiety (compound **9**), has better tumoricidal activity as compared to other synthesized derivatives and artesunate.

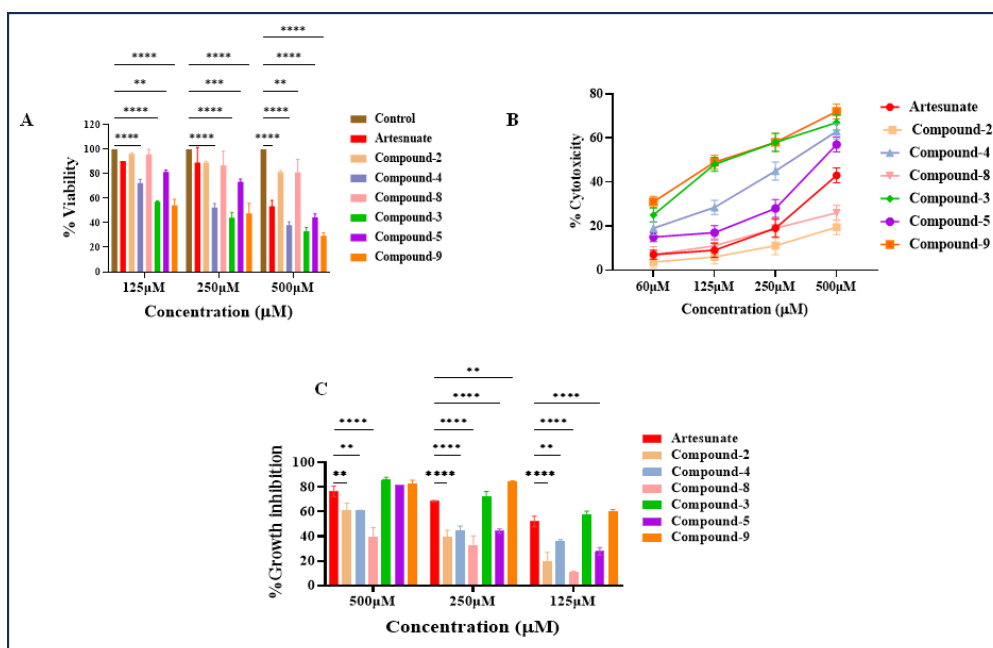


Figure 1: (A) Viability, (B) cytotoxicity and (C) growth inhibition of DL tumor cells in the presence of varying concentrations of the indicated treatment.

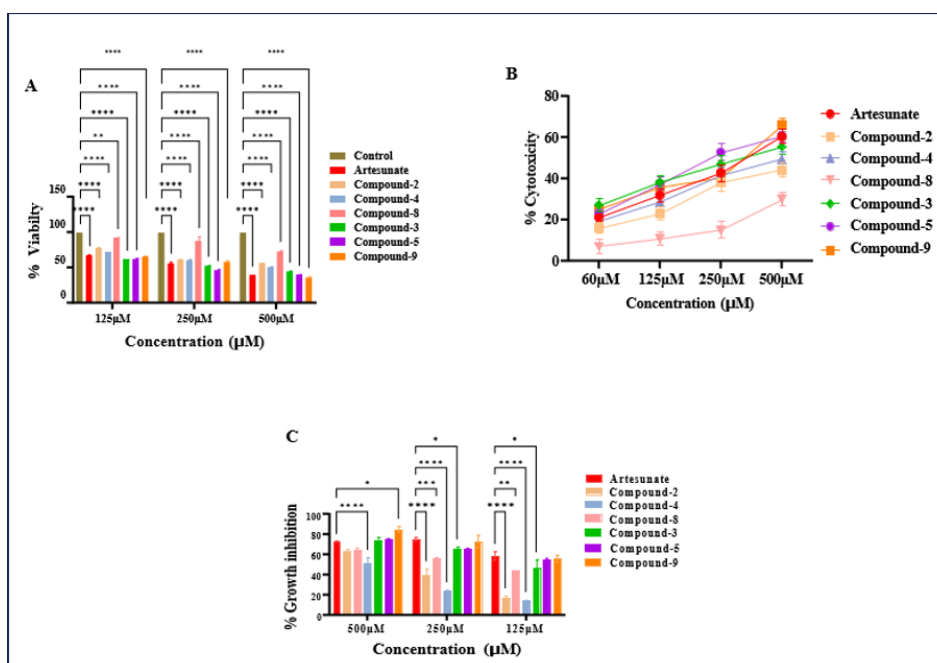


Figure 2: Study of the *in vitro* (A) Viability, (B) cytotoxicity and (C) growth inhibition of RAJI tumor cells in a concentration dependent manner.

At the highest concentration the viability upon compound **9** treatment was reduced to < 35 %, compared to 48 % when treated with artesunate or 78% in the presence of compound **8** ( $p<0.0001$ ). Compound **9** showed similar type of patten at lower concentration than other derivatives and artesunate. Result indicates compound **9** showed significant reduction of viability as compared to other derivatives against RAJI cell line.

Compound **9** also exhibited significant cytotoxicity upon releasing LDH as compared to other synthesized derivatives and artesunate against RAJI cell line. Compound **9** showed significant increment of cytotoxicity (70 %) at highest concentration as compared to artesunate (48 %) and compound **8** (30 %) ( $p<0.0001$ ).

In RAJI cells compound **9** showed 78 % growth inhibition, where the only artesunate treatment group showed 62 % growth inhibition ( $p<0.01$ ). Synthesized compound **3** and **5** also showed significant inhibition as compared to artesunate only treatment group. Compound **2,4** and **8** were significantly less potent as compared to compound **3, 5** and **9**. Result indicates that artesunate conjugated with azide decorated naphthalimide moiety (compound **9**), has better tumoricidal activity against RAJI cell line as compared to other synthesized derivatives and artesunate.

**Table 1.** IC<sub>50</sub> (μM) analysis of artesunate and synthesized compounds (**2,4,8,3,5** and **9**) in DL and RAJI cells.

Cell line	Artesunate	Compound <b>2</b>	Compound <b>4</b>	Compound <b>8</b>	Compound <b>3</b>	Compound <b>5</b>	Compound <b>9</b>
DL	602.2± 2.2	1801.4±0.9	302.63±1.3	1547.17±3.2	168.4 ± 3.3	458.04±0.9	157.23±3.6
RAJI	300.6± 5.4	765.80±2.3	456.77±1.5	1232.2 ± 2.4	279.32±2.4	228.6 ± 1.5	204.88±4.3

### 4.3.2 Biocompatibility and Hemocompatibility test:

The synthesized remodeled drugs were tested for hemocompatibility against red blood cells and biocompatibility against white blood cells. Result indicates that at highest concentration (100  $\mu$ M) the synthesized compounds **3,5** and **9** were tolerant towards human lymphocytes and monocytes resulted with moderate loss of viability as compared to artesunate. Synthesized compounds **3,5** and **9** were well tolerated towards RBC. Infact the percent lysis of compound **9** was lower than artesunate. Result indicates that our synthesized drugs are well tolerated against RBC and WBC.

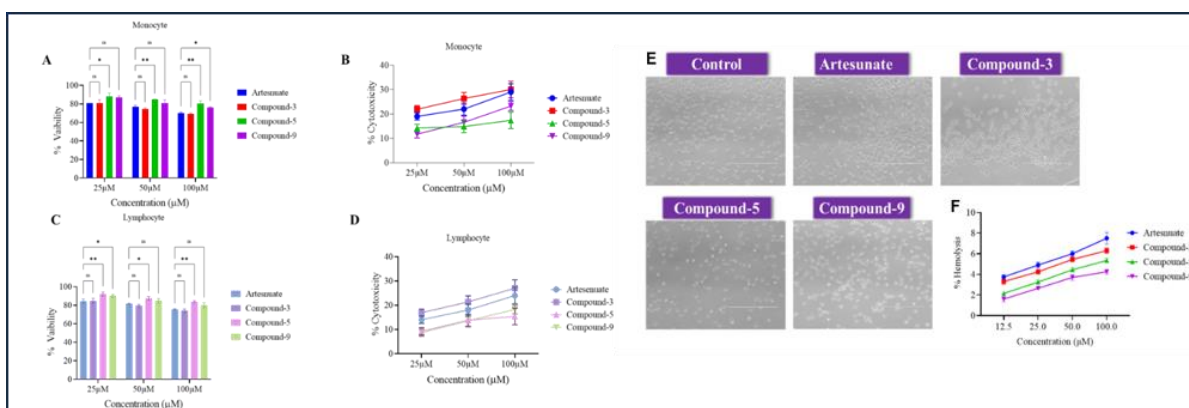


Figure 3: Biocompatibility study in human monocytes and lymphocytes in the presence of indicated formulations as judged by (A & C) viability and (B & D) cytotoxicity of the cells. Hemocompatibility analysis of human red blood cells (RBCs) in the presence of the indicated formulations. (E) Photographic presentation of RBCs in the presence of the indicated formulation after 4 hr of treatment. (F) The haemolysis percentage was studied for four hours in a concentration dependent manner.

### 4.3.3 Compound 9 inhibited migration in MCF-7 cell line:

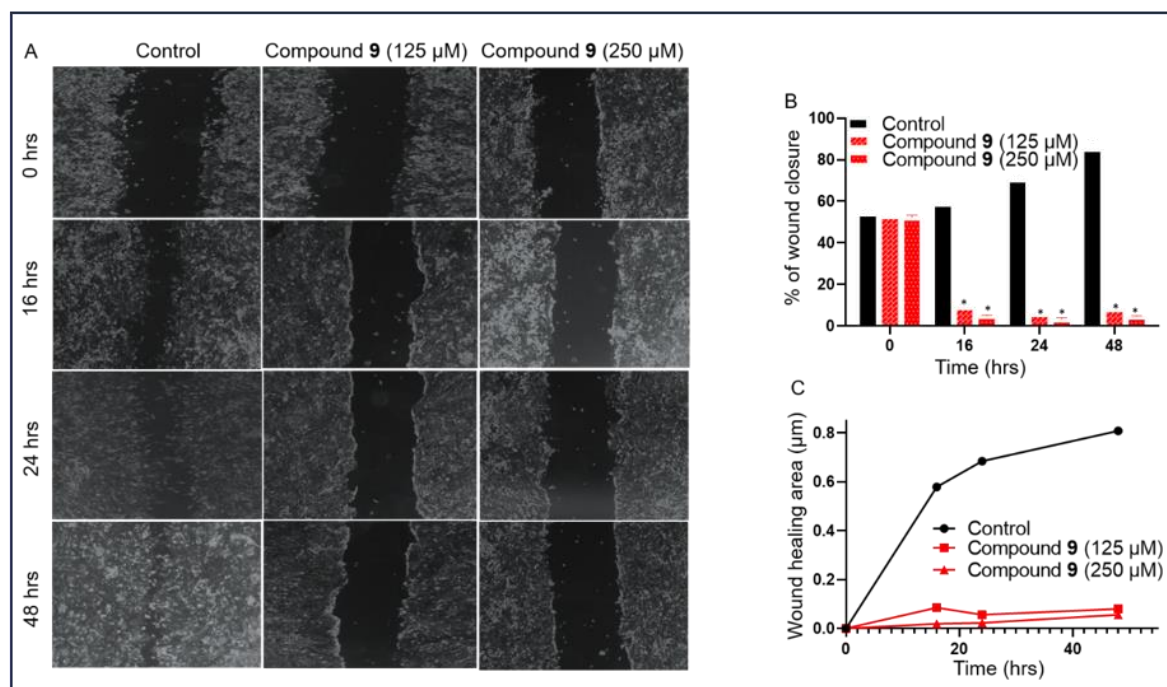


Figure 4: [A] A scratch wound was created in a full confluent layer of MCF-7 with a sterile microtips. Wound healing was monitored in a time dependent manner in presence of two different concentration of compound **9** and absence of compound **9**. [B] wound closure % percentage versus different time interval. [C] wound healing area versus different time interval.

From the wound healing assay, it was evident that compound **9** was able to significantly inhibit migration at 250 ( $p < 0.05$ ) and 150  $\mu$ M ( $p < 0.05$ ) as compared to control at different time interval.

### 4.3.4 Induction of apoptosis and cellular uptake by synthesized naphthalimide-FITC (compound 12) and naphthalimide-artesunate-FITC (compound 13):

Temporal uptake and apoptosis of compound 12 and 13 were studied against DL and Raji cell line with 50, 25 and 12.5  $\mu$ M respectively. Result

indicates that compound 12 and 13 showed similar type of uptake efficiency. But in at lower concentration compound 13 showed better uptake than compound 12 group. Compound 13 showed higher apoptosis at all concentrations than compound 12 against DL. Similar type of result was obtained against Raji cell-line.

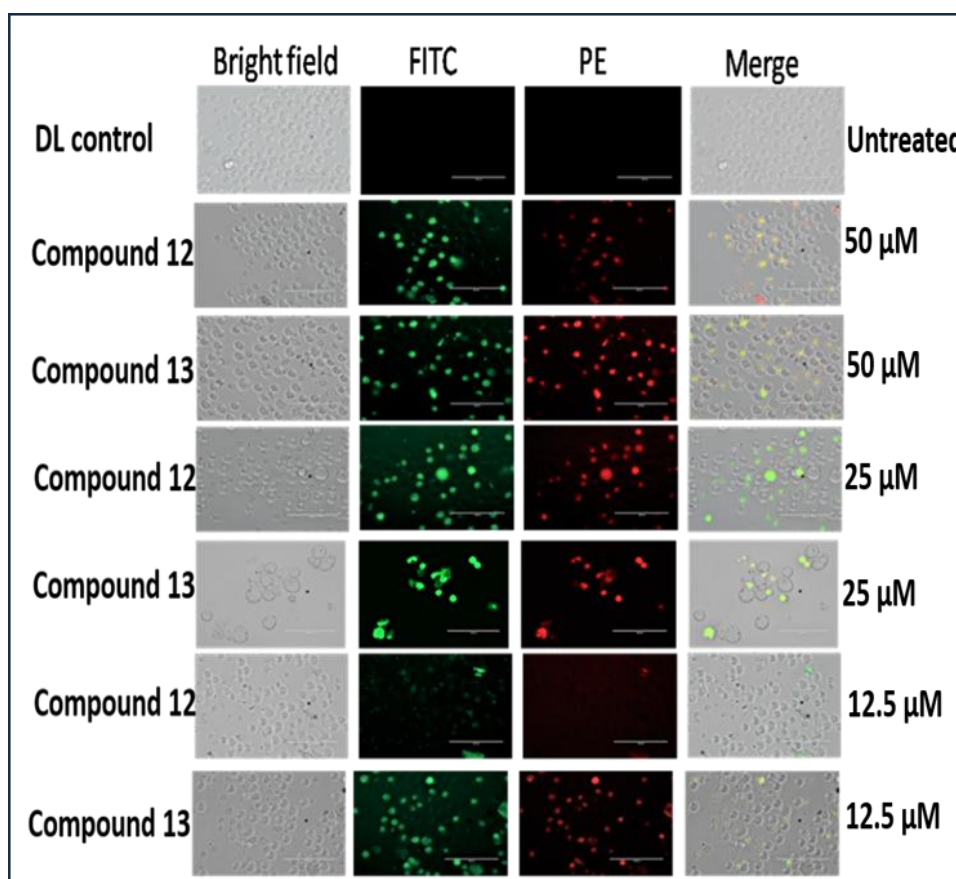


Figure 5: Induction of uptake and apoptosis in DL tumor cells. DL tumor cells were treated with three different drug doses (50  $\mu$ M, 25  $\mu$ M and 12.5  $\mu$ M) of compound **12** (substituted naphthalimide- FITC) or compound **13** (substituted naphthalimide- artesunate- FITC) for 8 hours. The cells were washed in PBS followed by staining with PE conjugated Annexin V for 45 minutes in Annexin buffer. Temporal uptake (green) and apoptosis (red) were captured in EVOS FL (magnification  $\times 400$ ).



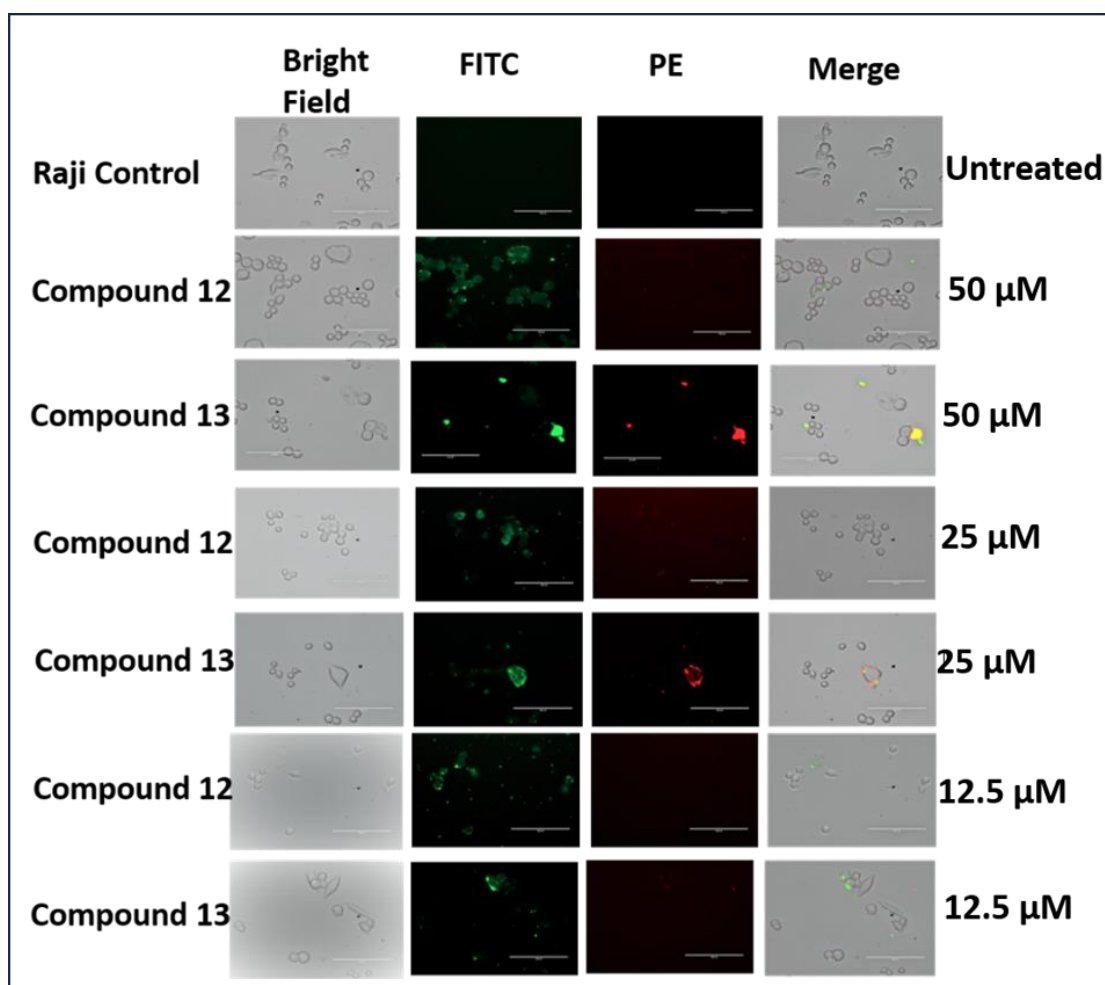


Figure 6: Induction of uptake and apoptosis in Raji. Raji cells were treated with three different doses (50  $\mu$ M, 25  $\mu$ M and 12.5  $\mu$ M) of compound 12 (substituted naphthalimide-FITC) or compound 13 (substituted naphthalimide- artesunate- FITC) for 8 hours. The cells were washed in PBS followed by staining with PE conjugated Annexin V for 45 minutes in Annexin buffer. Temporal uptake (green) and apoptosis (red) were captured in EVOS FL (magnification  $\times$ 400).

#### 4.3.5 Induction of cellular uptake by synthesized naphthalimide-artesunate-FITC (compound 13) and compound 12(fitc-naphthalimide) by fluorescence spectroscopy:

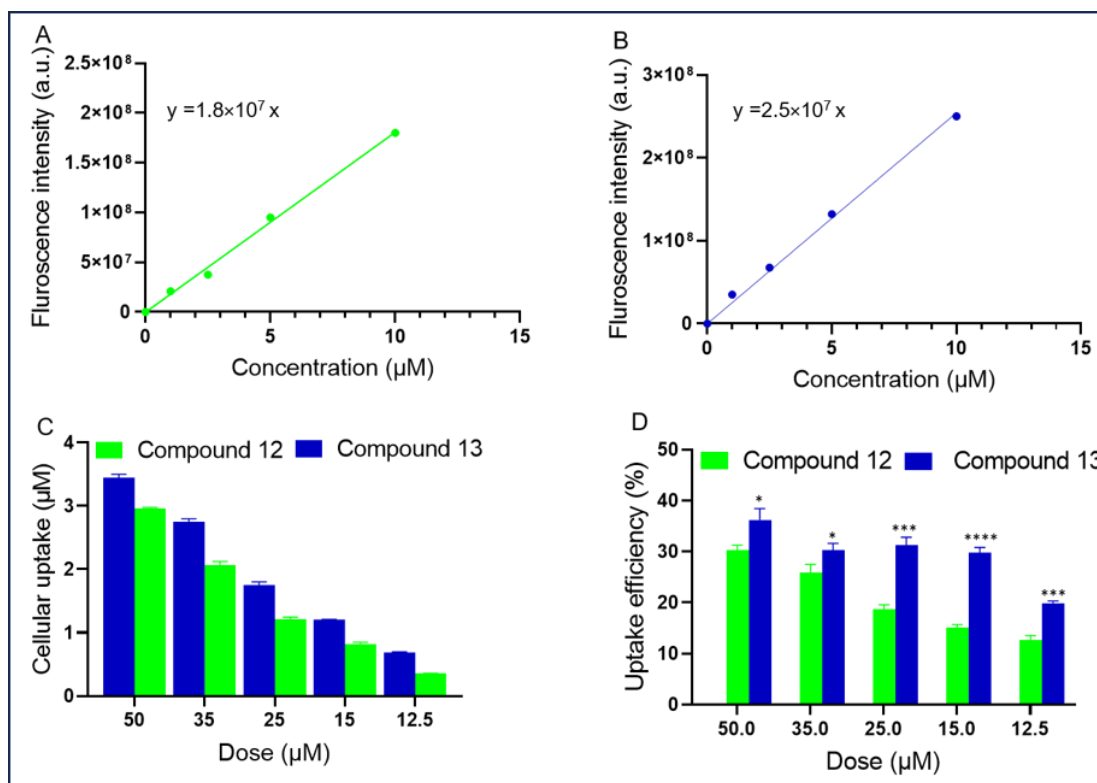


Figure 7: The *in vitro* cellular internalization of compounds **12** and **13** were calculated [C] by using a standard curve of different concentrations (10.0, 5.0, 2.5 and 1.0 μM) of compound **12** [A] and compound **13** [B]. [D] *In vitro* percentage of cellular uptake efficiency of compound **12** and compound **13** at different drug dose concentrations.

As shown in Figure 7, the uptake of Compound **13** ( $p < 0.05$ ) than Compound **12** by DL cells is significantly increased at higher concentration (50.0 and 35.0 μM) with eight-hour incubation time. However, the significant increment of cellular uptake of compound **13** ( $p < 0.001$ ) at lower concentration was observed than compound **12**. Even at lower concentration (12.5 μM). The percentage of cellular uptake efficiency in compound **13** was significantly increased than compound **12**.

#### 4.3.6 Induction of cellular uptake by synthesized naphthalimide-artesunate-FITC (compound 13) and compound 12 (fitc-naphthalimide) by Flow cytometry:

At eight-hour time interval with 12.5 $\mu$ M of compound **13** ( $p < 0.001$ ) showed significant increase of cellular uptake than compound **12** (figure 8).

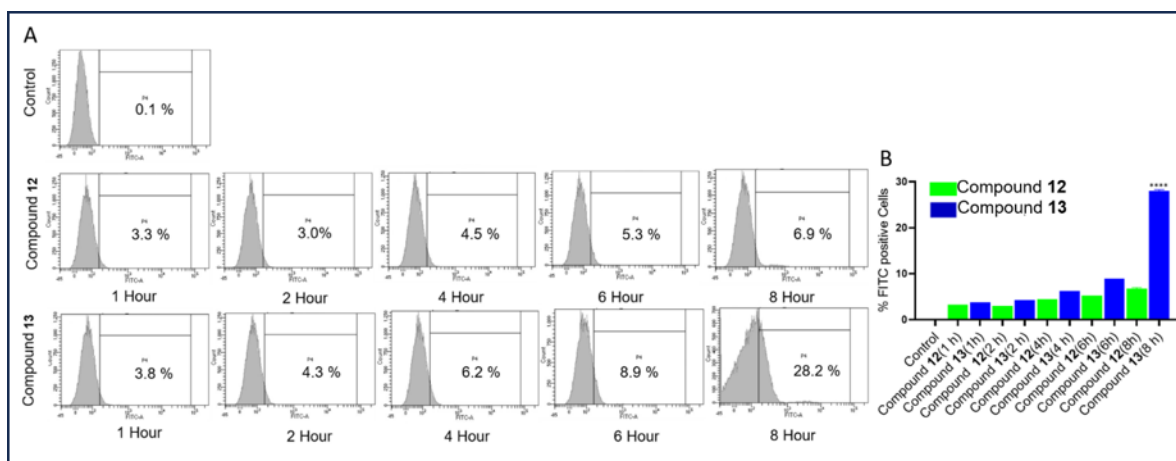


Figure 8: [A] Representative histograms of the *in vitro* cellular internalization of FITC conjugated compound **12** and **13** at different time point incubation (1,2,4,6 and 8 hours) with the lowest dose (12.5  $\mu$ M) used in Figure 7 [B] *in vitro* percentage of FITC positive internalization of compound **12** and **13** at the different time point incubation (1, 2, 4, 6 and 8 hours) with the lowest dose (12.5  $\mu$ M) used in Figure 8. Statistical analysis is done with compound 13 and compound 12 treated groups.

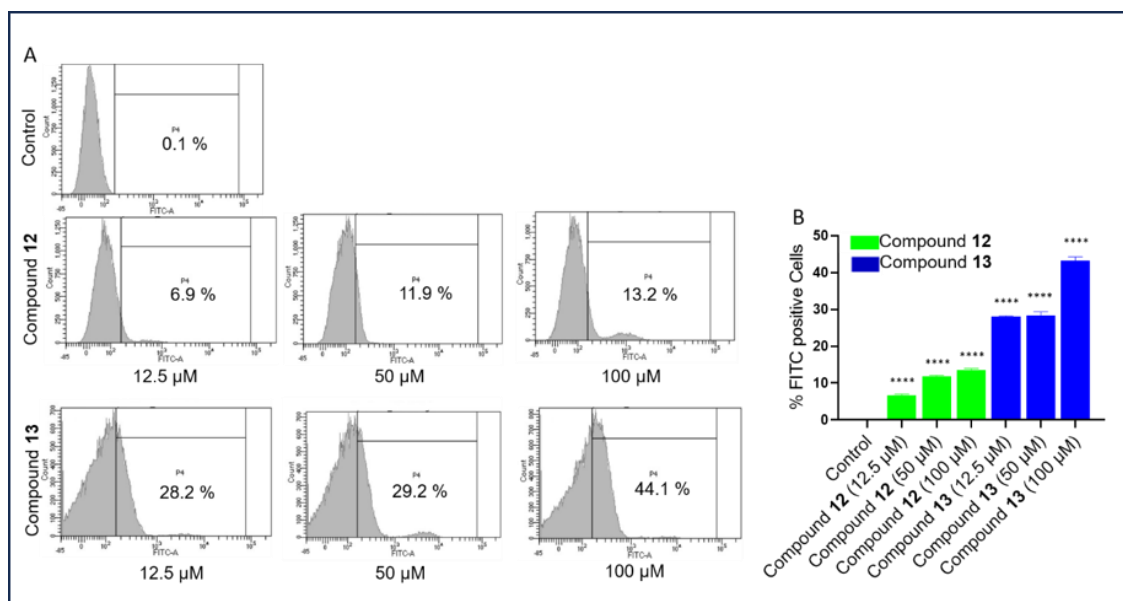


Figure 9: [A] Representative histograms of the *in vitro* cellular internalization of FITC conjugated compound **12** and **13** at 8-hour incubation of different dose (100.0, 50.0 and 12.5  $\mu$ M) [B] *in vitro* percentage of FITC positive internalization of compound **12** and **13** at 8-hour incubation of different dose (100.0, 50.0 and 12.5  $\mu$ M). Statistical analysis was done in between Control and compound **13** and **12** treated groups.

Compound **13** showed significant increment of the cellular uptake as compared to control at 100  $\mu$ M ( $p < 0.0001$ ), 50  $\mu$ M ( $p < 0.0001$ ) drug concentration than control group upon eight-hour incubation time. Compound **13** ( $p < 0.0001$ ) showed 28.2% of cellular uptake than control in 12.5  $\mu$ M of drug concentration. Whereas compound **12** ( $p < 0.0001$ ) only showed 6.9% uptake. This result indicates compound **13** showed 4% better uptake even at lowest concentration than compound **12**.

#### 4.3.7 *in vivo* Compound **9** protect and reduce DL tumor:

The *in vivo* tumoricidal effect of synthesized naphthalimide-artesunate hybrid drugs (**3,5** and **9**), intermediate conjugates (**2,4** and **8**) and

artesanate were tested. In Balb/c mice the  $5 \times 10^6$  number of DL tumor cells were injected in the right flank of the thigh region. As a result, a solid tumor was developed within ten days of the tumor cells implantation. After the visible solid tumor formation at day ten the treatment schedule was started. Total five injections (100  $\mu\text{g}$ /injection) (5 mg/kg of body weight) were given at an interval of 5 days. The DL group of mice was euthanized due to excessive tumor growth beyond 2000  $\text{mm}^3$  and the experiment was terminated for the DL control group. The mice of treated group were allowed to continue until the tumor size reached the permissible limit. The tumor volume was allowed to grow at a permissible limit and the mice were euthanized accordingly.

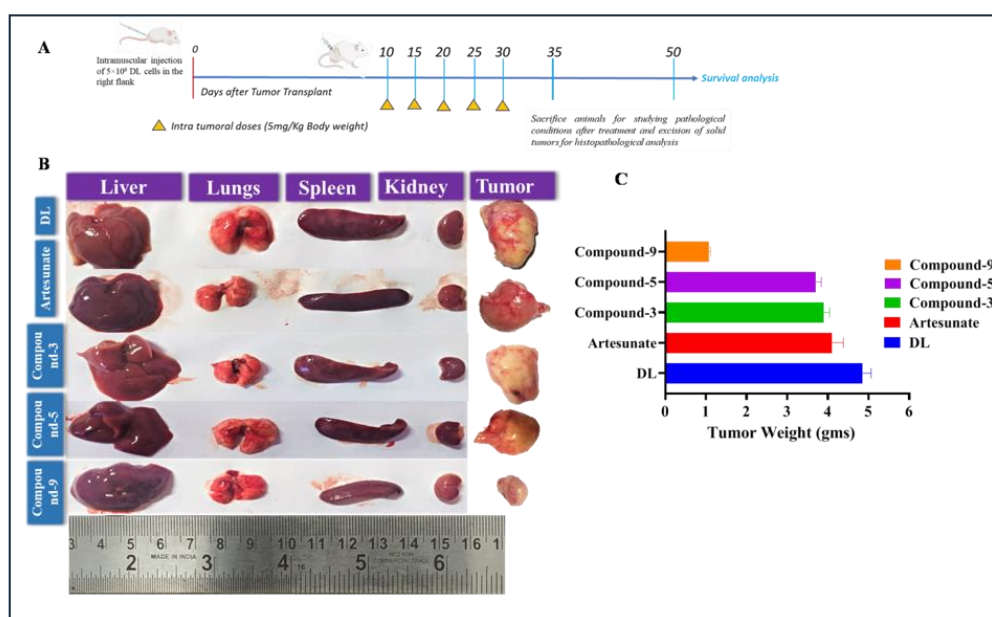


Figure 10: (A)Treatment schedule (B) Phenotypic presentation of excised vascularized organ and tumor (C) Weight of DL tumor in BALB/c mice.

In compound **9** treated group the significant reduction of tumor weight was observed in compared to the untreated DL group. Compound **5** and **3** treated group also showed tumor weight reduction as compared to the untreated DL group. In comparison with the untreated group, compound **9** treated group showed significant tumoricidal effect as the phenotypic

size of vascularized organs resembled with normal vascularized organs along with the reduction of tumor volume.

The treated group showed significant loss of the vascularized organs weight (g) than the untreated group and only artesunate treated group. Compound **9** showed significant loss of the excised vascular organs weight than the untreated group. From this study it was clear that compound **9** has the ability to prevent metastasis significantly in liver and spleen as compared to untreated group as the weight of the vascularized organ did not increase than the untreated group. Also, after tumor implantation there is no such loss of body weight was observed in the treated group as compared to untreated group. From the Kaplan -Meier survival analysis it was evident that after day 60 the compound **9** treated group was survived as compared to untreated, artesunate treated and compound **3,5** treated group.

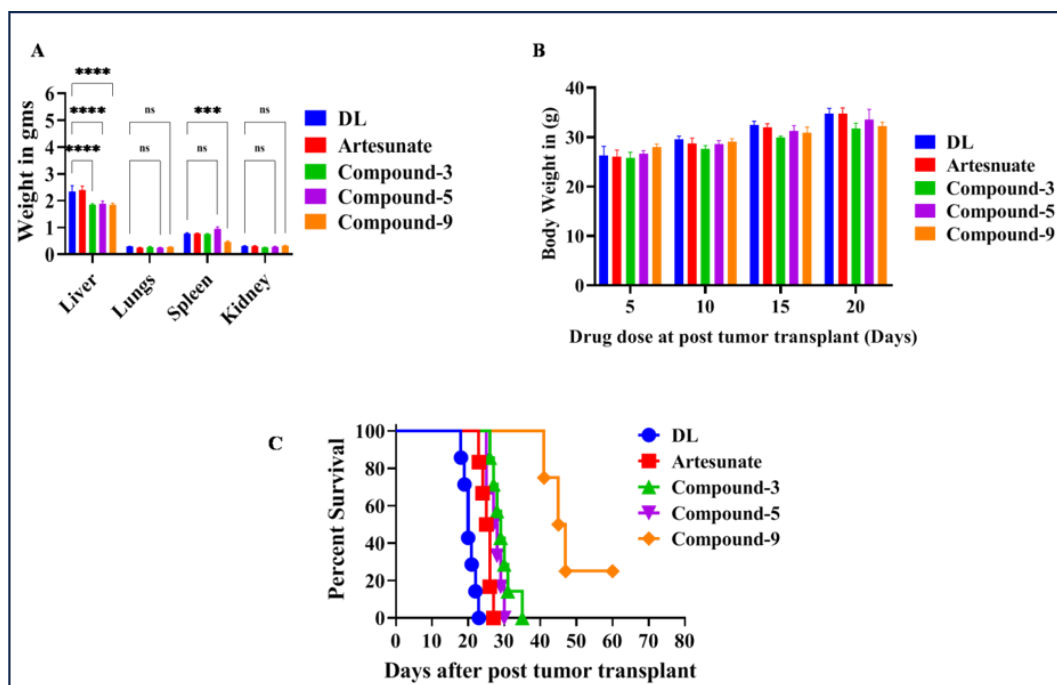


Figure 11: (A) Weight of vascularized organs, (B) body weight (g) and (C) Comparison between the Kaplan–Meier survival analysis of untreated and treated groups.

group was survived as compared to untreated, artesunate treated and compound **3,5** treated group.

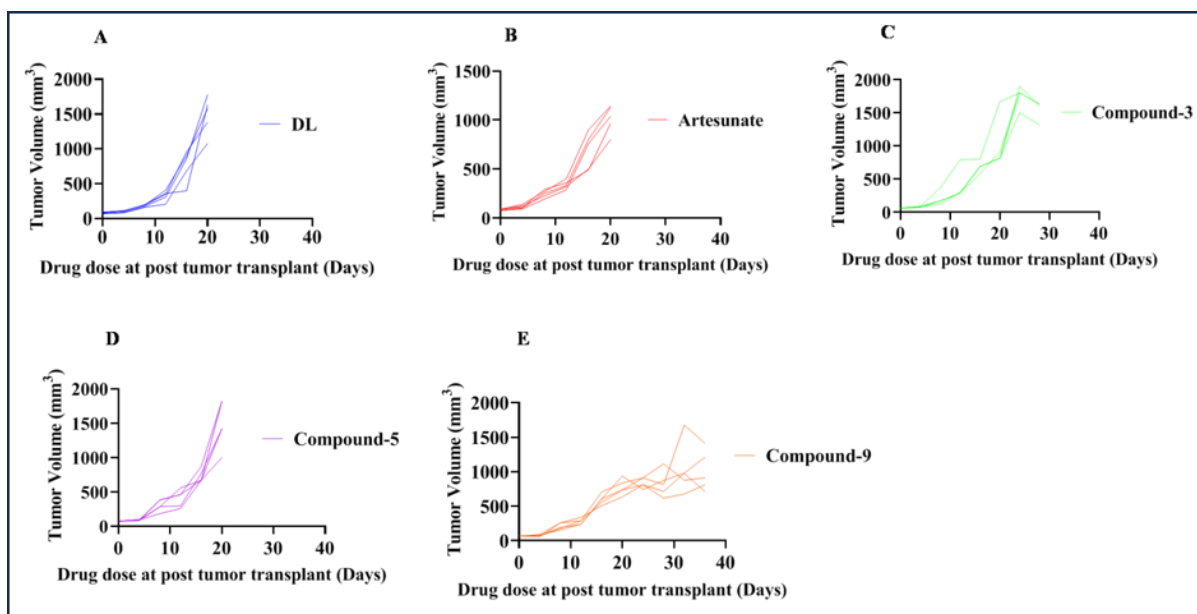


Figure 12: Analysis of tumor volume in untreated DL and treated groups in days after tumor transplantation.

From the tumor volume analysis after tumor transplantation the compound **9** treated group showed reduction of tumor volume as compared to another treated group (compound **5** and **3**), artesunate and DL untreated group. Compound **9** have better tumoricidal activity against lymphoma established as a solid tumor under skin.

Further we studied the concentration-dependent (50-200 µg/mouse) tumoricidal effect of compound **9** in DL lymphoma that developed as a solid tumor.

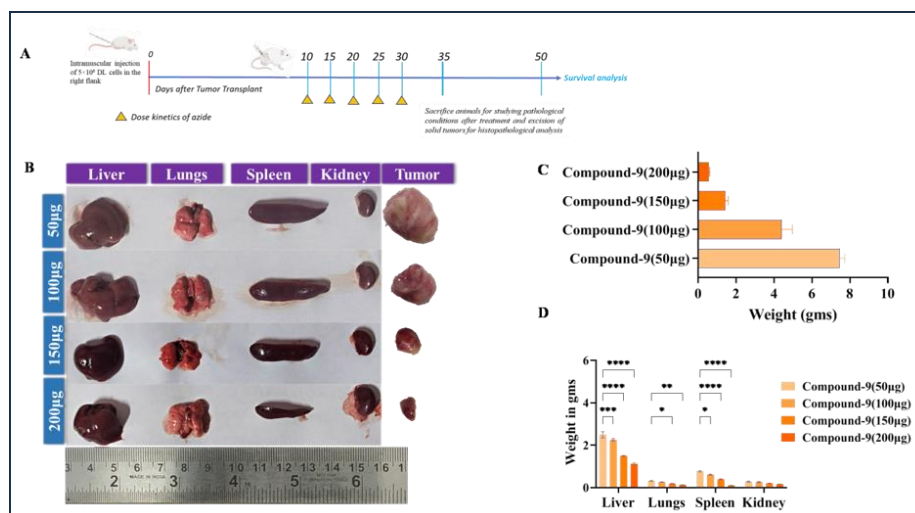


Figure 13: (A) Treatment schedule (B) Phenotypic demonstration of dissected vascularized organs and the tumor growth in the indicated treatment (C) Weight of dissected tumors in BALB/c mice treated with varying concentrations of compound **9**.

After palpable formation of DL tumor, the treatment schedule was started with 50,100,150 and 200 µg/mouse drug doses respectively with an interval of five days. From the phenotypic presentation of vascularized organs, it was clear that 200 µg/mouse drug dose treated group resembled more closely with the normal vascularized organs.

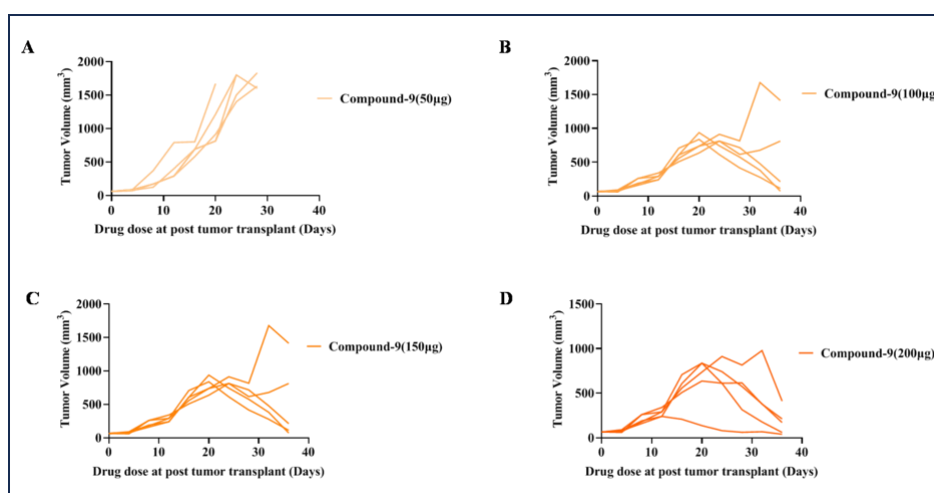


Figure 14: Tumoricidal effect of compound **9**. Analysis of tumor volume in different doses (A-D) of Compound **9** treated groups in days after tumor transplantation.



From the weight of the vascularized organs, it was evident that at highest concentration group the weight of the organs reduced, which indicated the inhibition of metastasis. Also, from the Kaplan-Meier survival analysis at highest concentration group showed better percent of survival after post tumor transplantation. After tumor transplantation the tumor volume was reduced in compound **9** treated (200 µg/mouse) group than other doses.

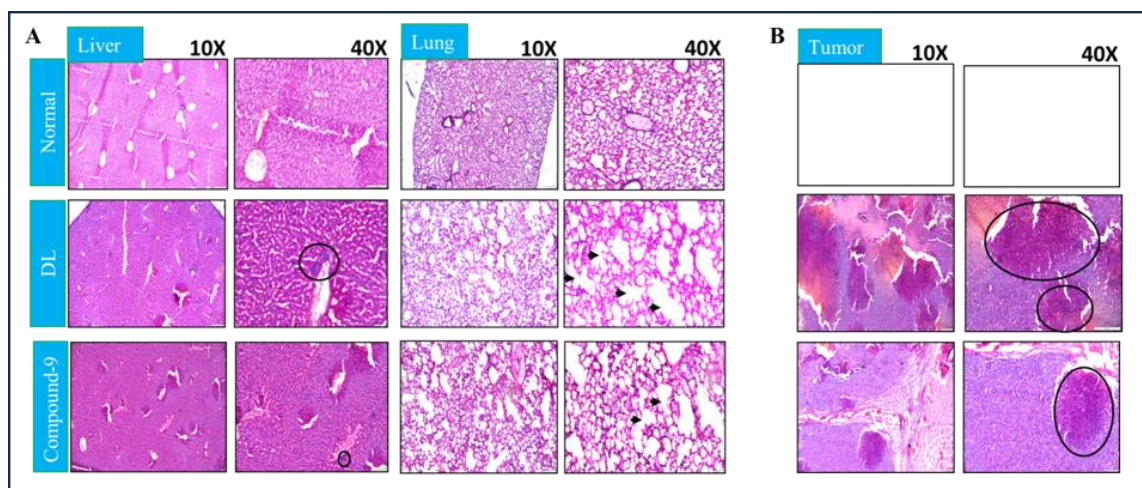


Figure 15: Histopathological analysis of (A) liver and lung in Normal (naïve control), DL (untreated tumor bearing) and compound **9** and (B) tumor derived from the above treatment condition. Magnification 10X & 40X. Reduction of concentrated tumor growth areas following treatment indicated by black circles.

Histopathological analysis of highly vascularized organs, including the liver and lung, showed a significant reduction in infiltrated tumor cells following treatment with compound **9** compared with the untreated DL control. Liver architecture in treated animals was restored to a large extent similar to that of normal littermates, which was severely disorganized and disrupted in the untreated DL group due to massive infiltration of tumor cells in hepatic portal areas (**Figure 15A**). Lung histology in the untreated DL group showed massive infiltration of tumor cells in lung alveoli, which was cleared in the treated group and restored to the level of normal

architecture (**Figure 15A**). Histopathology of the tumor mass in the untreated DL group showed extensive infestation of the parenchyma (neoplastic cells) and the stroma where the neoplastic cells were induced and in which they were dispersed. The solid pattern contained small tubules, and the hemorrhagic areas featured large, blood-filled spaces lined by tumor cells (**Figure 15B**). This architecture was abolished in the treated group largely as the tumor mass shrank and the extensive neoplastic conditions were reduced to minimal, suggesting the tumoricidal potential of the hybrid drug preparation.

#### **4.4 Discussion and Conclusion:**

The aim of this work is to design and synthesise a series of artesunate conjugated naphthalimide molecules against lymphoma. The hybrid compound **9** has remarkable cytotoxic as well as cytostatic effect in DL induced experimental murine lymphoma model. A synthesized hybrid molecule alone can regulate multiple targets that play a crucial function in the cancer cell viability, proliferation and metastasis. As compared to combination treatment a single medication is expected to enhance the patient prognosis by reducing adverse side effects and toxicity related issues.

The synthesized 4-azide decorated naphthalimide- artesunate (compound **9**) molecule showed potent tumoricidal activity by diminished cytotoxicity, growth arrest in human and murine lymphoma cells. The synthesized compound **13** (naphthalimide-artesunate-FITC) showed significant cellular uptake in DL cells than compound **12** (naphthalimide-FITC). The synthesized compound **9** showed significant reduction of tumor volume than the other synthesized compounds (compound **5** and **3**) and the DL control group. As compared to artesunate only, the hybrid

drug compound **9** demonstrated synergistic tumoricidal potential in that restricted the DL cell growth. The metastasis was significantly inhibited by compound **9** than the other synthesized groups. Our result strongly suggests that compound **9** could be used as a potential drug to treat solid lymphoma.

## References:

1. Subbiah, V. The next generation of evidence-based medicine. *Nat Med* **29**, 49–58 (2023).
2. Ashburn, T., Thor, K. Drug repositioning: identifying and developing new uses for existing drugs. *Nat Rev Drug Discov* **3**, 673–683 (2004).
3. Morgan DA, Ruscetti FW, Gallo RG. Selective in vitro growth of T lymphocytes from normal bone marrows. *Science* 1976; 193:1007-1008
4. Dara S, Dhamercherla S, Jadav SS, Babu CM, Ahsan MJ. Machine Learning in Drug Discovery: A Review. *ArtifIntell Rev.* 2022;55(3):1947-1999.
5. Hua Y, Dai X, Xu Y, Xing G, Liu H, Lu T, Chen Y, Zhang Y. Drug repositioning: Progress and challenges in drug discovery for various diseases. *Eur J Med Chem.* 2022 Apr 15; 234:114239.
6. Bento AP, Gaulton A, Hersey A, Bellis LJ, Chambers J, Davies M, Krüger FA, Light Y, Mak L, McGlinchey S, Nowotka M, Papadatos G, Santos R, Overington JP. The ChEMBL bioactivity database: an update. *Nucleic Acids Res.* 2014 Jan;42(Database issue): D1083-90.
7. Srinivas S, Freiha FS. Actinomycin D revisited in testicular cancer. A case report. *Tumori.* 1999 Jan-Feb;85(1):78-9.
8. Cavallo F, Boccadoro M, Palumbo A. Review of thalidomide in the treatment of newly diagnosed multiple myeloma. *Ther Clin Risk Manag.* 2007 Aug;3(4):543-52.

9. Rogers JE, Lam M, Halperin DM, Dagohoy CG, Yao JC, Dasari A. Fluorouracil, Doxorubicin with Streptozocin and Subsequent Therapies in Pancreatic Neuroendocrine Tumors. *Neuroendocrinology*. 2022;112(1):34-42.
10. Le Tourneau C, Raymond E, Faivre S. Sunitinib: a novel tyrosine kinase inhibitor. A brief review of its therapeutic potential in the treatment of renal carcinoma and gastrointestinal stromal tumors (GIST). *Ther Clin Risk Manag*. 2007 Jun;3(2):341-8.
11. Newman, D. J., & Cragg, G. M. (2020). *Natural Products as Sources of New Drugs over the Nearly Four Decades from 01/1981 to 09/2019. Journal of Natural Products*, 83(3), 770–803.
12. Cho AR, Choi WJ, Kwon YJ, Lee HS, Ahn SG, Lee JW. Mediterranean Diet and Naltrexone/Bupropion Treatment for Weight Loss in Overweight and Obese Breast Cancer Survivors and Non-Cancer Participants: A Pilot Randomized Controlled Trial. *Diabetes Metab Syndr Obes*. 2020 Sep 29; 13:3325-3335.
13. Thorn CF, Oshiro C, Marsh S, Hernandez-Boussard T, McLeod H, Klein TE, Altman RB. Doxorubicin pathways: pharmacodynamics and adverse effects. *Pharmacogenet Genomics*. 2011 Jul;21(7):440-6.
14. Dasari S, Tchounwou PB. Cisplatin in cancer therapy: molecular mechanisms of action. *Eur J Pharmacol*. 2014 Oct 5;740:364-78.
15. Virchow R. Cellular pathology as based upon physiological and pathological histology. Philadelphia: J.B. Lippincott, 1863.
16. Paget S. The distribution of secondary growths in cancer of the breast. *Lancet* 1889; 1:571-573

17. Watson JD, Crick FHC. Molecular structure of nucleic acids: structure for deoxyribose nucleic acid. *Nature* 1953; 171:737-738
18. Baltimore D. RNA-dependent DNA polymerase in virions of RNA tumour viruses. *Nature* 1970; 226:1209-1211
19. Warren JC. Inhalation of ethereal vapor for the prevention of pain in surgical operations. *Boston Med Surg J* 1846; 35:375-379
20. Roentgen K. On a new kind of rays. Stanton A, trans. *Nature* 1896;53:274-274
21. Curie P, Curie M, Bémont G. On a new, strongly radioactive substance contained in pitchblende. *CR (East Lansing, Mich)* 1898;127:1215-7.
22. Druker BJ, Guilhot F, O'Brien SG, et al. Five-year follow-up of patients receiving imatinib for chronic myeloid leukemia. *N Engl J Med* 2006; 355:2408-2417
23. Morgan DA, Ruscetti FW, Gallo RG. Selective in vitro growth of T lymphocytes from normal bone marrows. *Science* 1976; 193:1007-1008
24. Bosetti C, Rosato V, Gallus S, La Vecchia C. Aspirin and prostate cancer prevention. *Recent Results Cancer Res.* 2014; 202:93-100.
25. Bai RY, Staedtke V, Aprhys CM, Gallia GL, Riggins GJ. Antiparasitic mebendazole shows survival benefit in 2 preclinical models of glioblastoma multiforme. *Neuro Oncol.* 2011 Sep;13(9):974-82.
26. De Witt M, Gamble A, Hanson D, Markowitz D, Powell C, Al Dimassi S, Atlas M, Boockvar J, Ruggieri R, Symons M. Repurposing Mebendazole as a Replacement for Vincristine for the Treatment of Brain Tumors. *Mol Med.* 2017 Apr; 23:50-56.

27. Duran I, Carles J, Bulat I, Hellemans P, Mitselos A, Ward P, Jiao J, Armas D, Chien C. Pharmacokinetic Drug-Drug Interaction of Apalutamide, Part 1: Clinical Studies in Healthy Men and Patients with Castration-Resistant Prostate Cancer. *Clin Pharmacokinet*. 2020 Sep;59(9):1135-1148.
28. Lee M, Hong H, Kim W, Zhang L, Friedlander TW, Fong L, Lin AM, Small EJ, Wei XX, Rodvelt TJ, Miralda B, Stocksdales B, Ryan CJ, Aggarwal R. Itraconazole as a Noncastrating Treatment for Biochemically Recurrent Prostate Cancer: A Phase II Study. *Clin Genitourin Cancer*. 2019 Feb;17(1):92-96.
29. Tsubamoto H, Ueda T, Inoue K, Sakata K, Shibahara H, Sonoda T. Repurposing itraconazole as an anticancer agent. *Oncol Lett*. 2017 Aug;14(2):1240-1246.
30. Richardson P, Hideshima T, Anderson K. Thalidomide in multiple myeloma. *Biomed Pharmacother*. 2002 May;56(3):115-28.
31. García-Sanz R. Thalidomide in multiple myeloma. *Expert Opin Pharmacother*. 2006 Feb;7(2):195-213.
32. Tołoczko-Iwaniuk N, Dziemiańczyk-Pakieła D, Nowaszewska BK, Celińska-Janowicz K, Mityk W. Celecoxib in Cancer Therapy and Prevention - Review. *Curr Drug Targets*. 2019;20(3):302-315.
33. Chen C, Xu W, Wang CM. Combination of celecoxib and doxorubicin increases growth inhibition and apoptosis in acute myeloid leukemia cells. *Leuk Lymphoma*. 2013 Nov;54(11):2517-22.
34. Liu SH, Yu J, Creeden JF, Sutton JM, Markowiak S, Sanchez R, Nemunaitis J, Kalinoski A, Zhang JT, Damoiseaux R, Erhardt P, Brunicardi FC. Repurposing metformin, simvastatin and digoxin as a combination for targeted therapy for pancreatic ductal adenocarcinoma. *Cancer Lett*. 2020 Oct 28; 491:97-107.

35. Lemieszek MK, Stepulak A, Sawa-Wejksza K, Czerwonka A, Ikonomidou C, Rzeski W. Riluzole Inhibits Proliferation, Migration and Cell Cycle Progression and Induces Apoptosis in Tumor Cells of Various Origins. *Anticancer Agents Med Chem.* 2018;18(4):565-572.
36. McDonnell ME, Vera MD, Blass BE, Pelletier JC, King RC, Fernandez-Metzler C, Smith GR, Wrobel J, Chen S, Wall BA, Reitz AB. Riluzole prodrugs for melanoma and ALS: design, synthesis, and in vitro metabolic profiling. *Bioorg Med Chem.* 2012 Sep 15;20(18):5642-8.
37. Li F, Dou J, Wei L, Li S, Liu J. The selective estrogen receptor modulators in breast cancer prevention. *Cancer ChemotherPharmacol.* 2016 May;77(5):895-903.
38. Wickerham DL, Costantino JP, Vogel VG, Cronin WM, Cecchini RS, Ford LG, Wolmark N. The use of tamoxifen and raloxifene for the prevention of breast cancer. *Recent Results Cancer Res.* 2009; 181:113-9.
39. Kornienko A, Evidente A, Vurro M, Mathieu V, Cimmino A, Evidente M, van Otterlo WA, Dasari R, Lefranc F, Kiss R. Toward a Cancer Drug of Fungal Origin. *Med Res Rev.* 2015 Sep;35(5):937-67.
40. Morgen M, Jöst C, Malz M, Janowski R, Niessing D, Klein CD, Gunkel N, Miller AK. Spiroepoxytriazoles Are Fumagillin-like Irreversible Inhibitors of MetAP2 with Potent Cellular Activity. *ACS Chem Biol.* 2016 Apr 15;11(4):1001-11.
41. Mitrović A, Kos J. Nitroxoline: repurposing its antimicrobial to antitumor application. *Acta Biochim Pol.* 2019 Dec 13;66(4):521-531.



42. Zhang QI, Wang S, Yang D, Pan K, Li L, Yuan S. Preclinical pharmacodynamic evaluation of antibiotic nitroxoline for anticancer drug repurposing. *Oncol Lett*. 2016 May;11(5):3265-3272.
43. Brower V. Pioglitazone with imatinib in CML may reduce residual disease. *Lancet Oncol*. 2017 Feb;18(2): e70.
44. Egan JM. Targeting Stem Cells in Chronic Myeloid Leukemia with a PPAR- $\gamma$  Agonist. *N Engl J Med*. 2015 Nov 12;373(20):1973-5.
45. Keith RL, Blatchford PJ, Merrick DT, Bunn PA Jr, Bagwell B, Dwyer-Nield LD, Jackson MK, Geraci MW, Miller YE. A Randomized Phase II Trial of Pioglitazone for Lung Cancer Chemoprevention in High-Risk Current and Former Smokers. *Cancer Prev Res (Phila)*. 2019 Oct;12(10):721-730.
46. Handley N, Eide J, Taylor R, Wuertz B, Gaffney P, Ondrey F. PPAR $\gamma$  targeted oral cancer treatment and additional utility of genomics analytic techniques. *Laryngoscope*. 2017 Apr;127(4): E124-E131.
47. Ni X, Hu G, Cai X. The success and the challenge of all-trans retinoic acid in the treatment of cancer. *Crit Rev Food Sci Nutr*. 2019;59(sup1):S71-S80.
48. Tomita A, Kiyoi H, Naoe T. Mechanisms of action and resistance to all-trans retinoic acid (ATRA) and arsenic trioxide (As<sub>2</sub>O<sub>3</sub>) in acute promyelocytic leukemia. *Int J Hematol*. 2013 Jun;97(6):717-25.
49. Grever MR. Hairy cell leukemia: a successful model for experimental therapeutics--pentostatin and new ideas. *Leuk Lymphoma*. 2011 Jun;52 Suppl 2:25-8.
50. Johnston JB. Mechanism of action of pentostatin and cladribine in hairy cell leukemia. *Leuk Lymphoma*. 2011 Jun;52 Suppl 2:43-5.

51. Weyerhäuser P, Kantelhardt SR, Kim EL. Re-purposing Chloroquine for Glioblastoma: Potential Merits and Confounding Variables. *Front Oncol.* 2018 Aug 27; 8:335.
52. Nuzbrokh Y, Jauregui R, Oh JK, Moazami G, Sparrow JR, Tsang SH. Presumed Chloroquine Retinopathy with Short-term Therapy for Glioblastoma Multiforme. *JAMA Ophthalmol.* 2020 Nov 1;138(11):1215-1217.
53. Kimbung S, Chang CY, Bendahl PO, Dubois L, Thompson JW, McDonnell DP, Borgquist S. Impact of 27-hydroxylase (CYP27A1) and 27-hydroxycholesterol in breast cancer. *EndocrRelat Cancer.* 2017 Jul;24(7):339-349.
54. Arun BK, Gong Y, Liu D, Litton JK, Gutierrez-Barrera AM, Jack Lee J, Vornik L, Ibrahim NK, Cornelison T, Hortobagyi GN, Heckman-Stoddard BM, Koenig KB, Alvarez RR, Murray JL, Valero V, Lippman SM, Brown P, Sneige N. Phase I biomarker modulation study of atorvastatin in women at increased risk for breast cancer. *Breast Cancer Res Treat.* 2016 Jul;158(1):67-77.
55. Kozanoglu I, Yandim MK, Cincin ZB, Ozdogu H, Cakmakoglu B, Baran Y. New indication for therapeutic potential of an old well-known drug (propranolol) for multiple myeloma. *J Cancer Res Clin Oncol.* 2013 Feb;139(2):327-35.
56. Knight JM, Rizzo JD, Hari P, Pasquini MC, Giles KE, D'Souza A, Logan BR, Hamadani M, Chhabra S, Dhakal B, Shah N, Sriram D, Horowitz MM, Cole SW. Propranolol inhibits molecular risk markers in HCT recipients: a phase 2 randomized controlled biomarker trial. *Blood Adv.* 2020 Feb 11;4(3):467-476.

57. Lacouture ME, Mitchell EP, Piperdi B, Pillai MV, Shearer H, Iannotti N, Xu F, Yassine M. Skin toxicity evaluation protocol with panitumumab (STEPP), a phase II, open-label, randomized trial evaluating the impact of a pre-Emptive Skin treatment regimen on skin toxicities and quality of life in patients with metastatic colorectal cancer. *J Clin Oncol*. 2010 Mar 10;28(8):1351-7.
58. Zhang Z, Fan Y, Xie F, Zhou H, Jin K, Shao L, Shi W, Fang P, Yang B, van Dam H, Ten Dijke P, Zheng X, Yan X, Jia J, Zheng M, Jin J, Ding C, Ye S, Zhou F, Zhang L. Breast cancer metastasis suppressor OTUD1 deubiquitinates SMAD7. *Nat Commun*. 2017 Dec 13;8(1):2116.
59. Liu C, Lou W, Zhu Y, Nadiminty N, Schwartz CT, Evans CP, Gao AC. Niclosamide inhibits androgen receptor variants expression and overcomes enzalutamide resistance in castration-resistant prostate cancer. *Clin Cancer Res*. 2014 Jun 15;20(12):3198-3210. doi: 10.1158/1078-0432.CCR-13-3296. Epub 2014 Apr 16. Erratum in: *Clin Cancer Res*. 2017 Jan 1;23 (1):323.
60. Schweizer MT, Haugk K, McKiernan JS, Gulati R, Cheng HH, Maes JL, Dumpit RF, Nelson PS, Montgomery B, McCune JS, Plymate SR, Yu EY. A phase I study of niclosamide in combination with enzalutamide in men with castration-resistant prostate cancer. *PLoS One*. 2018 Jun 1;13(6):313-320
61. Barbosa EJ, Löbenberg R, de Araujo GLB, Bou-Chacra NA. Niclosamide repositioning for treating cancer: Challenges and nano-based drug delivery opportunities. *Eur J Pharm Biopharm*. 2019 Aug; 141:58-69.
62. Haumann J, van Kuijk SMJ, Geurts JW, Hoebbers FJP, Kremer B, Joosten EA, van den Beuken-van Everdingen MHJ. Methadone

- versus Fentanyl in Patients with Radiation-Induced Nociceptive Pain with Head and Neck Cancer: A Randomized Controlled Noninferiority Trial. *Pain Pract.* 2018 Mar;18(3):331-340.
63. Haumann J, Geurts JW, van Kuijk SM, Kremer B, Joosten EA, van den Beuken-van Everdingen MH. Methadone is superior to fentanyl in treating neuropathic pain in patients with head-and-neck cancer. *Eur J Cancer.* 2016 Sep; 65:121-9.
  64. Couto RD, Fernandes BJD. Low Doses Naltrexone: The Potential Benefit Effects for its Use in Patients with Cancer. *Curr Drug Res Rev.* 2021 Jan 26.
  65. Koukourakis GV, Kouloulis V, Zacharias G, Papadimitriou C, Pantelakos P, Maravelis G, Fotineas A, Beli I, Chaldeopoulos D, Kouvaris J. Temozolomide with radiation therapy in high grade brain gliomas: pharmaceuticals considerations and efficacy; a review article. *Molecules.* 2009 Apr 16;14(4):1561-77.
  66. Coiffier B, Sarkozy C. Diffuse large B-cell lymphoma: R-CHOP failure-what to do? *Hematology Am Soc Hematol Educ Program.* 2016 Dec 2;2016(1):366-378.
  67. Xu J, Liu JL, Medeiros LJ, Huang W, Khoury JD, McDonnell TJ, Tang G, Schlette E, Yin CC, Bueso-Ramos CE, Lin P, Li S. MYC rearrangement and MYC/BCL2 double expression but not cell-of-origin predict prognosis in R-CHOP treated diffuse large B-cell lymphoma. *Eur J Haematol.* 2020 Apr;104(4):336-343.
  68. Iaringbold P.G., Price R.A., Turner J.H. Phase I-II study of radiopeptide <sup>177</sup>Lu-octreotate in combination with capecitabine and temozolomide in advanced low-grade neuroendocrine tumors. *Cancer Biother. Radiopharm.* 2012;27(9):561–569.

69. Bouzinab, kaouthar, summers, helen, Stevens, M. F. G., Moody, C. J., Thomas, N. R., Gershkovich, P., ... Turyanska, L. (2020). *Delivery of temozolomide and N3-propargyl analog to brain tumors using an apoferritin nanocage. ACS Applied Materials & Interfaces.*
70. Ortiz R, Perazzoli G, Cabeza L, Jiménez-Luna C, Luque R, Prados J, Melguizo C. Temozolomide: An Updated Overview of Resistance Mechanisms, Nanotechnology Advances and Clinical Applications. *CurrNeuropharmacol.* 2021;19(4):513-537.
71. Zhao F, Vakhrusheva O, Markowitsch SD, Slade KS, Tsaur I, Cinatl J Jr, Michaelis M, Efferth T, Haferkamp A, Juengel E. Artesunate Impairs Growth in Cisplatin-Resistant Bladder Cancer Cells by Cell Cycle Arrest, Apoptosis and Autophagy Induction. *Cells.* 2020 Dec 9;9(12):2643.
72. Morris CA, Duparc S, Borghini-Fuhrer I, Jung D, Shin CS, Fleckenstein L. Review of the clinical pharmacokinetics of artesunate and its active metabolite dihydroartemisinin following intravenous, intramuscular, oral or rectal administration. *Malar J.* 2011 Sep 13; 10:263
73. Chen WJ, Mao X, Zhang YQ, Lin N. [Current research analysis and prospects on sensitization effect of artesunate on anti-cancer radiotherapy and chemotherapy]. *Zhongguo Zhong Yao Za Zhi.* 2019 Dec;44(23):5231-5239.
74. Khanal P. Antimalarial and anticancer properties of artesunate and other artemisinins: current development. *Monatsh Chem.* 2021;152(4):387-400.

75. Tilley L, Straimer J, Gnädig NF, Ralph SA, Fidock DA. Artemisinin Action and Resistance in *Plasmodium falciparum*. *Trends Parasitol.* 2016 Sep;32(9):682-696.
76. Egwu CO, Augereau JM, Reybier K, Benoit-Vical F. Reactive Oxygen Species as the Brainbox in Malaria Treatment. *Antioxidants (Basel).* 2021 Nov 24;10(12):1872.
77. Crespo-Ortiz MP, Wei MQ. Antitumor activity of artemisinin and its derivatives: from a well-known antimalarial agent to a potential anticancer drug. *J Biomed Biotechnol.* 2012; 2012:247597.
78. Ding, Y.; Wan, J.; Zhang, Z.; Wang, F.; Guo, J.; Wang, C. Localized Fe(II)-induced cytotoxic reactive oxygen species generating nanosystem for enhanced anticancer therapy. *ACS Appl. Mater. Interfaces* 2018, 10, 4439–4449.
79. Gopalakrishnan AM, Kumar N. Antimalarial action of artesunate involves DNA damage mediated by reactive oxygen species. *Antimicrob Agents Chemother.* 2015 Jan;59(1):317-25.
80. Chen, Y., Fan, Z., Yang, Y., & Gu, C. (2019). *Iron metabolism and its contribution to cancer (Review). International Journal of Oncology.*
81. Hamacher-Brady A, Stein HA, Turschner S, Toegel I, Mora R, Jennewein N, Efferth T, Eils R, Brady NR. Artesunate activates mitochondrial apoptosis in breast cancer cells via iron-catalyzed lysosomal reactive oxygen species production. *J Biol Chem.* 2011 Feb 25;286(8):6587-601.
82. Wang C, Youle RJ. The role of mitochondria in apoptosis. *Annu Rev Genet.* 2009; 43:95-118.
83. Groner, B., & Weiss, A. (2013). *Targeting Survivin in Cancer: Novel Drug Development Approaches. BioDrugs, 28(1), 27–39.*

84. Jamalzadeh L, Ghafoori H, Aghamaali M, Sariri R. Induction of Apoptosis in Human Breast Cancer MCF-7 Cells by a Semi-Synthetic Derivative of Artemisinin: A Caspase-Related Mechanism. *Iran J Biotechnol.* 2017 Sep 27;15(3):157-165.
85. Warry E, Hansen RJ, Gustafson DL, Lana SE. Pharmacokinetics of cyclophosphamide after oral and intravenous administration to dogs with lymphoma. *J Vet Intern Med.* 2011 Jul-Aug;25(4):903-8.
86. Ponticelli, C., Escoli, R., & Moroni, G. (2018). *Does cyclophosphamide still play a role in glomerular diseases? Autoimmunity Reviews.*
87. Wilmer JL, Erexson GL, Kligerman AD. Effect of acrolein on phosphoramidate mustard-induced sister chromatid exchanges in cultured human lymphocytes. *Cancer Res.* 1990 Aug 1;50(15):4635-8.
88. Slezakova S, Ruda-Kucerova J. Anticancer Activity of Artemisinin and its Derivatives. *Anticancer Res.* 2017; 37:5995–6003.
89. Zhao,L.X.;Wang,J.L.;Dai,X.P.;Zhizhong,J.I.SynthesisandAntitumour Activitiesof3-Substituted4-Oxo-3H-imidazo [5,1-d] [1,2,3,5] tetrazine-8-carboxylic Acids and Their Derivatives. *Chin. J.Med.Chem.*2001,11,263–269
90. Hira,S.K.; Mitra,K.; Srivastava,P.; Singh,S.; Vishwakarma,S.; Singh, R.; Ray, B.; Manna, P. P. Doxorubicin loaded pH responsive biodegradable ABA- type Amphiphilic PEG -b -aliphatic Polyketal -b - PEG block copolymer for therapy against aggressive murine lymphoma. *Nanomedicine* 2020, 24, No.102128.

91. Srivastava, P.; Hira, S. K.; Gupta, U.; Singh, V. K.; Singh, R.; Pandey, P.; Srivastava, D. N.; Singh, R. A.; Manna, P. P. Pepsin Assisted Doxorubicin Delivery from Mesoporous Silica Nanoparticles Downsizes Solid Tumor Volume and Enhances Therapeutic Efficacy in Experimental Murine Lymphoma. *ACS Appl. Bio Mater.* 2018, 1, 2133–2140.
92. Sinha, R., & Purkayastha, P. (2020). *Daunomycin delivery by ultrasmall graphene quantum dots to DNA duplexes: understanding the dynamics by resonance energy transfer. Journal of Materials Chemistry B*, 8(42), 9756–9763.
93. Alam, M. F., Varshney, S., Khan, M. A., Laskar, A. A., & Younus, H. (2018). *In vitro DNA binding studies of therapeutic and prophylactic drug citral. International Journal of Biological Macromolecules*, 113, 300–308.
94. Poklar, N., & Vesnaver, G. (2000). *Thermal Denaturation of Proteins Studied by UV Spectroscopy. Journal of Chemical Education*, 77(3), 380.
95. Bhuniya, A., Guha, I., Ganguly, N., Saha, A., Dasgupta, S., Nandi, P., Baral, R. (2020). NLGP Attenuates Murine Melanoma and Carcinoma Metastasis by Modulating Cytotoxic CD8<sup>+</sup> T Cells. *Frontiers in Oncology*, 10.
96. Zhang, J., Chen, X. G., Peng, W. B., & Liu, C. S. (2008). Uptake of oleoyl-chitosan nanoparticles by A549 cells. *Nanomedicine: Nanotechnology, Biology and Medicine*, 4(3), 208–214
97. Ibuki Y, Toyooka T. Nanoparticle uptake measured by flow cytometry. *Methods Mol Biol.* 2012; 926:157-66.



## **Abbreviations**

TMZ	Temozolomide
DEN	Dendrimer
PAMAM	Poly (amido amine)
BBB	Blood brain barrier
5-FU	5-flurouracil
MTIC	5-(3-methyltriazene-1-yl)-imidazole-4-carboxamide
AIC	5-aminoimidazole-4-carboxamide
UPLC	Ultra performance liquid chromatography
MALDI-TOF	Matrix associated laser desorption ionization-time of flight
DL	Dalton's lymphoma
ARTN	Artesunate
FITC	Fluorescein isothiocyanate
LC-MS	Liquid Chromatography mass spectroscopy
St-DNA	Salmon testis DNA
AO	Acridine orange
EB	Ethidium bromide
K <sub>b</sub>	Binding constant

## Publications:

1. RoyMahapatra, D., Singh,R., Sk,U.H., Manna, P. P. Engineered artesunate-naphthalimide hybrid dual drug for synergistic multimodal therapy against experimental murine lymphoma. *ACS Molecular Pharmaceutics*, 2024 (accepted)
2. Sk, U. H., Hira, S. K., Rej, A., RoyMahapatra, D., & Manna, P. P. Development of a PAMAM Dendrimer for Sustained Release of Temozolomide against Experimental Murine Lymphoma: Assessment of Therapeutic Efficacy. *ACS Applied Bio Materials* 2021, 4 (3), 2628-2638
3. Roy, R., Ria, T., RoyMahapatra, D., Sk,U.H. Single Inhibitors versus Dual Inhibitors: Role of HDAC in Cancer. *ACS Omega* 2023, 8, 19, 16532–16544
4. Sk,U.H., RoyMahapatra,D., Bhattacharya,S Selenium Nanoparticle in the Management of Oxidative Stress During Cancer Chemotherapy, *Handbook of Oxidative Stress in Cancer: Therapeutic Aspects*, (1-32), 2022

## Patent:

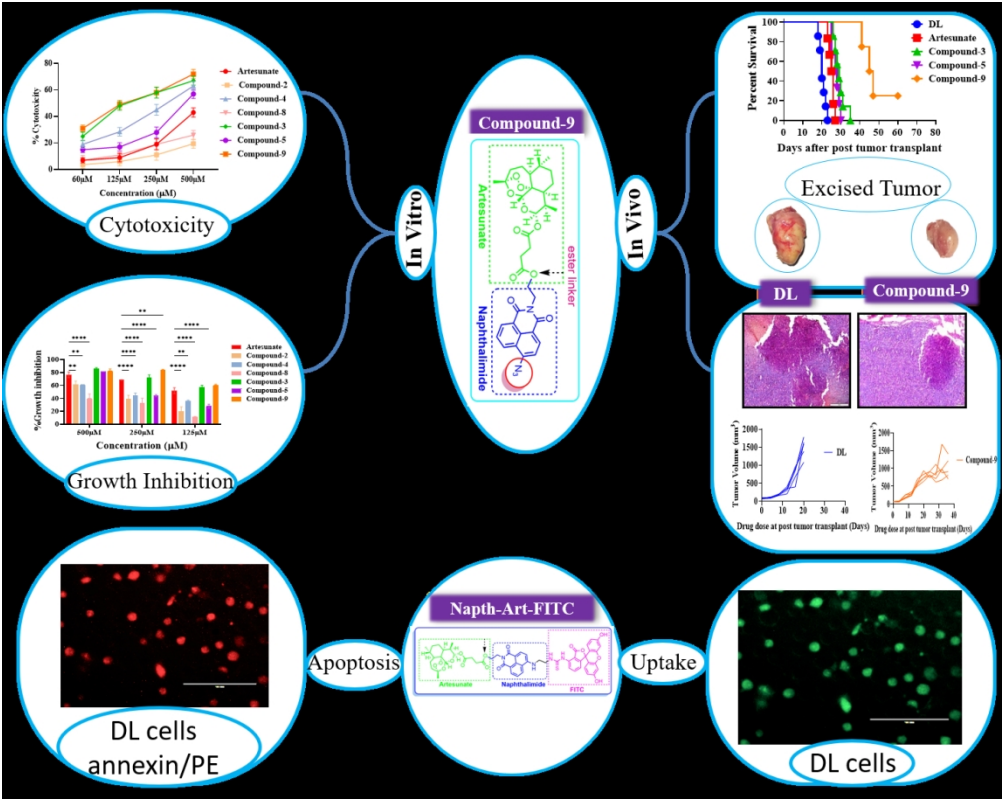
1. Part of the thesis work has been filed for Indian patent (**Application no. 202231032973**) entitled “Synthetically developed DNA-targeting naphthalimide-artesunate derivatives and their tumoricidal effect against lymphoma”

This document is confidential and is proprietary to the American Chemical Society and its authors. Do not copy or disclose without written permission. If you have received this item in error, notify the sender and delete all copies.

**Engineered artesunate-naphthalimide hybrid dual drug for synergistic multimodal therapy against experimental murine lymphoma**

Journal:	<i>Molecular Pharmaceutics</i>
Manuscript ID	mp-2023-00632k.R4
Manuscript Type:	Article
Date Submitted by the Author:	14-Jan-2024
Complete List of Authors:	RoyMahapatra, Debapriya; Chittaranjan National Cancer Institute Singh, Ranjeet ; Banaras Hindu University Faculty of Science Sk, Ugir; Chittaranjan National Cancer Institute, Clinical and Translational Research Manna, Partha; Banaras Hindu University, Zoology

SCHOLARONE™  
Manuscripts



TOC graphic

245x195mm (150 x 150 DPI)

# Engineered artesunate-naphthalimide hybrid dual drug for synergistic multimodal therapy against experimental murine lymphoma

Debapriya RoyMahapatra<sup>1#</sup>, Ranjeet Singh<sup>2#</sup>, Ugir Hossain Sk<sup>1§\*</sup> and Partha Pratim Manna<sup>2§\*</sup>

<sup>1</sup>Department of Clinical and Translational Research, Chittaranjan National Cancer Institute, Kolkata 700 026, West Bengal, India;

<sup>2</sup>Immunobiology Laboratory, Department of Zoology, Institute of Science, Banaras Hindu University, Varanasi 221005, India.

*# D.R. and R.S. are equal first authors*

*§ U.H.S. and P.P.M contributed equally to this paper*

Corresponding Authors, \*Email: [uhocju@gmail.com](mailto:uhocju@gmail.com) (U.Hossain Sk), [pp\\_manna@yahoo.com](mailto:pp_manna@yahoo.com) (P.P. Manna)

## Abstract

Lymphoma can effectively be treated with a chemotherapy regimen that is associated with adverse side effects due to increasing drug resistance, so there is an emergent need for alternative small molecule inhibitors to overcome the resistance that occurs in lymphoma management and overall increase the prognosis rate. A new series of substituted naphthalimide moieties conjugated via ester and amide linkages with artesunate were designed, synthesized, and characterized. In addition to the conjugates, to further achieve a theranostic molecule, FITC was incorporated via a multistep synthesis process. The DNA binding studies of these selected derivatives by UV/vis, fluorescence spectroscopy, and intercalating dye (EtBr, acridine orange)- DNA competitive assay, minor groove binding dye Hoechst 33342-DNA competitive assay suggested that the synthesized novel molecules intercalated between the two strands of DNA due to its naphthalimide moiety and its counterpart artesunate binds with the minor groove of DNA. Naphthalimide-artesunate conjugates inhibit the growth of lymphoma and induce apoptosis, including ready incorporation and reduction in cell viability. The remodeled drug has a significant tumoricidal effect against solid DL tumors developed in BALB/c mice in a dose-dependent manner. The novel drug appears to inhibit metastasis and increase the survival of the treated animals compared with untreated littermates.

**KeyWords:** Artesunate, naphthalimide, hybrid drug, DL lymphoma, tumoricidal activity, apoptosis

## Introduction

In cancer drug discovery after preclinical research, only 5% of drugs entered phase 1 clinical trials<sup>1</sup>. Therefore, an alternative approach is required that is much more time-saving and cost-saving. Ashburn and Thor first introduced the term drug repurposing-already FDA-approved drug, to be used totally in a new direction<sup>2</sup>. For chemotherapeutic drug discovery, DNA is considered to be one of the most important targets<sup>3</sup>. Therefore, an alternative DNA-targeting drug development approach is needed to synthesize novel molecules. The DNA-targeted drug cyclophosphamide crosslinks with the guanine bases of double-stranded DNA; as a result, cells are unable to uncoil, and replication is inhibited<sup>4</sup>. Cyclophosphamide in combination with rituximab, fludarabine, and mitoxantrone increased the remission rate by 57% to 61% in relapsed or refractory follicular lymphoma and mantle cell lymphoma patients<sup>5</sup>. There is an emergent need for small molecule inhibitors to overcome the resistance of current treatment in lymphoma. Another DNA-targeting drug, doxorubicin, efficiently damages DNA in activated B-cell-like DLBCL (diffuse large B-cell lymphoma)<sup>6</sup>. The natural product-derived drug etoposide efficiently inhibits replication by forming a complex with topoisomerase II; as a result, the formation of this complex induces double-stranded breaks in DNA and inhibits repair by topoisomerase II<sup>7</sup>. In a phase II clinical trial, the outcome revealed that etoposide, methyl prednisolone, high-dose cytarabine, and oxaliplatin (ESHAOx) can be an alternative option for patients with aggressive non-Hodgkin's lymphoma (NHL)<sup>8</sup>. Since then, the most efficient lymphoma management regimen (R-CHOP) has only been capable of increasing the five-year survival rate, limiting drug resistance among 30% of patients<sup>9</sup>. Herein, the naphthalimide moiety binds with double-stranded DNA by intercalation. DNA intercalating naphthalimide moiety-derived molecules have been proven to inhibit DNA duplication, enabling DNA conformational changes and interfering with DNA-protein interactions. Previously reported naphthalimide moiety-derived molecules are in clinical trials, such as mitonafide and amonafide. The amonafide analog [2-[2-(dimethylamino) ethyl]-1,3-dioxobenzo[de]isoquinolin-5-yl] urea was reported to intercalate with DNA, and in a phase I study against lymphoma, the pharmacokinetics (PK), maximum tolerated dose (MTD), dose-limiting toxicity, safety and antitumor activity were determined<sup>10</sup>. Several other derivatives of naphthalimide compounds were developed by changing substituents and altering side chain

modifications. It has been observed that by altering or modifying the linker, DNA intercalating properties vary in the different biophysical experimental evidence<sup>11</sup>. The antimalarial drug artesunate showed cytotoxicity in different lymphoma cell lines<sup>12</sup>. The cytotoxic effect of artesunate (ARTN) makes it a promising target as a chemotherapeutic agent. To increase bioavailability and reduce the systemic toxicity of the naphthalimide moiety, we will synthesize a novel DNA-targeted naphthalimide moiety with ARTN molecules by ester and amide linkage.

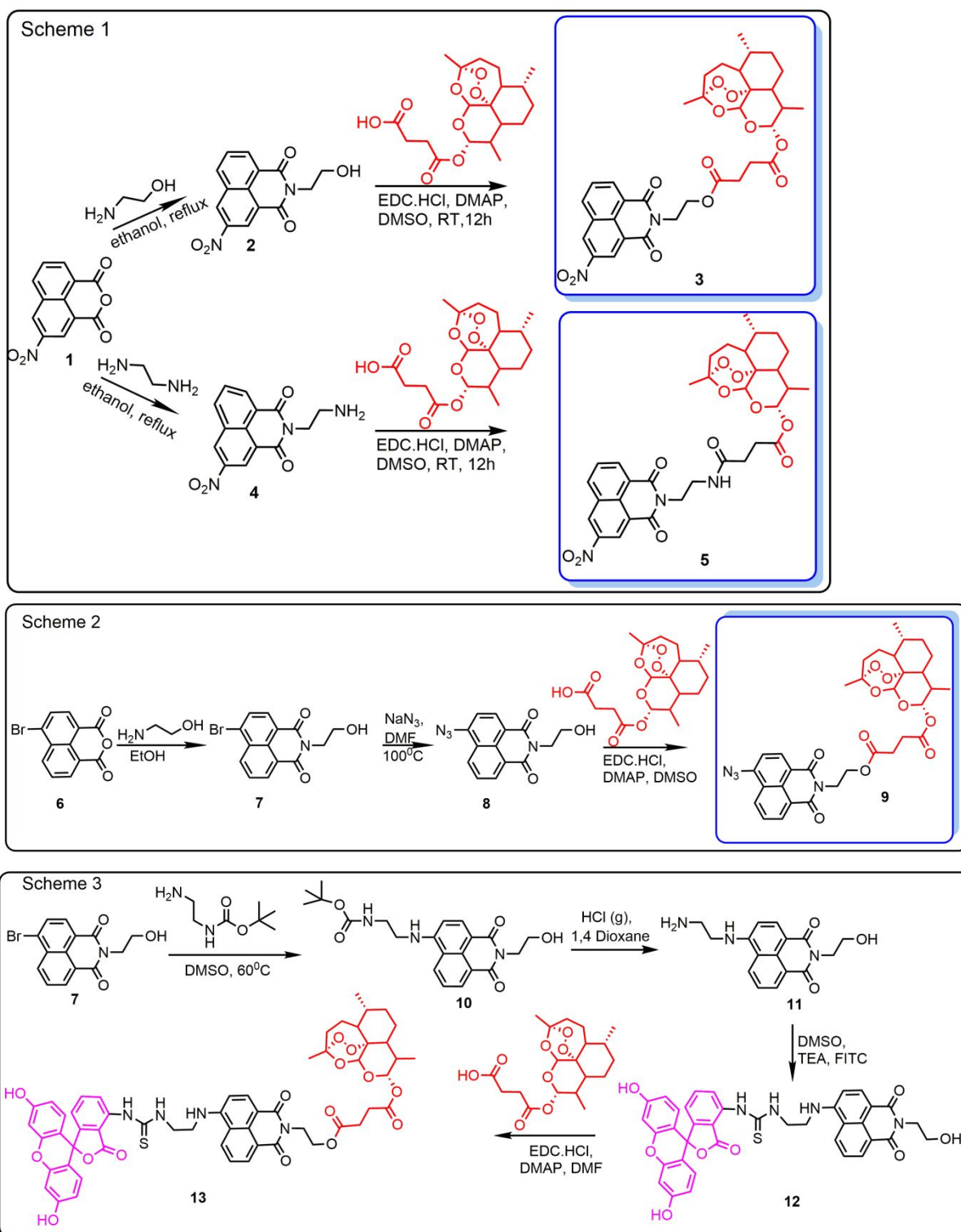
An ARTN-based multifunctional nanoplatform has been fabricated for anticancer treatment by several investigators. Activation of the thermosensitizer by using photodynamic therapy has been employed to produce reactive oxygen species in the presence of ARTN for therapy against H22 tumor-bearing mice<sup>13</sup>. A panel of dimer and hybrid compounds based on the natural scaffold of artemisinin was synthesized by coupling artemisinin derivatives, ARTN, and dihydroartemisinin with a panel of phytochemical compounds. The anticancer activity of these novel hybrids and dimers was evaluated against a cervical cancer cell line (HeLa) and metastatic melanoma cells (SK-MEL3, SK-MEL24, and RPMI-7951). Hybrid compounds fabricated by coupling ARTN with eugenol and tyrosol and a dimer compound containing curcumin were found to be most active and selective against cancer<sup>14</sup>. An artemisinin-estrogen hybrid was synthesized and investigated for in vitro biological activity against malaria parasites (*Plasmodium falciparum* 3D7), human cytomegalovirus (HCMV), and a panel of human cancer cells, including breast (MCF7, MDA-MB-231, MDA-MB-361, T47D) and cervical origin (HeLa, SiHa, C33A). The compounds showed significant antimalarial efficacy with low EC<sub>50</sub> values. The hybrid compounds exerted higher antiviral activity than the parent compound. An assembly of the hybrid compound significantly retarded the growth of all the cancer cells mentioned above compared with the parent compound and the reference drug cisplatin submicromolar EC<sub>50</sub> values (0.15-0.93  $\mu$ M) against breast cancer and C33A cell lines<sup>15</sup>. A series of hybrid compounds based on artemisinin and thymoquinone were also synthesized and investigated for their biological activity against the *Plasmodium falciparum* 3D7 strain, HCMV, leukemia cell lines, drug-sensitive CCRF-CEM and multidrug-resistant subline CEM/ADR5000. Thymoquinone-artemisinin-based hybrids exhibit excellent anticancer, antimalarial, and antiviral activities with low toxicity in addition to high selective activity<sup>16</sup>.

Naphthalimide derivatives were also designed and synthesized to modulate topoisomerase II and receptor tyrosine kinases (RTKs), targeting effective and selective antiproliferative activities against cancer cells. These derivatives demonstrated low IC<sub>50</sub> values, inhibited



1  
2  
3 angiogenesis-related RTKs, including PDGFR $\alpha$ , FGFR1, and VEGFR2, and possessed  
4 antiangiogenic activity<sup>17</sup>. Riphenylethylene-naphthalimide (TPE-naph) conjugates were  
5 synthesized by a molecular hybridization technique and evaluated for anticancer activity  
6 (cytotoxicity) against human cancer cell lines. TPE-naph conjugate bearing a morpholinyl  
7 group inhibits topoisomerase-II<sup>18</sup>.  
8  
9

10  
11 Our objective is to develop a successful nucleus-targeting (naphthalimide moiety) drug in  
12 combination with a nononcogenic drug (ARTN: antimalarial drug) upon remodeling in a new  
13 direction of drug discovery to validate antilymphoma activity. To validate the in vivo  
14 biodistribution, the synthesized DNA-targeting novel molecule was attached with FITC  
15 (imaging agent). The synthesized drug-DNA interactions were studied by UV/visible  
16 absorption and fluorescence spectroscopy. Synthesized drug-dye (EtBr, acridine orange and  
17 Hoechst 33342) displacement studies indicated the drug binding mode with DNA through  
18 intercalation or groove (major/minor) binding. Remodeling of 4-azide-naphthalimide and  
19 ARTN in a new formulation via an ester linker demonstrated antitumoral activity against DL  
20 tumor cells via growth inhibition and cytotoxicity of the tumor cells compared with either  
21 naphthalimide or ARTN alone. The azide-linked naphthalimide remodeled drug induces  
22 apoptosis in murine DL cells and is effective against the human lymphoma cell line RAJI and  
23 breast adenocarcinoma cell line MCF-7. DL tumors generated as solid tumors in BALB/c  
24 mice were inhibited by the azide-substituted ester-linked remodeled binary drug, resulting in  
25 a significant reduction in tumor volume, prevention of metastasis in deep organs and overall  
26 lifespan of the treated animals compared with untreated litters. Monotherapy with  
27 naphthalimide or ARTN did not produce any significant improvement. Ester- or amide-linked  
28 remodeled 3-nitro-naphthalimide conjugated ARTN also showed tumoricidal potential in vitro  
29 and in vivo, although the effect was significantly less than that of azide substituted-ester  
30 linked constructs.  
31  
32  
33  
34  
35  
36  
37  
38  
39  
40  
41  
42  
43  
44  
45  
46  
47  
48  
49  
50  
51  
52  
53  
54  
55  
56  
57  
58  
59  
60



**Figure1. Schemes 1 and 2: Synthesis of novel 3NO<sub>2</sub>-1,8-naphthalimide-artesunate conjugates via ester and amide (3 & 5); Scheme 2: 4Azide-1,8-Naphthalimide-artesunate conjugate (9). Scheme 3: Synthesis of 4-substituted 1,8-naphthalimide-conjugated artesunate with FITC (13)**

## Materials and methods

4-(dimethylamino) pyridine (DMAP), EDC. HCl, triethylamine (TEA), dimethylformamide (DMF), DMSO- $d_6$ ,  $CDCl_3$ , DMSO, DMF, EtBr, acridine orange (AO) and deoxyribonucleic acid (DNA) sodium salt from Salmon Testes were purchased from Sigma–Aldrich Chemical Co. Hoechst-33342 was purchased from Thermo Fisher, and ARTN was purchased from TCI Chemicals. N-(tert-butoxycarbonyl)-1,2- diaminoethane was purchased from Acros Organics. All other solvents and chemicals were purchased from Merck, India. All reactions were carried out under a nitrogen environment. Thin-layer chromatography (TLC) separations were performed on TLC Silica gel 60 F254 plates on aluminum sheets (Merck, Germany), and the spots were visualized with UV (254 nm) light. NMR spectroscopies were performed on a Bruker Avance-III 400 and 600 MHz spectrometer using commercially available  $CDCl_3$  and DMSO- $d_6$  solvents. Proton chemical shifts were reported in ppm ( $\delta$ ), and tetramethylsilane (TMS) was used as an internal standard. Coupling constants ( $J$ ) were reported in hertz (Hz). All the final compounds (**3**, **5**, **9** and **13**) were analysed through UPLC and reported >95% pure (indicated by chromatograms shown in the supplementary figures).

### Synthesis of compounds **3**, **5** and **9**

Synthesis of compound (**3**): A mixture of 3-nitro-1,8-naphthalic anhydride **1** (2.0 g, 0.0082 mol) and ethanolamine (1.50 g, 0.0247 mol) in ethanol (20 mL) was heated under reflux for 1.5 hr. The resulting mixture was concentrated by evaporating ethanol under reduced pressure and then cooled at 4°C. The solid separated was filtered, washed with cold ethanol and dried to afford **2** (1.8 g, 76%).  $^1H$ -NMR (DMSO- $d_6$ , 400 MHz):  $\delta$  9.45 (1H, Ar-H, s), 8.92 (1H, Ar-H, s), 8.76 (1H, Ar-H, d,  $J$ = 8.2 Hz), 8.66 (1H, Ar-H, d,  $J$ = 7.2 Hz), 8.04 (1H, Ar-H, t,  $J$ = 7.7 Hz), 4.81 (1H, t,  $J$ = 5.8 Hz), 4.16 (2H, t,  $J$ = 6.3 Hz), 3.64 (2H, t,  $J$ = 6.0 Hz) (Figure S1).

The compound was pure enough to be used directly for the preparation of compound **3**. Artesunate (1.61 g, 4.1 mmol) was placed in a round bottom flask in anhydrous DMSO (8.0 ml). Then, the coupling agent EDC·HCl (1.34 g, 6.9 mmol) and catalytic amount of DMAP (0.42 g, 3.4 mmol) were added and stirred to solubilize in an inert gas environment. Finally, 2-(2-hydroxyethyl)-5-nitro-1H-benzo[de]isoquinoline-1,3(2H)-dione (**2**) (1 g, 3.4 mmol) was added, and the solution was stirred for 12 h at R.T. The obtained product **3** was treated with EtOAc, successively washed with water and brine and dried over magnesium sulfate for the removal of water. Upon evaporation, the oily crude product was recovered, and the final white colored product **3** (1.18 g, 51%) was further purified through column chromatography

over silica-gel (100-200 mesh) in  $\text{CH}_2\text{Cl}_2$ : MeOH (99:01). In LCMS, the retention time was 4.05 min (Figure S2). Compound **3** showed EI-MS ( $\text{M}^+ + \text{Na}$ ):  $m/z$  670.6,  $^1\text{H}$ -NMR ( $\text{DMSO-d}_6$ , 400 MHz):  $\delta$  9.49 (1H, Ar-H, s), 8.98 (1H, Ar-H, s), 8.79 (1H, Ar-H, d,  $J = 7.84$  Hz), 8.70 (1H, Ar-H, d,  $J = 7.2$  Hz), 8.06 (1H, Ar-H, t,  $J = 7.8$  Hz), 5.49 – 5.44 (2H, m,  $J = 9.8$ , 13.92 Hz), 2.58 (2 H, d,  $J = 5.64$  Hz), 2.53 (1H, s), 2.18 – 2.12 (2H, m,  $J = 10.16$ , 12.4 Hz), 1.98 – 1.95 (1H, m,  $J = 10.84$  Hz), 1.78 (1H, s), 1.61-1.53 (2H, m,  $J = 7.28$ , 13.32 Hz), 1.46-1.28 (4H, m,  $J = 13.64$  Hz), 1.25 (3H, s), 1.19-1.09 (1H, m,  $J = 11.12$  Hz), 0.95 (1H, s), 0.89 (3H, d,  $J = 6.2$  Hz), 0.63 (3H, d,  $J = 7.0$  Hz) (Figure S3A).  $^{13}\text{C}$  NMR (100 MHz,  $\text{DMSO-d}_6$ , ppm):  $\delta$  171.70, 170.55, 162.72, 162.21, 145.61, 136.28, 133.91, 130.71, 129.67, 129.35, 129.14, 123.61, 122.78, 122.20, 103.47, 91.58, 90.52, 79.60, 61.05, 51.05, 44.44, 35.95, 35.79, 33.58, 31.40, 28.43, 28.28, 25.38, 24.06, 20.94, 19.94, 14.11, 11.45 (Figure S3B). HR-MS Calculated for  $\text{C}_{33}\text{H}_{36}\text{N}_2\text{O}_{12}$ , 652.2268; measured,  $\text{C}_{33}\text{H}_{36}\text{N}_2\text{O}_{12}\text{Na}$ , 675.2166 (Figure S3C)

### Synthesis of compound 5

A mixture of 3-nitro-1,8-naphthalic anhydride **1** (2 g, 0.0082 mol) and ethylenediamine (1.48 g, 0.025 mol) in ethanol (10 mL) was heated under reflux for 2 hrs (Figure 1, Scheme 1). The resulting mixture was concentrated by evaporating ethanol under reduced pressure and then cooled to 4°C. The solid separated was filtered, washed with cold ethanol and dried to afford **4** (2.0 g, 78%).  $^1\text{H}$ -NMR ( $\text{DMSO-d}_6$ , 400 MHz):  $\delta$  9.45 (1H, Ar-H, s), 8.93 (1H, Ar-H, s), 8.75 (1H, Ar-H, d,  $J = 8.2$  Hz), 8.66 (1H, Ar-H, d,  $J = 7.2$  Hz), 8.04 (1H, Ar-H, t,  $J = 7.7$  Hz), 4.08 (2H, t,  $J = 6.6$  Hz), 2.82 (2H, t,  $J = 6.6$  Hz), 2.07 (2H,  $-\text{NH}_2$ , broad peak) (Figure S4).

A magnetically stirred solution of **4** (0.74 g, 0.0019 mol) in anhydrous DMSO (5.0 mL) at room temperature was treated with artesunate (1 g, 0.0026 mol) in the presence of the coupling agent EDC·HCl (0.99 g, 0.0026 mol) and a catalytic amount of DMAP (0.32 g, 0.00083 mol) for 12 hrs. The obtained product was treated with EtOAc and successively washed with water and brine. Upon evaporation, the oily crude product was recovered, and the product was further purified through column chromatography over silica gel in  $\text{CH}_2\text{Cl}_2$ : MeOH (99:01). For further purification, the compound was treated simultaneously with a 50:50 hexane-chloroform mixture, ether-hexane mixture (40:10) and acetone. The pure compound was yellow compound **5** (1.15 g, 68%). The LCMS retention time was 3.75 min (Figure S2). Compound **5** showed EIMS ( $\text{M}^+ + \text{NH}_4^+$ ):  $m/z$  669.1.  $^1\text{H}$ -NMR ( $\text{DMSO-d}_6$ , 400 MHz):  $\delta$  9.48 (1H, Ar-H, s), 8.96 (1H, Ar-H, s), 8.78 (1H, Ar-H, d,  $J = 8.2$  Hz), 8.69 (1H, Ar-H, d,  $J = 7.2$  Hz), 8.06 (1H, Ar-H, t,  $J = 7.7$  Hz), 8.01 (2H, s), 5.56 (1H, d,  $J = 9.8$  Hz), 5.5 (1H,

s), 4.15 (2H, t,  $J$  = 5.7 Hz), 3.41 (2H, d,  $J$  = 5.8 Hz), 2.27 (2H, t,  $J$  = 6.84 Hz), 2.25-2.13 (2H, m,  $J$  = 14.2 Hz), 2.11-2.08 (1H, m,  $J$  = 12.48 Hz), 2.00-1.96 (1H, m,  $J$  = 14.32 Hz), 1.80 (1H, d,  $J$  = 3.32 Hz), 1.62-1.59 (2H, m,  $J$  = 11.56 Hz), 1.52-1.49 (1H, m,  $J$  = 13.36 Hz), 1.44-1.38 (2H, m,  $J$  = 10.32, 11.84 Hz), 1.33 (1H, s), 1.2 (3H, s), 1.23-1.14 (4H, m,  $J$  = 11.24, 4.64, 6.68 Hz), 0.95 (1H, s), 0.89 (3H, d,  $J$  = 6.16 Hz), 0.69 (3H, d,  $J$  = 7.04 Hz) (**Figure S5A**).  $^{13}\text{C}$  NMR (100 MHz, DMSO- $d_6$ , ppm):  $\delta$  170.96, 170.70, 162.82, 162.32, 145.64, 136.05, 133.71, 130.69, 129.45, 129.11, 124.00, 122.56, 103.51, 91.50, 90.46, 79.69, 68.40, 55.71, 54.81, 51.05, 44.54, 36.26, 35.95, 35.82, 33.63, 34.51, 29.55, 28.81, 25.40, 24.11, 20.92, 19.93, 11.58 (**Figure S5B**). HR-MS Calculated for  $\text{C}_{33}\text{H}_{37}\text{N}_3\text{O}_{11}$ , 651.2428; measured,  $\text{C}_{33}\text{H}_{37}\text{N}_3\text{O}_{11}\text{Na}$ , 674.1628 (**Figure S5C**)

### Synthesis of compound 9

To a solution of 4-bromo-1,8-naphthalic anhydride **6** (1.0 g, 0.0036 mol) in dry ethanol (6 mL) and 2-aminoethanol (0.44 g, 0.0072 mol) were added dropwise to the reaction mixture dissolved in dry ethanol (5 mL). The mixture was stirred, heated to reflux and continued for 4 hrs. The resulting mixture was allowed to cool at ice temperature and filtered; the obtained residue was washed with cold ethanol. The compound was obtained as a white solid **7** (0.85 g, yield 73.91%).  $^1\text{H}$ -NMR ( $\text{CDCl}_3$ , 400 MHz):  $\delta$  8.67 (1H, Ar-H, d,  $J$  = 7.3 Hz), 8.59 (1H, Ar-H, d,  $J$  = 8.6 Hz), 8.43 (1H, Ar-H, d,  $J$  = 7.9 Hz), 8.05 (1H, Ar-H, d,  $J$  = 7.8 Hz), 7.86 (1H, Ar-H, t,  $J$  = 8.3 Hz), 4.45 (2H, t,  $J$  = 5.2 Hz), 3.98 (2H, t,  $J$  = 5.2 Hz) (**Figure S6**).

**Compound 7** (1 g, 0.0031 mol) was added to 6 mL of DMF and stirred for 0.5 hrs to make a solution. Then,  $\text{NaN}_3$  (0.40 g, 0.0062 mol) in water (1 mL) was added to the mixture. The reaction mixture was heated to 95°C, and then the color of the solution turned from white turbid to brown clear solution. To terminate the reaction, water was added to the resulting reaction mixture. A yellow precipitate was separated out, collected through filtration and washed thoroughly with a cold ethanol-water mixture to yield the compound (0.70 g, yield 55.0%).  $^1\text{H}$ -NMR ( $\text{CDCl}_3$ , 400 MHz):  $\delta$  8.64 (1H, Ar-H, d,  $J$  = 7.16 Hz), 8.59 (1H, Ar-H, d,  $J$  = 7.92 Hz), 8.46 (1H, Ar-H, d,  $J$  = 8.2 Hz), 7.75 (1H, Ar-H, t,  $J$  = 7.8 Hz), 7.62 (1H, Ar-H, d,  $J$  = 7.96 Hz), 4.44 (2H, d,  $J$  = 5.2 Hz), 3.97 (2H, d,  $J$  = 5.1 Hz) (**Figure S7**)

Artesunate (0.50 g, 0.0017 moles) was placed in an RB flask in anhydrous DMSO (6.0 mL). Then, the coupling agents EDC and HCl (0.67 g, 0.0034 mol) and a catalytic amount of DMAP (0.108 g, 0.00085 mol) were added and stirred to solubilize in an inert gas environment until the solution became clear. After half an hour, compound **8** (0.50 g, 0.0017

mol) was added under stirring at R.T for 12 h, the color changed to brown. The obtained product was treated with EtOAc, successively washed with water and brine and dried over sodium sulfate for the removal of water. Upon evaporation, the crude product was recovered. The crude product was purified through column chromatography over silica gel (100-200 mesh) in EtOAc:hexane (20:80) to obtain desired compound **9** (0.97 g, 84%). In LCMS, the retention time was 4.37 min (Figure S2).  $m/z$  calculated for  $C_{33}H_{36}N_4O_{10}$  (**9**), 648.65; and corresponding EIMS found ( $M^{++}NH_4^+$ ): 666.4.  $^1H$ -NMR (DMSO- $d_6$ , 400 MHz):  $\delta$  8.57 (1H, Ar-H, d,  $J=7.00$  Hz), 8.52 (1H, Ar-H, d,  $J=8.00$  Hz), 8.46 (1H, Ar-H, d,  $J=8.4$  Hz), 7.89 (1H, Ar-H, t), 7.78 (1H, Ar-H, d,  $J=8.0$  Hz), 5.52-5.46 (2H, m,  $J=7.9, 11.72$  Hz), 4.32 (4H, s), 2.57 (2H, d,  $J=5.84$  Hz), 2.16-2.14 (2H, m,  $J=11.84$  Hz), 2.00 (1H, s), 1.57 (1H, s), 1.61-1.53 (2H, m,  $J=13.96$  Hz), 1.44-1.32 (4H, m,  $J=11.88, 13.32$  Hz), 1.26 (3H, s), 1.14 (1H, d,  $J=6.28$  Hz), 1.08 (1H, s), 0.88 (3H, d,  $J=6.0$  Hz), 0.62 (3H, d,  $J=7.0$ ) (Figure S8A).  $^{13}C$  NMR (150 MHz, DMSO- $d_6$ , ppm):  $\delta$  171.69, 170.58, 163.21, 162.80, 142.77, 131.57, 128.33, 128.21, 127.13, 123.38, 121.84, 117.84, 115.79, 103.46, 91.59, 90.61, 79.72, 61.23, 50.99, 44.36, 44.38, 38.44, 35.93, 35.82, 33.61, 31.44, 28.46, 28.33, 25.42, 24.07, 20.95, 19.94, 11.46 (Figure S8B). HR-MS calculated for  $C_{33}H_{36}N_4O_{10}$ , 648.2431; measured,  $C_{33}H_{36}N_4O_{10}+H_2O$  666.2192 (Figure S8C).

### Synthesis of compound 13

Boc-protected compound **10** was obtained in quantitative yield by reaction of compound **7** (1.0 g, 0.0031 mol) and N-tert-butoxy carbonyl 1,3-diamino ethane (1.0 g, 0.0062 mol) in anhydrous DMSO (8.0 ml) at 70°C for 16 hrs. The yellowish mixture was treated with ethyl acetate and washed with water and brine, followed by drying over sodium sulfate. The oily crude product was further purified by column chromatography over silica gel (100-200 mesh) in  $CH_2Cl_2$ : MeOH (99:1) to produce a red product (**10**) (680 mg, 54.4%).  $^1H$ -NMR (DMSO- $d_6$ , 600 MHz):  $\delta$  8.72 (1H, Ar-H, d,  $J=8.34$  Hz), 8.42 (1H, Ar-H, d,  $J=7.56$  Hz), 8.24 (1H, Ar-H, d,  $J=9.18$  Hz), 7.68 (1H, Ar-H, t,  $J=6.66$  Hz), 6.81 (1H, Ar-H, d,  $J=9.24$  Hz), 7.72 (2H, t,  $J=6.66$  Hz), 7.07 (2H, t,  $J=6.72$  Hz), 5.57 (1H, s), 4.79 (2H, t,  $J=5.04$  Hz), 4.11 (2H, t,  $J=7.56$  Hz), 3.57 (1H, m,  $J=6.78$  Hz), 3.43 (1H, m,  $J=5.82$  Hz), 3.27 (1H, m,  $J=5.88$  Hz), 1.3 (9H, s) (Figure S9A). HR-MS Calculated for  $C_{21}H_{25}N_3O_5$ , 399.1794; measured  $[C_{33}H_{36}N_4O_{10}+H]^+$ , 400.1859 (Figure S9B)

Dry HCl (g) was passed through a mixture of compound **10** (995 mg; 0.0025 mol) in 1,4-dioxane (10.0 mL) to afford the chloride salt of compound **11** (0.50 g, 60%).  $^1H$ -NMR

(DMSO-d<sub>6</sub>, 600 MHz):  $\delta$  8.86 (1H, Ar-H, d,  $J$ =9.42 Hz), 8.42 (1H, Ar-H, d,  $J$ =7.14 Hz), 8.27 (1H, Ar-H, d,  $J$ =7.62 Hz), 7.68 (1H, Ar-H, t,  $J$ =7.98 Hz), 6.85 (1H, Ar-H, d,  $J$ =9.54 Hz), 8.31 (2H, s),  $\delta$  4.13 (2H, t,  $J$ =5.32 Hz), 3.82 (1H, s), 3.68 (2H, t,  $J$ =5.46 Hz), 3.39 (1H, s), and 3.18 (2H, m, 6.36 Hz) (**Figure S10A**). <sup>13</sup>C NMR (100 MHz, DMSO-d<sub>6</sub>, ppm):  $\delta$  164.50, 163.70, 150.68, 134.49, 131.31, 129.78, 129.64, 124.84, 122.42, 120.83, 109.08, 104.48, 58.44, 41.94, 40.93, 37.82 (**Figure S10B**). HR-MS calculated for C<sub>16</sub>H<sub>17</sub>N<sub>3</sub>O<sub>3</sub>, 299.1270; measured, [C<sub>16</sub>H<sub>17</sub>N<sub>3</sub>O<sub>3</sub>+H]<sup>+</sup> 300.1336 (**Figure S10C**)

A solution of compound **11** (0.20 g; 0.0006 mol) in DMSO (8 mL) was further treated with fluorescein isothiocyanate (FITC) (0.27 g; 0.0007 mol) followed by TEA (0.120 g; 0.0012 mol). The resulting reaction medium was stirred overnight at room temperature under inert conditions. The desired orange colored compound **12** (200 mg, 48%) was purified through column chromatography over silica gel (100-200 mesh) in CH<sub>2</sub>Cl<sub>2</sub>: MeOH (90:10). <sup>1</sup>H-NMR (DMSO-d<sub>6</sub>, 600 MHz):  $\delta$  8.70 (1H, Ar-H, d,  $J$ =8.64 Hz), 8.44 (1H, Ar-H, d,  $J$ =6.84 Hz), 8.28 (1H, Ar-H, d,  $J$ =9.36 Hz), 7.73 (1H, Ar-H, d,  $J$ =7.8 Hz), 7.69 (1H, Ar-H, t,  $J$ =7.86 Hz), 10.14 (3H, s), 8.31 (1H, s), 8.17 (1H, s), 7.90 (1H, s), 7.18 (1H, d, 8.28 Hz), 6.99 (2H, d, 8.52 Hz), 6.68 (5H, d, 2.22 Hz), 6.61-6.56 (2H, m,  $J$ =8.76 Hz), 4.80 (1H, t, 5.94 Hz), 4.12 (2H, t, 6.9 Hz), 4.89 (2H, q, 6.0 Hz), 4.78 (2H, m, 6.6 Hz, 6.24 Hz) (**Figure S11A**). <sup>13</sup>C NMR (150 MHz, DMSO-d<sub>6</sub>, ppm):  $\delta$  168.91, 164.36, 163.53, 159.97, 152.35, 151.08, 141.53, 134.57, 131.16, 129.92, 129.47, 129.03, 127.09, 124.85, 122.45, 120.66, 113.06, 110.16, 108.61, 104.48, 102.72, 66.82, 65.38, 58.44, 46.21, 42.75, 42.50, 41.88, 40.53, 40.41, 40.28, 40.14, 39.99, 39.86, 39.72, 39.58, 15.63 (**Figure S11B**). HR-MS Calculated for C<sub>37</sub>H<sub>28</sub>N<sub>4</sub>O<sub>8</sub>S, 688.1628; measured, [C<sub>37</sub>H<sub>28</sub>N<sub>4</sub>O<sub>8</sub>S +H]<sup>+</sup> 689.1689 (**Figure S11C**).

The magnetically stirred solution of compound **12** (0.175 g, 0.0003 mol) in DMF (6.0 mL) was treated with artesunate (117.0 mg, 0.0003 mol) in the presence of the coupling agent EDC·HCl (73.0 mg, 0.0004 mol), with a catalytic amount of DMAP (31.0 mg, 0.0003 mol) and with TEA (0.030 mg; 0.0003 mol) for 12h at R.T. The volatiles were evaporated under vacuum, and the oily mass was purified through column chromatography over silica gel in CH<sub>2</sub>Cl<sub>2</sub>:MeOH (80:20) to produce pure orange-colored product **13** (82.0 mg; 30%). In LCMS, the retention time was 4.28 mins (**Figure S12**). <sup>1</sup>H-NMR (DMSO-d<sub>6</sub>, 400 MHz):  $\delta$  8.70 (1H, s), 6.87 (1H, s), 8.44 (2H, d, Ar-H,  $J$ =6.60 Hz), 8.29 (1H, t, Ar-H,  $J$ =6.00 Hz), 7.72 (1H, s, Ar-H), 7.69 (1H, s, Ar-H), 7.31-6.87 (5H, m), 6.71 (1H, s), 6.61 (1H, s), 5.68 (1H, s), 4.29 (1H, s), 4.11 (1H, t,  $J$ =6.64 Hz), 3.90 (1H, s), 3.66 (1H, s), 3.57 (1H, d,  $J$ =5.76 Hz), 3.40-3.32 (1H, m,  $J$ =7.04 Hz), 2.90 (2H, s), 2.80 (2H, s), 2.59 (1H, d,  $J$ =3.88 Hz), 2.31 (1H, d,  $J$ =10.4

Hz), 2.19-2.13(2H,m, J=13.48 Hz), 1.98-1.96(2H,m, J=10.8 Hz), 1.78(1H,s), 1.60-1.23(12H,m, J=9.56 Hz), 1.19-1.07(2H,m, J=4.36 Hz), 1.05-0.87(4H,m), 0.86-0.77(4H,m) (Figure S13A).

HR-MS calculated for  $C_{57}H_{56}N_4O_{15}S$ , 1068.3463; measured,  $[C_{57}H_{56}N_4O_{15}S + H]^+$  1069.3542 (Figure S13B).

### DNA binding study of the synthesized compounds (3, 5 and 9)

Ultraviolet–visible spectroscopy titrations: Novel compounds with st-DNA were studied at 25°C using a 1 cm path length quartz cuvette. Stock solutions of 1 mM concentrations of compounds 3, 5, and 9 were prepared in a mixture of MeOH-H<sub>2</sub>O solvent. Additionally, st-DNA stock solution was prepared by dissolving st-DNA (1.0 mg) in HPLC grade water (1.0 mL). The purity of st-DNA was monitored by determining the ratio of the absorbance at 260 and 280 nm, and the ratio of A<sub>260</sub>/A<sub>280</sub> was found to be 1.91, indicating that the st-DNA was sufficiently free from protein contamination. The concentration of st-DNA solution was spectrophotometrically determined to be  $4.84 \times 10^2 \mu\text{M}$  using its known molar absorption coefficient at 260 nm, which is  $6600 \text{ M}^{-1} \text{ cm}^{-1}$ . All stock solutions were stored at 0–4°C. Preparation of st DNA and the complexes was performed on the same day as the experiment was performed. UV–visible absorption titrations were performed by adding St-DNA to a quartz cuvette containing approximately 1.0 mM hybrid solution.

Fluorescence spectroscopy titrations: Fluorescence emission spectra were measured at 25°C using a 1 cm path length quartz cuvette. The compound concentration (1 mM) was kept constant and titrated with increasing amounts of st-DNA. Fluorescence spectra were recorded after each addition of st-DNA to the cuvette. The binding constant ( $K_b$ ) of a small molecule with DNA can be determined by following the equation  $\log[1/c] = \log [F/(F_0 - F)] + \log K_b$  equation 1, where  $K_b$  is the binding constant for the interaction of naphthalimide-DNA, and  $F_0$  and  $F$  denote the steady-state fluorescence intensities in the presence and absence of DNA, respectively. The values of  $K_b$  could be determined from the intercept and slope by plotting  $\log [1/c]$  against  $\log [F (F_0 - F)]$  (intercept =  $\log K_b$ ) equation 1.

### Competitive displacement assay

Ethidium bromide (EtBr) and acridine orange (AO) were used as intercalating dyes, whereas Hoechst33342 dye was used as a minor groove binder to validate the binding mode between the drugs and DNA. EtBr-DNA complexes were excited at 301 nm, and the emission spectra



were recorded in the presence of increasing concentrations of drug solution. Similarly, the AO-DNA complex was excited at 490 nm, and emission spectra were recorded from 500 to 750 nm in the presence of increased drug solution. The DNA Hoechst 33342 was excited at 343 nm in the presence of increasing concentrations of drug solution, and the emission spectra were recorded from 400-700 nm.

### Thermal denaturation studies

Compounds **3**, **5** and **9** were subjected to thermal denaturation studies with st-DNA solution. Fifty  $\mu$ M DNA and 1 mM solutions of compounds **3**, **5** and **9** were prepared in a methanol-water mixture. The thermal denaturation study of compounds **3**, **5** and **9** were prepared by using a 1:1 ratio of DNA to compound. The samples were then monitored at 260 nm using a Cary 100 Bio UV-Visible spectrophotometer fitted with a high-performance temperature controller, and heating was applied from 20°-100°C. The midpoint of the resultant melting temperature ( $T_m$ ) curve represents the point where half of the DNA melts. Thus, the thermal behavior of DNA in the presence of synthesized naphthalimide-artesunate derivatives (compounds **3**, **5** and **9**) provides useful information on the conformational changes and strength of the DNA-compound complexes.

### Ethics statement

This study was carried out in strict compliance with the recommendations for the care and use of laboratory animals of the National Regulatory Guidelines issued by the Committee for the Purpose of Supervision of Experiments on Animals (CPSEA), Ministry of Environment and Forest, Government of India. The protocol was approved by the Institutional Animal Ethics Committee, Banaras Hindu University. Mice were euthanized by ketamine HCl + xylazine as per CPCSEA guideline to reduce suffering to a minimum and were executed as per the AVMA Guidelines on Euthanasia (AVMA 2013).

### Mice, cell lines, and cell culture

Specific pathogenfree 6 to 8 weeksold female BALB/c mice were used for the study. Animals were purchased from the Charles River Laboratory and were maintained under pathogen-free conditions in the central animal facility of the institute. All protocols involving animal experiments were approved by the regulatory committee of Banaras Hindu University. DL cells were transplanted intraperitoneally into BALB/c (H2<sup>d</sup>) mice as described previously<sup>19</sup>. The cells were maintained in RPMI 1640 (Invitrogen, USA) with supplements including 10%

fetal bovine serum (HyClone, Logan, UT, USA), 100 U/mL penicillin, and 100 µg/mL streptomycin (Invitrogen). This culture medium was considered complete medium. The tumor cells used in the study were devoid of mycoplasma. RAJI and MCF-7 cells were purchased from ATCC.

### Cell viability assay

The effect of ARTN, 4-azide naphthalimide-ethanol (**8**), 3-nitro naphthalimide-ethanoamine (**4**), 3-nitro-naphthalimide-ethanol (**2**), 4-azide-naphthalimide-artesunate (**9**), 3-nitro naphthalimide artesunate-amide (**5**), and 3-nitro naphthalimide-artesunate-ester (**3**) on the viability of tumor cells were evaluated by a colorimetric XTT (sodium 3-[1-(phenylaminocarbonyl)-3,4-tetrazolium]-bis(4-methoxy-6-nitro) assay (Roche, Indianapolis, IN). Tumor cells were plated ( $5 \times 10^3$  cells/well) in 96-well culture dishes, incubated with different concentrations of the abovementioned compounds and incubated at 37°C and 5% CO<sub>2</sub> for 18 hours. The OD was measured at 450 nm in a plate reader (Synergy HT, BioTek, USA). The percent viable cell was calculated employing the formula below<sup>20</sup>.

$$\% \text{ Cell Viability} = \frac{\text{Experimental OD}_{450}}{\text{Control OD}_{450}} \times 100$$

### Cell growth inhibition assay

The growth inhibitory potential of the abovementioned compounds against DL and RAJI tumor cells were studied by MTT assay. Tumor target cells ( $5 \times 10^3$  cells/well) in a 96-well culture dish were treated with serial concentrations of the compounds. Following incubation at 37°C and 5% CO<sub>2</sub> for 48 hrs., the proliferation of tumor cells were assessed by MTT assay using a CellTiter 96 kit (Promega, USA). The absorbance (OD value) was measured at 570 nm in a plate reader (BioTek, USA)<sup>20</sup>. The percentinhibitions of tumor cells were calculated using the mentioned formula.

$$\% \text{ Growth Inhibition} = \left[ 1 - \frac{\text{Experimental OD}_{570}}{\text{Target OD}_{570}} \right] \times 100$$

where the experimental OD value indicates the values of tumor cells in the presence of the indicated formulations and the target OD indicates the corresponding values of tumor cells alone cultured in medium only.

### Cytotoxicity assay

The lytic activity of the above formulations against the tumor cells were measured by cytotoxicity assay using the CytoTox 96 Cytotoxicity assay kit from Promega, USA. Tumor target cells ( $5 \times 10^3$ ) were cocultured with varying concentrations of the indicated formulations in a 96-well culture dish. The culture dish was incubated for 18 hrs at 37°C and 5% CO<sub>2</sub>. Percent-specific lysis was determined from the formula below<sup>20</sup>.

$$\% \text{ Cytotoxicity} = \frac{(\text{Experimental} - \text{Effector Spontaneous} - \text{Target Spontaneous})}{(\text{Target Maximum} - \text{Target Spontaneous})} \times 100$$

### **Invitro Scratch wound healing assay**

Wound healing assay was performed in the MCF-7 cells that were grown in serum free media. The wound was created by scratching the confluent layers of the MCF-7 cells using a sterile microtips and immediately (at 0 hour) the image was captured. The cells were grown in the presence of different concentrations of compound **9** (150 μM, 250 μM) at different time points (16, 24 and 48 hour). The wound areas were calculated by using ImageJ software by calculating the distance between the edge. The wound closure percentages were calculated by using the following formula.

$$\text{wound closure \%} = [A(t=0h) - A(t=\Delta h) / A(t=0h)] \times 100$$

A(t=0h) is the wound area at 0 hour and A(t=Δh) is the wound area measured hours after the scratch assay was performed<sup>21</sup>.

### **Apoptosis and cellular uptake assay**

Evaluation of apoptotic cell death in DL, RAJI and MCF-7 tumor cells following treatment with the indicated formulations (250 μM) for 12 hours. Untreated cells were used as a positive control. The cells were washed in PBS and stained with PE-conjugated Annexin V for 30 minutes. These cells were washed in Annexin buffer. PE-conjugated Annexin V-positive cells were visualized under a fluorescence microscope (EVOS FL Cell Imaging System equipped with Plan Fluor, 40X, NA 0.75 objective, Life Technologies, USA) as described earlier. Temporal uptake of substituted naphthalimide-FITC (**12**) or substituted naphthalimide-artesunate-FITC (**13**) in DL, RAJI and MCF-7 cells was assessed, followed by observation of intracellular green fluorescence in the cells<sup>22</sup>.

### **Invitro cellular uptake study by fluorescence spectroscopy**

The cellular uptake of compound **12** and **13** were investigated by a quantitative study using fluorescence spectroscopy. DL cells ( $5 \times 10^3$ ) were seeded into the 96-well black plates and

incubated to form a confluent culture. Dose dependent treatment (50.0, 35.0, 25.0, 15.0 and 12.5  $\mu\text{M}$  concentration) of compound **12** and **13** were performed for 8-hours at 37°C in complete RPMI media. The cells were collected after 8 hours upon centrifugation (solution 1), followed by successive washing of the cells with PBS. RIPA lysis buffer was added to lyse the cells. After cell lysis the cell associated FITC conjugated compound **12** and **13** were quantified by analyzing the lysate in a fluorescence plate reader (SpectraMax i3x ( $\lambda_{\text{ex}}$  488 nm,  $\lambda_{\text{em}}$  515 nm). Fluorescent intensity of the supernatant was also determined. The concentration of the drug doses ( $\mu\text{M}$ ) was calculated by using the respective standard curves of different concentrations (10.0, 5.0, 2.5 and 1.0  $\mu\text{M}$ ) of compound **12** and **13** (supplementary S19).

Cellular uptake efficiency percentages were calculated by the following formula.

Cellular uptake efficiency (%) = (DL cell uptake FITC fluorescent intensity)  $\times$  100/ total amount of fluorescence (present in the cell suspension medium + DL-cell uptake FITC fluorescent intensity).

#### Cellular uptake study by FACS

DL cells were seeded ( $5 \times 10^5$ ) in six-well plates and cultured for 24 hours in complete medium. 12.5  $\mu\text{M}$  FITC-labeled compounds **12** and **13** were added and incubated for 1, 2, 4, 6 and 8 hours respectively. The treated cells were taken in a falcon tube and given a spin at 1650 RPM; the supernatant was discarded. The pellet was washed twice with 2% FBS enriched PBS (pH 7.4). The pellet was dissolved in 600  $\mu\text{l}$  sheath fluid and were analyzed using a FACS Calibur flow cytometer using ModFit software (BD Biosciences). A total of 50,000 events were collected and analysed for each sample. In another set of experiment, DL cells ( $5 \times 10^5$ ) were seeded in a six well plate and were cultured for 24 hours in complete medium. 100.0, 50.0 and 12.5  $\mu\text{M}$  FITC-labelled compound **12** and **13** were added and incubated for 8 hours. The treated cells were taken in a falcon tube and given a spin at 1650 RPM; the supernatant was discarded and the pellet was washed twice with 2% FBS enriched PBS (pH 7.4). The pellet was dissolved in 600  $\mu\text{l}$  sheath fluid and analyzed using a FACS Calibur flow cytometer using ModFit software (BD Biosciences). A total of 50,000 events were collected and analyzed for each sample.

#### Tissue processing and histopathological analysis

Tissues (liver, lung, spleen and lymph node) were collected from healthy control, DL tumor-bearing and vaccinated mice, fixed in normal buffered formalin (NBF) and processed. Formalin-fixed, paraffin-embedded tissue sections were stained with hematoxylin and eosin

(H&E) and examined for regions of tumor metastasis. Images were captured by a Nikon 80i research microscope ( $\times 400$ )<sup>23</sup>.

### **In vivo studies: Tumor challenge and treatment experiments**

DL tumors were maintained in vitro in RPMI 1640 (Invitrogen) supplemented with 10% FCS (Invitrogen) and in the peritoneal cavity of BALB/c (H2<sup>d</sup>) mice as mentioned earlier. Female BALB/c mice weighing 18-20 g (n=6/group) were transplanted intradermally in the left flank of the animal with DL tumor cells ( $5 \times 10^5$ ). At day 10, the treatment schedule was started, and altogether, 5 injections were given at an interval of 5 days. Tumor volume and weight were calculated using digital slide calipers. Control animals received vehicle only (PBS). Mice were observed until day 60, when final data collection was performed for Kaplan–Meier survival analysis<sup>24,25</sup>. Mice were randomized into experimental groups and at day 10 after tumor cell implantation, when the average tumor size reached palpable size, monitoring was initiated (day 0). The tumor volume was calculated as  $(\text{length} \times \text{width} \times \text{height})/2$ .

### **Statistical analysis.**

For each group, the mean  $\pm$  SD was calculated using the data collected from individual experiments (n= 3-5). Unpaired Student's t test and one- or two-way ANOVA were performed on the basis of demand. This was followed by multiple-comparison tests using PRISM statistical analysis software (Graph Pad, San Diego, CA, USA). The statistical significance was analyzed by the log-rank (MantelCox) test. A p value of  $<0.05$  was considered statistically significant. \* $<0.05$ , \*\* $<0.01$ , \*\*\* $<0.001$  and \*\*\*\* $<0.0001$ .

## **Results**

### **Synthesis and characterization of novel naphthalimide-artesunate compounds (3,5 and 9) and FITC-conjugated naphthalimide-artesunate compound 13.**

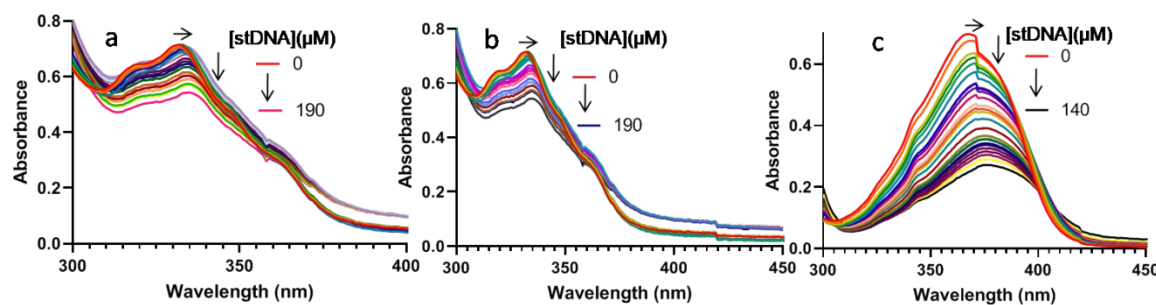
We designed, synthesized and characterized a series of DNA intercalative molecules containing a naphthalimide moiety conjugated with the antimalarial drug artesunate through a suitable linker via ester (**3**, **9** and **13**) and amide (**5**) bonds by a multistep synthetic procedure. The products were obtained in a multistep synthetic procedure followed by detailed characterizations. First, commercially available 3-nitro-1,8-naphthalic anhydride was reacted with ethanol amine to obtain compound **2** under refluxing conditions in ethanol. Compound **2** was further reacted with artesunate by utilizing a coupling reagent to afford final product **3**. The artesunate naphthalimide conjugate **3** was confirmed by <sup>1</sup>H-NMR spectroscopy data with

1  
2  
3  
4  
5  
6  
7  
8  
9  
10  
11  
12  
13  
14  
15  
16  
17  
18  
19  
20  
21  
22  
23  
24  
25  
26  
27  
28  
29  
30  
31  
32  
33  
34  
35  
36  
37  
38  
39  
40  
41  
42  
43  
44  
45  
46  
47  
48  
49  
50  
51  
52  
53  
54  
55  
56  
57  
58  
59  
60

$\delta$ 9.49- 8.06, the presence of the five aromatic protons (**Figure S3A**) was further confirmed by  $^{13}\text{C}$  NMR (**Figure S3B**) and HR-MS (**Figure S3C**). Nitro-substituted naphthalimide was introduced to further estimate the impact on anti-lymphoma validation. Therefore, commercially available 3-nitro 1,8-naphthalic anhydride **1** was considered and reacted with 1,2-ethylenediamine to obtain intermediate product **4** under refluxing conditions in an inert atmosphere. Compound **4** was further reacted with artesunate in the presence of a coupling agent to obtain the desired product compound **5**, which was further confirmed by  $^1\text{H}$ -NMR spectroscopy data with the presence of five aromatic protons with  $\delta$ 9.48- 8.08 (**Figure S5A**) and further confirmed by  $^{13}\text{C}$  NMR (**Figure S5B**) and HR-MS (**Figure S5C**). To obtain an azide substitution on the naphthalimide ring, we reacted starting material 4-bromo-1,8-naphthalic anhydride **6** with 2-aminoethanol to obtain desired product **7** under refluxing conditions in dry ethanol. Compound **7** was further converted to azide derivative **8**. The newly formed precursor compound **8** was further reacted with ARTN in the presence of a coupling agent to the desired product **9**. Compound **9** was further confirmed by  $^1\text{H}$ -NMR spectroscopy data with the presence of five aromatic protons with  $\delta$  8.57- 7.78 (**Figure S8A**) and further confirmed by  $^{13}\text{C}$  NMR (**Figure S8B**) and HR-MS (**Figure S8C**). For the synthesis of the theranostic lymphoma drug, the amino-terminal naphthalimide moiety (**11**) was conjugated with FITC for the validation of cellular bioavailability, and ARTN was attached to the naphthalimide moiety via an ester link (**13**), which was also characterized through  $^1\text{H}$  NMR and  $^{13}\text{C}$  NMR.

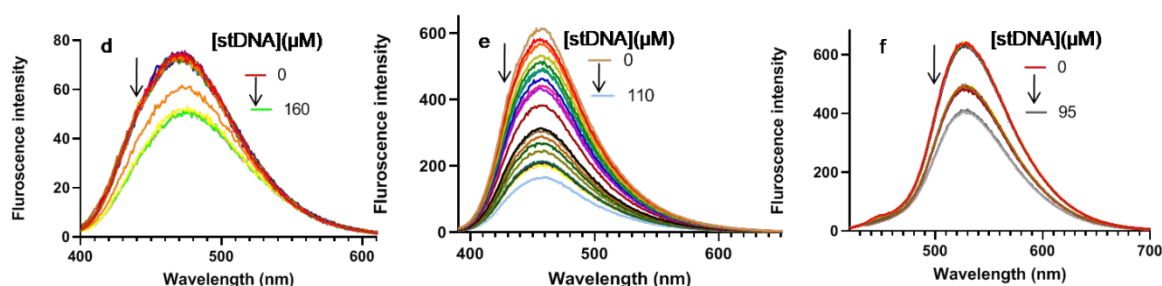
### DNA binding study of synthesized compounds (**3**, **5** and **9**)

UV-visible spectroscopy: Compounds **3**, **5** and **9** were analyzed by UV-visible spectroscopy. This study primarily monitored the changes in st-DNA topology upon incremental addition of DNA to the solution of compounds **3**, **5** and **9**. Compound **3** in the solution phase exhibited a prominent absorption band at 331 nm. In addition, DNA showed hypochromicity with a slight bathochromic shift from 331 nm to 333 nm (indicated by a 2 nm red shift) (**Figure 2**), indicating DNA intercalation with compound **3**. Similarly, compound **5** showed a prominent absorption band at 331 nm. The addition of st-DNA showed hypochromicity at 331 nm and a redshift from 331 nm to 334 nm, indicating an interaction between DNA and compound **5** (**Figure 2**). Compound **9**, upon the addition of st-DNA, showed a prominent absorption band at 367 nm, which resulted in hypochromicity at 367 nm along with a redshift to 376 nm (9 nm redshift) with the interaction of DNA (**Figure 2**). Ultimately, the results indicate that compounds **3**, **5** and **9** resulted in DNA intercalation between the two strands of st-DNA.



**Figure 2.** Effect on compounds **3**, **5** and **9** in a methanol-water mixture followed by incremental addition of DNA: (a) st-DNA addition (0 to 190  $\mu\text{M}$ ) on the absorption spectra of compound **3** (1 mM) in solution. The arrows indicate the hypochromicity at 331 nm, and a and 2 nm redshift from 331 nm to 333 nm. ;( b) st-DNA (0- 190  $\mu\text{M}$ ) on absorption spectra of compound **5** (1 mM), the arrows indicate the hypochromicity at 331 nm and redshift from 331 nm to 334 nm. (c)st-DNA (0-140  $\mu\text{M}$ ) on the absorption spectra of compound **9** (1 mM). The arrows indicates the hypochromicity at 367 nm and redshift from 367 nm to 376 nm.

**Fluorescence spectroscopy:** Fluorescence spectroscopy was performed to understand the mode of interaction between all three compounds (**3**, **5**, and **9**) and st-DNA to assess the electronic environment around the drug-DNA complex. The interaction of compound **3** with the DNA showed a prominent peak at 470.00 nm, scan condition:  $\lambda_{\text{ex}}$  400 nm,  $\lambda_{\text{emi}}$  410 – 680 nm (**Figure 3**). Following the addition of increasing concentrations of DNA, the fluorescence intensity gradually decreases. From equation 1 (mentioned in methodology section), the binding constant of compound **3** with DNA was ( $K_b = 5.3 \times 10^2 \text{ M}^{-1}$ ) at 470 nm. Similarly, compound **5** showed a prominent peak at 453.03 nm, scan condition:  $\lambda_{\text{ex}}$  380 nm,  $\lambda_{\text{emi}}$  390 – 680 nm (**Figure 3**). Upon incremental addition of DNA to the compound **5** solution, the emission peak intensity decreased gradually at 453.03 nm as the DNA seemed to lose its structural advances due to intercalation. From equation 1, the binding constant of compound **5** and DNA was ( $K_b = 5.3 \times 10^3 \text{ M}^{-1}$ ) at 453.03 nm. Compound **9** showed a prominent peak at 525.00 nm, scan condition:  $\lambda_{\text{ex}}$  410 nm,  $\lambda_{\text{emi}}$  420 – 700 nm (**Figure 3**). With the incremental addition of DNA to the compound **9** solution, the emission peak intensity decreased gradually at 525.00 nm. From equation 1, the binding constant of compound **9** and DNA was ( $K_b = 4.00 \times 10^3 \text{ M}^{-1}$ ) at 525 nm. The result indicates that the emission from the free drug (compounds **3**, **5** and **9**) decreases significantly upon binding to DNA, as the fluorophore seems to lose its structural advances due to intercalation with DNA.



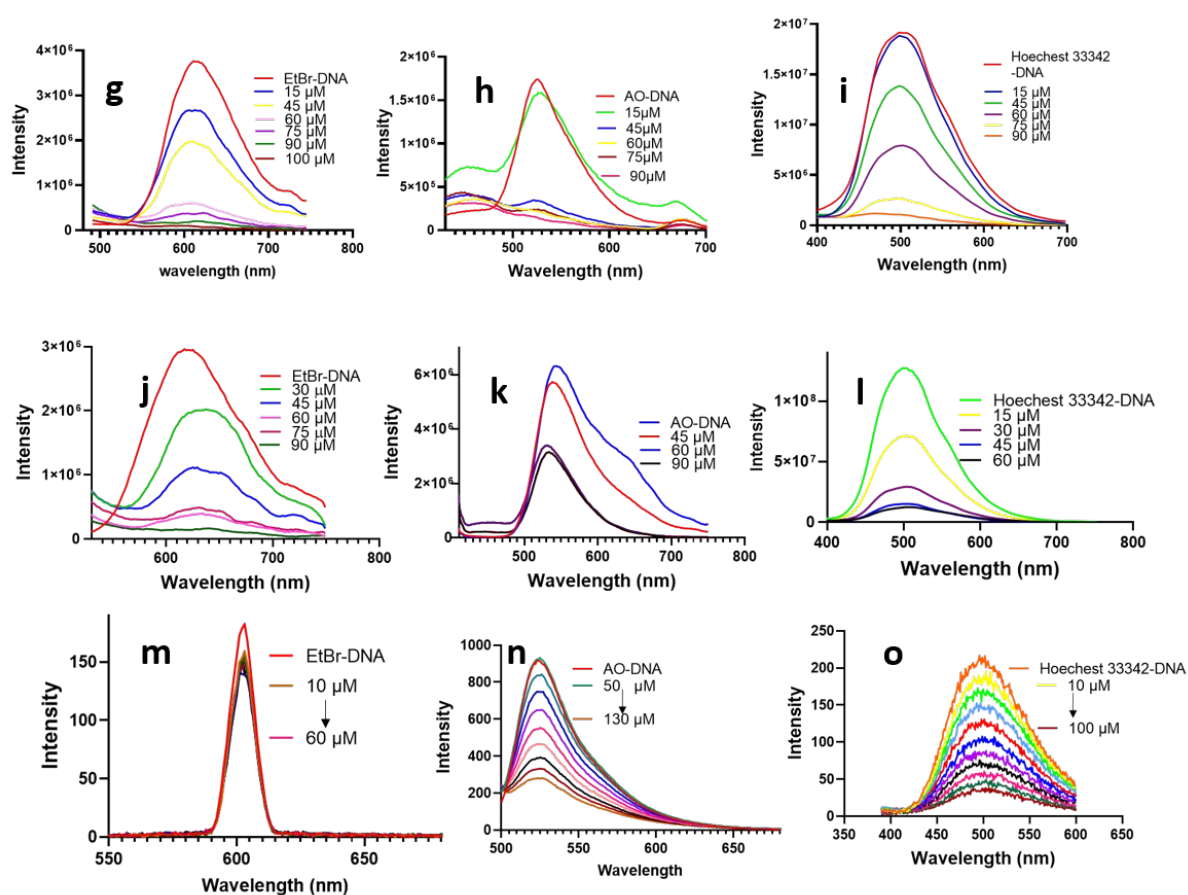
**Figure 3.** (d). Effect of incremental addition of st-DNA (0-160  $\mu\text{M}$ ) to compound **3** (1 mM) in a methanol-water mixture; (e). Effect of incremental addition of st-DNA (0-110  $\mu\text{M}$ ) to Compound **5** (1 mM) in a methanol-water mixture. The arrows indicate the decrease in fluorescence intensity upon incremental addition of DNA; (f). Effect of incremental addition of st-DNA (0-95  $\mu\text{M}$ ) to compound **9** (1 mM) in a methanol-water mixture. The arrows indicate the decrease upon incremental addition of DNA.

### Competitive displacement assay of compounds **3**, **5** and **9**

The EtBr displacement assay is usually performed to study the DNA binding mode. The incremental addition of compound **3** to the EtBr-DNA complex was able to displace EtBr from the complex as the emission intensity gradually decreased upon excitation at 510.00 nm (**g**). The results indicate that compound **3** binds with DNA by a mechanism similar to that of intercalator EtBr and replaces EtBr from the DNA helix; as a result, the fluorescence emission intensity gradually decreases (15  $\mu\text{M}$ -100  $\mu\text{M}$ ) with the addition of compound **3** (**Figure 4**). Compound **5** binds with DNA by a similar mechanism; as a result, it replaced EtBr from DNA, followed by a gradual decrease in the emission intensity upon  $\lambda_{\text{ex}}$  510.00 nm (**j**). Similarly, the incremental addition of compound **9** also replaced EtBr from the EtBr-DNA complex ( $\lambda_{\text{ex}}$  510.00 nm) (**m**), indicating the intercalative binding mode between compound **9** and DNA (**Figure 4**). The AO displacement assay is useful to determine the DNA intercalative binding mode, and the Hoechst-33342 displacement assay is used to study the DNA binding mode in the minor groove. Fluorescence intensity decreases in the presence of the incremental addition of compounds **3**, **5** and **9** in AO (**h**, **k** and **n**) excited at 480 nm and Hoechst 33342 (**i**, **l** and **o**) excited at 343 nm with the st-DNA complex (**Figure 4**). The AO-DNA complex was reported with  $\lambda_{\text{ex}}$  480 nm, and the emission spectra were recorded from  $\lambda_{\text{emi}}$  450-700 nm. The Hoechst-DNA complex was excited at 343 nm, and the emission spectra were recorded from 400 to 700 nm. Compounds **3**, **5** and **9** bind with DNA by a



mechanism similar to that of the intercalator AO and replace AO from the DNA helix; as a result, the fluorescence emission intensity decreases gradually (**h, k and n**) (**Figure 4**). The incremental addition of compound **3** (10  $\mu$ M -100  $\mu$ M) to the Hoechst-33342- DNA complex was able to displace Hoechst-33342 from the complex as the emission intensity gradually decreased (**i**). Compounds **3, 5 and 9** bind with DNA by a similar mechanism to Hoechst-33342 and replace Hoechst-33342 from the DNA helix; as a result, the fluorescence emission intensity decreases gradually (**i, l and o**) (**Figure 4**). The result obtained from the displacement assays indicates intercalative binding along with minor groove binding interaction of the synthesized compound (**3, 5 and 9**) with DNA. This result indicates that the part of the compounds (**3, 5 and 9**) with a naphthalimide moiety intercalates with st-DNA and that the part containing artesunate is a minor groove binder, as it can replace hoechst-33342.

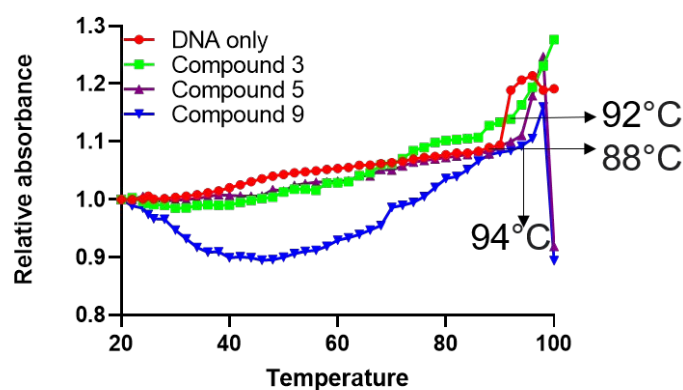


**Figure 4.** The st-DNA and EtBr complex was excited in the presence of increasing concentrations of compound 3. The fluorescence emission intensity decreases with incremental addition of compound 3, suggesting an intercalative mode of interaction with

the DNA helix. Scan conditions:  $\lambda_{ex} = 510 \text{ nm}$ ,  $\lambda_{emi} = 520 - 800 \text{ nm}$ (g). The AO-DNA complex will be excited at 480 nm, and the emission spectra will be recorded from 500-800 nm (h) with incremental addition of compound 3. The Hoechst-DNA complex will be excited at 343 nm, and the emission spectra will be recorded from 350 to 650 nm with incremental addition of compound 3(i). The St-DNA and EtBr complex was excited in the presence of incremental addition of compound 5. The fluorescence emission intensity decreases with incremental addition of Compound 5, suggesting an intercalative mode of interaction between compound 5 and DNA. Scan conditions:  $\lambda_{ex} = 510 \text{ nm}$ ,  $\lambda_{emi} = 520 - 800 \text{ nm}$  (j). The AO-DNA complex will be excited at 480 nm, and the emission spectra will be recorded from 500-800 nm (k) with incremental addition of compound 5. The Hoechst-DNA complex will be excited at 343 nm, and the emission spectra will be recorded from 400 to 800 nm (l) with incremental addition of compound 5. The St-DNA and EtBr complex was excited in the presence of incremental addition of compound 9. The fluorescence emission intensity decreases with incremental addition of Compound 9, suggesting an intercalative mode of interaction between compound 9 and DNA. Scan conditions:  $\lambda_{ex} = 510 \text{ nm}$ ,  $\lambda_{emi} = 520 - 700 \text{ nm}$  (m). The AO-DNA complex will be excited at 480 nm, and the emission spectra will be recorded from 500-800 nm with incremental addition of drug (n). The Hoechst-DNA complex will be excited at 343 nm, and the emission spectra will be recorded from 350 to 650 nm with incremental addition of drug (o).

### Thermal denaturation study

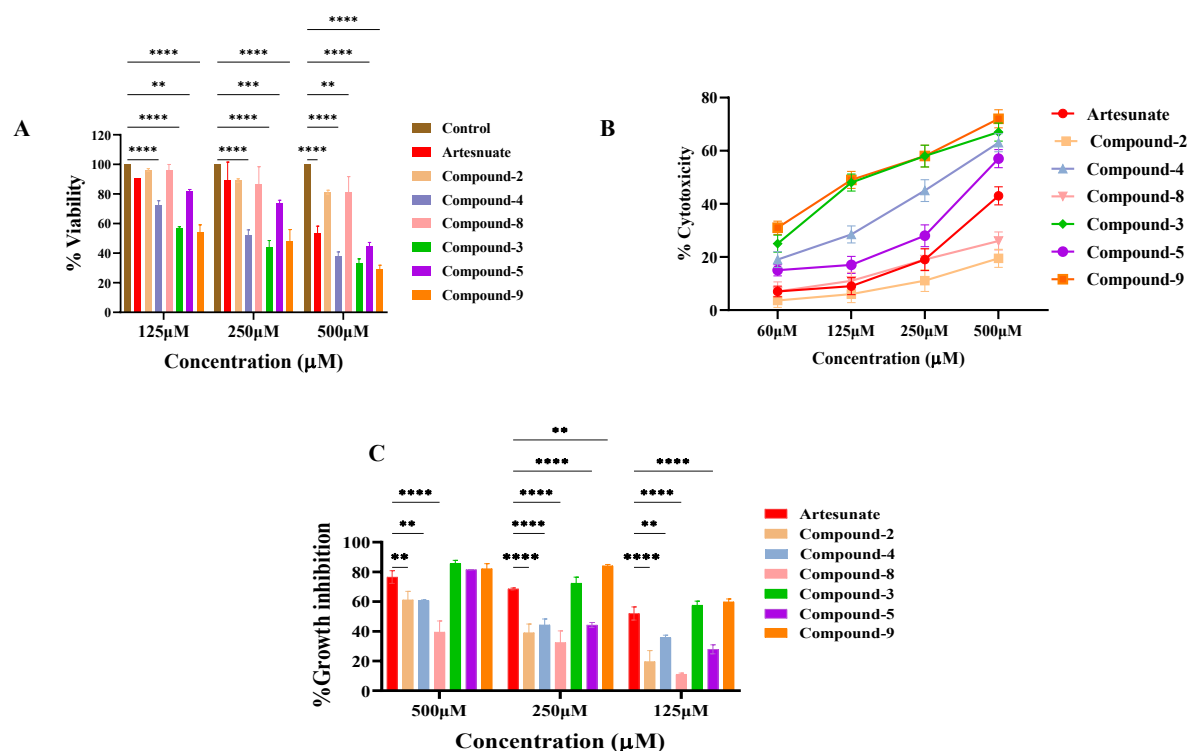
Additional evidence for intercalation was obtained from thermal denaturation studies. It is well known that the double-helical structure of DNA is very stable due to hydrogen bonding and base stacking interactions. With increasing temperature, the double helix dissociates into single strands due to the breaking of hydrogen bonding and stacking interactions. The temperature at which half of a DNA sample melts is known as the melting temperature ( $T_m$ ). A change in  $T_m$  may be observed if a molecule binds with DNA. The  $T_m$  value of free st-DNA is 88°C. The melting temperatures ( $T_m$ ) of DNA-compound 3, DNA-compound 5 and DNA-compound 9 were 92°C, 94°C, and 94°C, respectively (**Figure 5**), indicating that compounds 5 and 9 possessed higher DNA melting temperatures than compound 3.



**Figure 5. Thermal denaturation studies of compounds 3, 5 and 9 and st-DNA only. The  $T_m$  value of free st-DNA is 88°C. The melting temperatures ( $T_m$ ) of DNA-compound 3, DNA-compound 5 and DNA-compound 9 were 92°C, 94°C and 94°C, respectively.**

### **Artesunate-Naphthalimide azide arrests DL tumor cell growth**

We studied the tumoricidal effect of artesunate (ARTN), 3-NO<sub>2</sub>-naphthalimide-linked ethanol (compound 2), 3-NO<sub>2</sub>-naphthalimide-linked ethanol amine (compound 4), 4-azide naphthalimide-linked ethanol (compound 8), 3-NO<sub>2</sub>-naphthalimide-linked artesunate via ester (compound 3), 3-NO<sub>2</sub>-naphthalimide-linked artesunate via amide (compound 5), and 4-azidenaphthalimide-linked artesunate via ester (compound 9) on DL tumor cells (Scheme 1,2). We studied the tumoricidal potential of the synthesized components against DL and RAJI cells. The viability of the DL tumor cells was significantly reduced following treatment with compound 9 compared with ARTN or other naphthalimide derivatives (compound 2, 3, 4, 5, 8 and 9) in a concentration-dependent manner (**Figure 6A**). The viability of DL cells following treatment with compound 9 at the highest concentration (500 µM) was reduced to <30% compared to 60% when treated with ARTN or 80% in the presence of compound 8 (p<0.0001) (**Figure 6A**). At lower concentrations, a similar pattern was observed, with compound 9 performing significantly better than the other derivatives. Compound 9 demonstrated significant cytotoxicity by releasing LDH compared to similar treatment with ARTN or other naphthalimide compounds (**Figure 6B**). The percent cytotoxicity in DL cells after treatment with compound 9 at the highest concentration was 73% compared to 40% in the presence of artesunate only (p<0.001) and 20% when treated with compound 8 (p<0.001). The long-term growth inhibitory effect of compound 9 on DL cells demonstrated a significant reduction in tumor cell growth in a concentration-dependent manner (**Figure 6C**).



**Figure 6.** (A) Viability, (B) cytotoxicity and (C) growth inhibition of DL tumor cells in the presence of varying concentrations of the indicated treatment. The experiments were performed according to the methods described above. Viability and cytotoxicity was performed in 18 hours assay while growth inhibition was for 48 hours of treatment of DL cells in the presence of indicated compounds. The experiment was repeated 3 times with triplicate determination. A  $p$  value of  $<0.05$  was considered statistically significant. \*\* $<0.01$ , \*\*\* $<0.001$  and \*\*\*\* $<0.0001$ .

The percent growth inhibition by compound **9** in DL cells was 87% compared to 71% in cells treated with ARTN only ( $p<0.01$ ). The other two combination drugs, 3-NO<sub>2</sub>-naphthalimide-linked artesunate via amide (compound **5**) and 3-NO<sub>2</sub>-naphthalimide-linked ARTN via ester (compound **3**), also performed well, similar to compound **9**, compared with artesunate only ( $p<0.01$ ) (**Figure 6C**). Artesunate only or 3-NO<sub>2</sub>-naphthalimide with a hydroxyl linker (compound **2**), amide linker (compound **4**) or 4-azide naphthalimide linked ethanol (compound **8**) are significantly less potent, suggesting that conjugates of ARTN and 4-azide naphthalimide via an ester linker are a novel hybrid with better tumoricidal efficiency. We repeated the experiment in the human B-cell line RAJI to demonstrate the tumoricidal potential in human tumor cells as well, similar to that of DL cells, which are murine in origin (**Figure S14**). These results suggest that the remodeled hybrid combination drug is genuinely tumoricidal against tumor cells across the species barrier. We also determined the IC<sub>50</sub> values of the abovementioned compounds against DL and RAJI cells. Our data indicate that compound **9** has a significantly lower IC<sub>50</sub> value than the free ARTN or naphthalimide

moiety (before conjugation with ARTN) (**Table 1**). A similar trend was also observed in RAJI cells.

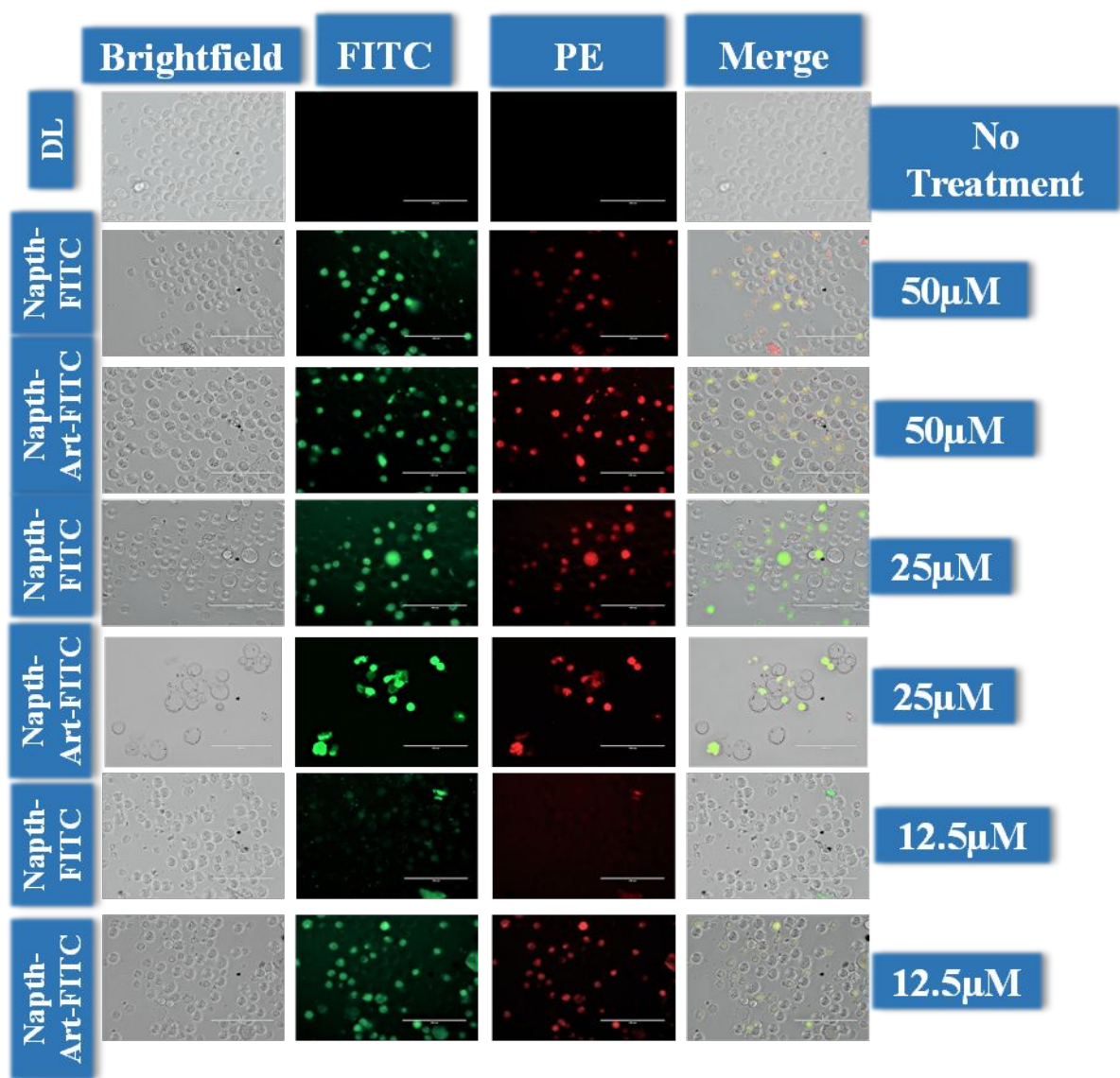
The hybrid remodeled drug was tested for its biocompatibility against human white blood cells and red blood cells (RBCs). All three compounds (**3**, **5** and **9**) of ARTN-Naphthalimide hybrid conjugates were relatively tolerant to human monocytes and lymphocytes with moderate loss of viability at the highest concentration (100  $\mu$ M) tested (**Figure S15A & C**). The drugs are also mildly cytotoxic against monocytes and lymphocytes and are well tolerated compared to artesunate (**Figure S15B & D**). The hybrid drugs are also tolerant to RBCs, with significantly low hemolysis of red blood cells (**Figure S16**). No significant damage was observed in RBCs following treatment (**Figure S16A**). Additionally, the percent lysis of RBCs in the presence of the linked hybrid drugs was lower (**Figure S16B**).

**Table 1.** *IC<sub>50</sub> analysis of the compounds in DL and RAJI cells.*

Cell Line	Artesunate (ARTN)	Compound-2	Compound-4	Compound-8	Compound-3	Compound-5	Compound-9
DL IC <sub>50</sub> ( $\mu$ M)	602.2 $\pm$ 2.2	1801.4 $\pm$ 0.9	302.63 $\pm$ 1.3	1547.17 $\pm$ 3.2	168.4 $\pm$ 3.3	458.04 $\pm$ 0.9	157.23 $\pm$ 3.6
RAJI IC <sub>50</sub> ( $\mu$ M)	300.6 $\pm$ 5.4	765.80 $\pm$ 2.3	456.77 $\pm$ 1.5	1232.2 $\pm$ 2.4	279.32 $\pm$ 2.4	228.6 $\pm$ 1.5	204.88 $\pm$ 4.3

#### **4-Substituted naphthalimide-artesunate-FITC (compound 13) uptake and induction of apoptosis in DL cells:**

We next studied the uptake and apoptosis of two compounds, compound **12** and compound **13**, in DL tumor cells. Temporal uptake of compound **12** or **13** showed similar uptake efficiency, although compound **13** showed significantly higher uptake at the lower concentration tested. At higher to medium concentrations, the uptake has similar efficiency (**Figure 7**). In contrast, compound **13** showed significantly higher apoptosis at all concentrations (high, medium, and low) than treatment with compound **12** (**Figure 7**). Similar results were observed with RAJI & MCF-7 cells (**Figure S17& S18**).



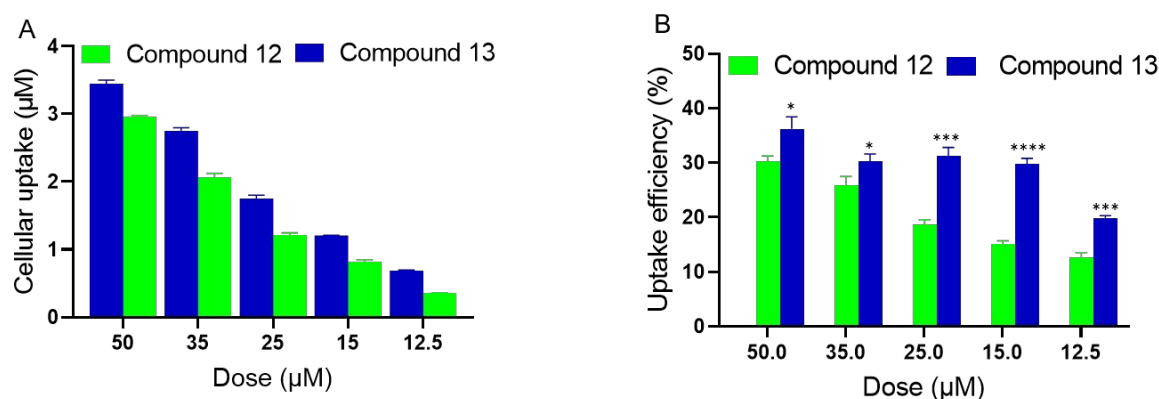
**Figure 7.** Temporal uptake and apoptosis in DL tumor cells. DL tumor cells were treated with various concentrations (50  $\mu$ M, 25  $\mu$ M and 12.5  $\mu$ M) of compound **12** (substituted naphthalimide-FITC) or compound **13** (substituted naphthalimide artesunate -FITC) for 8 hours. The cells were washed in PBS followed by staining with Annexin V-PE for 45 minutes in Annexin buffer (1 $\times$ ). Temporal uptake (green) and apoptosis (red) were captured in EVOS FL (magnification  $\times$ 400). Representative of 3 similar experiments are shown here.

We also performed quantitative fluorimetric analysis for the cellular uptake of compound **13** and compared with compound **12** in DL cells with respect to fluorescence intensity. cellular uptake and uptake efficiency.

As shown in **Figure 8A & B**, the uptake of compound **13** was significantly increased in DL cells at concentrations (50  $\mu$ M and 35  $\mu$ M) ( $p < 0.05$ ) in comparison to the compound **12** at eight-hrs incubation time point. The cellular uptake was also significant for compound **13** ( $p < 0.001$ ) at lower concentration compared to compound **12**. At lower concentration (12.5



$\mu\text{M}$ ) the percentage uptake efficiency for compound **13** was significantly increased compared with compound **12**. Fluorescence intensity of compound **13** was significantly higher compared to compound **12** in a concentration dependent manner (**Figure S19A & B**).



**Figure 8:** (A) Increased cellular uptake of compound **12** and **13** after drug treatment ( $\mu\text{M}$ ) in DL cells ( $5 \times 10^3$ ) for a duration of 8 hours; herein the data indicates the exact amount of drug internalized inside the DL cells ( $5 \times 10^3$ ); (B) The results were also presented in percentage of cellular uptake efficiency of compound **12** and compound **13** at following treatment with drug in a concentration dependent manner. Detail methodology was mentioned in the material method section. (Statistical comparison was performed between the two treatment groups).

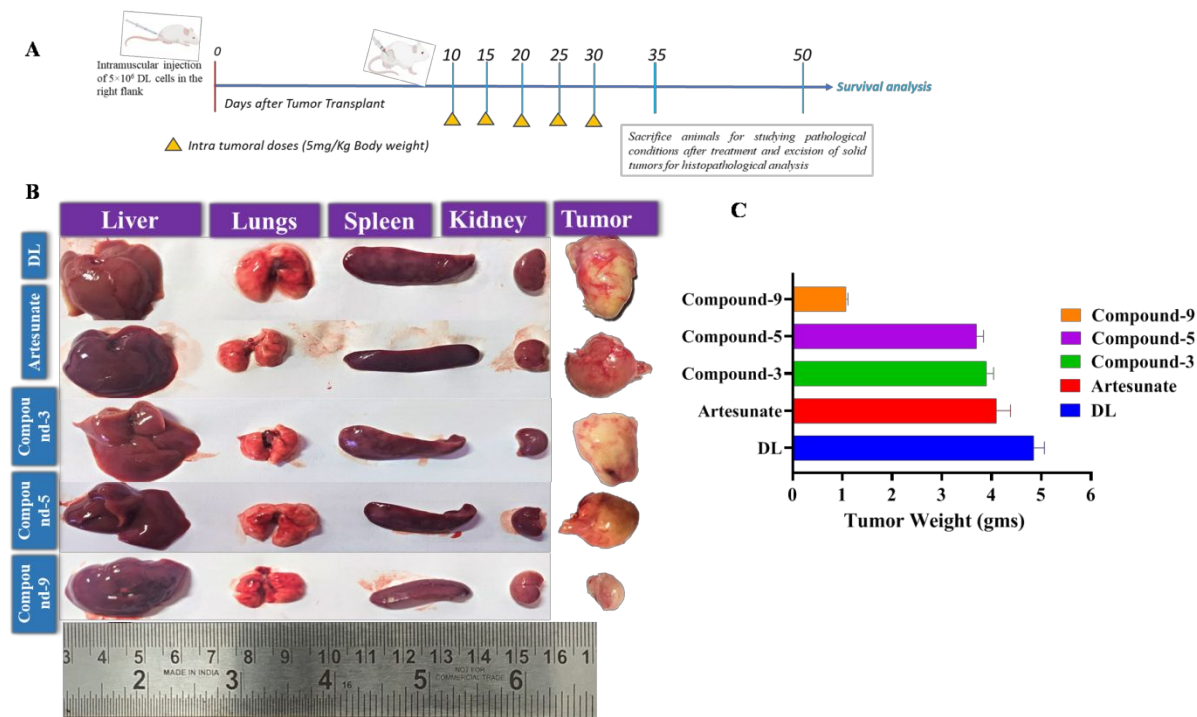
Besides fluorimetric study, we also performed FACS analysis for the uptake of compound **13** and compared to compound **12** in DL cells. In a time, kinetics study, compound **13** demonstrated significant uptake in DL cells compared to compound **12** (**Figure S20A & B**). At eight-hours time interval and in the presence of  $12.5 \mu\text{M}$  concentration, compound **13** treated cells showed significant increase of cellular uptake compared with similar treatment with compound **12** ( $p < 0.0001$ ) (**Figure S20A & B**).

Compound **13** also showed significant increment in cellular uptake compared to similar treatment with compound **12** at  $100 \mu\text{M}$  ( $p < 0.0001$ ),  $50 \mu\text{M}$  ( $p < 0.0001$ ) drug concentration after eight hours of incubation. The compound **13** showed 28.2% of cellular uptake whereas compound **12** showed 6.9% uptake at  $12.5 \mu\text{M}$  concentration ( $p < 0.001$ ) (**Figure S21A**). At highest concentration ( $100 \mu\text{M}$ ) there was significant enhancement in uptake of compound **13** (44.1%) compared to 13.2% when treated with compound **12** ( $p < 0.001$ ) (**Figure S21A & B**).

#### 4-Azide-naphthalimide-artesunate protects and reduces DL tumors

We then tested the efficiency of ARTN, compound **9**, compound **5** and compound **3** on DL tumor cells that developed as solid tumors in the right flank of the thigh region. **Figure 9A** shows the treatment schedule with the treatment started at day 10 post tumor development.

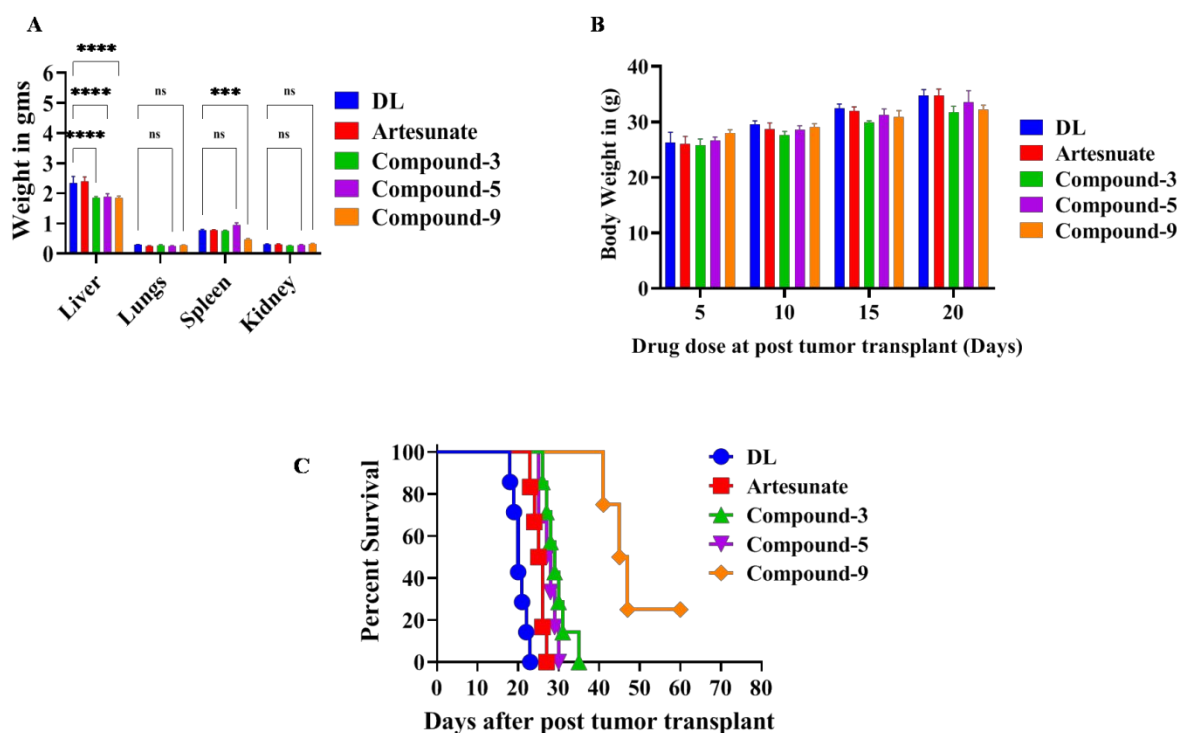
Altogether, 5 injections (100 µg/injection) (5 mg/kg of body weight) were given at an interval of 5 days. The DL group of mice was euthanized because excessive tumor growth beyond 2000 mm<sup>3</sup> and the experiment was terminated for the DL group. The other group of treated animals was allowed to continue until the tumor size reached the permissible limit. Following reaching the tumor volume to permissible limit, the intermediate compound treated group was euthanized accordingly (**Figure 9A**).



**Figure 9. (A) Treatment schedule, (B) Phenotypic presentation of excised vascularized organ and tumor, (C) Weight of DL tumors in BALB/c mice.**

Assessment of tumor weight in the untreated and treated groups showed a significant reduction in treatment with compound 9 compared with the untreated DL group. Other combinations also showed a significant reduction in tumor weight compared with the untreated DL group (**Figure 9C**). The phenotypic size of the liver, lung, spleen, kidney and tumor is presented in **Figure 9B**, suggesting a significant tumoricidal effect of compound 9 in lymphoma established as a solid tumor under the skin.

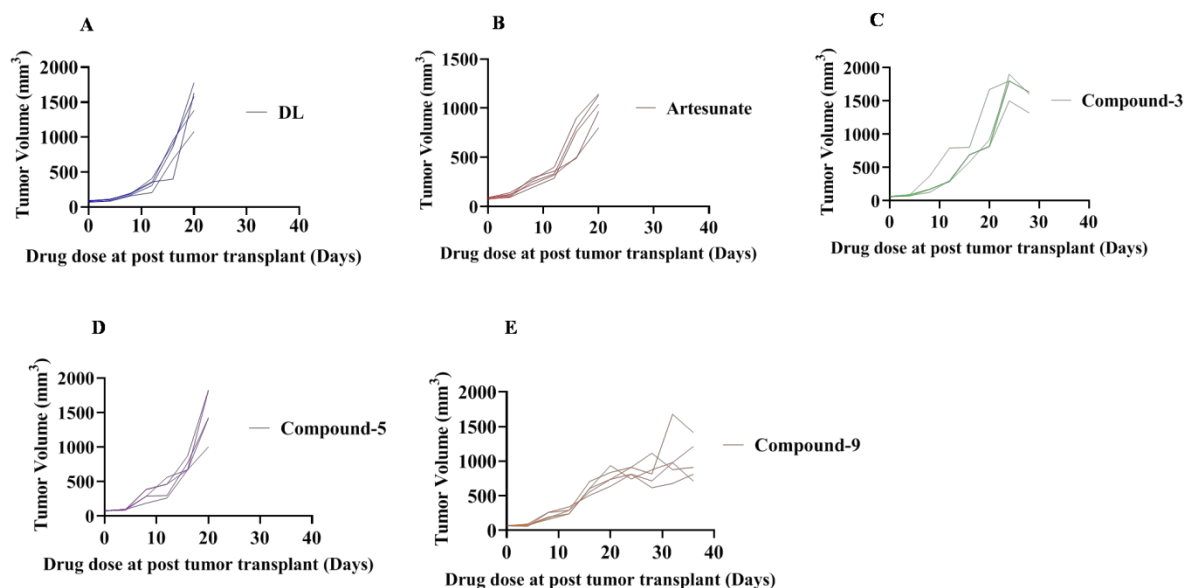




**Figure 10.** (A) Weight of vascularized organs, (B) body weight and (C) Kaplan–Meier survival analysis in untreated (DL) and treated groups.

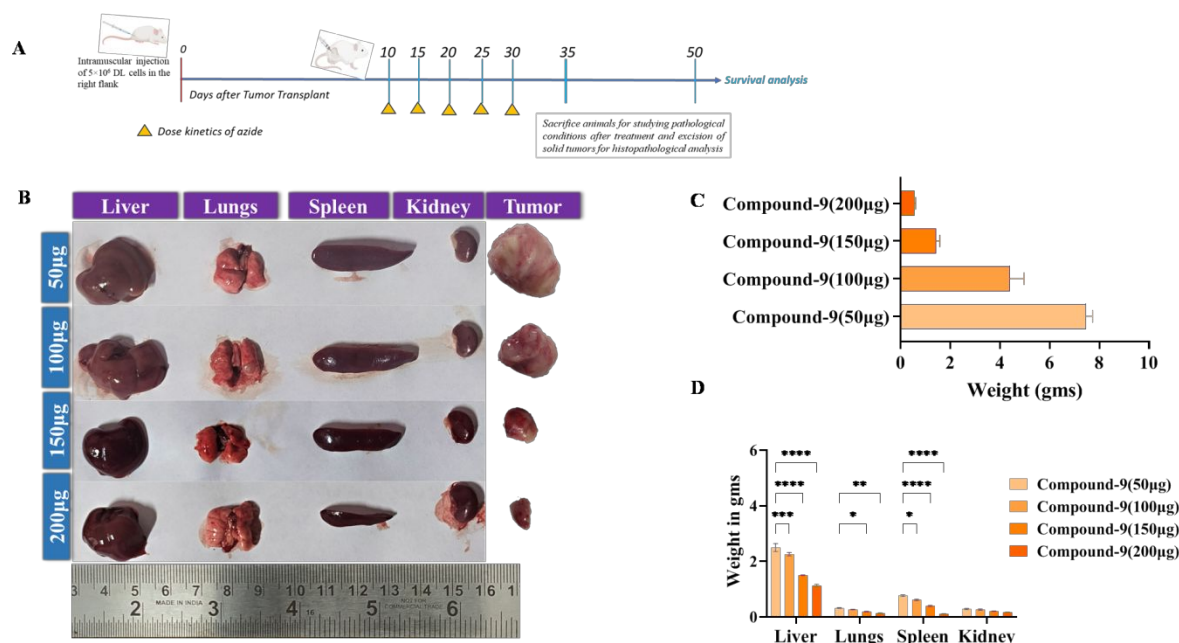
Our data also suggest that the inhibition of metastasis in vascularized organs such as the liver and spleen were significantly checked following treatment with compound 9 compared to untreated DL control and performed significantly better compared with treatment with the other combinations. (Figure 10A & B). Kaplan–Meier analysis for survival of the compound 9 treated group showed significantly higher survival compared with the untreated DL group (Figure 10C). Tumor volume analysis of each mouse in the respective group was presented in Figure 11, showing a significant effect of compound 9 in reducing the tumor volume compared with DL as well as with the other treatment groups.

We have performed in vitro cell migration assay in MCF-7 cells to demonstrate anti invasive effect of compound 9 in support of possible role of the compound 9 against metastasis by the DL tumor cells. MCF-7 cells were chosen because it is adherent in nature and is also responsive to compound 9 (Figure S18). As presented in wound healing assay, in both the concentration tested (125 & 250  $\mu$ M), compound 9 significantly prevent wound healing/invasion compared with untreated control ( $p < 0.05$ ) (Figure S22A). Percent wound healing and wound healing areas was significantly inhibited in the presence of compound 9 in comparison to untreated control (Figure S22B & C).

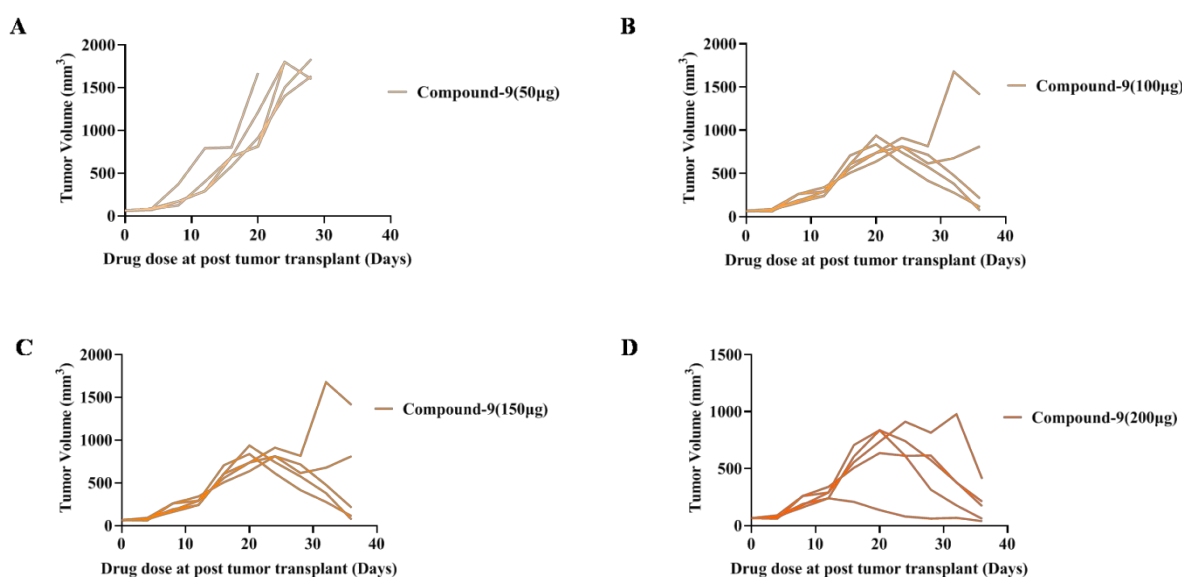


**Figure 11.** Analysis of tumor volume in untreated DL and treated groups in days after tumor transplantation. Data presented as the tumor volume of individual mouse in post tumor transplant either untreated (DL) or treated with the indicated compounds.

The tumoricidal effects of compound 8, compound 4, and compound 2 without ARTN were also studied to ascertain the effect of only naphthalimide against solid DL lymphoma. Our data suggest that in comparison to dual drug therapy, naphthalimide alone with various linker conditions is unable to provide the same degree of tumoricidal effect (**Figure S23A-C**). Kaplan–Meier survival analysis and tumor volume assessment indicated significantly lower outcomes in animal survival and less than optimal effects in the abatement of tumor volume in the presence of the indicated treatment (**Figure S24A-F**). We also tested the concentration-dependent (50–200 µg/mouse) tumoricidal effect of compound 9 in DL lymphoma that developed as a solid tumor (**Figure 12A-C**). The results suggest that at the highest concentration of the compound, there was dramatic remission of tumors in all tumor-bearing animals. There was a significant reduction in tumor mass and a reduction in the size of the vascular organs, including the spleen and liver (**Figure 12B & D**). Quantitative analysis of the weights of the liver and spleen demonstrated a sharp decline accompanied by increased (80%) survival of the treated animals at the highest concentration tested compared with the untreated control (**Figure 12D**).

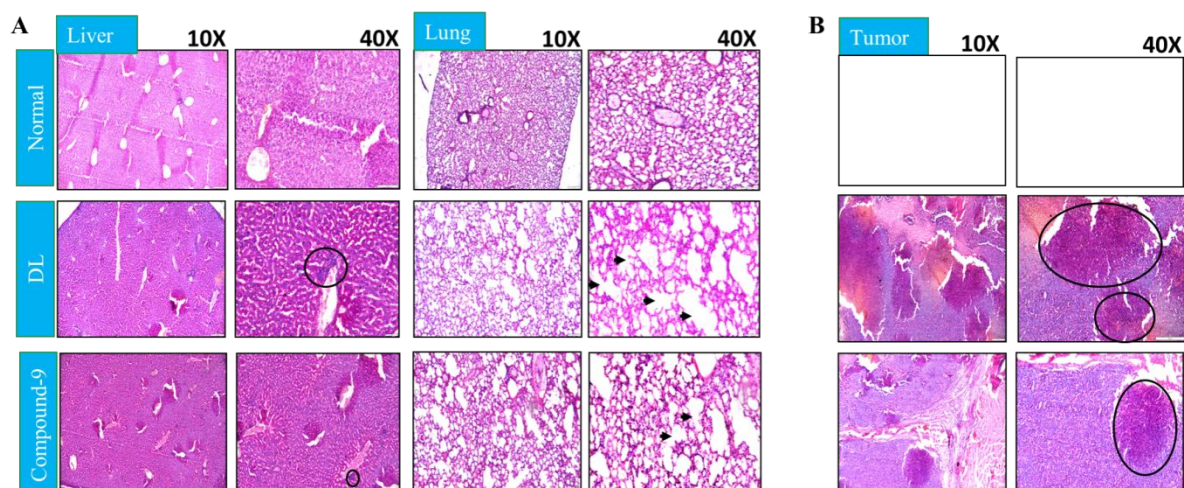


**Figure 12.** (A) Treatment schedule, (B) Phenotypic demonstration of dissected vascularized organs and the tumor growth in the indicated treatment. (C) Weight of dissected tumors in BALB/c mice treated with varying concentrations of compound 9. (D) Weight of the vascularised organs (liver, lung, spleen & kidney) following indicated treatment.



**Figure 13.** Tumoricidal effect of compound 9. (A-D) Tumor volume assessment in untreated and treated groups of individual animals following treatment with various concentrations of compound 9.

Treatment of compound 9 in DL tumor bearing mice also demonstrated a concentration dependent reduction in tumor volume suggesting efficacy of compound 9 in restricting the DL tumor growth developed as solid tumor (**Figure 13A-D**).



**Figure 14.** Histopathological analysis of (A) liver and lung in Normal (naïve control), DL (untreated tumor bearing) and 4-Azide-naphthalimide-artesunate (mice treated with compound 9) and (B) tumor derived from the above treatment condition. Magnification 10X & 40X. Reduction of concentrated tumor growth areas following treatment areas are indicated by black circles and arrows.

Histopathological analysis of highly vascularized organs, including the liver and lung, showed a significant reduction in infiltrated tumor cells following treatment with compound **9** compared with the untreated DL control. Liver architecture in treated animals was restored to a large extent similar to that of normal littermates, which was severely disorganized and disrupted in the untreated DL group due to massive infiltration of tumor cells in hepatic portal areas (**Figure 14A**). Lung histology in the untreated DL group showed massive infiltration of tumor cells in lung alveoli, which was cleared in the treated group and restored to the level of normal architecture (**Figure 14A**). Histopathology of the tumor mass in the untreated DL group showed extensive infestation of the parenchyma (neoplastic cells) and the stroma where the neoplastic cells were induced and in which they were dispersed. The solid pattern contained small tubules, and the hemorrhagic areas featured large, blood-filled spaces lined by tumor cells (**Figure 14B**). This architecture was abolished in the treated group largely as the tumor mass shrank and the extensive neoplastic conditions were reduced to minimal, suggesting the tumoricidal potential of the hybrid drug preparation.

Effector dendritic cells (DCs) generated from mice treated with remodeled hybrid drugs acquired tumoricidal properties against DL and YAC-1 cells. We determined the ex vivo cytotoxicity of these DCs against DL tumor cells. Our results indicate that DCs from compound **9**-treated animals acquired significant cytotoxicity against DL tumor cells within increasing E:T ratios. All other hybrid constructs and artesunate showed intermediate levels

of cytotoxic potential, indicating that the treatment generates a long-term antitumor immune response (**Figure S25A**). Similar results were observed against YAC-1 tumor cells (**Figure S25B**). Effector DC from compound **9** also became efficient for long-term growth inhibition of DL tumor cells with significant inhibition at the highest E:T ratio compared with artesunate alone ( $p < 0.0001$ ) (**Figure S25C**). Similar results were also observed with reference to YAC-1 tumor cells (**Figure S25D**).

## Discussion

All three compounds (**3**, **5** and **9**) differ with respect to the substituent on the naphthalimide moiety and the presence of a linker between ARTN and naphthalimide. Compound **5** contains an amide linker between ARTN and naphthalimide. The linker consists of an amide bond, which is considered stronger than the ester bond. In *in vitro* drug and DNA interactions, the results of different binding constants ( $K_b$ ) indicate that compound **5** has higher values, suggesting stable intercalation properties in comparison to the other two compounds (**3** and **9**). The stable interaction may also demonstrate the stability of the molecules (**5**), which consist of an amide linker between ARTN and 1,8- naphthalimide. In contrast, the results of the *in vitro* cell-based study (growth inhibition assay, cell cytotoxicity and cell viability) indicate superior anticancer effects of compounds **9** and **3** compared to compound **5**, with the order of efficacy being **9**>**3**>**5** (the  $IC_{50}$  value is inversely proportional to anticancer activity, indicating that compounds with higher  $IC_{50}$  values were the least effective compounds). In the cell-based assay, compounds **3** and **9** are comparatively less stable, which may be due to the presence of an ester bond bridge between artesunate and naphthalimide compared to compound **5** (consisting of an amide bond). The cytotoxicity of the hybrid molecules (compounds **3** and **9**) against tumor cells is due to the combined attack of free artesunate and naphthalimide molecules (after degradation in the presence of esterase enzyme), which act simultaneously on tumor cells, resulting in enhanced tumoricidal potential.

Hybrid drug molecules and their tumoricidal efficiency for the development of highly effective conjugate chemistry approaches are a way to improve the quality of drugs and medicines. A number of unique hybrid drugs provide an excellent toolkit for new and efficient biological activity, *e.g.*, anticancer and nonviral gene therapy, and act as templates for bactericidal properties and preventing antibiotic drug resistance. Many hybrids generated by click chemistry are in clinical trials, including conjugated ciprofloxacin to neomycin, tedizolid or trimethoprim. Despite sound progress in the treatment against malignancies, the

development of cancer resistance is an important area of great concern for cancer chemotherapy failure. Multitarget chemotherapy may be achieved using drug combinations, co delivery of drugs, or designing hybrid drugs. A single hybrid compound can modulate multiple targets that play pivotal roles in cancer cell growth, viability, proliferation, and metastasis and may have a simpler and unique pharmacokinetic profile to reduce or prevent the emergence of drug interactions at the interfaces and facilitate the process of drug development. In addition, a single medication may also be expected to enhance patient compliance due to a favorable treatment regimen, as well as fewer adverse reactions, including toxicity, compared to a combination regimen.

The synthesis of hybrid bioactive compounds involving either artesunate or naphthalimide has been attempted in multiple ways. Artemisinin-derived compounds containing a peroxide-decorated sesquiterpene lactone moiety form free radicals with high reactivity and possess diverse pharmaceutical properties, including in vitro and in vivo tumoricidal activity in addition to antimalarial properties. Hybridization of the artemisinin skeleton with other pharmacophores may provide novel anticancer candidates with high specificity and great potency against drug-resistant cancers<sup>26</sup>. Artemisinin and its semi synthetic derivatives are the mainstays of treatment against malaria, and artemisinin-based molecules, especially dimers derived from artemisinin, also exhibit excellent in vitro and in vivo tumoricidal activity. The structure-activity relationship (SAR) showed that the linker between the two artemisinin moieties has a significant role in anticancer activity; thus, the rational design of the linker may provide valuable therapeutic intervention for the treatment of cancer<sup>27</sup>. Artemisinin-derived dimers and dendrimers were developed and investigated for their anti-malarial activities against *Plasmodium falciparum* 3D7. Some dimers (Dimer 7) demonstrated low  $EC_{50}$  1.4 nm) compared to the standard drugs dihydroartemisinin ( $EC_{50}$  2.4 nm), artesunic acid ( $EC_{50}$  8.9 nm) and chloroquine ( $EC_{50}$  9.8 nm)<sup>28</sup>. For breast and prostate cancer treatment, a series of hybrid compounds based on tamoxifen, estrogens, and artemisinin were synthesized and showed tumoricidal activity against human prostate (PC-3) and breast cancer (MCF-7) cells. These studies suggest the high potential of hybridization of artemisinin and estrogens to augment the tumoricidal activities, demonstrating synergistic effects between the linked pharmacophores<sup>29</sup>. Naphthalimide and phenanthro[9, 10-d]imidazole conjugates were made and evaluated for their cytotoxicity and growth inhibition against human cancer cell lines in vitro. Additionally, other naphthalimide derivatives



1  
2  
3 inhibited topoisomerase-induced apoptosis and inhibited human topoisomerase (Topo-II $\alpha$ ) as  
4 a possible intracellular target<sup>30</sup>.  
5  
6

7  
8 The 4-azide naphthalimide-linked artesunate (compound **9**) hybrid, which we generated,  
9 showed a sound tumoricidal effect with respect to diminished viability, cytotoxicity,  
10 apoptosis and long-term growth arrest in human and murine lymphoma cells. The hybrid drug  
11 demonstrated promising and significant tumoricidal functions against established lymphoma-  
12 developed as a solid tumors in a concentration-dependent manner with vastly improved  
13 histopathological conditions compared with the untreated control. Artesunate, an artemisinin  
14 derivative impedes the growth of human breast cancer cell and nasopharyngeal cancer cell  
15 lines by arresting G1 cell cycle kinetics. Artesunate reduce solid tumor growth by inhibition  
16 of angiogenesis, induction of apoptosis and ferroptosis, generating reactive oxygen species  
17 followed by cell-cycle arrest. Naphthalimide acts by multiple mechanisms and target DNA  
18 damage via Topo I/II inhibition, and induce apoptosis, lysosomal membrane  
19 permeabilization, besides affecting Akt/mTOR signal pathway. Compared to artesunate only,  
20 the hybrid drug compound **9** demonstrated synergistic tumoricidal potential in restrict DL cell  
21 growth. The compound **9** hybrid also significantly check the tumor mass growth in the  
22 tumor site with consistent efficiency. In comparison to compound **9**, compounds **4** and **2**  
23 showed less antitumor potential, although significantly higher compared to artesunate alone  
24 or substituted with a naphthalimide linker (ester or amine). Taken together, our results  
25 strongly suggest that compound **9** could be used as a potential drug combination (hybrid)  
26 having synergistic potential and with promise as a novel therapeutic option to treat solid  
27 lymphoma, a common type of malignancy in humans.  
28  
29  
30  
31  
32  
33  
34  
35  
36  
37  
38  
39  
40  
41

## 42 43 Conclusion 44

45  
46 Despite tremendous potential for nanomedicine, reversing or completely stopping cancer  
47 progression and resistance is still one of the greatest challenges to all. Various nanomedicine  
48 approaches have been used using artesunate and naphthalimide for the generation of novel  
49 compounds to target various neoplasias. Our approach of hybridizing artesunate and  
50 naphthalimide for the treatment of lymphoma developed as a solid tumor in a mouse model is  
51 a new aspect in oncology. The hybrid drug not only reduced the IC<sub>50</sub> significantly compared  
52 with either artesunate or naphthalimide but also demonstrated profound tumoricidal  
53 properties, including increased survival, ablation of tumor volume to a minimum and  
54 prevention of metastasis. Overall, the potent hybrid drug exhibits a broad range of  
55  
56  
57  
58  
59  
60

tumoricidal activities interlinked with low toxicity and a high selectivity profile, producing synergistic effects between the linked pharmacophores.

## ASSOCIATED CONTENT

### Supporting Information.

The Supporting Information is available free of charge on the ACS Publications website Supplementary figures **S1–S25** (PDF).

## AUTHOR INFORMATION

### Corresponding Authors

\*(UHS). Email: [uhocju@gmail.com](mailto:uhocju@gmail.com); [ugirhossainsk@cnci.ac.in](mailto:ugirhossainsk@cnci.ac.in)

\*(PPM). E-mail: [pp\\_manna@yahoo.com](mailto:pp_manna@yahoo.com).

### Author Contributions

†D.R.M. and R.S. contributed equally.

Conflict of Interest: Part of the work has been filed for Indian patent (Appl. no. 202231032973).

### Funding Sources

This work was funded by a minor grant from the Institution of Eminence (IoE) by the Ministry of Human Resource and Development, Government of India, (No. R/Dev/D/IOE/Incentive/2021-22/32275) to Partha Pratim Manna by Banaras Hindu University and intramural grant support from Chittaranjan National Cancer Institute. UHS also acknowledges the financial support of CSIR-HRDG, New Delhi (grant number 80(0090)/20/EMR-II).

## ACKNOWLEDGMENT

DRM is thankful to the Indian Council of Medical Research, New Delhi (No. 45/03/2022-DDI/BMS) for senior research fellowship. RS thanks Indian council of medical council research (ICMR), India; No. 2021-12946/CMB-BMS for senior research fellowship. UHS. and DRM. would also like to acknowledge Director CNCI, Kolkata, for providing the necessary facility.

## ABBREVIATIONS



DL, Dalton's lymphoma; ARTN: Artesunate

## Reference

- (1) Kato, S.; Moulder, S. L.; Ueno, N. T.; Wheler, J. J.; Meric-Bernstam, F.; Kurzrock, R.; Janku, F. Challenges and Perspective of Drug Repurposing Strategies in Early Phase Clinical Trials. *Oncoscience***2015**, 2 (6), 576–580. <https://doi.org/10.18632/oncoscience.173>.
- (2) Ashburn, T. T.; Thor, K. B. Drug Repositioning: Identifying and Developing New Uses for Existing Drugs. *Nat Rev Drug Discov***2004**, 3 (8), 673–683. <https://doi.org/10.1038/nrd1468>.
- (3) Kumar, B.; Singh, S.; Skvortsova, I.; Kumar, V. Promising Targets in Anti-Cancer Drug Development: Recent Updates. *Curr Med Chem***2017**, 24 (42), 4729–4752. <https://doi.org/10.2174/0929867324666170331123648>.
- (4) Johnson, L. A.; Malayappan, B.; Tretyakova, N.; Campbell, C.; MacMillan, M. L.; Wagner, J. E.; Jacobson, P. A. Formation of Cyclophosphamide Specific DNA Adducts in Hematological Diseases. *Pediatric blood & cancer***2012**, 58 (5), 708. <https://doi.org/10.1002/pbc.23254>.
- (5) Forstpointner, R.; Dreyling, M.; Repp, R.; Hermann, S.; Hänel, A.; Metzner, B.; Pott, C.; Hartmann, F.; Rothmann, F.; Rohrberg, R.; Böck, H.-P.; Wandt, H.; Unterhalt, M.; Hiddemann, W.; German Low-Grade Lymphoma Study Group. The Addition of Rituximab to a Combination of Fludarabine, Cyclophosphamide, Mitoxantrone (FCM) Significantly Increases the Response Rate and Prolongs Survival as Compared with FCM Alone in Patients with Relapsed and Refractory Follicular and Mantle Cell Lymphomas: Results of a Prospective Randomized Study of the German Low-Grade Lymphoma Study Group. *Blood***2004**, 104 (10), 3064–3071. <https://doi.org/10.1182/blood-2004-04-1323>.
- (6) Mai, Y.; Yu, J. J.; Bartholdy, B.; Xu-Monette, Z. Y.; Knapp, E. E.; Yuan, F.; Chen, H.; Ding, B. B.; Yao, Z.; Das, B.; Zou, Y.; Young, K. H.; Parekh, S.; Ye, B. H. An Oxidative Stress-Based Mechanism of Doxorubicin Cytotoxicity Suggests New Therapeutic Strategies in ABC-DLBCL. *Blood***2016**, 128 (24), 2797–2807. <https://doi.org/10.1182/blood-2016-03-705814>.
- (7) Montecucco, A.; Zanetta, F.; Biamonti, G. Molecular Mechanisms of Etoposide. *EXCLI J***2015**, 14, 95–108. <https://doi.org/10.17179/excli2015-561>.
- (8) Sym, S. J.; Lee, D. H.; Kang, H. J.; Nam, S. H.; Kim, H. Y.; Kim, S. J.; Eom, H. S.; Kim, W. S.; Suh, C. A Multicenter Phase II Trial of Etoposide, Methylprednisolone, High-Dose Cytarabine, and Oxaliplatin for Patients with Primary Refractory/Relapsed Aggressive Non-Hodgkin's Lymphoma. *Cancer Chemother Pharmacol***2009**, 64 (1), 27–33. <https://doi.org/10.1007/s00280-008-0847-y>.
- (9) Wang, L.; Li, L.-R. R-CHOP Resistance in Diffuse Large B-Cell Lymphoma: Biological and Molecular Mechanisms. *Chin Med J (Engl)***2020**, 134 (3), 253–260. <https://doi.org/10.1097/CM9.0000000000001294>.
- (10) Mahadevan, D.; Northfelt, D. W.; Chalasani, P.; Rensvold, D.; Kurtin, S.; Von Hoff, D. D.; Borad, M. J.; Tibes, R. Phase I Trial of UNBS5162, a Novel Naphthalimide in Patients with Advanced Solid Tumors or Lymphoma. *Int J Clin Oncol***2013**, 18 (5), 934–941. <https://doi.org/10.1007/s10147-012-0475-8>.

- (11) Tandon, R.; Luxami, V.; Kaur, H.; Tandon, N.; Paul, K. 1,8-Naphthalimide: A Potent DNA Intercalator and Target for Cancer Therapy. *Chem Rec***2017**, *17* (10), 956–993. <https://doi.org/10.1002/tcr.201600134>.
- (12) Våtsveen, T. K.; Myhre, M. R.; Steen, C. B.; Wälchli, S.; Lingjærde, O. C.; Bai, B.; Dillard, P.; Theodossiou, T. A.; Holien, T.; Sundan, A.; Inderberg, E. M.; Smeland, E. B.; Myklebust, J. H.; Oksvold, M. P. Artesunate Shows Potent Anti-Tumor Activity in B-Cell Lymphoma. *J Hematol Oncol***2018**, *11* (1), 23. <https://doi.org/10.1186/s13045-018-0561-0>.
- (13) Zhao, P.-H.; Ma, S.-T.; Hu, J.-Q.; Zheng, B.-Y.; Ke, M.-R.; Huang, J.-D. Artesunate-Based Multifunctional Nanoplatfor for Photothermal/Photoinduced Thermodynamic Synergistic Anticancer Therapy. *ACS Appl. Bio Mater***2020**, *3* (11), 7876–7885. <https://doi.org/10.1021/acsabm.0c01026>.
- (14) Botta, L.; Filippi, S.; Bizzarri, B. M.; Zippilli, C.; Meschini, R.; Pogni, R.; Baratto, M. C.; Villanova, L.; Saladino, R. Synthesis and Evaluation of Artemisinin-Based Hybrid and Dimer Derivatives as Antimelanoma Agents. *ACS Omega***2020**, *5* (1), 243–251. <https://doi.org/10.1021/acsomega.9b02600>.
- (15) Fröhlich, T.; Kiss, A.; Wölfling, J.; Mernyák, E.; Kulmány, Á. E.; Minorics, R.; Zupkó, I.; Leidenberger, M.; Friedrich, O.; Kappes, B.; Hahn, F.; Marschall, M.; Schneider, G.; Tsogoeva, S. B. Synthesis of Artemisinin–Estrogen Hybrids Highly Active against HCMV, P. Falciparum, and Cervical and Breast Cancer. *ACS Med. Chem. Lett***2018**, *9* (11), 1128–1133. <https://doi.org/10.1021/acsmmedchemlett.8b00381>.
- (16) Fröhlich, T.; Reiter, C.; Saeed, M. E. M.; Hutterer, C.; Hahn, F.; Leidenberger, M.; Friedrich, O.; Kappes, B.; Marschall, M.; Efferth, T.; Tsogoeva, S. B. Synthesis of Thymoquinone–Artemisinin Hybrids: New Potent Antileukemia, Antiviral, and Antimalarial Agents. *ACS Med. Chem. Lett***2018**, *9* (6), 534–539. <https://doi.org/10.1021/acsmmedchemlett.7b00412>.
- (17) Wang, X.; Chen, Z.; Tong, L.; Tan, S.; Zhou, W.; Peng, T.; Han, K.; Ding, J.; Xie, H.; Xu, Y. Naphthalimides Exhibit in Vitro Antiproliferative and Antiangiogenic Activities by Inhibiting Both Topoisomerase II (Topo II) and Receptor Tyrosine Kinases (RTKs). *Eur J Med Chem***2013**, *65*, 477–486. <https://doi.org/10.1016/j.ejmech.2013.05.002>.
- (18) Rani, S.; Luxami, V.; Paul, K. Synthesis of Triphenylethylene-Naphthalimide Conjugates as Topoisomerase-II $\alpha$  Inhibitor and HSA Binder. *ChemMedChem***2021**, *16* (11), 1822–1832. <https://doi.org/10.1002/cmdc.202100034>.
- (19) Sk, U. H.; Hira, S. K.; Rej, A.; RoyMahapatra, D.; Manna, P. P. Development of a PAMAM Dendrimer for Sustained Release of Temozolomide against Experimental Murine Lymphoma: Assessment of Therapeutic Efficacy. *ACS Appl. Bio Mater***2021**, *4* (3), 2628–2638. <https://doi.org/10.1021/acsabm.0c01599>.
- (20) Hira, S. K.; Mishra, A. K.; Ray, B.; Manna, P. P. Targeted Delivery of Doxorubicin-Loaded Poly ( $\epsilon$ -Caprolactone)-b-Poly (N-Vinylpyrrolidone) Micelles Enhances Antitumor Effect in Lymphoma. *PLOS ONE***2014**, *9* (4), e94309. <https://doi.org/10.1371/journal.pone.0094309>.
- (21) Zeng, Q.; Han, Y.; Li, H.; Chang, J. Design of a Thermosensitive Bioglass/Agarose–Alginate Composite Hydrogel for Chronic Wound Healing. *J. Mater. Chem. B***2015**, *3* (45), 8856–8864. <https://doi.org/10.1039/C5TB01758K>.
- (22) Hira, S. K.; Ramesh, K.; Gupta, U.; Mitra, K.; Misra, N.; Ray, B.; Manna, P. P. Methotrexate-Loaded Four-Arm Star Amphiphilic Block Copolymer Elicits CD8<sup>+</sup> T Cell Response against a Highly Aggressive and Metastatic Experimental Lymphoma. *ACS*

- Appl. Mater. Interfaces***2015**, 7 (36), 20021–20033.  
<https://doi.org/10.1021/acsami.5b04905>.
- (23) Hira, S. K.; Rej, A.; Paladhi, A.; Singh, R.; Saha, J.; Mondal, I.; Bhattacharyya, S.; Manna, P. P. Galunisertib Drives Treg Fragility and Promotes Dendritic Cell-Mediated Immunity against Experimental Lymphoma. *iScience***2020**, 23 (10), 101623.  
<https://doi.org/10.1016/j.isci.2020.101623>.
- (24) Singh, R.; Gupta, U.; Srivastava, P.; Paladhi, A.; Sk, U. H.; Hira, S. K.; Manna, P. P.  $\Gamma$ c Cytokine-Aided Crosstalk between Dendritic Cells and Natural Killer Cells Together with Doxorubicin Induces a Healer Response in Experimental Lymphoma by Downregulating FOXP3 and Programmed Cell Death Protein 1. *Cytotherapy***2022**, 24 (12), 1232–1244.  
<https://doi.org/10.1016/j.jcyt.2022.07.012>.
- (25) Hira, S. K.; Mondal, I.; Bhattacharya, D.; Manna, P. P. Downregulation of Endogenous STAT3 Augments Tumoricidal Activity of Interleukin 15 Activated Dendritic Cell against Lymphoma and Leukemia via TRAIL. *Exp Cell Res***2014**, 327 (2), 192–208.  
<https://doi.org/10.1016/j.yexcr.2014.08.012>.
- (26) Gao, F.; Sun, Z.; Kong, F.; Xiao, J. Artemisinin-Derived Hybrids and Their Anticancer Activity. *Eur J Med Chem***2020**, 188, 112044.  
<https://doi.org/10.1016/j.ejmech.2020.112044>.
- (27) Zhang, B. Artemisinin-Derived Dimers as Potential Anticancer Agents: Current Developments, Action Mechanisms, and Structure–Activity Relationships. *Archiv der Pharmazie***2020**, 353 (2), 1900240. <https://doi.org/10.1002/ardp.201900240>.
- (28) Fröhlich, T.; Hahn, F.; Belmudes, L.; Leidenberger, M.; Friedrich, O.; Kappes, B.; Couté, Y.; Marschall, M.; Tsogoeva, S. B. Synthesis of Artemisinin-Derived Dimers, Trimers and Dendrimers: Investigation of Their Antimalarial and Antiviral Activities Including Putative Mechanisms of Action. *Chemistry – A European Journal***2018**, 24 (32), 8103–8113. <https://doi.org/10.1002/chem.201800729>.
- (29) Fröhlich, T.; Mai, C.; Bogautdinov, R. P.; Morozkina, S. N.; Shavva, A. G.; Friedrich, O.; Gilbert, D. F.; Tsogoeva, S. B. Synthesis of Tamoxifen-Artemisinin and Estrogen-Artemisinin Hybrids Highly Potent Against Breast and Prostate Cancer. *ChemMedChem***2020**, 15 (15), 1473–1479. <https://doi.org/10.1002/cmdc.202000174>.
- (30) Singh, I.; Luxami, V.; Paul, K. Synthesis of Naphthalimide-Phenanthro[9,10-d]Imidazole Derivatives: In Vitro Evaluation, Binding Interaction with DNA and Topoisomerase Inhibition. *Bioorganic Chemistry***2020**, 96, 103631.  
<https://doi.org/10.1016/j.bioorg.2020.103631>.

# Development of a PAMAM Dendrimer for Sustained Release of Temozolomide against Experimental Murine Lymphoma: Assessment of Therapeutic Efficacy

Ugir Hossain Sk,\* Sumit Kumar Hira, Abhinandan Rej, Debapriya RoyMahapatra, and Partha Pratim Manna\*



Cite This: *ACS Appl. Bio Mater.* 2021, 4, 2628–2638



Read Online

ACCESS |



Metrics & More



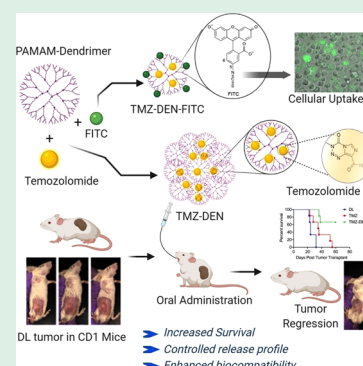
Article Recommendations



Supporting Information

**ABSTRACT:** Enhanced drug localization at the tumor sites with minimal toxicity was demonstrated using dendrimer-conjugated temozolomide for treating experimental lymphoma, developed as a solid tumor. Herein, we have constructed a polyamidoamine (PAMAM) dendrimer conjugated with temozolomide to enhance the stability of the active drug metabolites, derived from the prodrug temozolomide. Our results suggest that the active drug (5-(3-methyltriazene-1-yl)imidazole-4-carboxamide) (MTIC) (derived from temozolomide) showed stable and sustained release from the dendrimer–temozolomide conjugate, suggesting the suitability of the construct for therapy. Besides growth inhibition and direct killing, the dendrimer–temozolomide construct induced extensive apoptosis not only in parental Dalton lymphoma tumor cells but also in the doxorubicin-resistant form of the tumor cells. Dendrimer–temozolomide conjugation significantly reduced the solid tumor growth and increased the lifespan with better prognosis, including improved histopathology of the treated mice, while untreated littermates developed extensive metastasis and succumbed to death.

**KEYWORDS:** temozolomide, LC–MS, sustained drug release, MTIC stability, Dalton's lymphoma, tumoricidal activity



## INTRODUCTION

In advanced research, nanosized polymeric scaffolds are increasingly used in modern applications, ranging from diagnostics to therapeutics in health services.<sup>1</sup> Globular-shaped and treelike branched polymeric nanosized dendrimers have been investigated for a range of biomedical applications,<sup>2,3</sup> including drug<sup>3</sup> and gene delivery.<sup>4</sup> The commercially available polyamidoamine (PAMAM) or poly(amidoamine) dendrimers (DENS) are widely used in drug delivery applications because of their biocompatibility and low toxicity and are effective in solubilized lipophilic drugs in the aqueous media.<sup>5</sup> A toxicity study of PAMAM dendrimers with free terminal hydroxyl groups showed that the compounds are tolerant to cells up to 500 mg/kg and do not cause significant physiological impairment and remain noncytotoxic.<sup>2</sup> There have been reports where dendrimer surfaces were conjugated covalently with the drug molecules, targeting the ligand and imaging probe.<sup>6</sup> The PAMAM dendrimers (hydroxyl-terminated) are also proven to be nontoxic and have low immunogenicity.<sup>7</sup> It has been reported that generation-four PAMAM dendrimers with hydroxyl-terminated groups could cross the blood–brain barrier (BBB) in the animal model and selectively target activated microglia/macrophages in the brain without the attached targeting ligand.<sup>2,8</sup> PAMAM dendrimers with attached doxorubicin (DOX) demonstrated enhanced cytotoxicity against ovarian adenocarcinoma cells of human origin and

against DOX-sensitive and -resistant SKOV3 and SKVLB cells, respectively.<sup>9</sup> Our previous study demonstrated that the dendrimer-tagged estramustine and podophyllotoxin cause sustained release of the drugs and exhibit robust antitumor activity against carcinogen-induced skin cancer.<sup>6,10</sup> The uptake of the fluorescently labeled dendrimer in Caco-2 cells indicated the transport of the PAMAM dendrimer into the cytoplasm within 5 min of its exposure, while it takes 35 min to reach the nucleus.<sup>11</sup> The treatment of antisense oligo DNA–PAMAM dendrimer complexes in mice bearing human ovarian tumors exhibits a high accumulation of oligo complexes in the tumor microenvironment.<sup>12</sup> Similarly, intratumoral injection of the PAMAM-dendrimer-formulated angiostatin gene delivery inhibited tumor cell growth and reduced tumor-associated vascularization.<sup>13</sup>

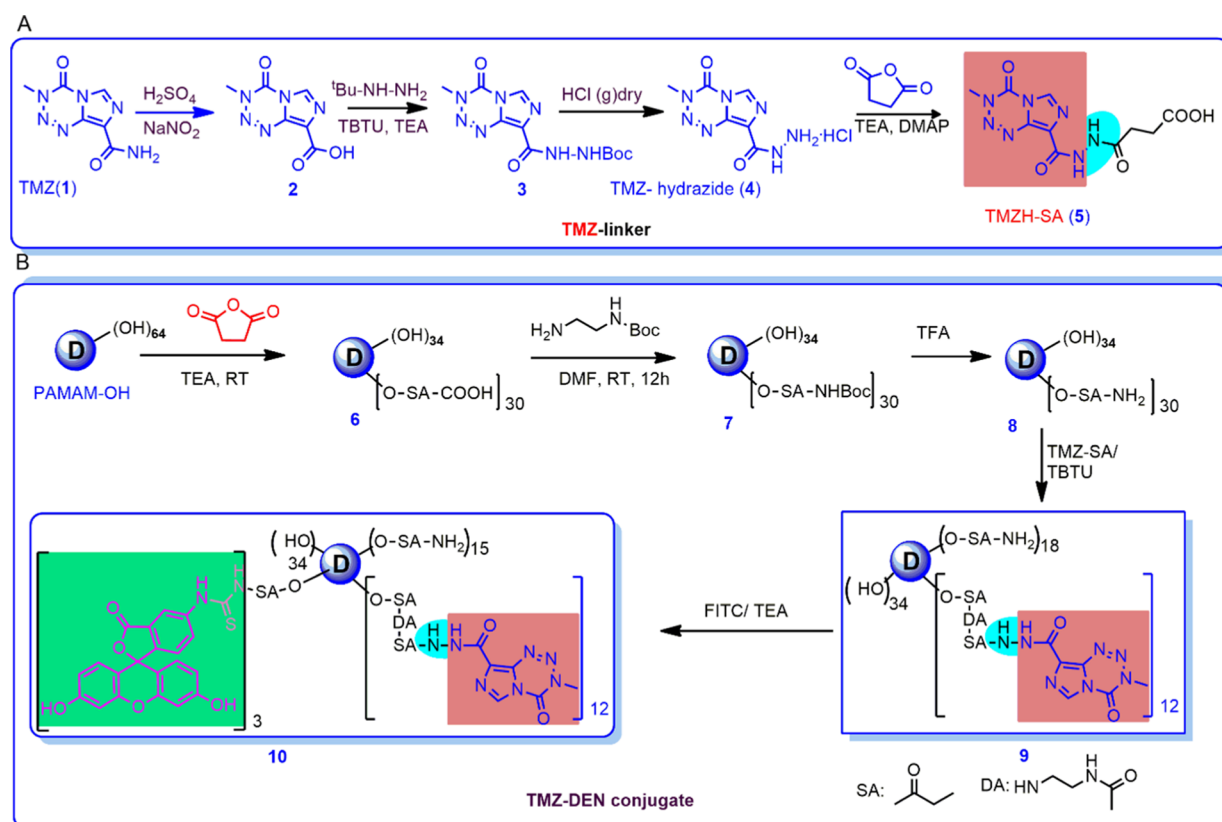
Temozolomide (TMZ) demonstrated broad-spectrum anti-tumor activity against recurrent glioblastoma multiforme, recurrent anaplastic astrocytoma, advanced malignant melanoma, and pediatric solid tumors.<sup>14</sup> It is recommended as a first-

**Received:** December 10, 2020

**Accepted:** February 23, 2021

**Published:** March 4, 2021





**Figure 1.** Temozolomide conjugate synthesis. (A) Synthesis of the temozolomide linker (TMZ-SA), (B) synthesis of the dendrimer-conjugated temozolomide (TMZ-DEN) (compound 9), and the dendrimer-attached FITC-TMZ (TMZ-DEN-FITC) (compound 10).

line chemotherapeutic for treating glioblastoma in the United States.<sup>15</sup> TMZ is a lipophilic prodrug and is an acid-stable DNA methylating agent, and it is capable of crossing the BBB upon oral administration.<sup>16</sup> TMZ hydrolyzes at physiological pH, liberating the active methyltriazeniumcations [via formation of the active hydrolyzed product (5-(3-methyltriazen-1-yl)imidazole-4-carboxamide (MTIC))] that exert antitumor activity via methylation of guanine and adenine nucleobases and is also simultaneously deactivated by the formation of 5-aminoimidazole-4-carboxamide (AIC).<sup>17</sup> Therefore, rapid in vivo clearance of TMZ needs repeated doses to achieve effective antitumor activity.<sup>18</sup> For a successful and viable drug delivery system, slower TMZ degradation kinetics is critically important.<sup>19</sup> Covalent conjugation of poly(2-methacryloyloxyethyl phosphorylcholine) with TMZ enhanced the stability of TMZ twofold and facilitated the extension of its half-life.<sup>20</sup> Besides that, chitosan-based nanoparticles for the delivery of TMZ in the glioblastoma showed a sevenfold improvement in its stability with a 2–6-fold higher cellular uptake in glioblastoma cells compared with the free drug.<sup>21</sup>

Herein, our objective is to conjugate TMZ with the PAMAM dendrimer via a hydrazide bond to stabilize the active part of the TMZ (MTIC) and maintain this activity for longer periods of time in the tumor microenvironment to enable tumoricidal activity against solid tumors like lymphoma. Our results suggest that the formed nanoconstruct has significant tumoricidal effects (reduced cell viability, growth inhibition, and direct cytotoxicity) compared with the free TMZ against parental Dalton's lymphoma (DL) cells in a concentration-dependent manner. In addition to that, the as-formed nanoconstruct (TMZ-DEN) is also tumoricidal

against DL tumor cells, refractory to doxorubicin (DOX) (DLR), suggesting the efficiency of the construct to overcome doxorubicin resistance. Therapy with TMZ-DEN significantly minimizes the tumor growth and reduces the extent of metastasis in vascular organs like the liver, lung, and spleen. Untreated DL solid tumors grow exponentially and uncontrollably, leading to extensive metastasis and death of the animals.

## MATERIALS AND METHODS

**Materials.** Details of reagents and all of the fine chemicals are given in the Supporting Information [Materials and Methods](#) section.

**Syntheses of Compounds 2–10.** The intermediates 2–4 were synthesized using a previously published procedure.<sup>22</sup> The detailed experimental data are presented in the [Supporting Information](#) section.

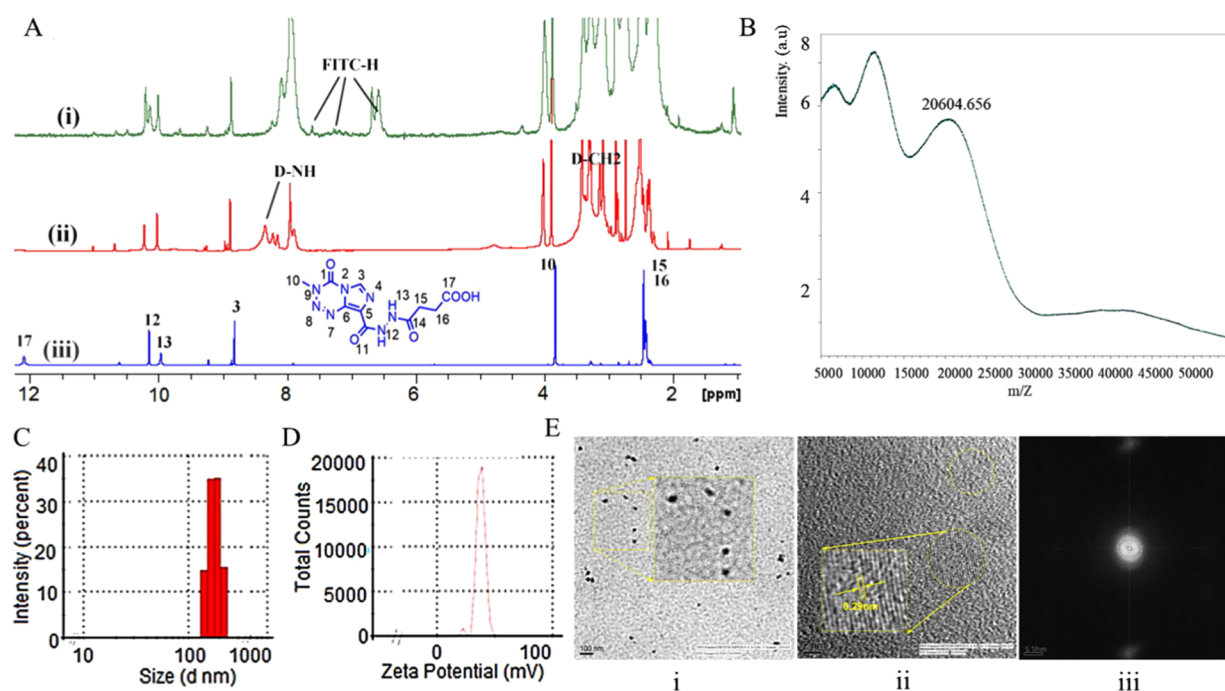
**Synthesis of the Temozolomide Linker.** Details are given in the Supporting Information [Materials and Methods](#) section.

**Dendrimer-Conjugated TMZ.** Details are given in the Supporting Information [Materials and Methods](#) section.

**Ultraperformance Liquid Chromatography (UPLC) Analysis.** Details are given in the Supporting Information [Materials and Methods](#) section.

**In Vitro Drug Release Study.** TMZ release was monitored in 0.1 M phosphate buffer (pH 7.4) at 37 °C. A concentration of (2 mg/mL) of the conjugate and 1 mg/mL TMZ-SA were maintained in a water bath with constant mixing at 37 °C, and at appropriate time points, 500  $\mu\text{L}$  of the samples was withdrawn from the incubation mixture and directly analyzed by liquid chromatography–mass spectrometry (LC–MS). The LC–MS/MS system was made up of a Waters-make Quattro micro API 4000 mass spectrometer equipped with a multimodal ionization (ESI) source system, attached with a binary solvent system, an autosampler, and a PDA detector. Peak separation was on a BEH C18 1.7  $\mu\text{m}$  column (2.1  $\times$  100 mm) eluting





**Figure 2.** Characterization of the dendrimer-conjugated temozolomide (TMZ-DEN). (A) Comparison of the <sup>1</sup>H proton NMR spectrum of the (i) TMZ-DEN covalent conjugation with FITC (top), (ii) temozolomide dendrimer conjugate (TMZ-DEN) (middle), and (iii) temozolomide linker (TMZ-SA) in DMSO-*d*<sub>6</sub>. (B) MALDI-TOF mass spectra of the TMZ-DEN showing increased molecular weight and were compared with the bifunctional dendrimer's molecular weight (compound 8, Figure S8B). The MALDI-TOF spectrum is available in the Supporting Information, which shows the 12 molecules of TMZ attachment in TMZ-DEN. (C) Particle size distribution. (D) ζ-Potential of the conjugate TMZ-DEN. (E) TEM pictures of the conjugate TMZ-DEN indicating (i) the size of the particles of around 7–9 nm, (ii) crystalline fringes of the nanoparticles, and (iii) crystalline characteristics being supported by the SAED pattern.

with a mobile phase system, which consisted of water and acetonitrile (95:5, v/v) at 0 min, containing 0.5 mmol ammonium formate as a modifier. A gradient flow was used with the initial condition 95:5, at 3 min to 95:5, and 50:50 (H<sub>2</sub>O/ACN) in 4 min and returning to 95:5 (H<sub>2</sub>O/ACN) in 6 min with a flow rate of 0.3 mL/min. The sample injection volume was 1.0 μL, and the column temperature was maintained at 20 °C.

**Mice.** Female CD-1 [CrI:CD-1(ICR)] mice were used in the study. Details are provided in the Supporting Information section.

**Cell Lines and the DL Solid Tumor Model in CD-1 Mice.** Details are given in the Supporting Information Materials and Methods section.

**Cell Viability, Growth Inhibition, and Cytotoxicity Assay.** Tumoricidal effects of TMZ-DEN or free TMZ against DL or doxorubicin-resistant DL cells and the other cell lines were assessed by cell viability and growth inhibition for short-term and long-term analyses. Direct cytotoxicity measurements demonstrated the cancer inhibitory potential of the construct.<sup>23</sup> Details on the methodology are presented in the Supporting Information Materials and Methods section.

**Apoptosis and Cellular Uptake Assay.** Evaluation of apoptotic cell death in parental and doxorubicin-resistant DL cells was made following treatment with free TMZ or TMZ-DEN for 12 h. Temporal uptake of TMZ in DL and DLR cells was assessed following treatment of the cells with fluorescein isothiocyanate (FITC)-tagged TMZ-DEN.<sup>24</sup> Details are presented in the Supporting Information Materials and Methods section.

**Hemolysis Assay.** RBC hemolysis in the presence of a free drug or a TMZ-DEN construct was performed according to the method described earlier.<sup>24</sup> Details are given in the Supporting Information Section.

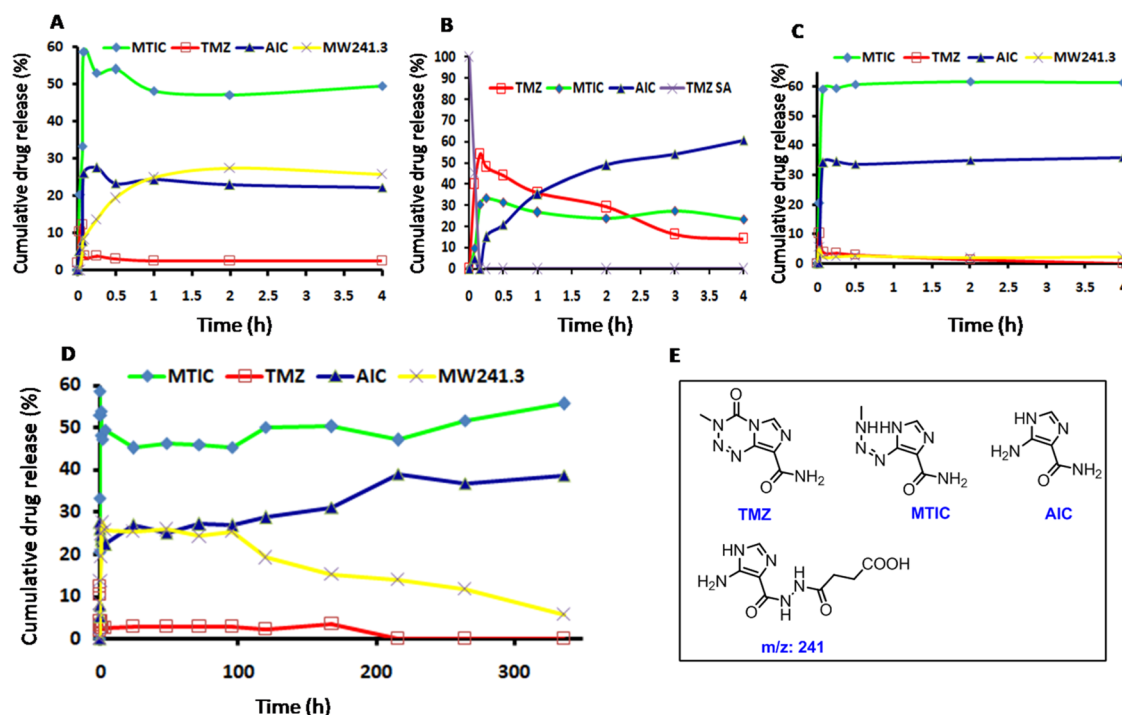
**Therapeutic Strategy, Histopathology, and Immunohistochemistry.** Development of the solid tumor and the therapeutic schedule was modeled on the basis of our earlier studies.<sup>25</sup> Tissue specimens were fixed in 10% neutral buffered formalin overnight, cut

into 5 μm thick sections, and stained with hematoxylin/eosin (H&E) or anti-Ki-67 as described earlier.

## RESULTS

**Synthesis of Dendrimer-Conjugated Temozolomide and Characterizations (9 and 10).** To develop effective chemotherapeutics against cancer, sustained release of the drug is a key factor, which may decide the outcome of the disease. We conjugated TMZ to the nanosized PAMAM dendrimer in multistep reaction pathways as presented in Figure 1. Initially, development of the TMZ linker (TMZ-SA) was made and most of the reactions followed the methods described earlier with little modification (Figure 1A). The formed nano-construct was characterized through <sup>1</sup>H NMR, <sup>13</sup>C NMR, and electronic metal-support interaction (EMSI), and the purity was confirmed by ultraperformance liquid chromatography–liquid chromatography–mass spectrometry (UPLC-LCMS) (Figure S1). In the second stage, the hydroxyl-terminated PAMAM dendrimer was modified to a partially amine-terminated dendrimer through a multistep process followed by TMZ conjugation. Finally, to validate cellular bioavailability, FITC was conjugated to form TMZ-DEN-FITC, and thus a multifunctional fluorescent probe was made (Figure 1B).

TMZ does not contain functional groups available for conjugation with the dendrimer; therefore, TMZ required modification on the side chain without compromising structural changes so that free TMZ can be released from the TMZ-DEN conjugate. The TMZ linker (TMZ-SA) was synthesized via a multistep synthesis process. First, TMZ was hydrolyzed by NaNO<sub>2</sub> in the presence of H<sub>2</sub>SO<sub>4</sub> to obtain a carboxylic acid derivative and it was characterized (Figure

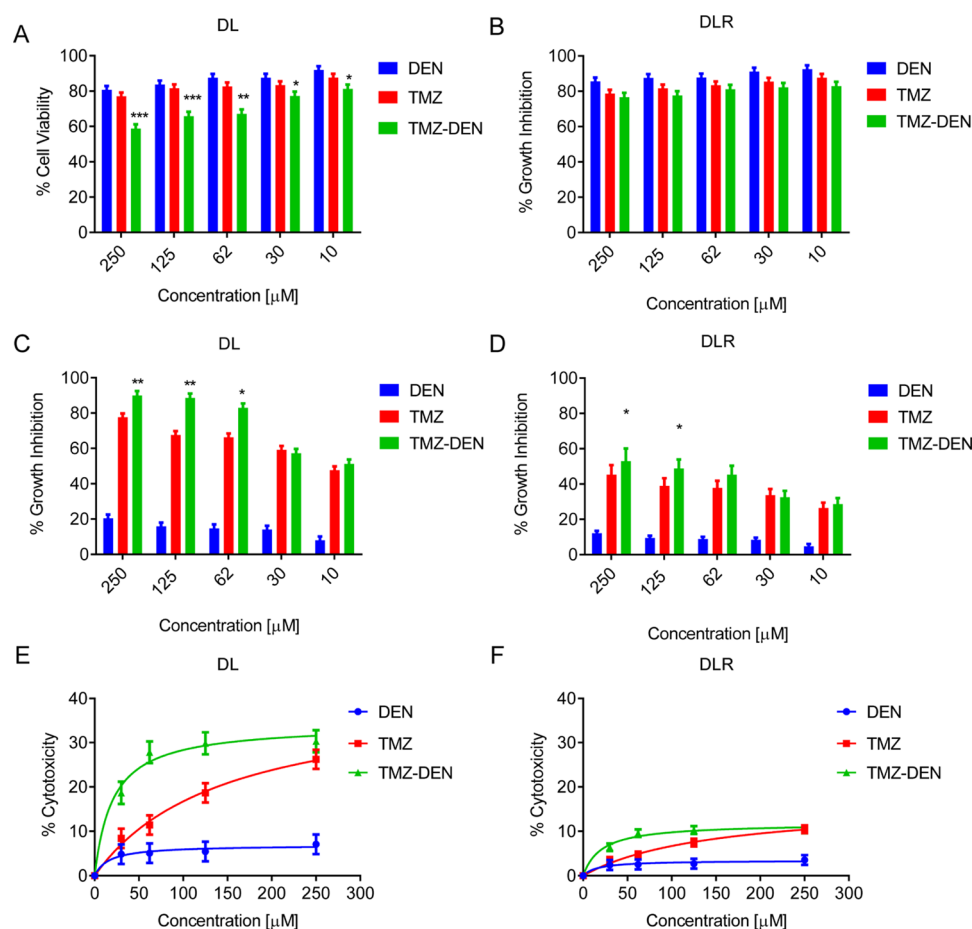


**Figure 3.** Controlled release profile of the TMZ degradation product from the TMZ-DEN conjugate, monitored by LC-MS. (A) Release profiles of TMZ metabolites from the TMZ-DEN conjugate in PBS buffer (pH 7.0) and showing the representative percentages of the four metabolites (MTIC, AIC, TMZ, and *m/z* 241). The graph indicates a decreased concentration of TMZ followed by an increased concentration of MTIC, active metabolites of the TMZ, until 4 h. (B) In vitro degradation of TMZ-SA in PBS (pH 7.0), which indicates the decreased TMZ concentration with time and continuous formation of the inactive metabolite AIC in 4 h. (C) Release of TMZ from TMZ-DEN in citrate buffer (pH 5.4), indicating the higher stability of MTIC with time. (D) Release study of TMZ-DEN in PBS buffer (pH 7.0) for 14 days, reflecting the all-time high percentage of MTIC compared to inactive metabolites AIC. (E) Structures of the metabolites detected during the release study.

S2A-C) (compound 2).<sup>15</sup> Further, compound 2 was converted to compound 3 by reacting *t*-butoxycarbonylhydrazide in the presence of TBTU as a coupling agent, appearing as a Boc-group in NMR at  $\delta$  1.47, and electron ionization mass spectra (EIMS)-mass confirmed the formation of the product (Figure S3A-C).<sup>23</sup> Compound 3 was deprotected with HCl (g) in 1,4-dioxane solvents, which gave TMZ-hydrazide (compound 4) as a solid product after precipitation, and this was further purified with anhydrous acetone, collected through filtration, and dried in a vacuum pump (Figure S4A-D).<sup>23</sup> The TMZ-hydrazide was acylated following treatment with succinic anhydride to yield TMZ-hydrazide-linked succinic acid (compound 5). The structure was characterized through NMR (<sup>1</sup>H and <sup>13</sup>C), DEPT, and EIMS, and the purity was checked by UPLC-LCMS analysis (Figures S1 and S5A-D). Compound 5 was confirmed in NMR by obtaining an additional peak (from TMZ) that appeared corresponding to the linker peak at  $\delta$ 2.49–2.46 ppm and in <sup>13</sup>C at 29.29 and 28.62 ppm corresponding to the methylene protons. The TMZ-SA was conjugated with a multifunctional PAMAM dendrimer.

The hydroxyl-terminated dendrimer was modified partially to amine termini with the multistep process presented in Figure 1B. First, PAMAM-OH was reacted with succinic acid in a basic condition to obtain 30 molecules of the acylated product of the dendrimer, as confirmed by NMR (Figure S6A) and matrix-assisted laser desorption/ionization (MALDI) (Figure S6B). This was further reacted with *N*-(*tert*-butoxycarbonyl)-1,2-diaminoethane using a coupling reagent to obtain compound 7 (Figure S7A,B), followed by Boc-de-

protection leading to the precursor molecules of the multifunctional PAMAM dendrimer (Figure 1B). The precursor was purified through dialysis and characterized by <sup>1</sup>H NMR (Figure S8A) and matrix-assisted laser desorption/ionization-time of flight (MALDI-TOF) (Figure S8B) spectroscopies, which indicated an average of 30 molecules of the primary amine available on the multifunctional PAMAM dendrimer (compound 8). The precursor molecules were conjugated with TMZ-SA using TBTU as a coupling agent in a 24 h reaction at room temperature (RT) to yield the dendrimer-conjugated TMZ, the desired product (compound 9). In the final product, the dendrimer was covalently conjugated with TMZ-SA via an amide bond. This hydrazide bond can be cleaved at physiological conditions in the presence of intracellular pH 5.4 (cancer cells' intracellular-level lysosomal pH). The linker between TMZ and the dendrimer was designed in such a way that the TMZ will be released by the cleaving of the HN-NH bond and generate the TMZ drug without structural alteration (Figure 1). Herein, 12 molecules of TMZ-SA were attached to the dendrimer surface via a linker and were stable in the pure form, as confirmed through UPLC analysis (Figure 1) and NMR and MALDI-TOF spectra (Figure S9A,B). The TMZ attachment to the PAMAM dendrimer was confirmed by NMR and MALDI-TOF analyses (Figure 2). The <sup>1</sup>H NMR spectra in Figure 2A show three NMR spectra and their comparison to identify and better characterize the peaks of the TMZ or FITC molecules within the conjugates (compound 9 or 10). The presence of the peak at  $\delta$ 10.18, 8.85, and 3.86 on the conjugates confirmed the formation of the PAMAM dendrimer, conjugated with TMZ-SA, and simultaneously,



**Figure 4.** Tumorcidal activity of TMZ–DEN against DL and DLR cells. Cell viability of (A) DL and (B) DLR cells as determined by the short-term XTT assay. Forty-eight hours growth inhibition of (C) DL and (D) DLR cells as assessed by the MTT assay. Determination of cytotoxicity in (E) DL and (F) DLR cells as measured by the 18 h LDH release assay using a commercially available kit. All of the determination in each experiment was made in triplicate. Data are presented as mean  $\pm$  standard deviation (SD) of one experiment of a minimum three independent experiments performed.

the disappearance of the peak at 12.12 ppm further supported the formation of the TMZ–DEN conjugate. The NMR data indicates that 12 TMZ–SA molecules attached to the PAMAM dendrimer via a covalent bond. The MALDI–TOF further confirmed the number of TMZ molecules conjugated in the TMZ–DEN conjugate (Figure 2B). The TMZ–DEN conjugate was further conjugated with FITC to allow the fluorescent probe (compound 10) to assess the cellular entry. In the FITC conjugate dendrimer, three molecules of FITC attachment were confirmed through NMR (Figures 2A and S10A) and MALDI–TOF (Figure S10B) characterizations, showing the characteristic peak at  $\delta$ 7.61, 7.3, 6.69, and 6.57, indicating the presence of FITC conjugation in the TMZ–DEN conjugates (Figure 2A). The formation of the amide bond between the dendrimer and the drug cleaves through hydrolysis or by enzymes, triggering the release of TMZ from TMZ–DEN. Dynamic light scattering (DLS) analysis indicates that the hydrodynamic diameter of TMZ–DEN was  $239 \pm 33.9$  nm and the  $\zeta$ -potential was  $37.6 \pm 3.3$  mV (Figure 2C,D). The positive  $\zeta$ -potential was due to the presence of an amide and a free amine group on the drug as well as on the dendrimer carrier. The DLS data provide the hydration sphere diameter, while transmission electron microscopy (TEM) shows the true particle size measurement. Therefore, the DLS data on the particle size was larger compared with the TEM-generated size.

The TMZ–DEN conjugate contains surface positive charge due to the presence of the amine functional group and TMZ contained nitrogen. Further, the positive surface charges assisted in aggregation in the aqueous solution, which resulted in larger particle sizes in the DLS experimental result. The morphological changes in the TMZ–DEN conjugate were studied by TEM, indicating that the size of the particles was around 7–9 nm with crystalline fringes, and the crystalline nature was further supported by the selected area electron diffraction (SAED) pattern (Figure 2E).

**Drug Release Study from Dendrimer Conjugates: Stability of the Active Metabolite MTIC.** At physiological pH, TMZ degraded into different parts; among them, MTIC is effective for alkylation and AIC is an inactive metabolite. The literature indicate slow stability of the TMZ, and its reported half-life is 1.5 h.<sup>22</sup> In our study, we focused on the stability of the active metabolite MTIC, derived from the prodrug TMZ, which generates methyl diazonium ions that mainly take part in DNA alkylation. The controlled release profiles of the TMZ–DEN conjugate were performed by liquid chromatography–mass spectroscopy (LC–MS). Release profiles of the different degraded molecules were monitored based on the molecular weight and their relative intensity in % of the mass  $m/z$ : 146 (AIC +  $\text{NH}_4$ ), 168 (MTIC), 194 (TMZ), 332 (TMZ–SA + Na), and  $m/z$  241 (possible structures are



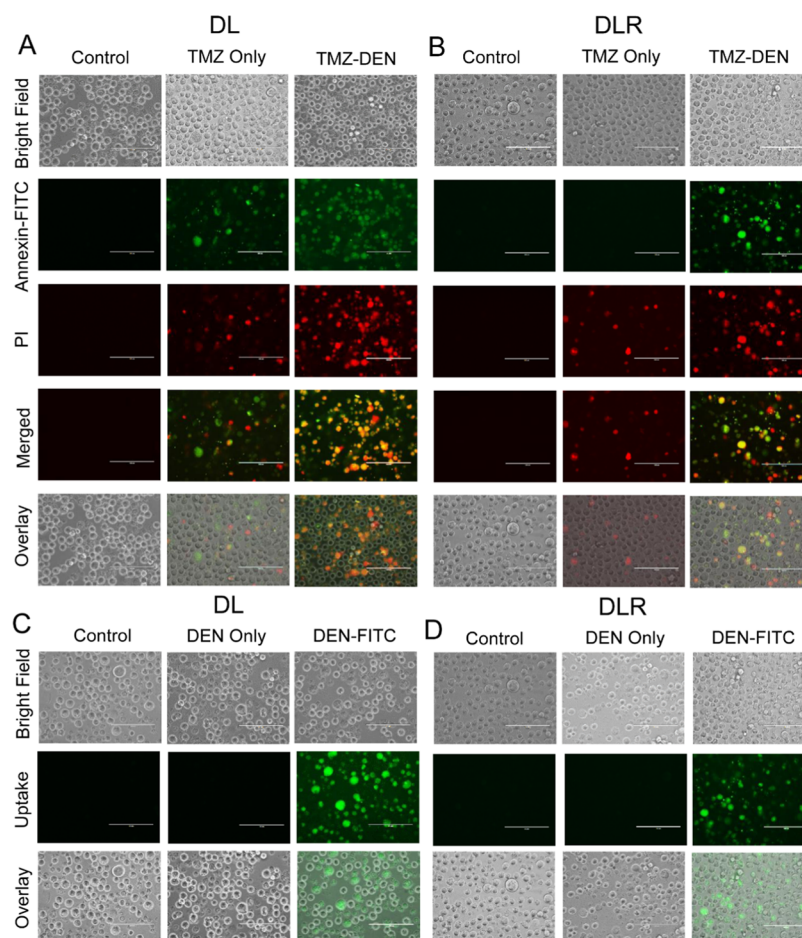
presented in Figure 3E) from the TMZ–DEN conjugate in phosphate-buffered saline (PBS) buffer (pH 7.0) and citrate buffer (pH 5.4) (Figure 3). The stability and degradation of free TMZ and from the conjugate (TMZ-SA) were studied in PBS (pH 7.0) and citrate buffer (pH 5.4) for 4 h (Figure 3A–C). The degradation pattern of the free drug TMZ (TMZ-SA, drug attached with a linker) in Figure 3B shows that the free drug (TMZ) degrades sharply to nearly 15% within the first 4 h. This was accompanied by a sharp increase of inactive metabolites like AIC and with 20% of the active component (MTIC) during the first 4 h. The production of the deactivated product AIC continuously increases with time at the cost of MTIC. Drug release from the TMZ–DEN conjugate in the PBS buffer is a little faster compared to that from the citrate buffer. Figure 3 indicates that the release of the drug from the conjugate was sustained and showed interchange among different metabolites, which were time-dependent in both buffer systems. The initial drug release of TMZ from the TMZ–DEN conjugate and simultaneous degradation to a component like MTIC with parts of AIC were noted. The active metabolite MTIC concentration increased with time and was stable in both of these release conditions (pH 7.0 and 5.4). However, slightly more % of MTIC has been reported in citrate buffer compared to PBS. The drug release from the conjugate in PBS showed a higher concentration of molecular weight (241.3), and this was generated because of the amide-bond (drug linker and dendrimer) cleavage compared to the hydrazide bond (where TMZ directly attached with the linker). The citrate buffer assisting the hydrazide-bond cleavage was faster, leading to a negligible amount of  $m/z$  241.3 formations and helping the formation of active MTIC (resisting the formation of AIC). The present data indicates that the dendrimer–TMZ conjugate was stable in both PBS and citrate buffer, and the drug release from the TMZ–DEN conjugate was a sustained and continuous event. The active metabolized MTIC released from the TMZ–DEN conjugate was stable in comparison to the unconjugated drug (Figure 3B); moreover, the MTIC concentration was higher in the citrate buffer during the 4 h release period. In the PBS buffer, the TMZ (around 12%) existed in the initial stage of the release, and the TMZ concentration remained at 5% up to 9 days (Figure 3D), whereas in the citrate buffer, the initial TMZ release was 10%, which went below 5% at the end of the 24 h study (Figure 3C). The drug released from the TMZ–DEN conjugates resulted in a similar release pattern, including variation in the cumulative drug release percentage at both pH conditions. This observation indicates that free TMZ was stable in the conjugated form in comparison with the unconjugated drug (TMZ-SA) in PBS. The initial release of the drug from TMZ–DEN was slower in the citrate buffer compared with that from the PBS buffer (Figure 3A,C). TMZ release from the TMZ-linker (TMZ-SA) molecule was faster in PBS compared with the release from the TMZ–DEN conjugate (Figure 3A,B). Our results indicate the stability of the TMZ-derived active metabolites (MTIC) in the TMZ–DEN conjugates in both the pH values, suggesting the highest all-time % active MTIC in comparison with the AIC (Figure 3A,C). The active metabolite MTIC acts as a hydrolyzed product of TMZ and is crucial for the generation of the DNA containing O6-guanine methylation. The unidentified product  $m/z$  at 241 was formed during the release from TMZ–DEN, indicating 30% release initially, which decreased to 10% on day 14 and there was a simultaneous increase in MTIC and AIC.

From these observations, it was assumed that the formation of the MTIC and AIC, both at the cost of  $m/z$  241, originated from the TMZ–DEN conjugate (Figure 3A,C).

**Tumoricidal Activity of TMZ–DEN.** The antitumor potential of TMZ–DEN was assessed against parental and doxorubicin-resistant DL tumor cells in short-term and long-term coculture (Figure 4). The percent viability in DL cells was reduced to <60% in the presence of TMZ–DEN (250  $\mu$ M) compared to the free drug (Figure 4A). For doxorubicin-resistant DLR cells, the construct is also effective in reducing the viability of the resistant cells, suggesting that the construct can be a good candidate to work against the drug-resistant cells (Figure 4B). Results from the 48 h 3-(4,5-dimethylthiazol-2-yl)-2,5-diphenyltetrazolium bromide (MTT) assay suggest significant growth inhibition of DL cells in all of the concentrations tested. At the highest concentration (250  $\mu$ M), the growth inhibition was nearly 100%, suggesting complete efficacy of the construct. The dendrimer alone failed to have any significant impact on the reduction of DL cell growth (Figure 4C). DLR cells were also susceptible to the long-term effect of the construct, with nearly 60% cell growth getting retarded at the highest concentrations tested (Figure 4D). Direct cytotoxicity measurement of the formed construct also showed significant cytolysis of the DL and DLR cells compared to the free drug in a concentration-dependent manner (Figure 4E,F). We also performed the  $IC_{50}$  analyses of DL, DLR, U87 (human primary glioblastoma), and C6 (rat glioma) cells in the presence of TMZ and TMZ–DEN.  $IC_{50}$  values of all of the cell lines were significantly higher in free TMZ compared with TMZ–DEN (Table S1). A significantly higher reduction in viability was observed against NIH3T3 cells in the presence of TMZ (250  $\mu$ M) alone compared with TMZ–DEN (Figure S11A). The free dendrimer also showed little toxicity although it is significantly less compared with the free TMZ. At a lower concentration (30  $\mu$ M), only the dendrimer or TMZ–DEN is significantly more tolerant compared with the free TMZ (Figure S11A). Like NIH3T3 cells, human peripheral blood mononuclear cells (PBMCs) were significantly more susceptible (loss of viability) to TMZ compared to the free dendrimer or TMZ–DEN (Figure S11B). At a concentration of 30  $\mu$ M, TMZ treatment caused 40% cell death compared to ~20% in the presence of the dendrimer alone or TMZ–DEN (Figure S11B).

Free TMZ was found to be extremely hemolytic (lysis of RBC), with as much as 25% lysis at a concentration of 250  $\mu$ M, while the free dendrimer or TMZ–DEN is tolerant to RBC (~5% lysis) (Figure S11C). At low concentrations (30–10  $\mu$ M), free TMZ has significant lytic potential compared with the free dendrimer or TMZ–DEN (Figure S11C). Besides DL and DLR cells, TMZ–DEN was also effective against human lymphoma cell lines (Raji, THP1, U937, and JE6.1) (Figure S12). Our result suggests that Raji and U937 cells are highly susceptible to TMZ–DEN compared with TMZ alone in a concentration-dependent manner (Figure S12A,C). THP1 and JE6.1 cells were also susceptible to TMZ–DEN; however, TMZ only induced similar levels of growth inhibition compared to TMZ–DEN (Figure S12B,D). Besides lymphoma cells, we also tested the tumoricidal effect of free TMZ and TMZ–DEN against U87 and C6. Our data suggests that TMZ–DEN has a significant antiproliferative effect compared with TMZ against both of the cell lines tested (Figure S13).

**Cellular Uptake and Apoptosis.** Compared to TMZ, TMZ–DEN caused extensive damage to the DL cells via

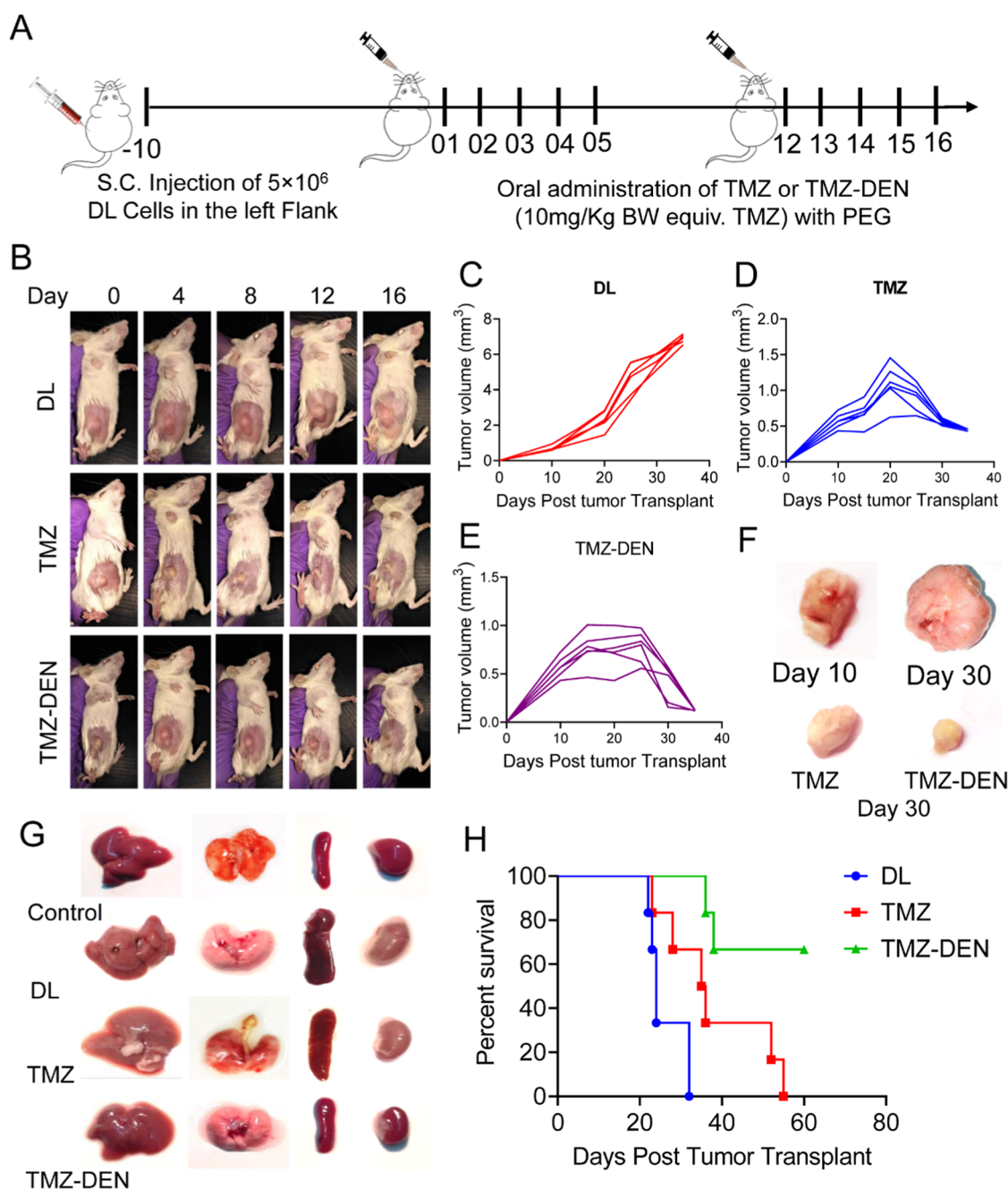


**Figure 5.** Induction of apoptosis and cellular uptake in DL and DLR cells treated with TMZ or TMZ–DEN. (A) DL or (B) DLR cells were either untreated or treated with the indicated formulation (50  $\mu$ M) for 8 h. The cells were washed in a complete medium and stained with FITC-conjugated Annexin V and PI (nuclear staining). Cellular uptake of FITC-tagged TMZ–DEN in (C) DL and (D) DLR cells was assessed following incubation with the formulation for 8 h followed by capturing of images under an inverted microscope.

apoptosis, which facilitates the uptake of propidium iodide (PI), indicating that the nanoconstruct induced DNA damage (Figure 5A). Like DL, DLR cells also showed susceptibility to the TMZ-loaded construct, while free TMZ remained ineffective in inducing any detectable levels of apoptosis as judged by the absence of Annexin V positive cells (Figure 5B). Overwhelming uptake of the FITC-conjugated TMZ–DEN construct suggests that the construct loaded with the drug can reach deep inside the tumor cells for the successful discharge of the payload (the drug) (Figure 5C). Compared to DL cells, DLR cells demonstrated significantly less uptake but noticeable enough to indicate that these cells too are susceptible to the TMZ-loaded dendrimer, despite their nearly 100% tolerance to doxorubicin (Figure 5D).

**Therapeutic Efficacy, Restriction of Metastasis, and Immune-Stimulation.** A solid tumor model of highly metastatic murine lymphoma called Dalton's lymphoma (DL) was studied to assess the efficacy of the TMZ-bearing construct. We were successful in implanting the DL tumor under the skin of CD-1 mice and grow it as a solid tumor in the right flank of the animals (female, 6–8 weeks old). The tumor formation under the skin was palpable after 8–10 days, which continued to grow and developed into a large tumor mass (Figure 6). A comprehensive therapy schedule was formulated involving the TMZ-loaded dendrimer (TMZ dose 10 mg/kg body weight) (Figure 6A). Altogether, 10 TMZ or

TMZ-loaded dendrimer (TMZ–DEN) doses were given in two batches (5 doses each) with a 7 day gap between the two batches. Individual images show that DL solid tumors in CD-1 mice were significantly reduced, four weeks (day 28) after the first treatment of TMZ or TMZ–DEN (Figure 6B). Tumor volume in the TMZ–DEN-treated group significantly reduced on day 30 compared with untreated DL, where tumor growth increased exponentially ( $P < 0.05$ ) (Figure 6C–E). The TMZ-treated group showed intermediate levels of inhibition in tumor growth but significantly more than the untreated group (Figure 6C,D). Weight of the animals bearing the untreated DL tumor increased from  $17.35 \pm 1.34$  on day 0 to  $31.45 \pm 0.83$  on day 20 (Table S2). Treatment with TMZ or TMZ–DEN reduced the weight of the animals to  $23.82 \pm 1.20$  and  $22.85 \pm 2.86$ , respectively, following treatment on day 20 (Table S2). The tumor size of the indicated treatment group is also presented for the TMZ–DEN-treated group on day 30 compared with the untreated or TMZ-treated animals in Figure 6F. The tumor weights of the untreated DL and TMZ–DEN-treated groups were  $6.88 \pm 0.22$  and  $0.12 \pm 0.002$  g, respectively, showing a significant difference ( $P < 0.01$ ) and the therapeutic efficacy of TMZ–DEN (Table S3 and Figure 6F). Our results also suggest that compared to untreated animals, the size and weight of metastasized vascularized organs like the liver, lung, spleen, and kidney were significantly reduced following therapy with TMZ–DEN (Figure 6G).



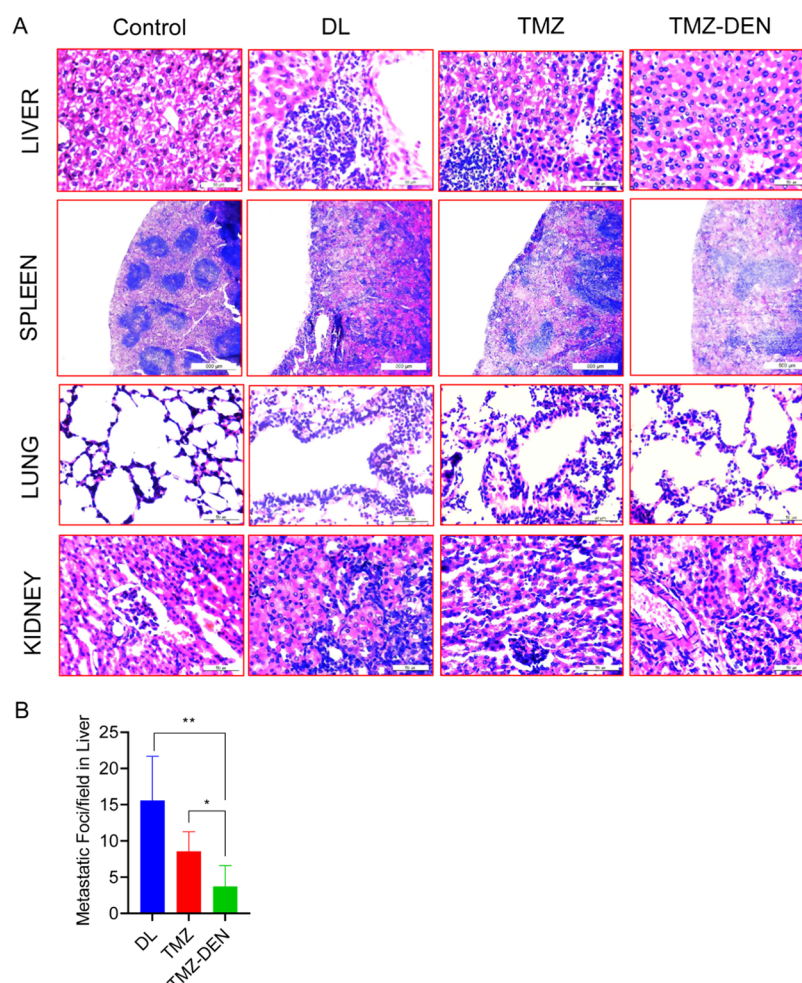
**Figure 6.** Therapeutic efficacy of TMZ–DEN against experimental murine lymphoma developed as a solid tumor in CD-1 mice. (A) Therapeutic schedule illustrating the time points of TMZ–DEN administration in DL solid tumor developed in CD-1 mice. TMZ–DEN (10 mg/kg) was orally administered on days 1–5 and on days 12–16. (B–E) Tumor volume was measured at an interval of 4 days, and the tumor was allowed to grow up to day 40 in untreated and respective treated groups when the final reading was taken. (F) On day 30, three mice from each group were sacrificed and the tumors were obtained. Images of solid DL tumor growth in CD-1 mice on day 0 (before treatment) and after 4 weeks (day 30) following treatment with TMZ–DEN. (G) Images of vascularized organs in healthy control, untreated, and indicated treated groups on day 30. (H) Kaplan–Meier survival analysis for the tumor-bearing mice following the above-mentioned treatment with TMZ–DEN.

The weights of these organs under the different treatment conditions are presented in Table S4, showing significant differences and therapeutic benefits of the formulation (TMZ–DEN). Survival (Kaplan–Meier analysis) studies of the TMZ–DEN-treated groups showed marked improvement and therapeutic potency of the formed construct over the untreated group. The TMZ–DEN-treated group outlived the untreated or TMZ-treated animals, and this significantly increased with 70% survival for the treated animals beyond day 60 when readings and quantization of survival were last recorded ( $P <$

0.05) (Figure 6H). Untreated tumor-bearing animals (DL) survived up to day 35, and the TMZ-only group extended the survival up to day 55 (Figure 6H).

In-depth study of the liver and spleen in untreated animals showed extensive metastasis with the tumor cells, while the TMZ–DEN-treated group has areas with normal architecture and removal of infiltrated tumor cells (Figure 7A). Treatment with only TMZ in the liver partially restricted the tumor metastasis compared with the untreated control. TMZ–DEN, in contrast, significantly ablated the surge in tumor cells and





**Figure 7.** Successful therapy with TMZ–DEN restricts metastasis in vascularized organs. (A) Hematoxylin and eosin (H&E) staining of the liver, spleen, lung, and kidney of healthy control, untreated, and treated groups on day 22. Metastatic foci are labeled and indicated with a red circle in the untreated group and with a green circle with TMZ–DEN treatment. (B) Quantitative estimation of metastatic foci in the liver of untreated and treated mice.

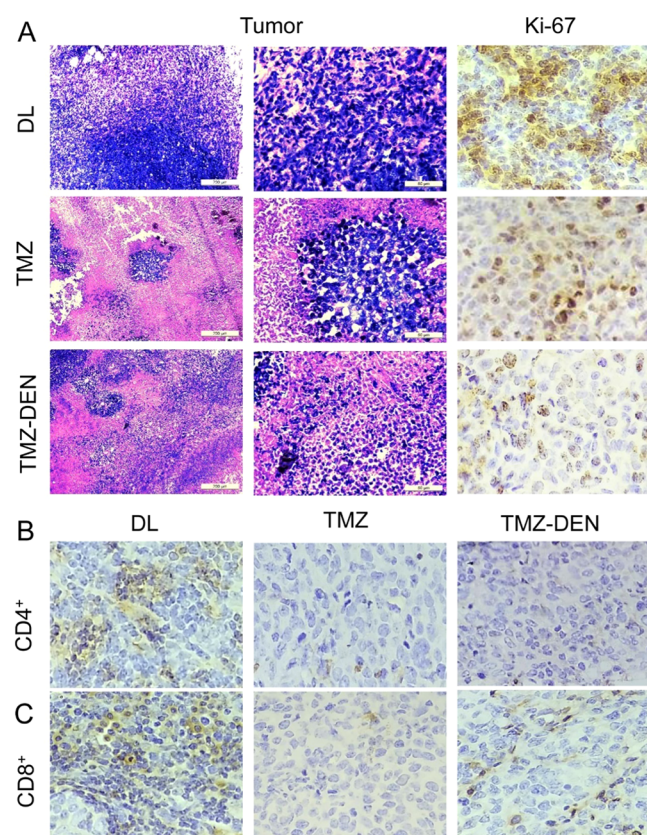
reduced their number dramatically in the entire expansion of the slides tested (Figure 7A).

In the spleen, extensive metastasis occurs in the cortex and the medullar regions, which was accompanied by the loss of the splenic architecture, only to be restored by TMZ–DEN therapy. We also looked into the histology of lungs and kidneys in the treated and untreated groups. These two organs were infested with tumor cells in the no-treatment control group, which significantly reduced following treatment with TMZ–DEN. Quantitative estimation of tumor foci in the liver demonstrated significant differences in the number of metastatic (tumor) foci between the untreated and treated groups (Figure 7B). The ratio of Ki-67<sup>+</sup>/Ki-67<sup>−</sup> was quantified by counting cells from 10 to 12 high-power field, randomly chosen from each indicated treatment group. The ratio of Ki-67<sup>+</sup>/Ki-67<sup>−</sup> of the TMZ–DEN group also decreased significantly compared with the untreated groups (Figure 8A). Data also suggest that DL tumor growth and subsequent metastasis recruited CD4<sup>+</sup> and CD8<sup>+</sup> T cells following inflammatory responses in organs like the spleen (Figure 8B,C). Treatment with TMZ or TMZ–DEN nearly obliterates the presence of T cells, which likely underwent senescence following therapy, resulting in improved prognosis. Serum levels of inflammatory cytokines like IL1 $\beta$  and IL-6 showed a

significant reduction following treatment with TMZ–DEN compared with the untreated or TMZ-treated group ( $p < 0.01$  and  $< 0.001$ ) (Figure S14). The serum TNF- $\alpha$  level did not show any significant changes among the groups (Figure S14).

## DISCUSSION AND CONCLUSIONS

Owing to its good bioavailability, tissue penetration, and modest side effects, TMZ is considered an attractive chemotherapeutic drug. Neoplasias like large B-cell lymphomas and primary CNS lymphomas are responsive to TMZ. Besides that, TMZ could also be useful for application against systemic diffuse large B-cell lymphomas (DLBLs). TMZ activity is associated with the function of the DNA repair enzyme, methyl-guanine DNA methyl transferase (MGMT). This enzyme is known to be a major mechanism of resistance to this drug in human cancers. Our results demonstrated that TMZ–DEN restricts uncontrolled tumor cell growth and may also serve as a potential alternative for treatment against drug-resistant lymphoma. Doxorubicin resistance in DLBL is common in treatment procedures, which can be potentially overcome using TMZ–DEN to improve and enhance the depth of response in patients with relapsed DLBL or primary CNS lymphoma.



**Figure 8.** Immune modulation by TMZ-DEN in DL solid tumor-bearing mice. (A) H&E-stained sections of the solid tumor. Staining of solid tumor sections with antimouse Ki-67 antibody for detecting the dividing cells to compare between untreated and treated groups. (B, C) Immunohistochemical staining of CD4<sup>+</sup> and CD8<sup>+</sup> T cells in the splenic sections of untreated and treated (TMZ or TMZ-DEN) groups. Representative of one experiment of three identical experiments is shown.

We have covalently attached temozolomide to the PAMAM dendrimer for preclinical assessment of its efficacy against malignant experimental lymphoma in mice. There is no report of TMZ application in clinical conditions or in experimental studies of lymphoma, developed as a solid tumor. TMZ-DEN demonstrated significant tumoricidal activity compared with the free drug. IC<sub>50</sub> analysis suggests significant advantage of the nanoconstruct over TMZ. The antiproliferative effect of the nanoconstruct was also observed against human and rat glioblastoma and glioma cells. The nanoconstruct has a significant edge over the free drug for therapeutic efficacy against lymphoma developed as a solid tumor. Besides augmenting the life expectancy of the treated animals, TMZ-DEN mobilized the antigen-specific CD4<sup>+</sup> and CD8<sup>+</sup> T cells in lymphoid organs like the spleen and significantly restricted metastasis. In addition, TMZ-DEN treatment downregulates the serum IL1 $\beta$  and IL-6 levels in mice with DL tumor. Both cytokines are considered proinflammatory in nature and are thought to be associated with exacerbation of the disease. Our novel construct significantly lowered the levels of these cytokines and thus improved the prognosis of the disease. Altogether, the novel nanoconstruct demonstrated a significant advancement and constitutes a new benchmark for application against lymphoma.

## ■ ASSOCIATED CONTENT

### Supporting Information

The Supporting Information is available free of charge at <https://pubs.acs.org/doi/10.1021/acsabm.0c01599>.

Materials and methods and supplementary Tables S1–S4 and Figures S1–S14 (PDF)

## ■ AUTHOR INFORMATION

### Corresponding Authors

Ugir Hossain Sk – Department of Clinical and Translational Research, Chittaranjan National Cancer Institute, Kolkata 700 026, West Bengal, India; Email: [uhocju@gmail.com](mailto:uhocju@gmail.com)

Partha Pratim Manna – Immunobiology Laboratory, Department of Zoology, Institute of Science, Banaras Hindu University, Varanasi 221005, India; [orcid.org/0000-0003-2939-0818](https://orcid.org/0000-0003-2939-0818); Email: [pp\\_manna@yahoo.com](mailto:pp_manna@yahoo.com)

### Authors

Sumit Kumar Hira – Cellular Immunology Laboratory, Department of Zoology, The University of Burdwan, Bardhaman 713104, India; [orcid.org/0000-0001-6113-4721](https://orcid.org/0000-0001-6113-4721)

Abhinandan Rej – Cellular Immunology Laboratory, Department of Zoology, The University of Burdwan, Bardhaman 713104, India

Debapriya RoyMahapatra – Department of Clinical and Translational Research, Chittaranjan National Cancer Institute, Kolkata 700 026, West Bengal, India

Complete contact information is available at:

<https://pubs.acs.org/doi/10.1021/acsabm.0c01599>

### Author Contributions

The manuscript was written through contributions of all authors. All authors have given approval to the final version of the manuscript. U.H.S and S.K.H. contributed equally to this work.

### Funding

U.H.S. acknowledges the financial support of CSIR-HRDG, New Delhi (grant number 80(0090)/20/EMR-II).

### Notes

The authors declare no competing financial interest.

## ■ ACKNOWLEDGMENTS

U.H.S. and D.R.M. would also like to acknowledge Director CNCI, Kolkata, for providing the necessary facility. U.H.S. acknowledges the Director of CSIR-IHBT, Palampur, India, for providing the Quick Hire Scientist Fellowship.

## ■ ABBREVIATIONS

TMZ, temozolomide; DOX, doxorubicin; DL, Dalton's lymphoma

## ■ REFERENCES

- (1) Prasad, M.; Lambe, U. P.; Brar, B.; Shah, I.; Manimegalai, J.; Ranjan, K.; Rao, R.; Kumar, S.; Mahant, S.; Khurana, S. K.; Iqbal, H. M. N.; Dhama, K.; Misri, J.; Prasad, G. Nanotherapeutics: An insight into healthcare and multi-dimensional applications in medical sector of the modern world. *Biomed. Pharmacother.* **2018**, *97*, 1521–1537.
- (2) Kannan, S.; Dai, H.; Navath, R. S.; Balakrishnan, B.; Jyoti, A.; Janisse, J.; Romero, R.; Kannan, R. M. Dendrimer-Based Postnatal Therapy for Neuroinflammation and Cerebral Palsy in a Rabbit Model. *Sci. Transl. Med.* **2012**, *4*, No. 130ra46.



- (3) Nishimoto, Y.; Nagashima, S.; Nakajima, K.; Ohira, T.; Sato, T.; Izawa, T.; Yamate, J.; Higashikawa, K.; Kuge, Y.; Ogawa, M.; Kojima, C. Carboxyl-, sulfonyl-, and phosphate-terminal dendrimers as a nanoplateform with lymph node targeting. *Int. J. Pharm.* **2020**, 576, No. 119021.
- (4) Wang, H.; Miao, W.; Wang, F.; Cheng, Y. A Self-Assembled Coumarin-Anchored Dendrimer for Efficient Gene Delivery and Light-Responsive Drug Delivery. *Biomacromolecules* **2018**, 19, 2194–2201.
- (5) Fox, L. J.; Richardson, R. M.; Briscoe, W. H. PAMAM dendrimer—cell membrane interactions. *Adv. Colloid Interface Sci.* **2018**, 257, 1–18.
- (6) Sk, U. H.; Dixit, D.; Sen, E. Comparative study of microtubule inhibitors—Estramustine and natural podophyllotoxin conjugated PAMAM dendrimer on glioma cell proliferation. *Eur. J. Med. Chem.* **2013**, 68, 47–57.
- (7) Sharma, A.; Porterfield, J. E.; Smith, E.; Sharma, R.; Kannan, S.; Kannan, R. M. Effect of mannose targeting of hydroxyl PAMAM dendrimers on cellular and organ biodistribution in a neonatal brain injury model. *J. Controlled Release* **2018**, 283, 175–189.
- (8) Nance, E.; Porambo, M.; Zhang, F.; Mishra, M. K.; Buelow, M.; Getzenberg, R.; Johnston, M.; Kannan, R. M.; Fatemi, A.; Kannan, S. Systemic dendrimer-drug treatment of ischemia-induced neonatal white matter injury. *J. Controlled Release* **2015**, 214, 112–120.
- (9) Yabbarov, N. G.; Posypanova, G. A.; Vorontsov, E. A.; Obyednyy, S. I.; Severin, E. S. A new system for targeted delivery of doxorubicin into tumor cells. *J. Controlled Release* **2013**, 168, 135–141.
- (10) Patial, V.; Sharma, S.; Sk, U. H. Dendrimer conjugated estramustine nanocrystalline 'Dendot': An effective inhibitor of DMBA-TPA induced papilloma formation in mouse. *Eur. J. Pharm. Sci.* **2017**, 109, 316–323.
- (11) Al-Jamal, K. T.; Ruenaroengsak, P.; Hartell, N.; Florence, A. T. An intrinsically fluorescent dendrimer as a nanoprobe of cell transport. *J. Drug Target.* **2006**, 14, 405–412.
- (12) Sato, N.; Kobayashi, H.; Saga, T.; Nakamoto, Y.; Ishimori, T.; Togashi, K.; Fujibayashi, Y.; Konishi, J.; Brechbiel, M. W. Tumor Targeting and Imaging of Intraperitoneal Tumors by Use of Antisense Oligo-DNA Complexed with Dendrimers and/or Avidin in Mice. *Clin. Cancer Res.* **2001**, 7, No. 3606.
- (13) Vincent, L.; Varet, J.; Pille, J.-Y.; Bompais, H.; Opolon, P.; Maksimenko, A.; Malvy, C.; Mirshahi, M.; Lu, H.; Vannier, J.-P.; Soria, C.; Li, H. Efficacy of dendrimer-mediated angiostatin and TIMP-2 gene delivery on inhibition of tumor growth and angiogenesis: In vitro and in vivo studies. *Int. J. Cancer* **2003**, 105, 419–429.
- (14) Wang, Y.; Stevens, M. F. G.; Chan, T.-m.; DiBenedetto, D.; Ding, Z.-x.; Gala, D.; Hou, D.; Kugelman, M.; Leong, W.; Kuo, S.-c.; Mas, J. L.; Schumacher, D. P.; Shutts, B. P.; Smith, L.; Zhan, Z.-Y. J.; Thomson, W. T. Antitumor Imidazotetrazines. 35. New Synthetic Routes to the Antitumor Drug Temozolomide. *J. Org. Chem.* **1997**, 62, 7288–7294.
- (15) Ostrom, Q. T.; Gittleman, H.; Fulop, J.; Liu, M.; Blanda, R.; Kromer, C.; Wolinsky, Y.; Kruchko, C.; Barnholtz-Sloan, J. S. CBTRUS Statistical Report: Primary Brain and Central Nervous System Tumors Diagnosed in the United States in 2008–2012. *Neuro-Oncology* **2015**, 17, iv1–iv62.
- (16) Adamson, C.; Kanu, O. O.; Mehta, A. I.; Di, C.; Lin, N.; Mattox, A. K.; Bigner, D. D. Glioblastoma multiforme: a review of where we have been and where we are going. *Expert Opin. Invest. Drugs* **2009**, 18, 1061–1083.
- (17) Zhang, J.; Malcolm, F. G. S.; Tracey, D. B. Temozolomide: Mechanisms of Action, Repair and Resistance. *Curr. Mol. Pharmacol.* **2012**, 5, 102–114.
- (18) Stevens, M. F. G.; Hickman, J. A.; Langdon, S. P.; Chubb, D.; Vickers, L.; Stone, R.; Baig, G.; Goddard, C.; Gibson, N. W.; Slack, J. A.; Newton, C.; Lunt, E.; Fizames, C.; Lavelle, F. Antitumor Activity and Pharmacokinetics in Mice of 8-Carbamoyl-3-methyl-imidazo[5,1-d]-1,2,3,5-tetrazin-4(3H)-one (CCRG 81045; M & B 39831), a Novel Drug with Potential as an Alternative to Dacarbazine. *Cancer Res.* **1987**, 47, No. 5846.
- (19) Patil, R.; Portilla-Arias, J.; Ding, H.; Inoue, S.; Konda, B.; Hu, J.; Wawrowsky, K. A.; Shin, P. K.; Black, K. L.; Holler, E.; Ljubimova, J. Y. Temozolomide Delivery to Tumor Cells by a Multifunctional Nano Vehicle Based on Poly( $\beta$ -L-malic acid). *Pharm. Res.* **2010**, 27, 2317–2329.
- (20) Skinner, M.; Ward, S. M.; Emrick, T. Versatile Synthesis of Polymer-Temozolomide Conjugates. *ACS Macro Lett.* **2017**, 6, 215–218.
- (21) Fang, C.; Wang, K.; Stephen, Z. R.; Mu, Q.; Kievit, F. M.; Chiu, D. T.; Press, O. W.; Zhang, M. Temozolomide Nanoparticles for Targeted Glioblastoma Therapy. *ACS Appl. Mater. Interfaces* **2015**, 7, 6674–6682.
- (22) Rudek, M. A.; Donehower, R. C.; Statkevich, P.; Batra, V. K.; Cutler, D. L.; Baker, S. D. Temozolomide in Patients with Advanced Cancer: Phase I and Pharmacokinetic Study. *Pharmacotherapy* **2004**, 24, 16–25.
- (23) Zhao, L. X.; Wang, J. L.; Dai, X. P.; Zhizhong, J. I. Synthesis and Antitumor Activities of 3-Substituted 4-Oxo-3H-imidazo[5,1-d][1,2,3,5] tetrazine-8-carboxylic Acids and Their Derivatives. *Chin. J. Med. Chem.* **2001**, 11, 263–269.
- (24) Hira, S. K.; Mitra, K.; Srivastava, P.; Singh, S.; Vishwakarma, S.; Singh, R.; Ray, B.; Manna, P. P. Doxorubicin loaded pH responsive biodegradable ABA-type Amphiphilic PEG-b-aliphatic Polyketal-b-PEG block copolymer for therapy against aggressive murine lymphoma. *Nanomedicine* **2020**, 24, No. 102128.
- (25) Srivastava, P.; Hira, S. K.; Gupta, U.; Singh, V. K.; Singh, R.; Pandey, P.; Srivastava, D. N.; Singh, R. A.; Manna, P. P. Pepsin Assisted Doxorubicin Delivery from Mesoporous Silica Nanoparticles Downsizes Solid Tumor Volume and Enhances Therapeutic Efficacy in Experimental Murine Lymphoma. *ACS Appl. Bio Mater.* **2018**, 1, 2133–2140.

# Single Inhibitors versus Dual Inhibitors: Role of HDAC in Cancer

Rubi Roy, Tasnim Ria, Debapriya RoyMahaPatra, and Ugir Hossain Sk\*



Cite This: *ACS Omega* 2023, 8, 16532–16544



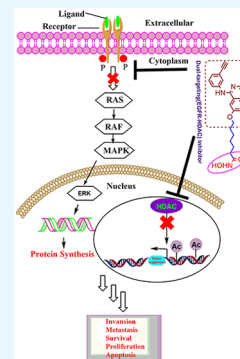
Read Online

ACCESS |

Metrics & More

Article Recommendations

**ABSTRACT:** Due to the multimodal character of cancer, inhibition of two targets simultaneously by a single molecule is a beneficial and effective approach against cancer. Histone deacetylase (HDAC) was widely investigated as a novel category of anticancer drug targets due to its crucial role in various biological processes like cell-proliferation, metastasis, and apoptosis. Numerous HDAC inhibitors such as vorinostat and panobinostat are clinically approved but have limited usage due to their low efficacy, nonselectivity, drug resistance, and toxicity. Therefore, HDACs with a dual targeting ability have attracted great attention. The strategy of combining a HDAC inhibitor with other antitumor agents has been proved advantageous for combating the nonselectivity and drug resistivity problems associated with single-target drugs. Henceforth, we have highlighted dual-targeting inhibitors to target HDAC along with topoisomerase, receptor tyrosine kinase inhibitors, and the zeste homolog 2 enzyme. Our Review mainly focuses on the impact of the substituent effect along with the linker variation of well-known HDAC-inhibitor-conjugated anticancer drugs.



## 1. INTRODUCTION

Cancer, a life-threatening disease, is one of the foremost reasons for death across the world.<sup>1</sup> India ranks third among the nations in terms of the highest number of incidences of cancer. Every year, over 13 hundred thousand people in India are suffering from cancer, as per the National Cancer Registry Programme Report. According to a report by the Indian Council of Medical Research (ICMR), the expected cancer incidence will increase to 29.8 million in 2025. Chemotherapy, targeted therapy, radiation therapy, immunotherapy, and stem cell therapy are the most common treatments for cancer. Despite impressive progress in biotechnologies and diagnosis, the development of novel anticancer drugs is still necessary for the management of cancer patients, losing the great challenge for scientists to cure cancer successfully. For the betterment of cancer treatment and to overcome the toxicity and adverse effect of the implicated drug, scientists have already put their eyes on targeted drug therapy, for which we have seen how a single drug efficiently acts against a specific target with high selectivity.<sup>2</sup> Tamoxifen was the first reported drug used in targeted therapy against breast cancer by targeting estrogen receptors.<sup>3</sup> Though the “one drug, one target” concept is a highly potent and specific treatment against cancer due to the absence of off-target side-effects, the single-target drug is not having significant success due to drug resistance, low pharmacokinetics, and poor patient compliance.<sup>4</sup> Owing to the complex character of cancer, a new therapy needs to be developed for successful long-term outcomes; therefore, a new direction for cancer drug discovery is necessary. Thus, the combination therapy approach has achieved a remarkable place in the area of cancer drug discovery to maximize efficacy and minimize drug resistance. Initially, in drug combination

therapy drug cocktails, physical mixtures of two or more compounds are used in combination.<sup>5</sup> Although combination therapy has had noteworthy success, many problems are associated with this therapy, such as drug solubility, drug resistance, and drug interactions. In addition, the possibility for drug–drug interactions and side effects are increasing, so dose adjustment is essential to avoid drug toxicity. For these boundaries of combination therapy, many research groups concentrate on molecular hybridization to develop a dual-targeting drug rather than a drug combination.<sup>6</sup> Thus, combination therapy has leaned toward the design of dual-target ligands in which a single molecule can target more than one site simultaneously, leading to synergistic effects and the potential to reduce the possible drug–drug interactions and drug-resistance and improve pharmacokinetics compared to physical mixtures of drugs molecules.<sup>7</sup>

## 2. COMPARISON OF SINGLE VERSUS DUAL INHIBITORS

A single inhibitor can specifically inhibit a target molecule. Therefore, a single inhibitor attacks only cancer cells, excluding normal cells; hence, it has high selectivity and effectivity and low toxicity. At first, although there is enthusiasm among clinicians, they soon have to face the problem that after giving

Received: January 12, 2023

Revised: March 18, 2023

Accepted: April 13, 2023

Published: May 1, 2023



the drug repeatedly the cancer cells develop resistance against the drug. Therefore, patients cannot survive for long time. The resistance is mainly due to the epigenetic altering of the target, so a drug molecule is unable to interact with the target and therefore the targeted therapy is not anymore useful. Since cancer is a complex disease, it is very easy to manipulate the single target, resulting in treatment failure. Since then, combination drug treatment has replaced single targeted drug therapy using two or more drugs in together to enhance the efficacy. At the same time, multiple drugs may increase the risk of drug–drug interactions and dose-limiting toxicities. Although combination therapy has been successful in cancer treatment, it is not useful further due to these disadvantages. Therefore, a single drug with the ability to target two targets simultaneously could serve as an effective strategy in cancer treatments.<sup>8</sup> Overcoming drug resistance and the toxicity of single-targeted inhibitors is the basis for the development of dual-targeting inhibitors. A recent report indicated a more favorable outcome with dual-targeting inhibitors in cancer treatment. For an example, the single-targeted drug erlotinib is the first line drug treatment for non-small-cell lung carcinoma (NSCLC) but limited in its usage due to drug resistance. A synergistic antitumor effect is produced in NSCLC when vorinostat (SAHA) and erlotinib are combined. This observation led to the search for a new effective treatment for human lung cancer. Although the effectiveness increases in combination therapy, since the two individual drugs are given together, there are several limitations including drug–drug interactions, toxicity, and drug resistance. However, combining SAHA and erlotinib a single molecule leads to efficacious outcomes due to reduce toxicity and drug–drug interactions along with enhanced efficacy.

**2.1. Dual-Targeting Inhibitor and Its Importance.** The concepts of dual-targeting inhibitors have been used from the beginning of modern pharmacology and have also achieved success in clinics.<sup>9</sup>

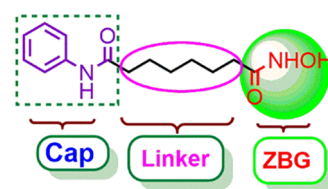
A dual-targeting inhibitor acts on two molecular targets simultaneously. In the past decade, dual-target drugs (chimeric drugs) have attracted considerable attention, which is a sharply growing research area for medicinal chemists. Through the inhibition of two antitumor agents involved in disease progression simultaneously, drug resistance is improved. Additionally, dual-target therapies can overcome the limitations of single-targeted drugs including drug–drug interactions, poor safety, a low therapeutic index value, low efficacy, and other side effects.<sup>4</sup>

Here in this Review, we consider the bifunctional single drug, which is a product of two known inhibitors that acts on two specific targets and results in the advantages of enhanced antitumor activity and reduced toxic effects.<sup>10</sup> To enhance the affinity and efficacy compared to their individual parent compounds, two molecules are combined to design new hybrid compounds.<sup>11</sup> The advantages of dual inhibitors is that they are more active than their constituent parent molecules individually, are less toxic, and have improved therapeutic index values and bioavailability.<sup>12</sup> Few dual-targeting inhibitors are now in clinical trials against cancer. A dual-targeting inhibitor CUDC-101,<sup>13</sup> an inhibitor of epidermal growth factor receptor (EGFR)/histone deacetylase (HDAC), and another inhibitor CUDC-907, a dual phosphoinositide 3-kinase (PI3K)/HDAC inhibitor,<sup>14</sup> have completed phase I and phase II clinical trials against solid tumors and relapsed/refractory diffuse large B-cell and high-grade B-cell lymphoma,

respectively. Therefore, the progress of dual-targeting inhibitors is gaining attention for discovering anticancer drugs that possess pharmacokinetic advantages compared to conventional cancer therapy.

## 2.2. HDAC as a Promising Dual-Targeting Inhibitor.

Mutations and aberrant expression of epigenetic regulators are important contributors that cause many types of cancer. HDAC plays an important role in tumor cell development and is an important target among epigenetic regulators. The HDAC enzyme catalyzes the deacetylation of both histone and nonhistone proteins.<sup>15</sup> SAHA, panobinostat, chidamide, belinostat, and romidepsin are known FDA-approved HDAC inhibitors.<sup>16</sup> In most of the HDAC inhibitors, three main pharmacophores are present: a Cap group (surface recognition group), a ZBG (zinc-binding group), and a linker required to connect the Cap group and the ZBG, which is represented in Figure 1. Hydroxamic acid, cyclic tetrapeptides, benzamides,



**Figure 1.** Schematic diagram of a HDAC inhibitor and its active functionality.

and fatty acids are the four types of HDAC inhibitors, which are categorized based on their structures.<sup>17</sup> HDAC inhibitors are efficient for the treatment of cancer, but there are several side effects. Due to the nonselective nature of the HDAC inhibitors, more efficient and selective HDAC inhibitors need to be developed. By developing isoform-selective HDAC inhibitors, toxicity is reduced but drug resistance is still a problem. HDAC inhibitors alone have been suffering some problems like efficacy, toxicity, and drug resistance, and these disadvantages are overcome by the strategy of designing HDAC inhibitors with dual-targeting capabilities.<sup>18</sup> Therefore, here in this Review we talk about HDAC-based dual-targeting inhibitors.<sup>19</sup> Other antitumor agents are easily linked with HDAC inhibitors due to their flexible structures. Other antitumor agents such as topoisomerase (Top) inhibitors and receptor tyrosine kinase (RTK) inhibitors, including vascular endothelial growth factor receptor (VEGFR), EGFR, zeste homolog 2 (EZH2), and c-Met inhibitors, exert a synergistic effect on the cellular process of cancer cells when combined with HDAC inhibitors. Therefore, the bifunctional single molecule (dual-targeted drug) has become a promising approach in the treatment of cancer and a rational strategy to solve the problems of single-targeted drugs.

## 3. STRATEGY TO DESIGN A DUAL-TARGETED INHIBITOR

The two known inhibitors are combined in a single molecule to act as a dual-targeting inhibitor. The inhibitors are combined through a linker or fused together to form a single bifunctional molecule that simultaneously inhibits two targets. Additionally, computation-based design has played an important role in drug development, which is expensive and time-intensive. The initial application of computational chemistry followed by high-throughput screening technologies has accelerated the drug discovery process. Therefore, this



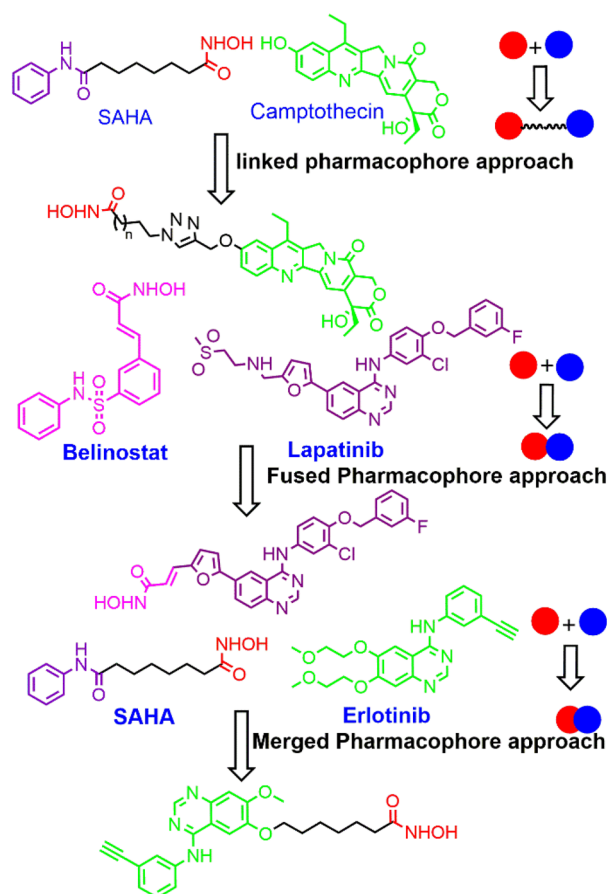
computational approach can be used also in the case of designing a dual-targeting inhibitor. Target identification, docking-based virtual screening, scoring functions, molecular similarity calculation, virtual library design, and sequence-based drug design are some methodologies involved in computer-aided drug design. Details of these two strategies are explained below.<sup>20</sup>

**3.1. Pharmacophore-Based Design of Dual-Target Kinase Drugs in Cancer.** In pharmacophore-based design, the distinct pharmacophores of two known inhibitors are combined in a single molecule. Pharmacophore-based design approaches are categorized into three types: (i) a suitable linker attached to an active moiety pharmacophore approach, (ii) the direct conjugation of the two active moieties pharmacophore approach, and (iii) the merged pharmacophore approach. In the linker pharmacophore approach, two different kinase drugs are combined via a linker and important structural features of two kinase inhibitors are retained in the new drug and may be effective against two targets (Figure 2). The growing amount of structural information is considered for linker-based drug design. This approach may be useful for designing a dual-target inhibitor. The fused pharmacophore approach is used to design a simple and small dual-targeting inhibitor. The fused pharmacophore approach allows for the overlap of the active space and ameliorates the pharmacokinetics as well as physicochemical properties of dual-target small molecules. The merged pharmacophore strategy requires lead compounds to have the same pharmacophore and share common fragments. Accordingly, the two small molecules are combined and synthesized into one molecule, but their respective pharmacophores remain, producing a smaller and simpler merged small molecule.<sup>21</sup>

**3.2. Computational Design of Dual-Target Kinase Drugs in Cancer.** Designing novel dual-targeted drugs based on a computational study is an alternative effective method, especially for novel kinase targets. From the knowledge of pharmacochimistry, proteomics, and computational chemistry, dual-targeted compounds are designed. For this design of dual-targeted drugs, the selection of target combinations and the virtual screening of dual-target small molecules are performed by applying techniques of data mining and structure analysis, respectively. The computational design strategies for dual-target kinase inhibitors are based on multiple docking, the use of pharmacophores, and fragment-based design.

Using multiple docking techniques of a small-molecule-based compound library with effective binding in the targeted site was evaluated.<sup>22</sup> Based on best hits, potential compounds were selected further for structural optimization for a molecular docking study. Due to the similar binding pocket present in the kinase, the result from the molecular docking study cannot offer appropriate predictions. In some cases, inverse docking approaches suffer from scoring algorithms and difficulty addressing target flexibility. Otherwise, improving the accuracy and false-positive rate for target selectivity prediction remains a challenge.

As an example, a hybrid molecule is formed by the combination of SAHA and the topoisomerase I (Top-I) inhibitor camptothecin.<sup>23</sup> It was reported experimentally that the newly formed hybrid compound is more effective than the parent molecules SAHA and camptothecin. To see if the new stuff actually works against HDAC and topoisomerase as confirmed by a computer-aided study, the binding modes of



**Figure 2.** Schematic representation of the pharmacophore-based design of a dual-targeting inhibitor.

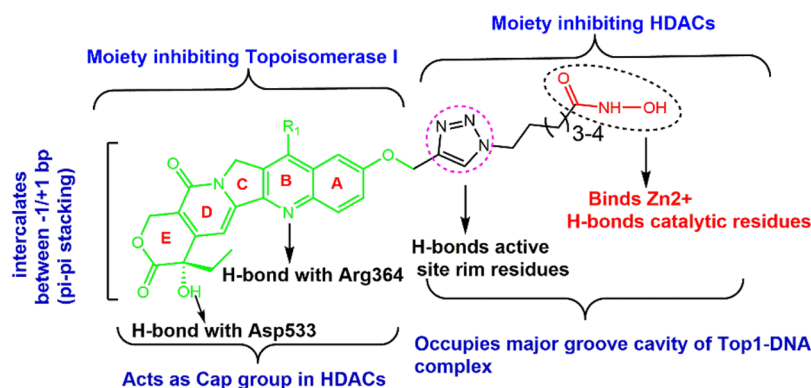
Top-I/HDAC hybrids have been predicted with their target receptors by a molecular docking study.

The hydroxyl group (ring E) and nitrogen atom (ring B) of camptothecin are formed hydrogen bonding with Asp533 and Arg364, respectively. The  $\pi$ -cation interaction is also observed with Lys425, and ring A and a hydroxamic acid group occupied the major groove cavity of the Top-I DNA complexes. Therefore, the interaction of camptothecin is not only preserved in the binding modes of the Top-I/HDAC hybrids but also enhanced due to the hydroxamic acid group of SAHA. Similarly, for the binding with the HDAC protein, we observe that camptothecin acts as a CAP group, oxygens of ring E form hydrogen bonds with Gly268, Asp269, Arg270, and Gly272, and hydroxamic acid coordinates with the  $\text{Zn}^{2+}$  ion in a bidentate manner. A triazole ring is involved in the formation of additional hydrogen bonds with His178 and Phe205, and that is observed only in the case of linkers containing five and six methylene groups (Figure 3).<sup>24</sup>

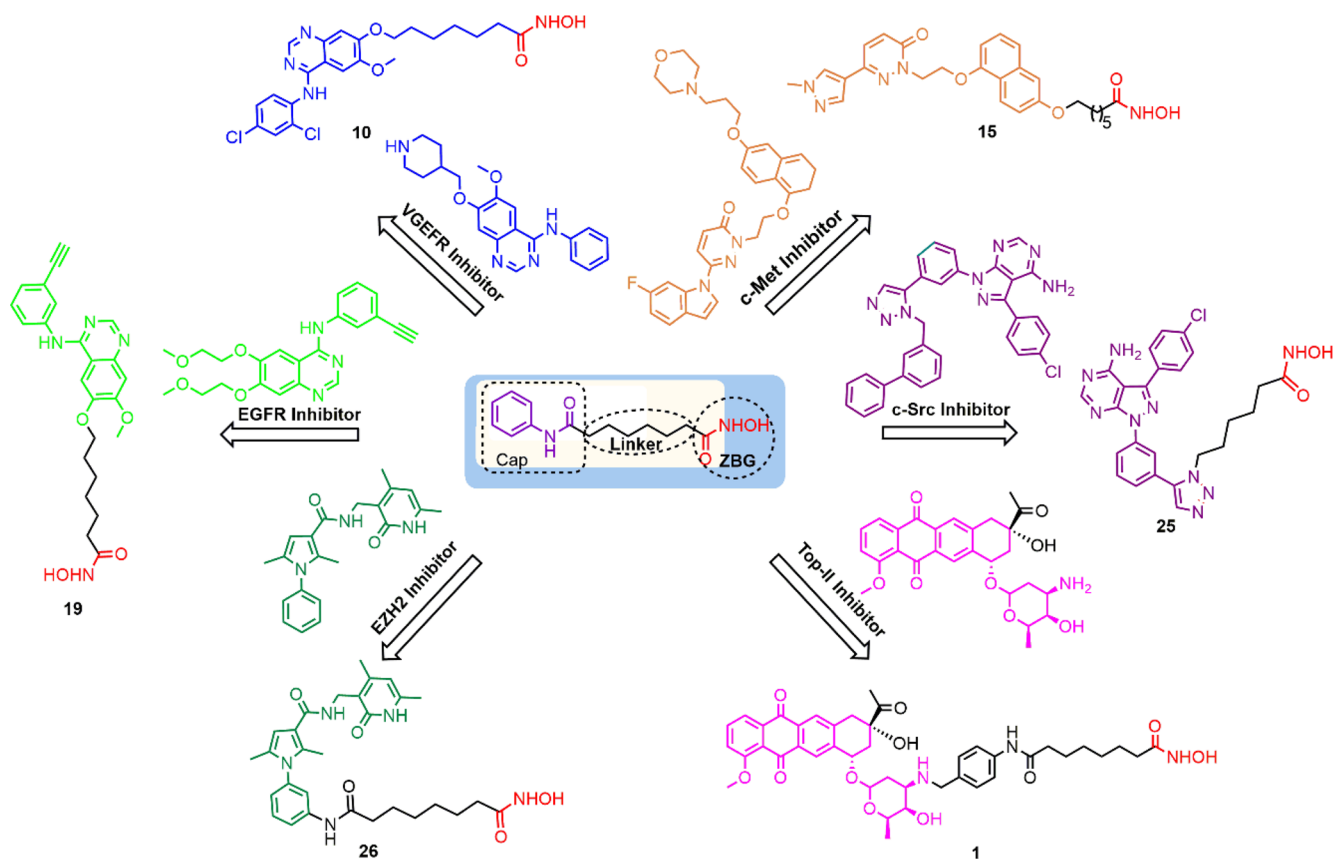
From this observation, it is concluded that the hybrid HDAC/Top molecule interacts with both target proteins and thus inhibits the function of two target simultaneously.

#### 4. DUAL TOPOISOMERASE/HISTONE DEACETYLASE INHIBITOR

DNA topoisomerase enzymes play crucial roles in many biological processes involving DNA cleavage and the relegation process.<sup>25</sup> To stop cell division and progression, topoisomerase enzymes that are responsible for breaking and reconnecting DNA strands are blocked by a topoisomerase inhibitor.<sup>26</sup>



**Figure 3.** Binding of a dual HDAC/Top inhibitor with the HDAC protein and the Top-I DNA complex via a docking study.



**Figure 4.** Respective dual-targeting inhibitors (1, 10, 15, 19, 25, and 26) presented in a pictorial form from their precursor molecules.

Camptothecin (Top-I inhibitor), DACA (Top-II inhibitor), doxorubicin, and daunorubicin (DAU; Top-I and Top-II inhibitor) are known topoisomerase inhibitors.<sup>27</sup>


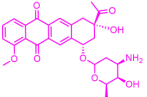
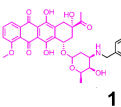
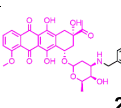
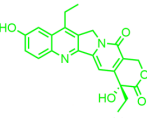
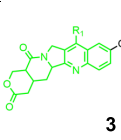
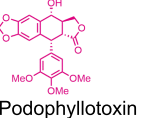
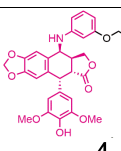
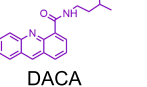
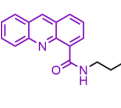
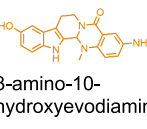
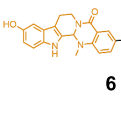
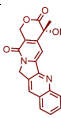
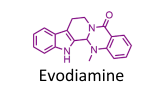
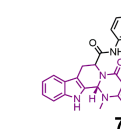
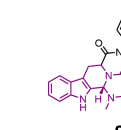
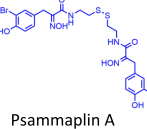
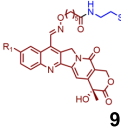
To design dual-targeted Top/HDAC inhibitors, the well-known SAHA has been incorporated or modified with other Top inhibitors. Herein, for the synthesis of a dual Top/HDAC inhibitor, the Top-II inhibitor DAU containing an amino group was conjugated via *N*-benzylation to HDAC. Additionally, a DAU-containing anthracycline moiety can act as a capping group that can conjugate with the hydroxamic acid of HDAC. Here, the hydroxamic acid of SAHA act as a zinc-binding pocket.<sup>28</sup>

Two types of dual HDAC and Top-II inhibitors were reported by Guerrant et al.,<sup>29</sup> where one is directly conjugated with DAU and SAHA and the other is DAU/triazolylaryl hydroxamate conjugates where SAHA and DAU are

conjugated by a triazole ring. The hybrid compound made directly from SAHA and DAU (1) (in Table 1) has shown better HDAC inhibitory activity than SAHA and also has shown the best cytotoxicity compared to the other reported bifunctional (SAHA and DAU) compounds.

The triazole-linked conjugate compounds of different linker lengths effectively inhibit HeLa cell with IC<sub>50</sub> values in the nanomolar range. From the result, it was indicated that linker length also plays an important role in inhibiting HDAC. Among all the developed molecules, the compound containing six methylene linkers (2) (in Table 1) has expressed a potency 70-fold greater than that of the standard drug SAHA. However, it was also observed that, despite the similar length, the triazole-linked compounds are 40-fold more active in comparison to amide-linked compounds.

Table 1. Novel Dual-Drug (HDAC/Top) Inhibitors and Their Anticancer Activities

SI No	HDAC Inhibitor	Targeted therapeutic molecule	Hybrid Molecule (HDAC and Topo)	Activity as dual drug inhibitor
1.	 SAHA	 Daunorubicin	 <b>1</b>   <b>2</b>	Dual Topo II/HDAC inhibitor. Better HDAC inhibitory activity than SAHA and show best cytotoxicity against DU-145 prostate carcinoma cell line. <sup>29</sup>  70-fold more potent than SAHA and IC50 value in nano-molar range also 40-fold more active and amide linked compound. <sup>29</sup>
2.		 Camptothecin (SN38)	 <b>3</b>	Dual Topo I/HDAC Inhibitor. Showed better cytotoxicity against DU-145 prostate cancer cell line. <sup>23</sup>
3.		 Podophyllotoxin	 <b>4</b>	Dual Topo I/HDAC Inhibitor. 10- to 20 fold more potent than SAHA. <sup>30</sup>
4.		 DACA	 <b>5</b>	Dual Topo I/HDAC inhibitor and potent anti-proliferative activity than SAHA and DACA. Induce cell-cycle arrest. <sup>31</sup>
5.		 3-amino-10-hydroxyevodiamine	 <b>6</b>	Triple Top I/II/HDAC inhibitor. Good anti-proliferative activity against MDA-MB-231 (breast cancer), HCT116 (colon cancer) and HLF (liver cancer) cell lines. <sup>32</sup>
6.	 CPT	 Evodiamine	 <b>7</b>   <b>8</b>	Dual HDAC/Topo Inhibitor. Hydroxamic acid containing compounds ( <b>7</b> ) are potent than the ortho-aminoanilide( <b>8</b> ). <sup>33</sup>
7.		 Psammaplin A	 <b>9</b>	Dual Topo I/HDAC inhibitor. good antiproliferative activity and cytotoxic potency in nanomolar range in solid tumor cell lines. <sup>34</sup>

Similarly, the same research group has designed molecules for getting dual-targeting Top/HDAC inhibitors by combining SN-38 (as the Top-I inhibitor) and SAHA via various linkers.<sup>23</sup> By further incorporating a triazole ring and modifying the linker length, plenty of compounds are synthesized. The HDAC inhibitory activity increases for the triazole ring present

in the alkyl linker. The dual-acting inhibitors were screened against the DU-145 prostate cancer cell line, and the result indicated that the novel molecule (**3**) showed better cytotoxicity than standard SAHA molecules.

The Zhang et al.<sup>30</sup> research group designed and synthesized Top-I/HDAC molecules with podophyllotoxin derivatives. A

Table 2. Novel Dual Drug Inhibitor HDAC as Common with Other Inhibitors (VGEFR/EGFR/PARP/c-Met)


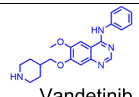
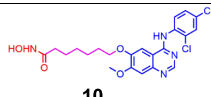
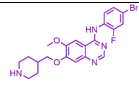
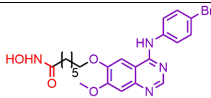
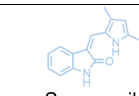
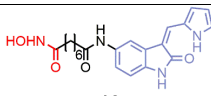
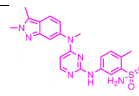
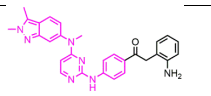
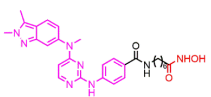
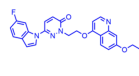
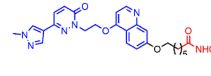
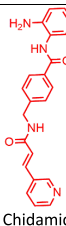
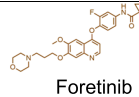
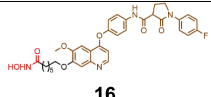
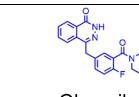
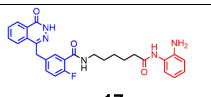
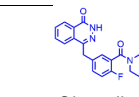
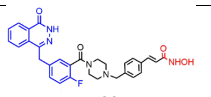
SI No	HDAC Inhibitor	Targeted molecule	Hybrid Molecule	Activity as dual drug inhibitor
1.		 Vandetinib	 <b>10</b>	showed excellent inhibitor against HDAC and VEGFR-2, exert effectiveness towards MCF-7 cancer cell line. <sup>37</sup>
2.		 Vandetinib	 <b>11</b>	Most inhibition activity against HDAC and VEGFR-2. 7-fold higher in comparison to standard drug. Great anti-proliferation potency against MCF-7 solid tumor cell line. <sup>38</sup>
3.		 Semaxanib	 <b>12</b>	Good cytotoxicity on breast cancer cell line MDA-MB231, leukemia cell line, CCRF-CEM and melanoma cell line MALME-3 in compare to SAHA. <sup>39</sup>
4.		 Pazopanib	 <b>13</b>	Ortho-aminoanilide and hydroxamic acid showed comparable HDAC inhibitory activity to MS-275 and SAHA respectively. <sup>40</sup>
			 <b>14</b>	
5.		 Selective c-Met inhibitor	 <b>15</b>	Four-fold more inhibitory activity than the standard drug Chidamide. <sup>49</sup>
6.		 Foretinib	 <b>16</b>	Good anti-proliferative activity against HCT-116, MCF-7 and A549 cell lines. <sup>51</sup>
7.		 Olaparib	 <b>17</b>	Good anti-proliferative activity than olaparib and SAHA in various cancer cells lines and 4.1-fold less cytotoxicity compared with SAHA to normal cells MCF-10A. <sup>55</sup>
8.		 Olaparib	 <b>18</b>	Active against PARP-1 and HDAC-1, which is as potent as olaparib and chidamide respectively. potent inhibitory activities against BRCA1/2-proficient K562 and MDA-MB-231 cells. <sup>56</sup>

Table 2. continued

SI No	HDAC Inhibitor	Targeted molecule	Hybrid Molecule	Activity as dual drug inhibitor
9.	SAHA	Erlotinib	19	CUDC-101 showed potent anti-proliferative activity than vorinostat (SAHA), erlotinib, lapatinib, and combinations of vorinostat/erlotinib and vorinostat/lapatinib. <sup>79</sup>
10.	Belinostat	Erlotinib	20 21	improved HDAC inhibition than SAHA and exhibited cytotoxic activity on all tested tumor cell lines. hydroxamic acid moiety containing hybrid molecule inhibit both HDAC class I and class II isoforms. <sup>64</sup>
11.		Lapatinib	22 23	displayed the most potential activity in inhibiting HDAC. potent and selective inhibition against EGFR/HER2 kinase. <sup>65</sup>

more flexible linker was introduced to increase the affinity of the hybrid molecules for the surfaces of HDAC enzymes. Therefore, a new series of hybrid molecules attached with an ether linkage were designed. Noticeable is that as the chain length increases the HDAC inhibitory activity increases according to the SAR study. The larger capping group PPT is associated with the HDAC inhibitor through a flexible ether linker, promoting the affinity between the compounds and the HDAC enzymes. The substitutions on the aromatic ring have shown further activity variability, indicating *meta*-substituted compounds have shown 10–20-fold higher potency than SAHA. *meta*-Substituted ether-linked podophyllotoxin derivatives (4) exhibited the best inhibitory activity against HDAC.

In 2014, the Yu et al. group reported a synthetic molecule WJ35435, a new class of hybrid molecule, by merging the pharmacophoric features of SAHA and DACA.<sup>31</sup> WJ35435, a dual targeting Top/HDAC inhibitor, showed better antiproliferative activity than individual known HDAC and Top inhibitors. The hybrid molecule WJ35435 (5) showed improved antiproliferative activity greater than that of DACA and vorinostat. The dual-targeted hybrid molecule inhibits the activity of both HDAC and topoisomerase I; as a result, DNA damage and cell cycle arrest happen at both G1 and G2 phases.

He et al. designed and synthesized a new series of hybrid compounds as triple-targeting antitumor agents by combining 3-amino-10-hydroxyevodiamine, a Top-I/Top-II inhibitor, and SAHA.<sup>32</sup> SAHA was conjugated to the evodiamine at the amino portion of 3-amino-10-hydroxyevodiamine to synthesize new dual Top/HDAC inhibitors. The evodiamine scaffold is connected with the zinc-binding group of SAHA via a linker oxadiazole ring. To improve the lipophilicity and

pharmacokinetic profiles, the incorporation of 1,3,4-oxadiazole rings was an effective strategy. All the hybrid compounds were reported HDAC1 inhibitors and have shown comparable activity to SAHA. Additionally, the hybrid 1,2,4-oxadiazole-containing compound (6) showed good antiproliferative activity against MDA-MB-231 (breast cancer), HCT116 (colon cancer), and HLF (liver cancer) cell lines compared to the individual parent drug.

Inspired by the above-mentioned work, the same research group has given more effort to design antitumor evodiamine derivatives. This group previously reported a triple Top-I/Top-II/HDAC inhibitor based on the synergistic effect of Top and HDAC inhibitors. The hybrid compound has shown good antiproliferative activity and a pro-apoptotic effect. However, in vivo antitumor effects led to in poor outcomes against antitumor activity, and further development is necessary. New HDAC/Top dual inhibitors were further developed and reported with admirable antitumor efficacy in both in vitro and in vivo.<sup>33</sup> In addition, hydroxamic acid (ZBG) containing compounds (7) are more potent than *ortho*-amino aniline (8). The *ortho*-amino aniline compound effectively induced apoptosis with G2/M cell cycle arrest. Further structural modifications were performed to increase efficacy.

Cincinelli et al. designed a new Top-I and HDAC hybrid inhibitor.<sup>34</sup> A series of dual-targeting inhibitors were synthesized by conjugating substituted (*E*)-7-oxyminomethyl CPTs with the active fragment of psammaplin A via an amide bond. The choice of the spacer length is a crucial factor for HDAC inhibition. The newly developed hybrid compounds are potent inhibitors of Top-I/HDAC dual inhibitory activity. The novel hybrid compound 6-(10-hydroxycamptothecin-7-



ylmethyleneaminoxy)hexanoic acid hydroxyamide (**9**) has good antiproliferative activity and cytotoxic potency in the nanomolar range in solid tumor cell lines compared to SAHA and irinotecan.

## 5. DUAL VASCULAR ENDOTHELIAL GROWTH FACTOR RECEPTOR (VEGFR) AND HDAC INHIBITORS

Vascular endothelial growth factor (VEGF) and VEGFR-2, the receptor tyrosine kinase of VEGF, are the key mediators for angiogenesis. When VEGFR-2 binds to VEGF, dimerization occurs between the ligand and the receptor and phosphorylation happens, thereby initiating downstream signaling; as a result, angiogenesis, tumor survival, and proliferations occur.<sup>35</sup> Therefore, the VEGFR/VEGFR-2 pathway is an important target for antiangiogenic therapy in cancer treatment. Bevacizumab is an FDA-approved monoclonal antibody, and the other small molecules sorafenib, sunitinib, vandetanib, and pazopanib are FDA-approved VEGFR-2 tyrosine kinase inhibitors used in various types of cancers.<sup>36</sup> However, VEGF/VEGFR-2 targeted therapy is not successful for a large number of patients. To overcome this problem, Shi's group, i.e., Peng et al., have developed novel VEGFR-2/HDAC dual inhibitors by combining 4-anilinoquinazoline with hydroxamic acid motifs of the HDAC inhibitor SAHA.<sup>37</sup> A series of compounds were designed and synthesized that simultaneously target both the VEGFR-2 and HDAC. All the compounds have modest VEGFR-2 inhibition in comparison to standard drugs. However, among them, the compound containing a 2,4-Cl substitution on the phenyl ring (**10**) showed an excellent inhibition against HDAC and VEGFR-2, exerting effectiveness toward the MCF-7 cancer cell line.

Peng et al. demonstrated a set of hybrid molecules containing *N*-phenylquinazolin-4-amine and hydroxamic acid side chain moieties of SAHA.<sup>38</sup> The hybrid molecule displayed great antiproliferation potency against MCF-7 solid tumors. All the synthesized compounds exhibited moderate inhibition against VEGFR-2 compared to vandetanib. The compound containing *N*-phenylquinazolin-4-amine moiety acts as a capping group for HDAC inhibitors. The length of the carbon chain linker highly influences HDAC inhibition, and for VEGFR-2 inhibition the position and type of halogen substitution on the phenyl ring are also important. Among the hybrids, the compound containing a 2-Br-substituted phenyl ring (**11**) exhibited the most inhibition activity against HDAC and VEGFR-2, and the inhibition was seven-fold higher in comparison to the standard drug. From further investigation, it was observed that compound **11** (in Table 2) has shown significant inhibitory activity against HDAC1, HDAC2, HDAC6, and HDAC8.

Additionally, Patel et al. reported dual-targeted inhibitors by combining semaxanib (SUS416), a known VEGFR-2 inhibitor, with SAHA.<sup>39</sup> From SAR, docking studies and in vitro cancer cell-based assays enzyme inhibitory activity has indicated that (*Z*)-*N*1-(3-((1*H*-pyrrol-2-yl)methylene)-2-oxoindolin-5-yl)-*N*8-hydroxyoctanediamide (**12**) is the lead molecule. The compound also showed cytotoxic effects against breast cancer cell line MDA-MB231, leukemia cell line CCRF-CEM, and melanoma cell line MALME-3 in comparison to SAHA. These results indicate for the further improvement of the hybrid compounds.

The FDA-approved drug pazopanib is effective against VEGFR inhibitors and used for the treatment of advanced

renal cell carcinoma.<sup>40</sup> Drug resistance and tumor relapsing have been reported in most patients who have received pazopanib.<sup>41</sup> A report indicates that combination therapy using pazopanib and HDAC enhances antitumor efficacy and minimizes drug resistance.<sup>42</sup> Based on this result, Zang et al. reported a novel set of molecules based on combining HDAC and pazopanib inhibitors.<sup>43</sup> Pazopanib is incorporated into the HDAC inhibitor pharmacophore to form pazopanib-based dual HDAC and VEGFR inhibitors. The two-hybrid compounds containing *ortho*-aminoanilide (**13**) and hydroxamic acid (**14**) have shown similar HDAC inhibitory activity to MS-275 and SAHA, respectively. Moreover, a phase I clinical study indicates that the combination of pazopanib and a HDAC inhibitor has shown an amazing result on pazopanib refractory diseases, so further assessment of *ortho*-aminoanilide-derived compounds is required.

## 6. DUAL C-MET AND HDAC INHIBITORS

Mesenchymal epithelial transition factor, a receptor of hepatocyte growth factor (HGF), is a prototypic member of the receptor tyrosine kinase (RTK) family. When HGF binds to c-Met, phosphorylation occurs and thereby activates c-Met signaling through the RAS/MAPK and PI3K/AKT pathways, which is involved in several biological activities.<sup>44</sup> Cell proliferation, progression, and metastasis happens due to the overexpression of HGF/c-Met signaling pathways.<sup>45</sup> Increased levels of both the c-Met and HGF are associated with poor clinical results in cancer patients.<sup>46</sup> Therefore, c-Met is a potential and attractive target for cancer therapy and drug development.<sup>47</sup> To stop tumor progression, the inhibition of c-Met alone is not sufficient and thus exhibits low efficacy or acquired resistance in clinical trials. The report indicates that HDACs influence c-Met and its downstream signaling pathway.<sup>48</sup> Therefore, the development of single hybrid molecules is needed that concurrently block both c-Met and HDAC, a promising strategy for cancer treatment.

The first c-Met/HDAC dual inhibitor was reported by Lu et al. by hybridizing the c-Met inhibitor and HDAC inhibitors together.<sup>49</sup> Modifications of the side chain of a known c-Met inhibitor do not show any significant effect.<sup>50</sup> To design a new hybrid compound, ZBG was incorporated at the quinoline moiety of the c-Met inhibitor, which conjugated with a pyridazinone-quinazoline moiety as a Cap group via a proper linker. All the designed compounds are effective toward c-Met kinase inhibition similar to c-Met inhibitors exhibit four fold greater inhibitory activity than the standard drug chidamide. The compound containing six carbon linkers (**15**) is most potent as a dual HDAC/c-Met inhibitor. For c-Met inhibition, linker length does not influence any significant role. The results confirmed that blockage of the c-Met and an HDAC pathway simultaneously by a single molecule was a novel approach for anticancer drug development.

A dual HDAC/c-Met inhibitor was discovered by Gong et al., via merging vorinostat (SAHA) and foretinib (a known c-Met inhibitor).<sup>51</sup> The hybrid molecules were synthesized using the pharmacophores of HDAC and c-Met inhibitor. All the synthesized compounds displayed antiproliferative activity against HCT-116, MCF-7, and A549 cell lines. The results showed that among all the synthesized hybrids, the hybrid compound (**16**) can promote the induction of apoptosis and block the G2/M phase.

## 7. DUAL POLY(ADP-RIBOSE) POLYMERASE (PARP) AND HDAC INHIBITORS

The PARP enzyme is involved in DNA repairing and various cellular processes including transcription. PARP 1 and PARP 2 are involved in the function of base excision pair (BER) and BER repairs single-strand DNA breaks. Inhibition of BER resulted as cell death. PARP inhibitors interfere with BER and as a result DNA repair occurs.<sup>52</sup> Therefore, PARP proteins are ideal targets for anticancer therapy.<sup>53</sup>

The first FDA-approved drug olaparib (PARP inhibitor) is used for the treatment of BRCA-mutated ovarian cancer. Rucaparib and niraparib were also approved by FDA to be used for BRCA-mutated ovarian cancer. However, these drugs have some disadvantages such as poor prognosis rate, low efficacy, and poor clinical outcomes in cancer patients.<sup>54</sup> Therefore, improvement of these drugs are necessary. It is reported that combinations of olaparib and HDAC inhibitors have enhanced anticancer effects. Therefore, to develop dual PARP and HDAC inhibitors, olaparib is conjugated with hydroxamic acid of SAHA.<sup>55</sup> All the synthesized compounds displayed PARP1/2 and HDAC1/6 inhibition activity compared to olaparib and vorinostat (SAHA). The piperazine unit plays an indispensable role in PARP-1 inhibition, not in PARP-2 inhibition. In particular, (*E*)-2-fluoro-*N*-(4-(3-(hydroxyamino)-3-oxoprop-1-en-1-yl)phenethyl)-5-((4-oxo-3,4-dihydrophthalazin-1-yl)methyl)benzamide (**17**) showed antiproliferative activity in compared with olaparib and SAHA in various cancer cell lines and was 4.1-fold less cytotoxic than SAHA to normal cells MCF-10A. Further study revealed that the compound **17** could induce the cleavage of PARP and regulate tumor cell growth and apoptosis.

For the synergistic inhibition of PARP-1 and histone deacetylases (HDACs), a hybrid molecule was developed by combining olaparib and chidamide, and it is an effective strategy for cancer treatment.<sup>56</sup> Chidamide, a HDAC inhibitor containing a benzamide group, is used in the treatment of refractory peripheral T-cell lymphoma.<sup>57</sup> Tian et al. designed a series of novel 2-fluoro-5-((4-oxo-3,4-dihydrophthalazin-1-yl)methyl)benzoic acid derivatives.<sup>56</sup> Different ZBGs such as benzamide or fluorine-substituted benzamide are introduced to replace hydroxamic acid, and various linkers that connect 3,4-(dihydrophthalazin-1-yl)methyl)benzoic acid to the ZBG moiety of chidamide were investigated to get most potent inhibitor. A benzamide-substituted olaparib hybrid compound (**18**) is active against PARP-1 and HDAC-1 and is as strong as olaparib and chidamide, respectively. Compound **18** has superior inhibitory activity toward BRCA1/2-proficient KS62 and MDA-MB-231 cells. Results indicate that compound **18** can be a promising dual PARP-1/HDAC-1 inhibitor for further studies.

## 8. EPIDERMAL GROWTH FACTOR RECEPTOR (EGFR)/HDAC DUAL INHIBITORS

EGFR is the key mediator for cancer cell progression and an important target among protein tyrosine kinase (PKT) inhibitors.<sup>58</sup> Erlotinib, gefitinib, and lapatinib, FDA-approved EGFR inhibitors, are effective against multiple solid tumors.<sup>59</sup> However, these drugs are only effective for a small portion of patients because of molecular heterogeneity and drug resistance.<sup>60</sup> To overcome drug resistance and poor prognosis, dual-targeted therapy is one of the recently developed strategies.<sup>61</sup> The pathways are inhibited by the inhibition of

histone deacetylases, encouraging the development of EGFR/HDAC inhibitors.<sup>62</sup>

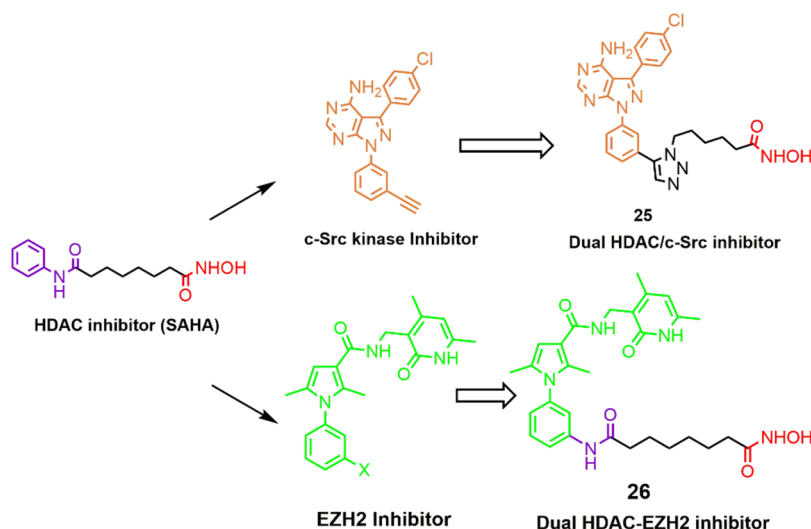
The dual-targeted EGFR/HDAC inhibitor combining the main pharmacophores of erlotinib and SAHA was reported by Cai et al.<sup>63</sup> Quinazoline and phenyl-amino moieties of erlotinib and the hydroxamic acid of SAHA are important for EGFR and HDAC inhibition, respectively. The methoxyethoxy functional group of erlotinib was suitable for incorporation in the hydroxamic acid functionality without affecting EGFR/HER2 binding affinity. The modification of chain length, the repositioning of hydroxamic acid, and substitution in the quinazoline ring have given a series of novel molecules that were mentioned. Among them, the hybrid compound 7-(4-(3-ethynylphenylamino)-7-methoxyquinazolin-6-yloxy)-*N*-hydroxyheptanamide (CUDC-101) has displayed excellent inhibitory activity against HDAC, EGFR, and HER2. CUDC-101 (**19**) has shown more potent antiproliferative activity than vorinostat (SAHA), erlotinib, lapatinib, and combinations of vorinostat/erlotinib and vorinostat/lapatinib. CUDC-101 has completed phase I clinical trials against solid tumors.

A novel dual-targeting inhibitor against EGFR and HDAC was developed by Baer et al. by the combining 4-anilinoquinazoline scaffold of erlotinib with ZBG hydroxamate or 2-aminoanilide moieties of HDAC inhibitors.<sup>64</sup> The combination of erlotinib with an *N*-(2-aminoaryl)benzamide motif linked by methylene ether can selectively inhibit class I HDAC isoforms in the submicromolar range. When the benzamide motif (**20**) is changed to a hydroxamic acid moiety, the hybrid molecule (**21**) inhibits both class I and class II HDAC isoforms. The resultant compound showed improve HDAC inhibition compared to SAHA and exhibited cytotoxic activity.

A series of another set of dual-targeting inhibitors against HDAC and EGFR were synthesized by Mahboobi et al. by combining lapatinib with a HDAC inhibitor.<sup>65</sup> The hydroxamic acid and benzamide were chosen as HDAC inhibitory headgroups and combined with the [3-chloro-4-(3-fluorobenzoyloxy)phenyl]quinazolin-4-yl-amine to obtain a chimerically designed compound. The designed hybrid molecules were structurally similar to belinostat, containing (*E*)-3-(aryl)-*N*-hydroxycarbamide as the ZBG, and displayed the most potent activity in inhibiting HDAC. The HDAC inhibitory activity is drastically reduced by positional changes in the *N*-hydroxyacrylamide moiety. The hybrid compounds 3-{5-[4-(3-chloro-4-(3-fluorobenzoyloxy)phenylamino)-quinazolin-6-yl]furan-2-yl}-*N*-hydroxyacrylamide hydrochloride monohydrate (**22**) and (*E*)-3-{3-[4-(3-chloro-4-(3-fluorobenzoyloxy)phenylamino)quinazolin-6-yl]phenyl}-*N*-hydroxyacrylamide (**23**) have also shown potent and selective inhibition against the EGFR/HDAC kinase.

## 9. DUAL-TARGETED AGENTS TARGETING HDAC AND C-SRC KINASE

A nonreceptor tyrosine kinase, c-Src, plays a crucial role in various cellular processes. Overexpression of c-Src is correlated with malignant potential.<sup>66</sup> Therefore, c-Src is an important therapeutic target in cancer therapy.<sup>67</sup> Compound **24** is the first selective inhibitor for c-Src.<sup>68</sup> A library of targeted inhibitors that may show a synergistic effect with the c-Src inhibitor was evaluated by Soellner et al.<sup>69</sup> It was reported that panobinostat was combined with c-Src and showed a synergistic effect.<sup>70</sup> HDAC inhibitors can downregulate c-Src



**Figure 5.** Synthetic approach of dual HDAC/c-Src and HDAC/EZH2 inhibitors.

levels through SRC transcription.<sup>71</sup> Taking into account the synergistic efficacy of c-Src and HDAC inhibitors, a set of dual-targeting inhibitors were designed and synthesized. In Figure 5 is shown that the PP2-alkyne scaffold of the c-Src inhibitor<sup>68</sup> attached to HDAC inhibitors via a triazole ring. The evolved hybrid compound has shown optimal efficiency to inhibit both the c-Src kinase and HDAC1. The excessive enhancement efficacy suggests that the chimera (25) acts more significantly in comparison to a HDAC inhibitor alone.

## 10. DUAL EZH2/HDAC INHIBITOR

An epigenetic enzyme, polycomb repressive complex 2 (PRC2), is the histone 3 lysine 27 (H3K27) methyltransferase that enhances zeste homologue 2 (EZH2), an epigenetic target, as it helps in the cell cycle, proliferation, and differentiation.<sup>72</sup> A high level of EZH2 is related to a variety of cancers. Some 2-pyridone-based EZH2 inhibitors are under clinical trial, and tazemetostat is approved for the treatment of cancer.<sup>73</sup>

Romanelli et al.<sup>74</sup> reported a series of EZH2 inhibitors that showed significant results by inducing cell growth arrest and apoptosis in different cell lines in breast MDA-MB231, leukemia K562, and neuroblastoma SK-N-BE cells. A branch of compounds were synthesized where pyrazole was replaced by a pyrrole ring to evaluate potent activity against EZH2. The compound 2-pyridone pyrrole decreased the H3K27me3 level and increased the level of p21 and p27 expression, weakening primary glioblastoma. Additionally, when the compound was combined with temozolomide and tazemetostat it showed a remarkable effect on cell viability. To improve the poor efficacy of HDAC inhibitors in solid tumors, the combination of EZH2 with HDAC inhibitors has been developed to boost apoptosis and DNA damage in patient-derived brain-tumor-initiating cell lines. Encouraged by these findings, dual EZH2/HDAC inhibitors have been designed and synthesized by combining EZH2 and SAHA. The new hybrid compound (26) in Figure 5 has displayed a noticeable inhibition in several cancers like leukemia U937 and THP1 along with solid cancers such as rhabdomyosarcoma RH4, glioblastoma U87, and neuroblastoma SH-N-SK; specifically, in U937 and RH4 cells the hybrid can control HDAC- and EZH2-dependent histone markers to induce cell cycle arrest in the G1 phase, which

results in apoptosis with an increase in the expression of cell differentiation markers. Lastly, it could be concluded that these findings must open a new era with the foremost application of EZH2/HDAC synchronized inhibition in cancer therapy in the near future.

## 11. SIGNIFICANCE OF THE REVIEW

Dual-target therapies can overcome the limitations over single-targeted drugs therapy or a physical mixture combination, including drug–drug interaction, poor safety, low therapeutic index value and other side effects. Histone deacetylase was widely investigated as an anticancer drug target due to its crucial role in various biological processes like cell-proliferation, metastasis, and apoptosis. In this Review, we mainly focus on dual-targeting inhibitors based on HDAC with other antitumor agents and their effectivity in cancer treatments compared to single-target HDAC inhibitors. Numerous known HDAC inhibitors, including vorinostat and panobinostat, are clinically approved but limited in their usage due to their low efficacy, drug resistance, and toxicities; additionally they are nonselective in nature. Therefore, combining HDAC inhibitors with other antitumor agents, topoisomerase inhibitors, RTK pathway inhibitors, and EZH2 in a single molecule exert a synergistic effect on cellular processes in cancer cells.<sup>75</sup> The rationale for the development of dual-targeting inhibitors is to enhance efficacy over the single-target drugs against cancer.

The reported literature indicates that CUDC-101 acted as a dual-targeting EGFR/HDAC inhibitor by combining SAHA and erlotinib. The compound CUDC-101 inhibited the breast cancer cell line MCF-7, and the result shows that the hybrid molecule was more effective than the parent compounds SAHA, erlotinib, and lapatinib. Additionally, CUDC-101 was reported to be more effective than the different combinations of SAHA + erlotinib and SAHA + lapatinib against the MCF-7 cell line. In addition, an in vivo experiment indicates the effectiveness of CUDC-101 against non-small-cell lung cancer (NSCLC), liver, breast, head and neck, colon, and pancreatic cancers.<sup>6</sup> From these results, we can say that a single bifunctional molecule that simultaneously inhibits HDAC and EGFR will be more beneficial than single targeting inhibitor in cancer resistance.



## 12. CONCLUSION

A new avenue will be opened in cancer treatment through the discovery of dual-targeting drugs. The FDA approved 124 small molecules of single targeted drugs until 2022, and thousands of small molecules are also in clinical trial. However, the single-target small molecules have some disadvantages like drug resistance and low efficiency. In order to solve these problems, a single molecule with a dual targeting ability has evolved for cancer treatment and has entered a rapid development stage. The limitations of small molecules of single-targeted drugs or drug combinations will be overcome with the discovery of dual-targeted drugs. The dual-targeting inhibitors target two oncogenic targeted sites simultaneously and thus have low adverse effects and high therapeutic value, as well as show synergistic effects. In this Review we focus on HDAC-based dual-targeted inhibitors. HDAC has a key role in regulating gene expression and cellular function. Over-expression of HDAC is responsible for many types of cancer. Therefore, it is an important chemotherapeutic target for the treatment of multiple cancers. All the dual-targeting inhibitors mentioned above are laboratory-based synthesized molecules, and they have great opportunities to enter into clinic. For an example, CUDC-101, a dual-targeting inhibitor against EGFR and HDAC, and CUDC-907, a dual-targeting inhibitor against PI3K and HDAC, have entered clinics. The phase I clinical trial of CUDC-101 was done against head and neck squamous cell carcinoma and showed good preclinical activity. The phase I and phase II studies of femepinostat (CUDC-907) were reported with relapsed/refractory diffuse large B cell and high-grade B-cell lymphoma.<sup>14,76</sup> The phase II study of the compound CUDC-907 gives encouraging results, and it has been approved by FDA for the treatment of relapsed or refractory DLBCL. A new kind of HDAC dual drug inhibitor EDO-S101, a combination of SAHA and bendamustine, inhibits both DNA and HDAC. A phase I study of this drug was done against chronic lymphoblastic leukemia (CLL) to investigate its safety and pharmacokinetics. The FDA has approved the dual drug EDO-S101 against cutaneous T-cell lymphoma.<sup>77</sup> In spite of these advantages, there are some disadvantages. In dual-targeted drugs, two main pharmacophores of the known inhibitor are combined and converted into a larger volume molecule than the parent compounds. Therefore, the problems of dual-targeting drugs are poor selectivity, membrane permeability, binding affinity, and pharmacological properties. It is a challenging task to select multiple targets in combination with HDAC with high specificity. Therefore, the knowledge of target–disease relationships, and pathway–target–drug–disease correlations are needed for in-depth understanding. Thus, the challenge for dual-target agents is to balance the two activities when combining two different pharmacophores with the desired pharmacological properties and safety profiles. Therefore, it is very much emergent and necessary to explore further, and structural optimization is also needed due to the improvement of cytotoxicity and antiproliferative activity. Despite the challenges, it is expected that in the near future the development of HDAC-based dual-targeted inhibitors will play a prominent role in cancer drug discovery.

## AUTHOR INFORMATION

### Corresponding Author

Ugir Hossain Sk – Department of Clinical and Translational Research, Chittaranjan National Cancer Institute, Kolkata, West Bengal 700026, India; [orcid.org/0000-0001-7393-454X](https://orcid.org/0000-0001-7393-454X); Email: [uhocju@gmail.com](mailto:uhocju@gmail.com), [ugirhossainsk@cnci.ac.in](mailto:ugirhossainsk@cnci.ac.in)

### Authors

Rubi Roy – Department of Clinical and Translational Research, Chittaranjan National Cancer Institute, Kolkata, West Bengal 700026, India

Tasnim Ria – Department of Clinical and Translational Research, Chittaranjan National Cancer Institute, Kolkata, West Bengal 700026, India

Debapriya RoyMahaPatra – Department of Clinical and Translational Research, Chittaranjan National Cancer Institute, Kolkata, West Bengal 700026, India

Complete contact information is available at:

<https://pubs.acs.org/10.1021/acsomega.3c00222>

### Notes

The authors declare no competing financial interest.

## ACKNOWLEDGMENTS

The authors thank the Director of CNCI, Kolkata for providing the necessary facility along with Junior Research Fellow (T.R.) support. Additionally, R.R. and U.H.S. acknowledge CSIR-HRDG for providing a CSIR fellowship [09/0030(13107)/2021-EMR-I] and research grant no. 80(0090)/20/EMR-II. D.R.M. also acknowledges ICMR for providing Senior Research Fellowship.

## REFERENCES

- (1) Dhuguru, J.; Ghoneim, O. A. Quinazoline Based HDAC Dual Inhibitors as Potential Anti-Cancer Agents. *Molecules* **2022**, *27* (7), 2294.
- (2) Baudino, T. A. Targeted Cancer Therapy: The Next Generation of Cancer Treatment. *Curr. Drug Discov Technol.* **2015**, *12* (1), 3–20.
- (3) Jordan, V. C. The Role of Tamoxifen in the Treatment and Prevention of Breast Cancer. *Curr. Probl. Cancer* **1992**, *16* (3), 134–176.
- (4) Talevi, A. Multi-Target Pharmacology: Possibilities and Limitations of the “Skeleton Key Approach” from a Medicinal Chemist Perspective. *Front Pharmacol* **2015**, *6*, 205.
- (5) Mokhtari, R. B.; Homayouni, T. S.; Baluch, N.; Morgatskaya, E.; Kumar, S.; Das, B.; Yeager, H. Combination Therapy in Combating Cancer. *Oncotarget* **2017**, *8* (23), 38022–38043.
- (6) Hesham, H. M.; Lasheen, D. S.; Abouzid, K. A. M. Chimeric HDAC Inhibitors: Comprehensive Review on the HDAC-Based Strategies Developed to Combat Cancer. *Med. Res. Rev.* **2018**, *38* (6), 2058–2109.
- (7) Anighoro, A.; Bajorath, J.; Rastelli, G. Polypharmacology: Challenges and Opportunities in Drug Discovery: Miniperspective. *J. Med. Chem.* **2014**, *57* (19), 7874–7887.
- (8) Giordano, S.; Petrelli, A. From Single- to Multi-Target Drugs in Cancer Therapy: When Aspecificity Becomes an Advantage. *CMC* **2008**, *15* (5), 422–432.
- (9) Raghavendra, N. M.; Pingili, D.; Kadasi, S.; Mettu, A.; Prasad, S. V. U. M. Dual or Multi-Targeting Inhibitors: The next Generation Anticancer Agents. *Eur. J. Med. Chem.* **2018**, *143*, 1277–1300.
- (10) Fu, R.-G.; Sun, Y.; Sheng, W.-B.; Liao, D.-F. Designing Multi-Targeted Agents: An Emerging Anticancer Drug Discovery Paradigm. *Eur. J. Med. Chem.* **2017**, *136*, 195–211.

- (11) Ivasiv, V.; Albertini, C.; Gonçalves, A. E.; Rossi, M.; Bolognesi, M. L. Molecular Hybridization as a Tool for Designing Multitargeted Drug Candidates for Complex Diseases. *Curr. Top. Med. Chem.* **2019**, *19* (19), 1694–1711.
- (12) Gao, Y.; Zhang, H.; Lirussi, F.; Garrido, C.; Ye, X.-Y.; Xie, T. Dual Inhibitors of Histone Deacetylases and Other Cancer-Related Targets: A Pharmacological Perspective. *Biochem. Pharmacol.* **2020**, *182*, 114224.
- (13) Lai, C.-J.; Bao, R.; Tao, X.; Wang, J.; Atayan, R.; Qu, H.; Wang, D.-G.; Yin, L.; Samson, M.; Forrester, J.; Zifcak, B.; Xu, G.-X.; DellaRocca, S.; Zhai, H.-X.; Cai, X.; Munger, W. E.; Keegan, M.; Pepicelli, C. V.; Qian, C. CUDC-101, a Multitargeted Inhibitor of Histone Deacetylase, Epidermal Growth Factor Receptor, and Human Epidermal Growth Factor Receptor 2, Exerts Potent Anticancer Activity. *Cancer Res.* **2010**, *70* (9), 3647–3656.
- (14) Oki, Y.; Kelly, K. R.; Flinn, I.; Patel, M. R.; Gharavi, R.; Ma, A.; Parker, J.; Hafeez, A.; Tuck, D.; Younes, A. CUDC-907 in Relapsed/Refractory Diffuse Large B-Cell Lymphoma, Including Patients with MYC-Alterations: Results from an Expanded Phase I Trial. *Haematologica* **2017**, *102* (11), 1923–1930.
- (15) Ho, T. C. S.; Chan, A. H. Y.; Ganesan, A. Thirty Years of HDAC Inhibitors: 2020 Insight and Hindsight. *J. Med. Chem.* **2020**, *63* (21), 12460–12484.
- (16) Paris, M.; Porcelloni, M.; Binaschi, M.; Fattori, D. Histone Deacetylase Inhibitors: From Bench to Clinic. *J. Med. Chem.* **2008**, *51* (6), 1505–1529.
- (17) Ververis, K.; Hiong, A.; Karagiannis, T. C.; Licciardi, P. V. Histone Deacetylase Inhibitors (HDACIs): Multitargeted Anticancer Agents. *Biologics* **2013**, *7*, 47–60.
- (18) Peng, X.; Sun, Z.; Kuang, P.; Chen, J. Recent Progress on HDAC Inhibitors with Dual Targeting Capabilities for Cancer Treatment. *Eur. J. Med. Chem.* **2020**, *208*, 112831.
- (19) Liu, T.; Wan, Y.; Xiao, Y.; Xia, C.; Duan, G. Dual-Target Inhibitors Based on HDACs: Novel Antitumor Agents for Cancer Therapy. *J. Med. Chem.* **2020**, *63* (17), 8977–9002.
- (20) Shaker, B.; Ahmad, S.; Lee, J.; Jung, C.; Na, D. In Silico Methods and Tools for Drug Discovery. *Computers in Biology and Medicine* **2021**, *137*, 104851.
- (21) Sun, D.; Zhao, Y.; Zhang, S.; Zhang, L.; Liu, B.; Ouyang, L. Dual-Target Kinase Drug Design: Current Strategies and Future Directions in Cancer Therapy. *Eur. J. Med. Chem.* **2020**, *188*, 112025.
- (22) Pawelczyk, A.; Sowa-Kasprzak, K.; Olender, D.; Zaprutko, L. Molecular Consortia—Various Structural and Synthetic Concepts for More Effective Therapeutics Synthesis. *IJMS* **2018**, *19* (4), 1104.
- (23) Guerrant, W.; Patil, V.; Canzonieri, J. C.; Yao, L.-P.; Hood, R.; Oyelere, A. K. Dual-Acting Histone Deacetylase-Topoisomerase I Inhibitors. *Bioorg. Med. Chem. Lett.* **2013**, *23* (11), 3283–3287.
- (24) Kashyap, K.; Kakkar, R. In Silico Study of the Synergistic Antitumor Effect of Hybrid Topoisomerase-HDAC Inhibitors. *Pure Appl. Chem.* **2021**, *93* (10), 1213–1228.
- (25) Pommier, Y.; Sun, Y.; Huang, S.-Y. N.; Nitiss, J. L. Roles of Eukaryotic Topoisomerases in Transcription, Replication and Genomic Stability. *Nat. Rev. Mol. Cell Biol.* **2016**, *17* (11), 703–721.
- (26) Binaschi, M.; Zunino, F.; Capranico, G. Mechanism of Action of DNA Topoisomerase Inhibitors. *Stem Cells* **1995**, *13* (4), 369–379.
- (27) Seo, Y. H. Dual Inhibitors Against Topoisomerases and Histone Deacetylases. *J. Cancer Prev* **2015**, *20* (2), 85–91.
- (28) Piccart-Gebhart, M. J. Anthracyclines and the Tailoring of Treatment for Early Breast Cancer. *N Engl J. Med.* **2006**, *354* (20), 2177–2179.
- (29) Guerrant, W.; Patil, V.; Canzonieri, J. C.; Oyelere, A. K. Dual Targeting of Histone Deacetylase and Topoisomerase II with Novel Bifunctional Inhibitors. *J. Med. Chem.* **2012**, *55* (4), 1465–1477.
- (30) Zhang, X.; Bao, B.; Yu, X.; Tong, L.; Luo, Y.; Huang, Q.; Su, M.; Sheng, L.; Li, J.; Zhu, H.; Yang, B.; Zhang, X.; Chen, Y.; Lu, W. The Discovery and Optimization of Novel Dual Inhibitors of Topoisomerase II and Histone Deacetylase. *Bioorg. Med. Chem.* **2013**, *21* (22), 6981–6995.
- (31) Yu, C.-C.; Pan, S.-L.; Chao, S.-W.; Liu, S.-P.; Hsu, J.-L.; Yang, Y.-C.; Li, T.-K.; Huang, W.-J.; Guh, J.-H. A Novel Small Molecule Hybrid of Vorinostat and DACA Displays Anticancer Activity against Human Hormone-Refractory Metastatic Prostate Cancer through Dual Inhibition of Histone Deacetylase and Topoisomerase I. *Biochem. Pharmacol.* **2014**, *90* (3), 320–330.
- (32) He, S.; Dong, G.; Wang, Z.; Chen, W.; Huang, Y.; Li, Z.; Jiang, Y.; Liu, N.; Yao, J.; Miao, Z.; Zhang, W.; Sheng, C. Discovery of Novel Multiacting Topoisomerase I/II and Histone Deacetylase Inhibitors. *ACS Med. Chem. Lett.* **2015**, *6* (3), 239–243.
- (33) Huang, Y.; Chen, S.; Wu, S.; Dong, G.; Sheng, C. Evodiamine-Inspired Dual Inhibitors of Histone Deacetylase 1 (HDAC1) and Topoisomerase 2 (TOP2) with Potent Antitumor Activity. *Acta Pharm. Sin B* **2020**, *10* (7), 1294–1308.
- (34) Cincinelli, R.; Musso, L.; Artali, R.; Guglielmi, M. B.; La Porta, I.; Melito, C.; Colelli, F.; Cardile, F.; Signorino, G.; Fucci, A.; Frusciante, M.; Pisano, C.; Dallavalle, S. Hybrid Topoisomerase I and HDAC Inhibitors as Dual Action Anticancer Agents. *PLoS One* **2018**, *13* (10), No. e0205018.
- (35) Hoebe, A.; Landuyt, B.; Highley, M. S.; Wildiers, H.; Van Oosterom, A. T.; De Bruijn, E. A. Vascular Endothelial Growth Factor and Angiogenesis. *Pharmacol. Rev.* **2004**, *56* (4), 549–580.
- (36) Jeong, W.; Doroshow, J. H.; Kummar, S. United States Food and Drug Administration Approved Oral Kinase Inhibitors for the Treatment of Malignancies. *Curr. Probl. Cancer* **2013**, *37* (3), 110–144.
- (37) Peng, F.-W.; Wu, T.-T.; Ren, Z.-W.; Xue, J.-Y.; Shi, L. Hybrids from 4-Anilinoquinazoline and Hydroxamic Acid as Dual Inhibitors of Vascular Endothelial Growth Factor Receptor-2 and Histone Deacetylase. *Bioorg. Med. Chem. Lett.* **2015**, *25* (22), 5137–5141.
- (38) Peng, F.-W.; Xuan, J.; Wu, T.-T.; Xue, J.-Y.; Ren, Z.-W.; Liu, D.-K.; Wang, X.-Q.; Chen, X.-H.; Zhang, J.-W.; Xu, Y.-G.; Shi, L. Design, Synthesis and Biological Evaluation of N-Phenylquinazolin-4-Amine Hybrids as Dual Inhibitors of VEGFR-2 and HDAC. *Eur. J. Med. Chem.* **2016**, *109*, 1–12.
- (39) Patel, H.; Chuckowree, I.; Coxhead, P.; Guille, M.; Wang, M.; Zuckermann, A.; Williams, R. S. B.; Librizzi, M.; Paranal, R. M.; Bradner, J. E.; Spencer, J. Synthesis of Hybrid Anticancer Agents Based on Kinase and Histone Deacetylase Inhibitors. *Med. Chem. Commun.* **2014**, *5* (12), 1829–1833.
- (40) Brotelle, T.; Bay, J.-O. [Pazopanib for treatment of renal cell carcinoma and soft tissue sarcomas]. *Bull. Cancer* **2014**, *101* (6), 641–646.
- (41) Torok, S.; Rezeli, M.; Kelemen, O.; Vegvari, A.; Watanabe, K.; Sugihara, Y.; Tisza, A.; Marton, T.; Kovacs, I.; Tovari, J.; Laszlo, V.; Helbich, T. H.; Hegedus, B.; Klikovits, T.; Hoda, M. A.; Klepetko, W.; Paku, S.; Marko-Varga, G.; Dome, B. Limited Tumor Tissue Drug Penetration Contributes to Primary Resistance against Angiogenesis Inhibitors. *Theranostics* **2017**, *7* (2), 400–412.
- (42) Tavallai, S.; Hamed, H. A.; Grant, S.; Poklepovic, A.; Dent, P. Pazopanib and HDAC Inhibitors Interact to Kill Sarcoma Cells. *Cancer Biol. Ther.* **2014**, *15* (5), 578–585.
- (43) Zang, J.; Liang, X.; Huang, Y.; Jia, Y.; Li, X.; Xu, W.; Chou, C. J.; Zhang, Y. Discovery of Novel Pazopanib-Based HDAC and VEGFR Dual Inhibitors Targeting Cancer Epigenetics and Angiogenesis Simultaneously. *J. Med. Chem.* **2018**, *61* (12), 5304–5322.
- (44) Peruzzi, B.; Bottaro, D. P. Targeting the C-Met Signaling Pathway in Cancer. *Clin. Cancer Res.* **2006**, *12* (12), 3657–3660.
- (45) Liu, X.; Newton, R. C.; Scherle, P. A. Developing C-MET Pathway Inhibitors for Cancer Therapy: Progress and Challenges. *Trends Mol. Med.* **2010**, *16* (1), 37–45.
- (46) Straussman, R.; Morikawa, T.; Shee, K.; Barzily-Rokni, M.; Qian, Z. R.; Du, J.; Davis, A.; Mongare, M. M.; Gould, J.; Frederick, D. T.; Cooper, Z. A.; Chapman, P. B.; Solit, D. B.; Ribas, A.; Lo, R. S.; Flaherty, K. T.; Ogino, S.; Wargo, J. A.; Golub, T. R. Tumour Micro-Environment Elicits Innate Resistance to RAF Inhibitors through HGF Secretion. *Nature* **2012**, *487* (7408), 500–504.

- (47) Jia, J.; Zhu, F.; Ma, X.; Cao, Z. W.; Li, Y. X.; Chen, Y. Z. Mechanisms of Drug Combinations: Interaction and Network Perspectives. *Nat. Rev. Drug Discov.* **2009**, *8* (2), 111–128.
- (48) Matsumoto, Y.; Motoki, T.; Kubota, S.; Takigawa, M.; Tsubouchi, H.; Gohda, E. Inhibition of Tumor-Stromal Interaction through HGF/Met Signaling by Valproic Acid. *Biochem. Biophys. Res. Commun.* **2008**, *366* (1), 110–116.
- (49) Lu, D.; Yan, J.; Wang, L.; Liu, H.; Zeng, L.; Zhang, M.; Duan, W.; Ji, Y.; Cao, J.; Geng, M.; Shen, A.; Hu, Y. Design, Synthesis, and Biological Evaluation of the First C-Met/HDAC Inhibitors Based on Pyridazinone Derivatives. *ACS Med. Chem. Lett.* **2017**, *8* (8), 830–834.
- (50) Xing, W.; Ai, J.; Jin, S.; Shi, Z.; Peng, X.; Wang, L.; Ji, Y.; Lu, D.; Liu, Y.; Geng, M.; Hu, Y. Enhancing the Cellular Anti-Proliferation Activity of Pyridazinones as c-Met Inhibitors Using Docking Analysis. *Eur. J. Med. Chem.* **2015**, *95*, 302–312.
- (51) Hu, H.; Chen, F.; Dong, Y.; Liu, Y.; Gong, P. Discovery of Novel Dual C-Met/HDAC Inhibitors as a Promising Strategy for Cancer Therapy. *Bioorg. Chem.* **2020**, *101*, 103970.
- (52) Weil, M. K.; Chen, A. P. PARP Inhibitor Treatment in Ovarian and Breast Cancer. *Curr. Probl. Cancer* **2011**, *35* (1), 7–50.
- (53) Morales, J.; Li, L.; Fattah, F. J.; Dong, Y.; Bey, E. A.; Patel, M.; Gao, J.; Boothman, D. A. Review of Poly (ADP-Ribose) Polymerase (PARP) Mechanisms of Action and Rationale for Targeting in Cancer and Other Diseases. *Crit. Rev. Eukaryot. Gene Expr.* **2014**, *24* (1), 15–28.
- (54) Jackson, S. E.; Chester, J. D. Personalised Cancer Medicine. *Int. J. Cancer* **2015**, *137* (2), 262–266.
- (55) Yuan, Z.; Chen, S.; Sun, Q.; Wang, N.; Li, D.; Miao, S.; Gao, C.; Chen, Y.; Tan, C.; Jiang, Y. Olaparib Hydroxamic Acid Derivatives as Dual PARP and HDAC Inhibitors for Cancer Therapy. *Bioorg. Med. Chem.* **2017**, *25* (15), 4100–4109.
- (56) Tian, Y.; Xie, Z.; Liao, C. Design, Synthesis and Anticancer Activities of Novel Dual Poly(ADP-Ribose) Polymerase-1/Histone Deacetylase-1 Inhibitors. *Bioorg. Med. Chem. Lett.* **2020**, *30* (8), 127036.
- (57) Moradei, O.; Vaisburg, A.; Martell, R. E. Histone Deacetylase Inhibitors in Cancer Therapy: New Compounds and Clinical Update of Benzamide-Type Agents. *Curr. Top. Med. Chem.* **2008**, *8* (10), 841–858.
- (58) Sergina, N. V.; Moasser, M. M. The HER Family and Cancer: Emerging Molecular Mechanisms and Therapeutic Targets. *Trends Mol. Med.* **2007**, *13* (12), S27–S34.
- (59) Press, M. F.; Lenz, H.-J. EGFR, HER2 and VEGF Pathways: Validated Targets for Cancer Treatment. *Drugs* **2007**, *67* (14), 2045–2075.
- (60) Huang, L.; Fu, L. Mechanisms of Resistance to EGFR Tyrosine Kinase Inhibitors. *Acta Pharmaceutica Sinica B* **2015**, *5* (5), 390–401.
- (61) Rubin, B. P.; Duensing, A. Mechanisms of Resistance to Small Molecule Kinase Inhibition in the Treatment of Solid Tumors. *Lab Invest* **2006**, *86* (10), 981–986.
- (62) Marks, P. A.; Xu, W.-S. Histone Deacetylase Inhibitors: Potential in Cancer Therapy. *J. Cell Biochem* **2009**, *107* (4), 600–608.
- (63) Cai, X.; Zhai, H.-X.; Wang, J.; Forrester, J.; Qu, H.; Yin, L.; Lai, C.-J.; Bao, R.; Qian, C. Discovery of 7-(4-(3-Ethynylphenylamino)-7-Methoxyquinazolin-6-Yloxy)-N-Hydroxyheptanamide (CUDc-101) as a Potent Multi-Acting HDAC, EGFR, and HER2 Inhibitor for the Treatment of Cancer. *J. Med. Chem.* **2010**, *53* (5), 2000–2009.
- (64) Beckers, T.; Mahboobi, S.; Sellmer, A.; Winkler, M.; Eichhorn, E.; Pongratz, H.; Maier, T.; Ciossek, T.; Baer, T.; Kelter, G.; Fiebig, H.-H.; Schmidt, M. Chimerically Designed HDAC- and Tyrosine Kinase Inhibitors. A Series of Erlotinib Hybrids as Dual-Selective Inhibitors of EGFR, HER2 and Histone Deacetylases. *Med. Chem. Commun.* **2012**, *3* (7), 829.
- (65) Mahboobi, S.; Sellmer, A.; Winkler, M.; Eichhorn, E.; Pongratz, H.; Ciossek, T.; Baer, T.; Maier, T.; Beckers, T. Novel Chimeric Histone Deacetylase Inhibitors: A Series of Lapatinib Hybrids as Potent Inhibitors of Epidermal Growth Factor Receptor (EGFR), Human Epidermal Growth Factor Receptor 2 (HER2), and Histone Deacetylase Activity. *J. Med. Chem.* **2010**, *53* (24), 8546–8555.
- (66) Thomas, S. M.; Brugge, J. S. Cellular Functions Regulated by Src Family Kinases. *Annu. Rev. Cell Dev. Biol.* **1997**, *13*, 513–609.
- (67) Martin, G. S. The Hunting of the Src. *Nat. Rev. Mol. Cell Biol.* **2001**, *2* (6), 467–475.
- (68) Brandvold, K. R.; Steffey, M. E.; Fox, C. C.; Soellner, M. B. Development of a Highly Selective C-Src Kinase Inhibitor. *ACS Chem. Biol.* **2012**, *7* (8), 1393–1398.
- (69) Ko, K. S.; Steffey, M. E.; Brandvold, K. R.; Soellner, M. B. Development of a Chimeric C-Src Kinase and HDAC Inhibitor. *ACS Med. Chem. Lett.* **2013**, *4* (8), 779–783.
- (70) Marks, P. A.; Breslow, R. Dimethyl Sulfoxide to Vorinostat: Development of This Histone Deacetylase Inhibitor as an Anticancer Drug. *Nat. Biotechnol.* **2007**, *25* (1), 84–90.
- (71) Kostyniuk, C. L.; Dehm, S. M.; Batten, D.; Bonham, K. The Ubiquitous and Tissue Specific Promoters of the Human SRC Gene Are Repressed by Inhibitors of Histone Deacetylases. *Oncogene* **2002**, *21* (41), 6340–6347.
- (72) Gulati, N.; Béguelin, W.; Giulino-Roth, L. Enhancer of Zeste Homolog 2 (EZH2) Inhibitors. *Leuk. Lymphoma* **2018**, *59* (7), 1574–1585.
- (73) Fioravanti, R.; Stazi, G.; Zwergel, C.; Valente, S.; Mai, A. Six Years (2012–2018) of Researches on Catalytic EZH2 Inhibitors: The Boom of the 2-Pyridone Compounds. *Chem. Rec* **2018**, *18* (12), 1818–1832.
- (74) Romanelli, A.; Stazi, G.; Fioravanti, R.; Zwergel, C.; Di Bello, E.; Pomella, S.; Perrone, C.; Battistelli, C.; Strippoli, R.; Tripodi, M.; del Bufalo, D.; Rota, R.; Trisciuoglio, D.; Mai, A.; Valente, S. Design of First-in-Class Dual EZH2/HDAC Inhibitor: Biochemical Activity and Biological Evaluation in Cancer Cells. *ACS Med. Chem. Lett.* **2020**, *11* (5), 977–983.
- (75) Duan, Y.-C.; Zhang, S.-J.; Shi, X.-J.; Jin, L.-F.; Yu, T.; Song, Y.; Guan, Y.-Y. Research Progress of Dual Inhibitors Targeting Crosstalk between Histone Epigenetic Modulators for Cancer Therapy. *Eur. J. Med. Chem.* **2021**, *222*, 113588.
- (76) Landsburg, D. J.; Barta, S. K.; Ramchandren, R.; Batlevi, C.; Iyer, S.; Kelly, K.; Micallef, I. N.; Smith, S. M.; Stevens, D. A.; Alvarez, M.; Califano, A.; Shen, Y.; Bosker, G.; Parker, J.; Soikes, R.; Martinez, E.; von Roemeling, R.; Martell, R. E.; Oki, Y. Fimepinostat (CUDC-907) in Patients with Relapsed/Refractory Diffuse Large B Cell and High-Grade B-Cell Lymphoma: Report of a Phase 2 Trial and Exploratory Biomarker Analyses. *Br. J. Haematol.* **2021**, *195* (2), 201–209.
- (77) Kraus, M.; Bader, J.; Mehrling, T.; Driessen, C. Edo- S101, a New Alkylating Histone-Deacetylase Inhibitor (HDACi) Fusion Molecule, Has Superior Activity Against Myeloma and B Cell Lymphoma and Strong Synergy with Proteasome Inhibitors in Vitro. *Blood* **2014**, *124* (21), 2249–2249.





# Selenium Nanoparticle in the Management of Oxidative Stress During Cancer Chemotherapy

# 133

Ugir Hossain Sk, Debapriya RoyMahapatra, and Sudin Bhattacharya

## Contents

Introduction .....	2678
Cancer and Stages of Carcinogenesis .....	2678
Insight into the Role of Reactive Oxygen Species in Cancer .....	2679
Different Aspects of Cancer Chemotherapy .....	2681
Selenium and Its Efficacy .....	2683
Development of Nano Selenium for Application in the Field of Cancer .....	2684
Nano Selenium in Combination with Antineoplastic Drugs for Cancer Therapy .....	2686
Differently Functionalized/Decorated Nano Selenium with Anticancer Drugs in Cancer Therapy .....	2687
Organo Diselenide Nano Composite as the Carrier of Cancer Chemotherapeutic Drugs ....	2692
Conclusion and Future Direction .....	2702
References .....	2703

## Abstract

Reactive oxygen species (ROS) plays a substantial role in all the stages of carcinogenesis leading to the onset of the disease cancer. Cancer cells contain higher level of reactive oxygen species than the normal counterpart. Cancer chemotherapy, one of the trademark treatments for cancer, got the approval over 75 years ago. Continuous research thereafter has developed highly active therapeutic drugs for different types of cancer. Generation of oxidative stress is one of the main cell-killing mechanisms of the therapeutic drugs. Both the

---

Bhattacharya: Retired

---

U. H. Sk · D. RoyMahapatra

Clinical and Translational Research, Chittaranjan National Cancer Institute, Kolkata, West Bengal, India

S. Bhattacharya (✉)

Chittaranjan National Cancer Institute, Kolkata, West Bengal, India

e-mail: [sudinb19572004@yahoo.co.in](mailto:sudinb19572004@yahoo.co.in)

conventional chemotherapy and targeted therapy can produce certain degree of oxidative stress. The different degree of ROS level present in different cancer cells and different level of ROS produced by the therapeutic drugs determine the sensitivity of the cancer cells toward therapy. However the ROS produced during therapy not only kills cancer cells but at the same time destroys normal cells also resulting in different types of systemic toxicity and limiting the efficacy of the treatment. The trace element selenium is present in different selenoenzymes in mammals including humans which act as antioxidant and tissue protectant. Different selenium compounds are being developed and being experimented to reduce the toxic manifestation of the antineoplastic drugs. But the narrow difference between the beneficial dose and the toxic dose limits its uses. Selenium nanoparticles have shown much less toxicity toward normal cells than other selenium compounds while displaying excellent antioxidant properties. Nano selenium can be decorated by different cancer targeted molecules and can be loaded with different anticancer drugs for therapy to reduce the oxidative stress-related systemic toxicity. Organoselenium nanocomposite loaded with anticancer drugs are also being developed for treatment against cancer with reduced toxicity.

The present book chapter will cover the present scenario on the use of nano selenium in combination with anticancer drugs, decorated nano selenium with anticancer drugs, decorated nano selenium loaded with anticancer drugs, and organoselenium nanocomposite loaded with anticancer drugs for treatment of cancer with reduced drug-induced toxicity.

---

**Keywords**

Cancer chemotherapy · Toxicity · Oxidative stress · Nano selenium · Nanocomposite

---

---

**Introduction****Cancer and Stages of Carcinogenesis**

Cancer, a disease of uncontrolled cellular growth, is heterogeneous in nature and has very high mortality rate. 90% of human cancers are caused by chemicals and the rest are caused by viruses and radiation (Malarkey et al. 2013). It is a big challenge to the human being. It is revealed from epidemiological studies that human cancers are formed through multistage cellular transformations which include tumor initiation, promotion, malignant conversion, and progression. This is also very clearly demonstrated through several experimental animal models. During cancer development a normal cell is converted into a malignant one through several cellular and molecular changes. Several factors such as chronic inflammation, environmental pollutants, ionizing radiation, UV, polycyclic aromatic hydrocarbon, viruses, bacteria, endogenous irritants, etc. have the capability to initiate the carcinogenesis process. Structural changes of DNA occur in the initiation stages which eventually produce

important genetic and chromosomal changes resulting in preneoplastic cells. These changes are irreversible in nature and the genetic damage is dose dependent. Selective clonal expansion of the initiated cells occurs in the promotion stage causing the mutated cells to grow with enhanced proliferation and/or reduced apoptosis. This promotional stage is reversed on the removal of the promoting agents. The progression stage is irreversible where preneoplastic cells are transformed to neoplastic state as a result of some molecular and cellular changes. But this changes are much complicated than what is thought.

## Insight into the Role of Reactive Oxygen Species in Cancer

Reactive oxygen species (ROS) are derived from oxygen and are chemically very reactive. It may be a radical with unpaired electron such as hydroxyl radical ( $\text{OH}^\cdot$ ), superoxide anion radical ( $\text{O}_2^{\cdot-}$ ), peroxy radical ( $\text{ROO}^\cdot$ ), nitrogen dioxide radical ( $\text{NO}_2^\cdot$ ), nitric oxide radical ( $\text{NO}^\cdot$ ), and peroxyxynitrite radical ( $\text{ONOO}^\cdot$ ) and non-radical as hydrogen peroxide ( $\text{H}_2\text{O}_2$ ) which is known as the store of reactive oxygen species. Very recently it was proved that carbonate anion radical ( $\text{CO}_3^{\cdot-}$ ) is formed instead of hydroxyl radical ( $\text{OH}^\cdot$ ) from Fenton reaction under physiological condition. Also during inflammation, nitrosoperoxy carbonate ( $\text{ONOOOCO}_2^\cdot$ ) is generated which is decomposed to form carbonate anion radical which ultimately executes oxidative modification of DNA (Fleming and Burrows 2020). ROS plays critical roles in all the stages of carcinogenesis leading to the onset of cancer. ROS are produced both endogenously by different metabolic reactions and exogenously on exposure to chemicals, automobile exhaust, cigarette smoke, polycyclic aromatic hydrocarbon, etc. ROS is required to maintain normal physiological function of cells such as protein phosphorylation, different cell signalling process to maintain cellular homeostasis, apoptosis, differentiation, and immunity. This beneficial role of ROS continues as long as it is produced and maintained properly in the cells and present in the cell in low level. Cells possess antioxidant defense system in the form of enzymes such as glutathione peroxidase (GPx), catalase (CAT), superoxide dismutase (SOD), and nonenzymatic small molecule glutathione. These antioxidant defense systems of the cell work to maintain a steady state of ROS by removing the excess ROS from the system and maintain redox homeostasis. Under certain pathological conditions such as chronic inflammation, continuous exposure to toxic chemicals such as polycyclic aromatic hydrocarbon, ionizing radiation, etc., the production of ROS is enhanced manifold, and the balance between production and removal of ROS by host antioxidant system is lost in favor of the former, and the cells enter in a state called oxidative stress. Under this condition oxidative modification of DNA, protein, lipid, and sugar molecule by ROS in the cell takes place. Formation of 8-hydroxy-2'-deoxyguanosine (8-OHdG) is one of the main ROS-mediated DNA modification. Also the ROS-mediated lipid oxidation products are very reactive and form DNA adducts such as 1, N6 – ethenodeoxyguanosine and 1, N2 – ethenodeoxyguanosine. Under normal physiological condition, these DNA damages are repaired by the repair system of the cell and

protect cells from DNA modification and chromosomal breaks. These DNA damages must be repaired before DNA replication; otherwise it will result in G-T transversions causing error in DNA replication resulting mutation and genomic instability (Takehashi et al. 2013). The number of damaged DNA which evades repair dictates the severity of mutation. Mutated tumor suppressor gene and oncogenes do show this transversions in many human cancers. The initiation and progression stages of carcinogenesis see the mutation of several tumor suppressor genes. 8-OHdG can interact with DNA methyl transferase resulting DNA hypomethylation. Oncogene hypomethylation enhances its expression and activity (Klaunig and Kamendulis 2004; Klaunig and Wang 2018). It is an early event and also frequently happened in the carcinogenesis process. Unwanted gene expression and simultaneous silencing of genes which produce antioxidant and anticancer defenses occur due to DNA hypomethylation. P53 is called the guardian of genome and is found mutated in more than 50% of cancer cases. In experimental mouse model deficient in p53 gene, mice spontaneously developed malignancy. P53 mutation disrupts NRF2 activation and its function, reducing its antioxidant response. This results in the decrease of the expression of NQO1 and HO-1, the two antioxidant enzymes, with accumulation of ROS in the cells. Upregulation of ROS positively influences and activates several cell signalling pathways such as nuclear factor kappa B (NFkB) which helps inflammation, protein kinase D (PKD), phosphoinositide 3-kinase (PI3K)/Akt, and mitogen-activated protein kinase (MAPK)/extracellular signal-regulated kinase 1/2 (ERK1/2) through mutation of KRAS oncogenes. At the same time, it downregulates protein PTEN and tyrosine phosphatase 1B (PTP1B) which negatively regulate (PI3K)/Akt signalling favoring cell survival. So redox homeostasis is deregulated due to enhanced production of ROS. All these changes help cancer cell to proliferate and survive (Moloney and Cotter 2018; Aggarwal et al. 2019). Cancer cells due to metabolic reprogramming utilize high amount of glucose compared to normal cells in order to meet the requirement of high energy and maintain a good amount of ROS, much higher than that in normal cells, to stimulate cell proliferation and induce genetic instability. Like normal cells, cancer cells also utilize transcription factor nuclear factor erythroid 2-related factor 2 (Nrf2) and antioxidant enzymes such as glutathione S-transferase, glutathione peroxidase, thioredoxin reductase, superoxide dismutase, catalase, etc. to maintain the required high ROS level and redox balance, for the cell division and proliferation. Any further increase of ROS will create oxidative stress for the cancer cells as it fails to adapt to the resulting condition and cell death occurs. Since normal cells have low level of ROS as well as its antioxidant system to maintain redox balance and normal growth, any further elevation of ROS level due to certain abnormality is counteracted by the induced antioxidant system. So if the ROS level can be enhanced beyond the threshold level of ROS of cancer cells by either enhancing it or by depleting the antioxidant system, creating a condition which is detrimental to cancer cell viability, it may be possible to selectively kill the cancer cells without affecting the normal cells (Saikolappan et al. 2019; Gandin et al. 2018).

## Different Aspects of Cancer Chemotherapy

Cancer chemotherapy is one of the most important and powerful mode of treatment for people suffering from cancer using single or combination of drugs. This trademark cancer treatment got approval over 75 years ago. The traditional cancer therapeutic drugs target rapidly dividing cells like cancer cells, but the targeted pathways are also required for the functioning of normal cells. Due to this non-specific nature, it also targets normal cells such as bone marrow cell, cells of the digestive tract, and hair follicles destroying normal cells along with cancer cells. These drugs work through damaging both nuclear and mitochondrial DNA synthesis and interfering with cell cycle. Due to poor pharmacokinetics in the body, some of the conventional cancer therapeutic drugs often require high dose to be effective and result off-target accumulation which leads to systemic toxicity (Yhee 2013). According to their mode of action, these agents are classified as alkylating agents such as bis(chloroethyl) nitrosourea (BCNU, carmustine), 1-(2-chloroethyl)-3-cyclohexyl-1-nitrosourea (CCNU, lomustine), cyclophosphamide, cisplatin, carboplatin, and oxaliplatin; anthracyclines such as daunorubicin, doxorubicin, idarubicin, epirubicin, and mitoxantrone; antimetabolites such as 5-fluorouracil, mercaptopurine, methotrexate, cytarabine, gemcitabine, cladribine, fludarabine, and thioguanine; topoisomerase I and II inhibitors such as irinotecan, topotecan, lamellarin D, camptothecin, etoposide, teniposide, and amsacrine; and plant alkaloids such as vinblastine and vincristine. These drugs through their DNA damaging action induce defects in mitochondrial function resulting enhanced ROS production. Expression of antioxidant genes was also reduced resulting further enhancement of ROS level (Yang et al. 2018; Gomes et al. 2015). So the cancer cells which have already high ROS level cannot cope with the further increase of ROS and undergo cell death through apoptosis or necrosis (Castaldo et al. 2016). ROS acts as the mediator of different caspases activation or upregulation of death receptor protein during drug-induced apoptosis of cancer cells. The nonspecific generation of ROS by these drugs in the normal tissues produces hepatotoxicity, nephrotoxicity, cardiotoxicity, myelotoxicity, and ototoxicity. Another toxic manifestation of chemotherapeutic drugs is gastrointestinal disorder mediated also through oxidative stress (Rtibi et al. 2018). Oxidative stress is also the causative factor for the damage of the cognitive function which is another major toxic effect of cancer chemotherapy during and after treatment of nearly 75% of cancer survivor (Bagnall-Moreaul et al. 2019; Jiang et al. 2018). The severity of these toxic manifestation forced reduction of chemotherapeutic dose or withdrawal of chemotherapy. The required level of ROS in cancer cells is very critical in killing these cells. Reduced level of ROS in cancer cells is also implicated in resistance of these cells toward chemotherapy as lower ROS/enhanced antioxidant level was found in resistant cells compared to the sensitive parental cells. Chronic maintenance of oxidative stress in cancer cells during exposure of cancer cells to chemotherapy results in drug-induced resistance toward therapy, while acute oxidative stress kills them (Hwang et al. 2007; Mahalingaiah and Singh 2014). The differences of ROS level in different types of



cancer cells and the different degree of oxidative stress induction by the antineoplastic drugs play critical role on the sensitivity of cancer cells toward therapy. Some cancer cells have the ability to adapt to chronic enhancement of oxidative stress by inducing the antioxidant mechanism and evade ROS-mediated apoptotic cell death. The alteration of redox balance of this section of cancer cells confers chemoresistance toward chemotherapy through the mechanism of perturbation of cell cycle process, promotion of epithelial to mesenchymal transition, or conversion to cancer like stem cell and endoplasmic reticulum induced autophagy (Kim et al. 2019). As mentioned before rapidly dividing normal cells such as bone marrow cell, cells of the digestive tract and hair follicles are more prone to chemotherapy-induced DNA damage by the oxidative stress generated, and if the damages are not repaired, it results in mutation and carcinogenesis which finally produce secondary cancers which are very refractory in nature. In order to circumvent the toxicity imparted by the conventional chemotherapeutic drugs, novel approach was made to target solely cancer cells by inhibiting specific pathways which are essential for cancer development and progress. These are classified as small molecule inhibitor of tyrosine kinase (TKI), mTOR inhibitors, monoclonal antibodies and onco-immunological agents (Baudino 2015). The theoretical idea is that the treatment will be more efficacious and less toxic. While targeting specific proteins and/or antibodies to disrupt the cell signalling process for cancer cell proliferation, inhibition of new blood vessel formation, and migration of cancer cell, most of these drugs also enhanced ROS level which acts as the mediator through multimodal action and thus also have toxic manifestation on normal cells (Teppo et al. 2017). Initially targeted therapy was considered to target a single gene or protein involved in cancer cell proliferation through inducing or silencing the particular gene/protein, and subsequent research widened the targets for clinical use, and the level of ROS plays a significant role in their efficacy or resistance to therapy in most cases. Because of the capability of the targeted drugs to target multiple genes or proteins, combination with standard chemotherapeutic drugs does not always enhance oxidative stress rather reduce the level of ROS. Several reports including clinical trials revealed that cetuximab a monoclonal antibody approved for the treatment of head and neck squamous cell carcinoma (HNSCC) and colorectal cancer (CRC) reduced the efficacy of oxaliplatin when combined with it through interfering with ROS production by targeting the particular proteins dual oxidase 2 (DUOX2) and Nox 1 required by oxaliplatin (Santoro et al. 2016; Dahan et al. 2009). On the contrary cetuximab is also reported to induce killing of cancer cells through ROS-mediated apoptotic pathway (Lu et al. 2016; Cao et al. 2016). Another example is the monoclonal antibody trastuzumab, approved for treatment of HER2-positive breast cancer patient, which enhanced doxorubicin-induced cardiotoxicity when used in combination through in part modulating oxidative stress by inhibiting ErbB2 in the cardiomyocytes (Belmonte et al. 2015; Zhang et al. 2012). However trastuzumab, like all other chemotherapeutic drug resistance, also confers resistance to treatment frequently by upregulating the antioxidant reduced thioredoxin-1 (Trx-1) activity which binds with tumor suppressor phosphatase and tensin homolog (PTEN) resulting in loss of function of PTEN protein (Sadeghirizi et al. 2016; Meuillet et al. 2004). It is reported that Trx-1

upregulation results in resistance to chemotherapy by conventional chemotherapeutic drugs and ROS level plays a critical role in the drug acquired resistance (Wangpaichitr et al. 2012). Lapatinib, a tyrosine kinase inhibitor, is approved for clinical use against HER2-positive breast cancer, but it confers resistance to treatment due to lowering of ROS level through Nrf2 activation. Experimentally it was revealed that enhancement of ROS level by Nrf2 blocker sensitizes the cancer cell to lapatinib therapy (Zhang et al. 2016).

## Selenium and Its Efficacy

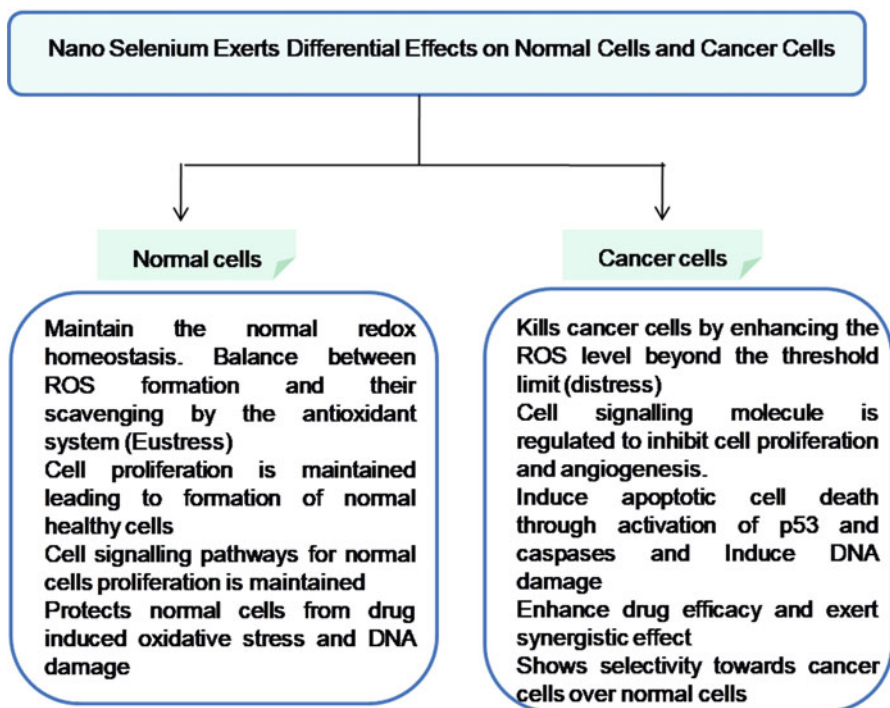
Development of small molecules to stabilize normal cell while sensitizing the cancer cells to chemotherapy is an emerging field of research and is being pursued in different laboratories all over the world. The element selenium, after its discovery in 1817 by the Swedish scientist Dr. Jöns Jacob Berzelius, was initially known as a toxic element for livestock until 1957 when the importance of selenium for the living system came to light through the revolutionary work of Dr. Klaus Schwartz and Dr. Calvin Foltz who discovered that liver necrosis was inhibited by dietary selenium in rats (Schwarz and Foltz 1957). Subsequent research revealed that selenium is an essential trace element for human being for normal physiological activity and immune function required in small amount and found toxic when present in high level. Epidemiological studies brought to light the fact that selenium is inversely related to incidence of cancer in the region where selenium level is low. Plasma concentration of 120–160 ng selenium/ml through intake of 100–150 µg selenium/day was found beneficial to reduce the risk of cancer as compared with the level of selenium at less than 120 ng/ml, but this effect depends upon the baseline level of selenium and on the cancer type. Surprisingly depleted selenium level and its overexpression do both invite diseases. Depleted level of selenium causes enhanced cancer incidence among many other diseases and its overexpression causes genotoxicity (Fairweather-Tait et al. 2011). It is initially thought that selenium exerts its beneficial role through the function of different selenoproteins present in the mammalian system. It is also revealed that selenium is highly essential as redox modulator and acts as an antioxidant in normal cellular functions. Twenty-five selenoproteins in humans have so far been reported, most of them function as enzymes and a few have nonenzymatic character. Selenium has been incorporated at the catalytic site of selenoproteins as selenocysteine (Avery and Hoffmann 2018; Arnér 2020). At the beginning it was assumed that the antioxidant, anti-inflammatory, and anticancer properties of selenium are mediated by the selenoenzymes present in the body. Subsequent preclinical cancer chemoprevention research enlightened the fact that (i) high dose of both organic and inorganic selenium is required for significant cancer chemoprevention; (ii) selenoenzymes reach its maximum level with the uptake of selenium at nutritional dose; and (iii) selenocompounds, not capable of producing selenoenzymes, still exhibit significant cancer chemoprevention. All these findings are in favor of some different mechanism of selenium cancer prevention in addition to that played by the selenoenzymes

(Ganther and Lawrence 1997; Roy et al. 2010). It was also revealed that selenium can act as antioxidant as well as prooxidant. These findings led the scientists to develop small molecule containing selenium which can counter the oxidative stress and cancer, utilizing the knowledge of the antioxidant and prooxidant character of selenium. These compounds showed high affinity toward cancer cells in terms of their accumulation and localization, and the uptake is surprisingly different for different compounds with the mechanism still not clear (Gandin et al. 2018). Selenium had shown to sensitize tumor cells toward conventional anticancer drugs (Cao et al. 2004; Fakih et al. 2005; Hu et al. 2008; Li et al. 2007; Schroeder et al. 2004; Thant et al. 2008). Efforts are also being made to utilize the selenium compounds as adjuvant with standard anticancer drugs in preclinical studies to enhance the efficacy of the therapeutic drugs by protecting the normal cells with simultaneous killing of the cancer cells through modulating different resistance biomarkers resulting in a synergistic effect (Zakharia et al. 2018; Roy et al. 2014; Chakraborty et al. 2011; Chakraborty et al. 2015; Ghosh et al. 2015; Patra et al. 2018; Spengler and Gajdacs 2019; Song et al. 2018; Rustum et al. 2018). The difference between the nutritional level and the cancer preventive supranutritional level of selenium is approximately 20-fold, whereas the difference between the supranutritional level and the selenium toxic level is merely 1-fold. The narrow window between the beneficial dose and the toxic dose of the selenium compounds is the main obstacle toward finding lead selenium compounds for clinical use. But the overall outcome of these studies showed very promising and significant results.

## Development of Nano Selenium for Application in the Field of Cancer

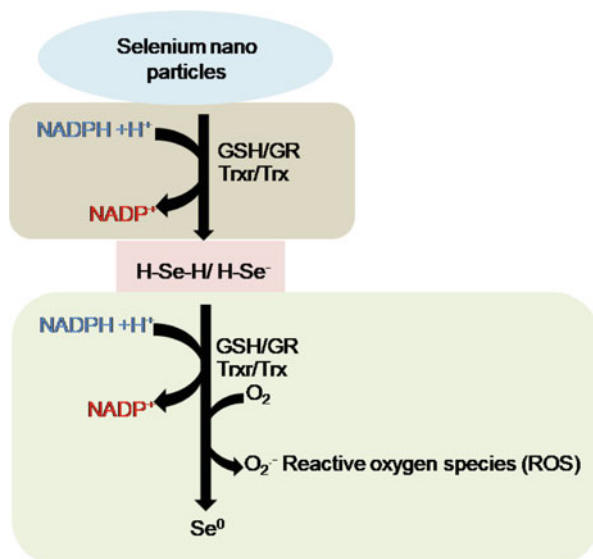
Nanobiotechnology has been emerged as an emerging field in cancer therapy to overcome the toxic manifestation imparted by the therapeutic drugs in cancer therapy by delivering smaller amount of the drug to the cancer cells and its surrounding tissues and sparing other tissues. The immune cells present in the tumor extracellular matrix/microenvironment and the enhanced permeability and retention (EPR) effect may play a significant role in the entry of nonmaterial into the cancer cells and its retention and distribution. In human, accumulation, retention, and distribution differ in different patients and cancer types (Shi et al. 2020).

Nano selenium has been found to be less toxic than inorganic and organic selenium compounds in experimental animal model (Wang et al. 2007; Zhang et al. 2008; Bhattacharjee et al. 2019). Cytotoxicity of nano selenium toward cancer cells of different origin as well as its selection of cancer cells over normal cells is well documented (Chen et al. 2008; Zhao et al. 2018; Cruz et al. 2019) (Fig. 1). The major cell-killing mechanism of nano selenium involves generation of reactive oxygen species in cancer cells (Fig. 2), loss of mitochondrial membrane potential, activation of caspases, and finally apoptosis. Nano selenium also plays significant role in cell cycle arrest and can upregulate Mir 16 protein which has direct influence on cyclin D1 and Bcl2 protein to mediate apoptotic cell death of cancer cells (Liao



**Fig. 1** Differential effects of nano selenium between normal cells and cancer cells

**Fig. 2** Generation of ROS by nano selenium



et al. 2020). Intraperitoneal application of nano selenium in experimental animals bearing hepatic H22 cancer cells showed manifold accumulation of selenium in cancer cells compared to normal tissue and killed cancer cells through generation of reactive oxygen species (Wang et al. 2014). The antioxidant and the therapeutic activity of nano selenium are mainly attributed to modulation of redox state. Nano selenium was also reported to have cancer chemopreventive property against lung carcinogenesis through reduction of oxidative stress and restoration of antioxidant enzymes (Ali et al. 2013). Very recently, nano selenium is proved to enhance the in vivo residence time of cytokine-induced killer (CIK) cells and enhance the therapeutic efficacy of CIK cell therapy through metabolization into selenocysteine and also generation of reactive oxygen species inducing apoptosis (Liu et al. 2020). The low toxicity, in vivo biodegradability, biocompatibility, and facile synthesis facilitate its utilization as an adjuvant with cancer chemotherapeutic drugs and as the drug carrier by surface decoration with different target molecules targeting specifically cancer cells and releasing the drug (Liu et al. 2015). In this book chapter, we discuss the potential of differently functionalized stable nano selenium in modulating cancer chemotherapeutic drug-induced toxicity with enhancement of their therapeutic efficacy. We have given our utmost effort to cover as much information as possible.

---

## **Nano Selenium in Combination with Antineoplastic Drugs for Cancer Therapy**

An in vitro study showed that nano selenium synergistically enhanced the antitumor efficacy of the drug adriamycin when applied in combination against the human hepatocellular carcinoma cells Bel7402 (Tan et al. 2009). In vitro and in vivo application of nano selenium in combination with irinotecan enhanced the cytotoxicity of irinotecan and controlled the adverse effect imparted by the cancer therapeutic drug. The tumor cell death occurred through p53 and caspase-mediated apoptosis. Nano selenium displayed the beneficial role through differentially modulating the Nrf2-ARE pathway in normal and tumor cells (Gao et al. 2014). Cyclophosphamide (CP) is an anticancer drug widely used clinically, but its application is severely impaired due to profound organ toxicity. In order to find whether nano selenium has the potential to modulate the organ toxicity generated by cyclophosphamide without compromising their therapeutic efficacy, it is applied in combination with the drug in a preclinical tumor-bearing mouse model. Nano selenium significantly reduced CP-induced hepatotoxicity and genotoxicity by alleviating ROS production and antioxidant enzyme level in cyclophosphamide (CP)-treated mice. By controlling ROS production, it inhibited CP-induced DNA damage and chromosomal aberrations (Bhattacharjee et al. 2014). Pulmonary injury caused by CP was also inhibited by treatment with nano selenium through modulation of pulmonary oxidative stress resulting in reduction of CP-induced DNA damage in pulmonary cells (Bhattacharjee et al. 2015). In tumor-bearing mice, nano selenium improved the antioxidant status in

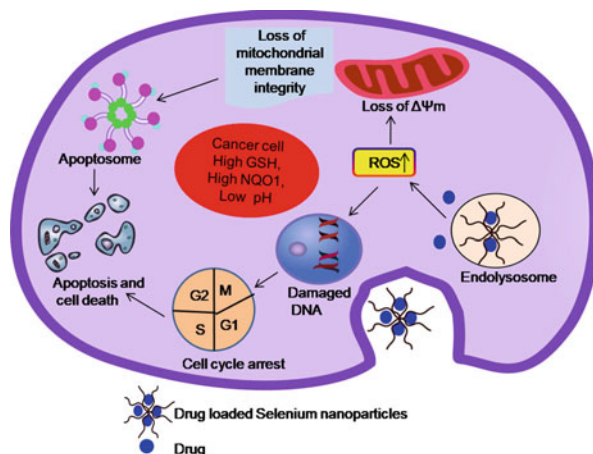
the normal tissues by reducing CP-induced oxidative stress on one side and synergistically enhanced the antitumor efficacy of CP through enhancing the oxidative stress in the tumor cells on the other side. It also displayed the antiangiogenic potential of nano selenium. It is interesting to note that pre-treatment with nano selenium offered better protection (Bhattacharjee et al. 2017). An unpublished work from the same group also showed similar chemoprotective and chemosensitizing activity of nano selenium when applied in combination with cisplatin through differentially modulating oxidative stress induced by cisplatin. In another experiment reported from a different group, nano selenium protected cisplatin-induced DNA damage, chromatin damage, and spermatotoxicity through restoration of cisplatin-induced depletion of antioxidant status and decrease of cisplatin-induced enhanced ROS and reactive nitrogen species level (Rezvanfar et al. 2013). Shafaei et al. published a work where they found that intramuscular application of nano selenium enhanced the cisplatin-induced depleted level of serum and kidney antioxidant enzymes SOD, CAT, and GPX while reduced the enhanced MDA level in rat. In contrast to these observations, they also reported that nano selenium had negative effect on the cisplatin-induced serum creatinine and urea levels (Shafaei et al. 2019). Anastrozole, an aromatase inhibitor, plays a pivotal role in the management of breast cancer, but its use causes serious side effects such as osteoporosis which causes bone fracture. The process of bone loss generates high amount of ROS which in turn causes other cell damage. The depleted level of bone density and enhanced bone resorption resulted from anastrozole treatment was significantly inhibited by nano selenium treatment which was assumed to reduce ROS formation also (Vekariya et al. 2013). In another in vitro study, selenium nanoparticles enhanced the sensitivity of PLGA encapsulated 5-fluorouracil (nano 5-FU) against colon and breast cancer cells. In contrast to generally observed phenomenon, application of nano selenium reduced nano 5-FU-induced elevated malondialdehyde and nitric oxide level and rebalanced the redox state (Abd-Rabou et al. 2019). Nano selenium, prepared by green synthesis, in combination with doxorubicin exhibited higher anticancer effect against MCF-7 human breast carcinoma cell than the individual treatment with higher LDH release (Ramamurthy et al. 2013).

---

### **Differently Functionalized/Decorated Nano Selenium with Anticancer Drugs in Cancer Therapy**

Different formulations were and are being employed to decorate surface of nano selenium to prepare stable nanocomposite capable to load different drugs and cancer cell targeted biomaterials (Fig. 3). It was observed that cellular uptake of nano selenium decorated with 11-mercapto-1-undecanol (Se@MUN) was higher in normal human cells as compared with nano selenium. Cisplatin-induced nephrotoxicity is a well-known phenomenon in patients treated with cisplatin and ROS plays a critical role in it. Se@MUN successfully protected normal

**Fig. 3** Representative picture of entry of drug-loaded decorated nano selenium into the cancer cells



human renal cells (HK2) from cisplatin-induced nephrotoxicity by inhibiting drug-induced high production of ROS. It ameliorated the reduced cell viability and fragmentation of DNA and blocked cisplatin-induced caspase 3 activation (Li et al. 2011). 5 PAMAM dendrimer-stabilized selenium nanoparticle was prepared as the carrier of cisplatin and siRNA to treat cisplatin-resistant A549/DDP cells. The nanocomposite G5@Se-DDP as well as G5@Se-DDP-siRNA did not show any apparent tissue toxicity compared to normal group. Both these two nanocomposite displayed much higher cytotoxicity than cisplatin against both normal and resistant cancer cells. Both reduced the in vivo A549/DDP tumor growth, but the effect of G5@Se-DDP-siRNA is much more prominent. The co-delivery of cisplatin and siRNA to the tumor cell resulted in synergistic action to reverse multidrug resistance. The apoptotic cell death occurred through upregulation of caspase 3 and downregulation of P-AKT, P-ERK, cyclin D1, and c-myc which indirectly indicated involvement of ROS in cell killing (Zheng et al. 2015). Lipid-coated selenium-calcium carbonate nanocomposite was used to load cisplatin and treated against bone osteosarcoma cells (MNNG/HOS) in vitro and in vivo. Pt/Se@CaCO<sub>3</sub> nanoparticles displayed synergistic cytotoxic activity in vitro with maximum generation of intracellular ROS in comparison with cisplatin, sodium selenite, Pt@CaCO<sub>3</sub> nanoparticle, and Se@CaCO<sub>3</sub> nanoparticle. In the in vivo study, the nanocomposite displayed synergistic antitumor activity with nearly 1:1 delivery of selenium and cisplatin to the tumor cells. The nanocomposite also did not show any significant toxicity in the kidney, lung, liver, heart, and spleen tissue which highlighted the efficacy of co-delivery of selenium and cisplatin in the nano form as a new therapeutic avenue (Zhao et al. 2019). 5-Fluorouracil (5-FU) is widely considered for treatment of several types of cancers specially cancer of the digestive system, but the drug acquired resistance and tissue toxicity are the barrier for successful 5-FU therapy. In order to circumvent the adverse effect of 5-FU, Liu et al. prepared selenium nanoparticle



stabilized with 5-FU and 5-FU-Se and applied in vitro and in vivo cancer model. It was observed that 5-FU surface stabilization significantly increased the cellular uptake of nano selenium and displayed high selectivity toward cancer cells. A broad-spectrum cytotoxicity was observed against different cancer cells like MCF-7, A375, Colo201, HepG2, and PC-3, whereas it displayed much less toxicity to normal cells of human origin. A375 cell, the most susceptible to 5-FU-Se of all the cancer cells tested, was chosen for some detailed study, and it was revealed that the nano selenium composite caused loss of mitochondrial membrane potential and caspase-mediated cancer cell death occurred. The activation of caspases was mediated by elevated ROS level. Strong synergistic action was noted between nano selenium and 5-FU in the nanocomposite. An in vivo mouse was selected to find the LD50 value and hepatotoxicity of the nano material. LD50 value was much higher and the hepatotoxicity was much lower as compared with selenomethionine. The observations opened up a new hope for successful treatment for human with 5-FU particularly for melanoma cancer (Liu et al. 2012). The anthracycline doxorubicin (DOX) has been used as a frontline anticancer drug to treat human cancers. But its use is severely affected due the toxicity generated in the heart, liver, kidney, and brain and by acquired resistance. Different research groups are trying to reduce these obstacles through targeted delivery of DOX to the tumor cells. Nano selenium is being utilized for this purpose. DOX was loaded in chitosan-stabilized nano selenium decorated with RGD peptide, and the product RGD-SeNP-DOX, sensitive to acidic pH, was found to inhibit angiogenesis in HUVE cells (HUVECs) by downregulating VEGF-VEGFR and p-ERK/p-AKT expression. Apoptotic cell death through caspase 3, 7, 8, and 9 activation was mediated by ROS-induced DNA fragmentation indicated by PARP cleavage. In vivo experiment with MCF7 cells-bearing nude mice revealed that the RGD-Se-DOX nanoparticle significantly reduced tumor growth and angiogenesis through activation of caspases, p53 phosphorylation, and downregulation of VEGF, VEGFR, and ERK protein. It also imparted much less toxicity to the kidney, liver, and heart as compared with DOX treatment. All these results showed that it has the potential for further studies for clinical application (Fu et al. 2016). Mesoporous nano selenium (MSe) loaded with DOX and surface coated with human serum albumin (HAS-MSe@DOX) is an unique redox-dependent nanocomposite which enhanced drug delivery and accumulation into the cancer cells under high level of glutathione. The nanocomposite synergistically killed cancer cells against in vitro and in vivo breast cancer model and also found nontoxic compared to free DOX and thus enhanced the efficacy of chemotherapy (Zhao et al. 2017). Curcumin-loaded selenium nanoparticles were used in combination with CD44-targeted pegylated hyaluronic acid-DOX nanoparticle to treat HCT 116 cells in vitro and Ehrlich ascites carcinoma in vivo. The combination therapy exerted a synergistic anticancer activity. The anticancer effect was mediated through enhanced ROS level, loss of mitochondrial potential, and apoptosis in HCT 116 cells. The combination therapy also displayed anti-inflammatory, antimetastatic, and CD44 inhibitory activities. In vivo treatment reduced the tumor burden and enhanced the survival



of the animals significantly (Kumari et al. 2018). In another approach liposomal DOX-Se nanoparticle was prepared to treat cancer cells in vitro and in vivo. The nanocomposite showed significantly higher cytotoxic effect mediated by apoptosis against A549 cells compared to nano DOX and enhanced the antitumor efficacy of DOX in vivo (Xie et al. 2018). Xia et al. reported the synthesis of folic acid (FA)-modified selenium nanoparticle loaded with DOX (FA-Se@DOX) to treat human cervical cancer which expresses folic acid receptor. It showed much higher accumulation in the tumor site compared to other organs. FA-Se@DOX significantly inhibited HeLa cell growth through activation of caspase 3 and p53 and inhibition of Ki67. The nano material was also well tolerated in different organs which showed its potential to treat cervical carcinoma effectively (Xia et al. 2018a). In another report cyclic peptide functionalized nano selenium was prepared and then loaded with DOX. The resulting nanocomposite RGDfC-Se@DOX was used to treat against A549 cells and A549 xenograft model. In comparison to free DOX or Se@DOX, it exhibited significantly higher antiproliferative and anti-invasive properties and induced apoptotic cell death. It also showed significantly higher antitumor efficacy in comparison to Se@DOX (Xia et al. 2018b). The observation that several cancer cells have high expression of Nanog protein led to the synthesis of peptide functionalized selenium nanoparticle loaded with DOX and attached with siRNA (anti-Nanog). The resulting nanocomposite RGDfC-SeNPs@DOX/siRNA showed significantly better anticancer property than RGDfC-SeNPs@DOX, RGDfC-SeNPs/siRNA, and free DOX, against hepatic cancer. It inhibited cell proliferation and killed cancer cells through caspase 3-mediated apoptosis. It showed higher accumulation specifically to the tumor site and did not have any apparent toxicity to the other organs and thus showed an alternate and better treatment modality (Xia et al. 2018c). Wang et al. in their paper reported versatile nano selenium composite to carry DOX for synergistic phototherapy-chemotherapy to treat cervical cancer. The resulting ultrasmall selenium composite Se@SiO<sub>2</sub>-FA-CuS/DOX was found to be highly effective in eliminating the cancer. It also did not exert any noticeable toxicity to the major organs, and thus the nanoplatform showed its potential for clinical application in future (Wang et al. 2018). One of the main drawbacks of DOX is its acquired resistance to cancer cell. The multidrug resistance protein mainly p-glycoprotein plays a critical role in the efflux of the anticancer drug from the cancer cells inhibiting intracellular drug accumulation. In order to circumvent the drug resistance, pH-responsive N-trimethyl chitosan-folic acid fabricated selenium nanoparticle (SeNP@TMC-FA) was utilized as the nanocarrier of DOX to treat resistant ovarian cancer cells (NCI/ADR-RES). The lower pH of cancer cells than their normal counterpart and the presence of folate receptor on the cancer cells were utilized with the hope that it would bypass MDR protein and would accumulate in the cancer cells. In fact the cytotoxicity was enhanced by tenfold compared to free DOX. Moreover it displayed much lower toxicity on the normal cells. It induced cancer cell death through caspase 3 and PARP activation. Overall DOX-SeNPs@TMC-FA was proved to be an excellent candidate for clinical

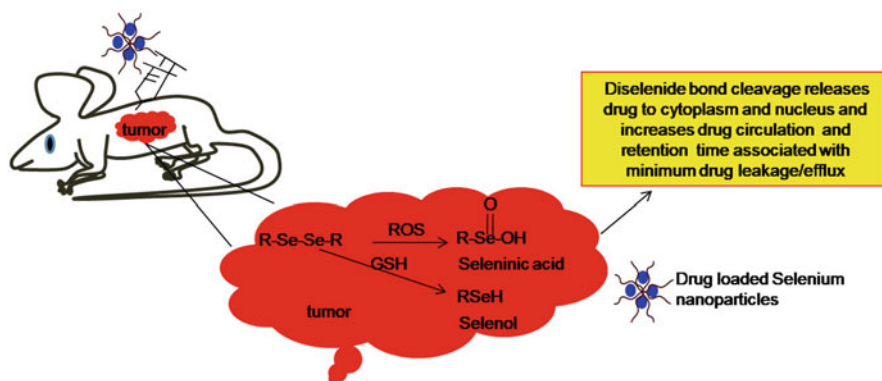
treatment for DOX resistant cancer cell (Luesakul et al. 2018). Utilizing two cancer-specific ligands RC12 and PG6 by conjugating them with nano selenium through chitosan linker, Fang et al. prepared SeNPs-DOX-ICG-RP nanocomposite and applied it along with NIR laser irradiation against HepG2 cells, and L02 normal cells. The nanocomposite showed specific selectivity toward HepG2 over normal L02 cells and had significantly higher cytotoxicity than the control groups. The ligands helped cellular intake of the nano selenium-drug composite through the process of endocytosis in the integrin overexpressed tumor cells, and NIR laser application activated the nano product to release the drugs to the cancer cells. The combination treatment substantially enhanced the production of ROS in the cancer cell facilitating death of the cancer cells (Fang et al. 2018). In similar type of work, selenium nanoparticle fabricated with galactose was used to carry DOX to the tumor site. GA-Se@DOX enhanced cellular uptake of DOX by hepatic cancer (HepG2) cells in comparison with free DOX and Se@DOX. It exhibited enhanced cytotoxicity in comparison to free DOX and Se@DOX through apoptosis. The apoptotic cell death was mediated through activation of caspases and proteins of Bcl-2 family. It also displayed excellent anticancer activity in vivo compared with Se@DOX. It also did not show any apparent toxicity to major organs like the kidney, heart, liver, lung, and spleen. All these findings are in favor of the nanocomposite as a novel and promising candidate for the clinical application against hepatocellular carcinomas (Xia et al. 2019). Continuous research has also developed nano hydroxyapatite doped with selenium to carry DOX, and the rod-shaped Se-n-HA-DOX seems to be a promising candidate for prevention of osteosarcoma recurrence and promoting osteogenesis (Gao et al. 2021). But no preclinical data is available yet. The frontline cancer chemotherapeutic drug paclitaxel (PTX) is being commonly used to treat several types of cancer, but it has serious drawbacks like low bioavailability, non-selectivity, and oxidative stress-induced peripheral neuropathy which has limited its efficacy. Nano selenium stabilized with pluronic F-127 was utilized to carry PTX to the tumor site. The anticancer activity was highly increased against MCF7 (breast), HeLa (ovarian), HT29 (colon), and A549 (lung) cancer cell lines compared to free PTX. Enhanced ROS production, loss of mitochondrial membrane potential, and subsequent activation of caspase 3 played vital role in the apoptotic cell death of the cancer cells treated with the nanocomposite. However the fact that it has antiproliferative activity against normal cells also warrants further modifications of the Pluronic F-127-Se@PTX (Bidkar et al. 2017). Nano selenium combined with biodegradable hyaluronic acid (HA) was used to deliver paclitaxel to the tumor cells having highly expressed CD44 protein which acts as HA receptor. The HA-Se@PTX significantly enhanced the cellular uptake of PTX by A549 lung cancer cells (NSCLC) and inhibited the cell proliferation better than free PTX or Se@PTX through caspase and PARP mediated apoptosis. It also had higher anticancer activity in vivo in comparison to free PTX or Se@PTX, and the toxicity imparted in animals was negligible. It is a very promising candidate for clinical application against lung cancer (Zou et al. 2019). The multikinase inhibitor sorafenib is the drug of choice

for the treatment of patients suffering from hepatic carcinoma. However poor hydrophilicity and nonspecificity toward cancer cells often limit its efficacy. PLGA-PEG-PLGA gel was used to entrap and carry chitosan-stabilized nano selenium and sorafenib, and the thermolabile injectable final product gel-SOR-LUF-SeNp was applied in combination with X-ray against HepG2-bearing immune-compromised animal. Tumor volume and weight were reduced appreciably compared to the control groups; at the same time, it was found nontoxic to different organs. Selenium content in the tumor was much higher than the other control groups. Analysis of different marker protein such as caspase 3, CD34, and Ki67 revealed that the hydrogel induced apoptosis and remarkably inhibited cell proliferation of the tumor cells and angiogenesis (Zheng et al. 2019). Anti-EGFR therapy is often applied to treat patients suffering from nasopharyngeal cancer (NPC), but it also induces side effects arising from oxidative stress resulting dose reduction. The unwanted drug-induced toxicities coupled with acquired resistance and high cost of treatment restrict its application (Morita et al. 2021). In order to manage patients with NPC, Huang et al. rationally designed stable nano selenium-based multifunctional nanocomposite Se-5Fu-Gd-P(Cet/YI-12) through combination of stabilized nano selenium (TW80-SeNPs), gadolinium agent, 5-FU, G5 PAMAM, cetuximab, YI-12 peptide, and 3,3'-dithiobis (sulfosuccinimidyl propionate). The nanoplatform is sensitive to high GSH level and low pH which is the characteristic feature of cancer cells. The Se-5Fu-Gd-P(Cet/YI-12) nanocomposite was found highly selective than Se-5Fu-Gd-P(Cet) toward cancer cells (CNE) over normal cells (L02). It displayed significantly high antiproliferative, anticancer (lowest IC<sub>50</sub> value), and antiangiogenic activity and penetration to CNE spheroids compared to other control groups. Interestingly intracellular ROS level was reduced in Se-5Fu-Gd-P(Cet/YI-12)-treated cancer cells than Se-5Fu-Gd-P(Cet) and Se-5Fu-Gd nanoparticles proving its superior ROS scavenging potential. In vivo study using CNE cell-bearing nude animals revealed much higher accumulation of Se-5Fu-Gd-P(Cet/YI-12) nanoparticle at the tumor site compared with the controls and also compared to other organs. The combined observations point out the nanocomposite as very good candidate for targeted therapy of NPC (Huang et al. 2019).

---

### **Organo Diselenide Nano Composite as the Carrier of Cancer Chemotherapeutic Drugs**

The idea is based on the fact that cancer cells possess abundant glutathione and ROS for their growth where as normal cells these are masterly controlled. Also radiation induced lots of ROS in the cells and it becomes much higher in the cancer cells. Organo diselenide of diverse structure is being cross-linked with different types of nano formulations, and the resulting nanocomposite is utilized to encapsulate different anticancer drugs with the idea that under the influence of abundant glutathione and/or ROS, namely, H<sub>2</sub>O<sub>2</sub>, the diselenide bond will undergo reductive or oxidative



**Fig. 4** Bond cleavage of diselenide of the drug-loaded selenium nano composite to disassemble the nano structure releasing the drug and selenium

cleavage (Fig. 4) and the change in the ultrastructure of the nano material will facilitate controlled release of the anticancer drugs to the tumor site in higher amount resulting in low toxicity, evading drug resistance with enhancement of drug efficacy. The presence of selenium is an added advantage. Facile and stable cross-linking of the nanocomposite carrying the drug with the potential to disassemble and release the drug at the tumor site is highly needed. Otherwise, if the drug is leaked during its circulation in the blood stream, it will result in the loss of efficacy and unwanted profound toxicity. In the year 2011, Ma et al. reported successful synthesis of diselenide bonded nano polymeric micelles (PEG-PUS<sub>2</sub>Se-PEG) utilizing di-(1-hydroxyundecyl) diselenide which is capable to load DOX and is sensitive to the clinically compatible  $\gamma$  radiation dose releasing it at the tumor site. It was also shown that the sensitivity toward radiation is due to the presence of diselenide bond in the micelles which is cleaved by the radiation-induced ROS facilitating structural change and release of DOX. The report did not reveal any preclinical data (Ma et al. 2011). In such an approach, nano sheet was developed containing selenium small molecule and coordinated with cisplatin. The product EG-Se/Pt showed preferential cytotoxicity against cancer cell over normal cell and displayed excellent broad-spectrum anticancer activity against A549, MCF7, and HT-29 cells compared to cisplatin through generation of ROS and subsequently caspase-independent apoptosis. It also reduced tumor growth in vivo without incurring any loss of weight of the treated animals compared to cisplatin (Zeng et al. 2014). Li et al. reported synthesis of cisplatin coordinated organoselenium-polylysine dendrimer nanoparticles and treated HepG2 cells in vitro, but it showed similar cytotoxicity as cisplatin. In vivo experiment with mammary cancer-bearing animal revealed similar therapeutic efficacy as cisplatin but displayed much less toxicity (Li et al. 2016). Diselenide-conjugated poly(ethylene glycol)-b-poly(L-lactide) nanomicelles were prepared to encapsulate docetaxel (M-P-Se/DTX) and treated against MCF-7 cells. Cancer cells contain plenty of glutathione for its stabilization, and under the reductive influence of glutathione, the diselenide is cleaved, and the micelles are disassembled resulting

sustained release of docetaxel. Docetaxel is a frontline drug for treatment of breast cancer, but drug resistance limits its efficacy. M-P-Se/DTX showed excellent anti-cancer activity than M-P/DTX which also highlighted the influence of selenium. The micelles also showed highly compatible to blood. The findings warrant further preclinical work in vivo (Zeng et al. 2015). Diselenide cross-linked micelles (DCM) were designed and synthesized to encapsulate and deliver DOX to the tumor site. In the presence of ROS especially  $H_2O_2$  which is abundant in the tumor site, the diselenide bond of the nanocarrier DCM/DOX is cleaved to form selenic acid prompting structural change of the nanocarrier resulting sustained release and enhanced uptake of DOX to the tumor cells. In fact DCM/DOX displayed enhanced anticancer activity than free DOX and non-cross-linked micelles (NCM)/DOX in vitro and in vivo against human prostate adenocarcinoma cells (PC3). Substantial reduction of tumor volume was also observed by DCM/DOX treatment which also showed negligible toxicity to the major organs in comparison to free DOX and NCM/DOX (Deepagan et al. 2016). Diselenium bonded diamine was cross-linked with brominated dimethoxy pillararene (BDMP5) to prepare the nanocapsule which was utilized to encapsulate DOX. To make it tumor targeting, its surface was further decorated with RGD peptide. RGD peptide has an affinity for integrins which are upregulated in the cancer cells compared to healthy normal cells. The RGD-DOX-DiSe-Cap could penetrate the cancer cells and under the influence of GSH/ $H_2O_2$  release DOX in which the anticancer activity against MCF7 cells is much better than DOX-DiSe-Cap. At the same time, it was found to be well tolerated by the normal NIH-3T3 cells (Fu et al. 2019). Wei et al. designed and synthesized (mPEG-PCL-Se)<sub>2</sub> micelles by coupling di (1-hydroxyethylene)diselenide with poly-( $\epsilon$ -caprolactone)-based polymer through a sequence of reactions. It was then used to load DOX resulting in the DOX-loaded micelles which facilitate controlled and effective delivery of DOX to the nuclei of the oral cancer cells (HN30) at the influence of reductive tumor microenvironment. Although the formulation showed significant cytotoxicity against the cancer cell, no elaborative cytotoxicity data was included in the report (Wei et al. 2016). With a view to enhance the anticancer efficacy with reduced toxicity of paclitaxel (PTX) through controlled release and accurate delivery, bis(decanoic acid)-diselenide was prepared and then diselenide containing and folic acid conjugated polymeric micelles PCL-(SeSe-PEG-FA)<sub>2</sub> having nano structure was prepared to load paclitaxel. Diselenide bond is sensitive to redox change, and cleavage of the diselenide bond disassembled the nano structure of the micelles and releases the drugs in the cytoplasm of the cells. Breast cancer cells have folate receptor and the folic acid present in the micelles specifically targeted the cancer cells. The paclitaxel-loaded micelles were subject to treat breast cancer in vitro and in vivo. PTX-PCL-(SeSe-PEG-FA)<sub>2</sub> significantly inhibit growth of 4T1 breast cancer cells compared to the PTX non-folate micelles and PTX non-selenium-non-folate micelles. The blank micelles PCL-(SeSe-PEG-FA)<sub>2</sub> were found nontoxic, and PTX-PCL-(SeSe-PEG-FA)<sub>2</sub> showed highest cytotoxicity compared to all the other formulations. In vivo experiment with a 4T1-induced solid tumor model, the PTX-PCL-(SeSe-PEG-FA)<sub>2</sub>, showed highest activity in reducing tumor growth and found safe as it did not induce significant

myelosuppression and any collateral tissue damage compared to free PTX (Behroozi et al. 2018). Diselenide-linked nano polymeric micelles were prepared from di-(1-hydroxyundecyl) diselenide, 2-ethoxy-2-oxo-1,3,2-dioxaphospholane (EOP), and 2-(but-3-yn-1-yloxy)-2-oxo-1,3,2-dioxaphospholane (BYP), and the product [PEEP-b-PBYP-Se]<sub>2</sub> was linked with a derivative of DOX through a suitable linker. The final nano polymeric prodrug [PEEP-b-(PBYP-hyd-DOX)-Se]<sub>2</sub> was biocompatible and stable in normal physiological state but cleavable under acidic pH and under reducing condition. The nano DOX prodrug facilitated much more DOX accumulation in HeLa cells compared to free DOX and efficiently killed the HeLa and HepG2 cancer cells. The preliminary in vitro therapeutic data showed that it is a very good candidate for efficient cancer therapy (Ma et al. 2018). In an effort to prepare stable diselenide-based nanocarrier, Zhai et al. selected di-(4,1-hydroxybenzylene) diselenide to prepare biocompatible diselenide-linked copolymer PEG-b-PBSe to load topo 1 inhibitor camptothecin (CPT) and topo 2 inhibitor DOX, and the resulting complex was subjected to visible light irradiation to synthesize core cross-linked nanomicelles CPT/DOX-CCM. In vitro cytotoxicity study against EMT-6 and MCF-7 cells showed apoptotic induced cell death, and the effect was remarkable compared to CPT and DOX. The effect was synergistic. Studies also revealed marked cell internalization of the nanocomposite with subsequent release of the drugs to nuclei and cytoplasm. In vivo therapeutic activity against EMT-6 tumor-bearing mice showed its superiority over CPT or DOX and did not induce any organ toxicity (Zhai et al. 2017). A carboxymethyl pullulandi-(4,1-hydroxybenzylene)diselenide amphiphilic nano conjugate Pu-HBSe was synthesized to prepare  $\beta$ -lapachone-DOX-loaded visible light-induced core cross-linked nanocomposite  $\beta$ -lapachone/DOX-CCM. The basic idea behind the preparation is that core cross-linking will give the required stability of the product;  $\beta$ -lapachone will produce ROS in the cancer cells through highly expressed NQO1 compared to normal cells. ROS has dual role here. It will disassemble the nano structure facilitating controlled release of DOX in the cancer cells and itself will help killing the cancer cells by enhancing the ROS level. In vivo experiment against HepG2 xenograft mice showed  $\beta$ -lapachone/DOX-CCM had substantially higher anticancer efficacy than free DOX and other DOX controls including non-cross-linked  $\beta$ -lapachone/DOX-NCM, and the treatment resulted highest level of apoptotic cell death compared to other control groups. Also  $\beta$ -lapachone/DOX-CCM treatment had higher animal survivability and showed no heart and kidney toxicity and weight loss of the treated animal in comparison to free DOX. This approach added a new dimension in this area of research and has great potential to be used clinically (Li et al. 2019). In a slightly different approach, Li et al. used Pu-HBSe to load redox-sensitive boronated DOX prodrug and  $\beta$ -lapachone to prepare  $\beta$ -lapachone/BDOX-CCS and applied it in combination with ultrasound to improve its accumulation in tumor vasculature and deep penetration within the tumor. It exhibited strong induction of ROS and reduction of cell viability against HepG2 cancer cells as compared to free DOX and other controls. Strong nuclear accumulation of DOX was observed in  $\beta$ -lapachone/BDOX-CCS-treated cancer cells in comparison to BDOX-CCS-treated cells. B-Lapachone/BDOX-CCS in combination with tumor directed



ultrasound irradiation displayed excellent *in vivo* antitumor activity with high survival rate and showed no apparent nephrotoxicity and cardiotoxicity in the tumor-bearing animals compared with free DOX. The combination therapy facilitated deep penetration of the drugs into the tumor site. The CCS nanocomposite was assessed for its systemic toxicity in normal animal to compare with free DOX by measuring different blood parameters biochemically. The blood analysis revealed that though the nanocomposite displayed much less hepato- and nephrotoxicity than DOX, it still had slight systemic and liver toxicities (Li et al. 2020a). A unique nano structure was designed and synthesized by combining Pu-HBSe conjugate and nanodiamond-DOX through self-assemble process and subsequent visible light irradiation. The product NDX-CCS was assessed for its cytotoxic potential against HepG2 cells, and the results revealed highest cytotoxic potential with lowest IC<sub>50</sub> value as compared to free DOX and other control groups. Treatment with NDX-CCS *i.v.* coupled with ultrasound ray against tumor-bearing mice reduced the tumor burden of the animals significantly, while free DOX had moderate effect. The nanocomposite treatment did not show any detectable toxicity in different major organs like the heart, liver, kidney, lung, and spleen compared to free DOX proving that it is biocompatible. Free DOX can penetrate deep into the tumor region and can accumulate there, but due to insufficient half-life, coupled with poor retention in the cells and high clearance, it is pumped out from the tumor resulting loss of efficacy which is overcome by NDX-CCS (Li et al. 2020b). Very recently Li et al. designed and synthesized clinically used anticancer drug pemetrexed (Pem) and cytosine diselenide (Cyt-Se-Se-Cyt) nano assemblies through hydrogen bonding self-assemble method. The amphiphilic product (Pem/Se) was subjected to combination of chemotherapy with immunotherapy and radiation therapy *in vitro* and *in vivo* against MDA-MB-231 breast cancer cells. Stronger inhibitory activity was observed from combination therapy with Pem/Se and  $\gamma$  radiation than Pem/Se and only Pem. Formation of more ROS by radiation, cleavage of diselenide bond resulting in formation of seleninic acid, and dissociation of hydrogen bonds play a critical role behind the stronger activity of the nano assemblies plus radiation. Higher generation of ROS in the cancer cells by the combination therapy-induced apoptotic cell death. The ionic character of Pem restricts its permeation through cell membrane which was overcome through combination with the diselenide as Pem/Se nano formulation exerted significantly higher anticancer activity than Pem, proving higher cellular intake. *In vivo* anticancer activity on MDA-MB-231 xenograft model revealed that both Pem/Se and Pem/Se plus  $\gamma$  radiation reduced tumor size with better activity observed from combination treatment. Both these modes of treatment did not show any hepatotoxicity and cardiotoxicity which was supported by histopathological analysis of different organs. Formation of seleninic acid may act as an antioxidant (Obieziurska et al. 2020) simultaneously to prevent tissue damage from the toxic effect of the therapeutic drug and radiation. Immunoactivation of the NK cells was evident from the findings that human leukocyte antigen E was downregulated and CD49b and IFN $\gamma$  were upregulated in cancer tissues. The combination therapy also enhanced NK cell activity in lung metastasis in a breast cancer mouse model. The pemetrexed-diselenide nano assemblies showed excellent promise for clinical application in future (Li et al. 2020c).

**Table 1** Caption

<i>Sl. no.</i>	Drug	SeNP	Target	Reference
1.	5-Fluorouracil	Combination treatment with 5-FU and selenious acid	Activation of caspases and PARP activation in RKO cells	Thant et al. (2008)
2.	Selenium	SeNP	Cytotoxic against PC-3 cancer cells, suppresses the growth of LNCaP cancer cells, and triggers tumor cell apoptosis by increasing cellular uptake. Upregulates miR-16 and downregulates two key targets of miR-16: cyclin D1 and BCL-2	Liao et al. (2020)
3.	Adriamycin	Combination treatment of adriamycin with SeNPs	Inhibits proliferation of hepatic cancer cells Bel7402	Tan et al. (2009)
4.	Irinotecan	Irinotecan combined with selenium nanoparticles	Elevation of apoptosis and selective modulation of Nrf2-ARE pathway	Gao et al. (2014)
5.	Cyclophosphamide	Protective effect of selenium nanoparticle against cyclophosphamide	Reduction of CP-induced oxidative stress and DNA damage in peripheral blood and bone marrow cells of mice	Bhattacharjee et al. (2014)
6.	Cisplatin	Protective effect of selenium nanoparticles against cisplatin-induced spermatotoxicity, DNA damage, and chromatin abnormality	Reduction of free radical toxic stress and spermatogenic DNA damage	Shafae et al. (2019)
7.	Anastrozole	Anastrozole combined with selenium nanoparticles	Lowers bone toxicity and reduction of overall bone damage in mice	Vekariya et al. (2013)
8.	Doxorubicin	Galactose-modified SeNPs loading with doxorubicin	Induction of HepG2 cell apoptosis and efficiently acted against in vivo tumor model	Xia et al. (2019)

(continued)



**Table 1** (continued)

<i>Sl. no.</i>	Drug	SeNP	Target	Reference
9.	Doxorubicin	SeNPs conjugating with targeting cyclic peptide (Arg-Gly-Asp-D-Phe-Cys [RGDfC]) for fabricating tumor-targeting delivery carrier RGDfC-SeNPs and, then, loaded with doxorubicin for improving the antitumor efficacy of doxorubicin in non-small cell lung carcinoma therapy	Inhibition of A549 cell proliferation and migration/ invasion. Elevation of apoptosis	Xia et al. (2018b)
10.	Paclitaxel (PTX)	SeNPs loaded with paclitaxel	Antiproliferative activity against lung (A549), breast (MCF7), cervical (HeLa), and colon (HT29) cancer cells. G <sub>2</sub> /M phase arrest and loss of mitochondrial membrane potential	Bidkar et al. (2017)
11.	Doxorubicin	Folic acid-modified SeNPs loaded with doxorubicin	Cellular uptake in human cervical carcinoma HeLa cells by endocytosis. By accumulating at the tumor site, as a result significant antitumor efficacy of the folic acid-modified SeNP loaded with DOX in vivo against HeLa cells. Also exerts HeLa cells' proliferation and induction of apoptosis	Xia et al. (2018a)
12.	Sorafenib	A thermosensitive hydrogel nanosystem loaded with combination of sorafenib and luciferase-SeNPs	Elevation of apoptosis in HepG2 cells through reducing the expression of Ki67 and CD34 and activating caspase 3 signalling pathway. Showing	Zheng et al. (2019)

(continued)

**Table 1** (continued)

<i>Sl. no.</i>	Drug	SeNP	Target	Reference
			antitumor effect on HepG2 cell-induced tumor-bearing nude mice	
13.	DOX	Synthesis of biocompatible and biodegradable diselenide-containing polyphosphoester using reduction-responsive di-(1-hydroxylundecyl) diselenide as an initiator to polymerization; after that doxorubicin (DOX) derivative containing an azide group was linked onto the side chain	The DOX release increases with maximum accumulative release from the prodrug NPs. Inhibition efficacy against HeLa cell and HepG2 cell	Ma et al. (2018)
14.	Selenium-platinum coordination compounds	Preparation of selenium-containing molecules (EGSe) with cisplatin (CDDP) by coordination	EG-Se/Pt induces cell apoptosis via ROS. Inhibition tumor growth in tumor-bearing mice	Zeng et al. (2014)
15.	Selenium-platinum coordination dendrimers	Preparation of monodisperse selenium-platinum coordination dendrimers with a selenium-platinum core buried inside	The complexes showed cellular uptake. The anticancer efficiency and low toxicity compared to normal in vivo	Li et al. (2016)
16.	Docetaxel (DTX)	Synthesis of amphiphilic poly(ethylene glycol)-b-poly(L-lactide) containing diselenide bond followed by DTX loading for the formation of redox active micelles	The DTX-loaded redox micelles showed the significant inhibition effect to MCF-7 cells	Zeng et al. (2015)
17.	DOX	The diselenide cross-linked micelles (DCM) were spontaneously derived from selenol-bearing triblock copolymers consisting of polyethylene glycol and polypeptide derivatives. During micelle formation, doxorubicin (DOX) was effectively encapsulated in the hydrophobic core	In tumor-bearing mice, DOX-DCM delivered more drugs at the tumor site and suppressed tumor growth	Deepagan et al. (2016)

(continued)

**Table 1** (continued)

<i>Sl. no.</i>	Drug	SeNP	Target	Reference
18.	DOX	Synthesis of RGD peptide-decorated and doxorubicin-loaded selenium nanoparticles (RGD-NPs)	Inhibition of angiogenesis by induction of apoptosis and cell cycle arrest in human umbilical vein endothelial cells (HUVECs) via suppression of VEGF-VEGFR2-ERK/AKT signalling axis by triggering ROS-mediated DNA damage. Inhibition of MCF-7 tumor growth and angiogenesis in nude mice	Fu et al. (2016)
19.	DOX	The diselenide-centered biodegradable triblock copolymers methoxyl poly(ethylene glycol)- <i>b</i> -poly( $\epsilon$ -caprolactone)- <i>b</i> -methoxyl poly(ethylene glycol) (mPEG-PCL-Se) <sub>2</sub> were synthesized by the combination of ring-opening polymerization using di (1-hydroxyethylene) diselenide and loaded with drug DOX	Increment of cellular uptake by oral squamous carcinoma (HN30) cells. Inhibition of HN30 cells	Wei et al. (2016)
20.	Paclitaxel	The insoluble anticancer drug paclitaxel (PTX) was loaded into the oxidation-reduction (redox)-responsive micelle system based on a diselenide-containing triblock copolymer, poly( $\epsilon$ -caprolactone)-bis(diselenide-methoxy poly(ethylene glycol)/poly(ethylene glycol)-folate) [PCL-(SeSe-mPEG/PEG-FA) <sub>2</sub> ]	Enhanced uptake in 4T1 breast cancer cells and tumor growth was delayed in mice	Behroozi et al. (2018)

(continued)

**Table 1** (continued)

<i>Sl. no.</i>	Drug	SeNP	Target	Reference
21.	Camptothecin (CPT) and doxorubicin (DOX)	Self-assembly and visible light-induced core cross-linking of diselenide-rich nanoparticles fabricated from PEG-b-PBSe diblock copolymers followed by encapsulation with dual drug CPT and DOX lead to cross-linked micelles (CPT/DOX-CCM)	Stable in physiological conditions with minimal drug leakage. Extension of blood circulation time	Zhai et al. (2017)
22.	$\beta$ -Lapachone/DOX-CCM	A carboxymethyl pullulan-di-(4,1-hydroxybenzyl) diselenide amphiphilic nano conjugate Pu-HBSe was synthesized to prepare $\beta$ -lapachone-DOX-loaded visible light-induced core cross-linked nano composite $\beta$ -lapachone/DOX-CCM	In vivo experiment against HepG2 xenograft mice showed $\beta$ -lapachone/DOX-CCM had substantially higher anticancer efficacy than free DOX. Also the treatment resulted highest level of apoptotic cell death. The $\beta$ -lapachone/DOX-CCM treatment had higher animal survivability and showed no toxicity of the treated animal	Li et al. (2019)
23.	$\beta$ -Lapachone/BDOX-CCS	A carboxymethyl pullulan-di-(4,1-hydroxybenzyl) diselenide amphiphilic nano conjugate Pu-HBSe to load redox-sensitive boronated DOX prodrug and $\beta$ -lapachone to prepare $\beta$ -lapachone/BDOX-CCS and applied it in combination with ultrasound	Induction of ROS and reduction of cell viability against HepG2 cancer cells as compared to free DOX. Nuclear accumulation of DOX was observed in $\beta$ -lapachone/BDOX-CCS-treated cancer cells in comparison to BDOX-CCS-treated cells. Same formulation in combination with tumor directed ultrasound	Li et al. (2020a)

(continued)

**Table 1** (continued)

<i>Sl. no.</i>	Drug	SeNP	Target	Reference
			irradiation displayed excellent in vivo antitumor activity with high survival rate	
24.	Doxorubicin	Synthesized by combining Pu-HBSe conjugate and nanodiamond-DOX through self-assemble process and subsequent visible light irradiation	Cytotoxic against HepG2 cells and the treatment with NDX-CCS i.v. coupled with ultrasound ray against tumor-bearing mice, indicates decrease tumor size	Li et al. (2020b)
25	Pemetrexed-diselenide nano assemblies	Drug pemetrexed and cytosine diselenide (Cyt-Se-Se-Cyt) nano assemblies through hydrogen bonding self-assemble method	Immunoactivation of the NK cells was evident from the findings that human leukocyte antigen E was downregulated; CD49b and IFN $\gamma$ were upregulated in cancer tissues. The combination therapy enhanced NK cell activity in lung metastasis in a breast cancer mouse model	Li et al. (2020c)

## Conclusion and Future Direction

Nanotechnology has been evolved as an important tool in the biomedical science research for the treatment of different inflammatory diseases including cancer. Due to its much lesser toxicity compared to other selenium compounds, nano selenium has proved its immense potential for cancer prevention and therapy through controlling the redox homeostasis of the normal and infected cells. The results from use of nano selenium as an adjuvant with cancer chemotherapeutic drugs to reduce the toxic manifestation and enhancement of efficacy of the drugs have opened up an area of further extensive research. Use of differently surface functionalized nano selenium with cancer cell specific ligands, antibody, peptide, etc. and loaded with anticancer drugs to carry and deliver the drugs in a controlled manner at the tumor site showed immense promise for its clinical application. Nano polymeric micelles

linked with organo diselenide are being utilized to load different anticancer drugs and controlled release at the tumor site to evade drug resistance and toxicity (Table 1). These approaches have also yielded very promising results. The ultimate target is to reduce the ROS-induced toxicity and enhance efficacy of the drugs. Nano selenium is unique in the sense that it can exert its beneficial role on the normal tissue and can kill the cancerous cells and simultaneously can be functionalized to load the anticancer drugs and release it to the cancerous site. The preliminary in vivo studies showed the nanoplateforms are nontoxic in nature and the anticancer drugs did not make any collateral tissue damage. To achieve the goal, the preliminary preclinical results are to be extended in an elaborate manner to see toxicity profile of the nanocomposite to make it ready for clinical trial for further development for translation stage from bench side to bedside. Extensive work is to be undertaken to make them relevant for clinical application. Improved functionalization of the nano selenium and pharmacokinetics study are two essential requirements in this regard. The development of stable properly functionalized nano selenium loaded with antitumor drugs having high specificity and affinity for the circulating tumor cells as in lymphoma and leukemia is the need of the hour.

---

## References

- Abd-Rabou AA, Shalby AB, Ahmed HA (2019) Selenium nanoparticles induce the chemosensitivity of fluorouracil nanoparticles in breast and colon cancer cells. *Biol Trace Elem Res* 187(1):80–91
- Aggarwal V, Tuli HS, Varol A et al (2019) Role of reactive oxygen species in cancer progression: molecular mechanisms and recent advancements. *Biomolecules* 9:735. <https://doi.org/10.3390/biom9110735>
- Ali EN, El-Sonbaty SM, Salem FM (2013) Evaluation of selenium nanoparticles as a potential chemopreventive agent against lung carcinoma. *Int J Pharm Biol Chem Sci (IJPBCS)* 2(4):38–46
- Arner ESJ (2020) Common modifications of selenocysteine in selenoproteins. *Essays Biochem* 64(1):45–53
- Avery JC, Hoffmann PR (2018) Selenium, selenoproteins, and immunity. *Nutrients* 10(9):1203
- Bagnall-Moreaul C, Sovira Chaudhry S, Salas-Ramirez K et al (2019) Chemotherapy-induced cognitive impairment is associated with increased inflammation and oxidative damage in the hippocampus. *Mol Neurobiol* 56(10):7159–7172
- Baudino TA (2015) Targeted cancer therapy: the next generation of cancer treatment. *Curr Drug Discov Technol* 12:3–20
- Behroozi F, Abdkhodaie M-J, Abandansari HS (2018) Engineering folate-targeting diselenide-containing triblock copolymer as a redox-responsive shell-sheddable micelle for antitumor therapy in vivo. *Acta Biomater* 76:239–256
- Belmonte F, Das S, Sysa-Shah P et al (2015) ErbB2 overexpression upregulates antioxidant enzymes, reduces basal levels of reactive oxygen species, and protects against doxorubicin cardiotoxicity. *Am J Physiol Heart Circ Physiol* 309:H1271–H1280
- Bhattacharjee A, Basu A, Ghosh P, Biswas J, Bhattacharya S (2014) Protective effect of Selenium nanoparticle against cyclophosphamide induced hepatotoxicity and genotoxicity in Swiss albino mice. *J Biomater Appl* 29(2):303–317
- Bhattacharjee A, Basu A, Biswas J, Bhattacharya S (2015) Nano-Se attenuates cyclophosphamide-induced pulmonary injury through modulation of oxidative stress and DNA damage in Swiss albino mice. *Mol Cell Biochem* 405(1–2):243–256

- Bhattacharjee A, Basu A, Biswas J, Sen T & Bhattacharya S. (2017) Chemoprotective and chemosensitizing properties of selenium nanoparticle (Nano-Se) during adjuvant therapy with cyclophosphamide in tumor-bearing mice. *Mol Cell Biochem* 424:13–33
- Bhattacharjee A, Basu A, Bhattacharya S (2019) Selenium nanoparticles are less toxic than inorganic and organic selenium to mice in vivo. *Nucleus* 62(3):259–268
- Bidkar AP, Sanpui P, Ghosh SS (2017) Efficient induction of apoptosis in cancer cells by paclitaxel-loaded selenium nanoparticles. *Nanomedicine (Lond)* 12(21):2641–2651
- Cao S, Durrani FA, Rustum YM (2004) Selective modulation of the therapeutic efficacy of anticancer drugs by selenium containing compounds against human tumor xenografts. *Clin Cancer Res* 10:2561–2569
- Cao S, Xia M, Mao Y et al (2016) Combined oridonin with cetuximab treatment shows synergistic anticancer effects on laryngeal squamous cell carcinoma: involvement of inhibition of EGFR and activation of reactive oxygen species-mediated JNK pathway. *Int J Oncol* 49:2075–2087
- Castaldo SA, Freitas JR, Conchinha NV, Madureira PA (2016) The tumorigenic roles of the cellular REDOX regulatory systems. *Oxidative Med Cell Longev* 2016:8413032. <https://doi.org/10.1155/2016/8413032>
- Chakraborty P, Roy SS, Sk UH, Bhattacharya S (2011) Amelioration of cisplatin-induced nephrotoxicity in mice by oral administration of diphenylmethyl selenocyanate. *Free Radic Res* 45:177–187
- Chakraborty P, Roy SS, Bhattacharya S (2015) Molecular mechanism behind the synergistic activity of diphenylmethyl selenocyanate and cisplatin against murine tumor model. *Anti-Cancer Agents Med Chem* 15:501–510
- Chen T, Wong Y-S, Zheng W, Baib Y, Huangb L (2008) Selenium nanoparticles fabricated in *Undaria pinnatifida* polysaccharide solutions induce mitochondria-mediated apoptosis in A375 human melanoma cells. *Colloids Surf B: Biointerfaces* 67:26–31
- Cruz LY, Wang D, Liu J (2019) Biosynthesis of selenium nanoparticles, characterization and X-ray induced radiotherapy for the treatment of lung cancer with interstitial lung disease. *J Photochem Photobiol B* 191:123–127
- Dahan L, Sadok A, Formento J-L et al (2009) Modulation of cellular redox state underlies antagonism between oxaliplatin and cetuximab in human colorectal cancer cell lines. *Br J Pharmacol* 158(2):610–620
- Deepagan VG, Kwon S, You DG et al (2016) In situ diselenide-crosslinked polymeric micelles for ROS-mediated anticancer drug delivery. *Biomaterials* 103:56–66
- Fairweather-Tait SJ, Bao Y, Broadley MR et al (2011) Selenium in human health and disease. *Antioxid Redox Signal* 14(7):1337–1383
- Fakih M, Cao S, Durrani FA, Rustum YM (2005) Selenium protects against toxicity induced by anticancer drugs and augments antitumor activity: a highly selective, new, and novel approach for the treatment of solid Tumors. *Clin Colorectal Cancer* 5:132–135
- Fang X, Li C, Zheng L, Yang F, Chen T (2018) Dual-targeted selenium nanoparticles for synergistic photothermal therapy and chemotherapy of tumors. *Chem–An Asian J* 13(8):996–1004
- Fleming AM, Burrows CJ (2020) On the irrelevancy of hydroxyl radical to DNA damage from oxidative stress and implications for epigenetics. *Chem Soc Rev* 49:6524–6528
- Fu X, Yang Y, Li X (2016) RGD peptide-conjugated selenium nanoparticles: antiangiogenesis by suppressing VEGF-VEGFR2-ERK/AKT pathway. *Nanomedicine* 12(6):1627–1639
- Fu S, Li F, Zang M et al (2019) Diselenium-containing ultrathin polymer nanocapsules for highly efficient targeted drug delivery and combined anticancer effect. *J Mater Chem B* 7:4927–4932
- Gandin V, Khalkar P, Braude J, Fernandes AP (2018) Organic selenium compounds as potential chemotherapeutic agents for improved cancer treatment. *Free Radic Biol Med* 127:80–97
- Ganther HE, Lawrence JR (1997) Chemical transformations of selenium in living organisms. Improved forms of selenium for cancer prevention. *Tetrahedron* 53(36):12299–12310
- Gao F, Yuan Q, Gao L (2014) Cytotoxicity and therapeutic effect of irinotecan combined with selenium nanoparticles. *Biomaterials* 35:8854–8866

- Gao J, Huang J, Shi R et al (2021) Loading and releasing behavior of selenium and doxorubicin hydrochloride in hydroxyapatite with different morphologies. *ACS Omega* 6(12):8365–8375
- Ghosh P, Roy SS, Basu A, Bhattacharjee A, Bhattacharya S (2015) Sensitization of cisplatin therapy by a naphthalimide based organoselenium compound through modulation of antioxidant enzymes and p53 mediated apoptosis. *Free Radic Res* 49:453–471
- Gomes AL Júnior, Paz MFCJ, da Silva LIS et al (2015) Serum oxidative stress markers and genotoxic profile induced by chemotherapy in patients with breast cancer: a pilot study. *Oxidative Med Cell Longev* 2015:212964. <https://doi.org/10.1155/2015/212964>
- Hu H, Li GX, Wang L et al (2008) Methylseleninic acid enhances taxane drug efficacy against human prostate cancer and Down-regulates antiapoptotic proteins BCL-XL and survivin. *Clin Cancer Res* 14:1150–1158
- Huang J, Huang W, Zhang Z et al (2019) Highly uniform synthesis of selenium nanoparticles with EGFR targeting and tumor microenvironment-responsive ability for simultaneous diagnosis and therapy of nasopharyngeal carcinoma. *ACS Appl Mater Interfaces* 11(12):11177–11193
- Hwang IT, Chung YM, Kim JJ et al (2007) Drug resistance to 5-FU linked to reactive oxygen species modulator 1. *Biochem Biophys Res Commun* 359:304–310
- Jiang Z-G, Winocur G, Wojtowicz JM et al (2018) PAN-811 prevents chemotherapy-induced cognitive impairment and preserves neurogenesis in the hippocampus of adult rats. *PLoS One* 13(1):e0191866. <https://doi.org/10.1371/journal.pone.0191866>
- Kakehashi A, Wei M, Fukushima S, Wanibuchi H (2013) Oxidative stress in the carcinogenicity of chemical carcinogens. *Cancers* 5:1332–1354
- Kim E-K, Jang MG, Song M-E et al (2019) Redox-mediated mechanism of chemoresistance in cancer cells. *Antioxidants* 8:471. <https://doi.org/10.3390/antiox8100471>
- Klaunig JE, Kamendulis LM (2004) The role of oxidative stress in carcinogenesis. *Annu Rev Pharm Toxicol* 44:239–267
- Klaunig JE, Wang Z (2018) Oxidative stress in carcinogenesis. *Curr Opin Toxicol* 7:116–121
- Kumari M, Prasad Purohit MP, Patnaik S et al (2018) Curcumin loaded selenium nanoparticles synergize the anticancer potential of doxorubicin contained in self-assembled, cell receptor targeted nanoparticles. *Eur J Pharm Biopharm* 130:185–199
- Li S, Zhou Y, Wang R et al (2007) Selenium sensitizes MCF-7 breast cancer cells to doxorubicin-induced apoptosis through modulation of phospho-AKT and its downstream substrates. *Mol Cancer Ther* 6:1031–1038
- Li Y, Li X, Wong Y-S et al (2011) The reversal of cisplatin-induced nephrotoxicity by selenium nanoparticles functionalized with 11-mercapto-1-undecanol by inhibition of ROS-mediated apoptosis. *Biomaterials* 32:9068–9076
- Li T, Smet M, Dehaen W, Xu H (2016) Selenium–platinum coordination dendrimers with controlled anticancer activity. *ACS Appl Mater Interfaces* 8(6):3609–3614
- Li H, Li Q, Hou W et al (2019) Enzyme-catalytic self-triggered release of drugs from a nanosystem for efficient delivery to nuclei of tumor cells. *ACS Appl Mater Interfaces* 11(46):43581–43587
- Li Q, Hou W, Li M et al (2020a) Ultrasound combined with core cross-linked nanosystem for enhancing penetration of doxorubicin prodrug/beta-lapachone into tumors. *Int J Nanomedicine* 2020:4825–4845
- Li M, Li Q, Hou W et al (2020b) A redox-sensitive core-crosslinked nanosystem combined with ultrasound for enhanced deep penetration of nanodiamonds into tumors. *RSC Adv* 10:15252–15263
- Li T, Pan S, Gao S et al (2020c) Diselenide–pemetrexed assemblies for combined cancer immuno-, radio-, and chemotherapies. *Angew Chem* 59(7):2700–2704
- Liao G, Tang J, Wang D et al (2020) Selenium nanoparticles (SeNPs) have potent antitumor activity against prostate cancer cells through the upregulation of miR-16. *World J Surg Oncol* 18:81–91
- Liu W, Li X, Wong Y-S et al (2012) Selenium nanoparticles as a carrier of 5-fluorouracil to achieve anticancer synergism. *ACS Nano* 6(8):6578–6591
- Liu T, Zeng L, Jiang W (2015) Rational design of cancer-targeted selenium nanoparticles to antagonize multidrug resistance in cancer cells. *Nanomedicine* 11(4):947–958



- Liu T, Xu L, He L (2020) Selenium nanoparticles regulates selenoprotein to boost cytokine-induced killer cells-based cancer immunotherapy. *Nano Today* 35:100975. <https://doi.org/10.1016/j.nantod.2020.100975>
- Lu H, Li X, Lu Y et al (2016) ASCT2 (SLC1A5) is an EGFR-associated protein that can be co-targeted by cetuximab to sensitize cancer cells to ROS-induced apoptosis. *Cancer Lett* 381(1):23–30
- Luesakul U, Puthong S, Neamati N, Muangsin N (2018) pH-responsive selenium nanoparticles stabilized by folate-chitosan delivering doxorubicin for overcoming drug-resistant cancer cells. *Carbohydr Polym* 181:841–850
- Ma N, Xu H, An L et al (2011) Radiation-sensitive diselenide block co-polymer micellar aggregates: toward the combination of radiotherapy and chemotherapy. *Langmuir* 27(10):5874–5878
- Ma G, Liu J, He J et al (2018) Dual-responsive polyphosphoester-doxorubicin prodrug containing a diselenide bond: synthesis, characterization, and drug delivery. *ACS Biomater Sci Eng* 4(7):2443–2452
- Mahalingaiah PKS, Singh KP (2014) Chronic oxidative stress increases growth and tumorigenic potential of MCF-7 breast cancer cells. *PLoS One* 9(1):e87371. <https://doi.org/10.1371/journal.pone.0087371>
- Malarkey DE, Hoenerhoff M, Maronpot RR (2013) Chapter 5: Carcinogenesis: mechanisms and manifestations. In: Haschek and Rousseaux's handbook of toxicologic pathology. 3, pp 107–146
- Meuillet EJ, Mahadevan D, Berggren M et al (2004) Thioredoxin-1 binds to the C2 domain of PTEN inhibiting PTEN's lipid phosphatase activity and membrane binding: a mechanism for the functional loss of PTEN's tumor suppressor activity. *Arch Biochem Biophys* 429(2):123–133
- Moloney JN, Cotter TG (2018) ROS signalling in the biology of cancer. *Semin Cell Dev Biol* 80:50–64
- Morita M, Iizuka-Ohashi M, Watanabe M et al (2021) Oxidative stress induces EGFR inhibition-related skin cell death. *J Clin Biochem Nutr* 68(3):235–242
- Obieziurska M, Agata J, Pacuła AJ, Laskowska A et al (2020) Seleninic acid potassium salts as water-soluble biocatalysts with enhanced bioavailability. *Materials* 13:661. <https://doi.org/10.3390/ma13030661>
- Patra AR, Roy SS, Basu A, Bhuniya A, Bhattacharjee A, Hajra S, Sk UH, Baral R, Bhattacharya S (2018) Design and synthesis of coumarin-based organoselenium as a new hit for myeloprotection and synergistic therapeutic efficacy in adjuvant therapy. *Sci Rep* 8:2194
- Ramamurthy CH, Sampath KS, Arunkumar P et al (2013) Green synthesis and characterization of selenium nanoparticles and its augmented cytotoxicity with doxorubicin on cancer cells. *Bioprocess Biosyst Eng* 36(8):1131–1139
- Rezvanfar MA, Rezvanfar MA, Shahverdi AR et al (2013) Protection of cisplatin-induced spermatotoxicity, DNA damage and chromatin abnormality by selenium nano-particles. *Toxicol Appl Pharmacol* 266:356–365
- Roy SS, Ghosh P, Sk UH, Chakraborty P, Biswas J, Mandal S, Bhattacharjee A, Bhattacharya S (2010) Naphthalimide based novel organoselenocyanates: finding less toxic forms of selenium that would retain protective efficacy. *Bioorg Med Chem Lett* 20:6951–6956
- Roy SS, Chakraborty P, Biswas J, Bhattacharya S (2014) 2-[5-Selenocyanato-pentyl]-6-amino-benzo[de]isoquinoline-1,3-dione inhibits angiogenesis, induces p53 dependent mitochondrial apoptosis and enhances therapeutic efficacy of cyclophosphamide. *Biochimie* 105:137–148
- Rtibi K, Selmi S, Grami D et al (2018) Contribution of oxidative stress in acute intestinal mucositis induced by 5 fluorouracil (5-FU) and its pro-drug capecitabine in rats. *Toxicol Mech Methods* 28(4):262–267
- Rustum YM, Chintala S, Durrani FA, Bhattacharya A (2018) Non-coding micro RNAs and hypoxia-inducible factors are selenium targets for development of a mechanism-based combination strategy in clear-cell renal cell carcinoma-bench-to-bedside therapy. *Int J Mol Sci* 19(11):3378–3397
- Sadeghirizi A, Yazdanparast R, Aghazadeh S (2016) Combating trastuzumab resistance by targeting thioredoxin-1/PTEN interaction. *Tumour Biol* 37(5):6737–6747

- Saikolappan S, Kumar B, Shishodia G et al (2019) Reactive oxygen species and cancer: a complex interaction. *Cancer Lett* 452:132–143
- Santoro V, Jia R, Thompson H et al (2016) Role of reactive oxygen species in the abrogation of oxaliplatin activity by cetuximab in colorectal cancer. *J Natl Cancer Inst* 108(6):djv394. <https://doi.org/10.1093/jnci/djv394>
- Schroeder CP, Goeldner EM, Schulze-Forster K et al (2004) Effect of selenite combined with chemotherapeutic agents on the proliferation of human carcinoma cell lines. *Biol Trace Elem Res* 99:17–25
- Schwarz K, Foltz CM (1957) Selenium as an integral part of factor 3 against dietary necrosis liver degeneration. *J Am Chem Soc* 79(12):3292–3293
- Shafae MMA, Mohamed HS, Ahmed SA, Kandeil MA (2019) Effect of selenium and nano-selenium on cisplatin-induced nephrotoxicity in albino rats. *Ukr Biochem J* 91:86–95
- Shi Y, Meel R, Chen X, Lammers T (2020) The EPR effect and beyond: Strategies to improve tumor targeting and cancer nanomedicine treatment efficacy. *Theranostics* 10(17):7921–7924
- Song M, Kumaran MN, Gounder M et al (2018) Phase I trial of selenium plus chemotherapy in gynecologic cancers. *Gynecol Oncol* 150:478–486
- Spengler G, Gajdác M, Mar' MA et al (2019) Adjuvant selenium supplementation in the form of sodium selenite in postoperative critically ill patients with severe sepsis. *Molecules* 24:336–350
- Tan L, Jia X, Jiang X et al (2009) In vitro study on the individual and synergistic cytotoxicity of adriamycin and selenium nanoparticles against Bel7402 cells with a quartz crystal microbalance. *Biosens Bioelectron* 24:2268–2272
- Teppo H-R, Soini Y, Karihtala P (2017) Reactive oxygen species-mediated mechanisms of action of targeted cancer therapy. *Oxidative Med Cell Longev* 2017:1485283. <https://doi.org/10.1155/2017/1485283>
- Thant AA, Wu Y, Lee J et al (2008) Role of caspases in 5-FU and selenium-induced growth inhibition of colorectal cancer cells. *Anticancer Res* 28:3579–3592
- Vekariya KK, Kaur J, Tikoo K (2013) Alleviating anastrozole induced bone toxicity by selenium nanoparticles in SD rats. *Toxicol Appl Pharmacol* 268:212–220
- Wang H, Zhang J, Yu H (2007) Elemental selenium at nano size possesses lower toxicity without compromising the fundamental effect on selenoenzymes: comparison with selenomethionine in mice. *Free Radic Biol Med* 42:1524–1533
- Wang X, Sun K, Tan Y, Wu S, Zhang J (2014) Efficacy and safety of selenium nanoparticles administered intraperitoneally for the prevention of growth of cancer cells in the peritoneal cavity. *Free Radic Biol Med* 72:1–10
- Wang Y, Liu X, Deng G et al (2018) Se@SiO<sub>2</sub>-FA-CuS nanocomposites for targeted delivery of DOX and nano selenium in synergistic combination of chemo-photothermal therapy. *Nanoscale* 2018(10):2866–2875
- Wangpaichitr M, Sullivan EJ, Theodoropoulos G et al (2012) The relationship of thioredoxin-1 and cisplatin resistance: its impact on ROS and oxidative metabolism in lung cancer cells. *Mol Cancer Ther* 11(3):604–615
- Wei C, Zhang Y, Xu et al (2016) Well-defined labile diselenide-centered poly( $\epsilon$ -caprolactone)-based micelles for activated intracellular drug release. *J Mater Chem B* 4:5059–5067
- Xia Y, Xu T, Zhao M et al (2018a) Delivery of doxorubicin for human cervical carcinoma targeting therapy by folic acid-modified selenium nanoparticles. *Int J Mol Sci* 19(11):3582
- Xia Y, Chen Y HL et al (2018b) Functionalized selenium nanoparticles for targeted delivery of doxorubicin to improve non-small-cell lung cancer therapy. *Int J Nanomedicine* 13:6929–6939
- Xia Y, Xu T, Wang C et al (2018c) Novel functionalized nanoparticles for tumor-targeting co-delivery of doxorubicin and siRNA to enhance cancer therapy. *Int J Nanomedicine* 13:143–159
- Xia Y, Zhong J, Zhao M et al (2019) Galactose-modified selenium nanoparticles for targeted delivery of doxorubicin to hepatocellular carcinoma. *Drug Deliv* 26(1):1–11
- Xie Q, Deng W, Yuan X et al (2018) Selenium-functionalized liposomes for systemic delivery of doxorubicin with enhanced pharmacokinetics and anticancer effect. *Eur J Pharm Biopharm* 122: 87–95

- Yang H, Villani RM, Wang H et al (2018) The role of cellular reactive oxygen species in cancer chemotherapy. *J Exp Clin Cancer Res* 37:266. <https://doi.org/10.1186/s13046-018-0909-x>
- Yhee JY (2013) Chapter 13: The EPR effect in cancer therapy. In: Bae YH et al (eds) *Cancer targeted drug delivery: an elusive dream*, pp 621–632
- Zakharia Y, Bhattacharya A, Rustum YM (2018) Selenium targets resistance biomarkers enhancing efficacy while reducing toxicity of anti-cancer drugs: preclinical and clinical development. *Oncotarget* 9(12):10765–10783
- Zeng L, Li Y, Li T et al (2014) Selenium–platinum coordination compounds as novel anticancer drugs: selectively killing cancer cells via a reactive oxygen species (ROS)- mediated apoptosis route. *Chem Asian J* 9(8):2295–2302
- Zeng X, Zhou X, Li M et al (2015) Redox poly(ethylene glycol)-b-poly(L-lactide) micelles containing diselenide bonds for effective drug delivery. *J Mater Sci Mater Med* 26(9):234–245
- Zhai S, Hu X, Hu Y et al (2017) Visible light-induced crosslinking and physiological stabilization of diselenide-rich nanoparticles for redox-responsive drug release and combination chemotherapy. *Biomaterials* 121:41–54
- Zhang J, Wang X, Xu T (2008) Elemental selenium at nano size (Nano-Se) as a potential chemopreventive agent with reduced risk of selenium toxicity: comparison with Se-methylselenocysteine in mice. *Toxicol Sci* 101(1):22–31
- Zhang S, Liu X, Bawa-Khalfe T et al (2012) Identification of the molecular basis of doxorubicin-induced cardiotoxicity. *Nat Med* 18(11):1639–1644
- Zhang R, Qiao H, Chen S et al (2016) Berberine reverses lapatinib resistance of HER2-positive breast cancer cells by increasing the level of ROS. *Cancer Biol Ther* 17(9):925–934
- Zhao S, Yu Q, Pan J et al (2017) Redox-responsive mesoporous selenium delivery of doxorubicin targets MCF-7 cells and synergistically enhances its anti- tumor activity. *Acta Biomater* 54:294–306
- Zhao G, Wu X, Chen P et al (2018) Selenium nanoparticles are more efficient than sodium selenite in producing reactive oxygen species and hyper-accumulation of selenium nanoparticles in cancer cells generates potent therapeutic effects. *Free Radic Biol Med* 126:55–66
- Zhao P, Li M, Chen Y et al (2019) Selenium-doped calcium carbonate nanoparticles loaded with cisplatin enhance efficiency and reduce side effects. *Int J Pharm* 570:118638. <https://doi.org/10.1016/j.ijpharm.2019.118638>
- Zheng W, Cao C, Liu Y (2015) Multifunctional polyamidoamine-modified selenium nanoparticles dual-delivering siRNA and cisplatin to A549/DDP cells for reversal multidrug resistance. *Acta Biomater* 11:368–380
- Zheng L, Li C, Huang X et al (2019) Thermosensitive hydrogels for sustained-release of sorafenib and selenium nanoparticles for localized synergistic chemoradiotherapy. *Biomaterials* 216: 119220
- Zou J, Su S, Chen Z et al (2019) Hyaluronic acid-modified selenium nanoparticles for enhancing the therapeutic efficacy of paclitaxel in lung cancer therapy. *Artif Cells Nanomed Biotechnol* 47(1): 3456–3464

**FORM 5**  
**THE PATENTS ACT, 1970**  
**(39 of 1970)**  
**&**  
**THE PATENTS RULES, 2003**  
**DECLARATIONAS TO INVENTORSHIP**  
**(See section10(6) and rule13(6))**

**1. APPLICANT(S)**

NAME	NATIONALITY	ADDRESS
CHITTARANJAN NATIONAL CANCER INSTITUTE (CNCI)	Indian	37 S.P. Mukherjee Road, Kolkata, West Bengal, 700 026, India

Hereby declare that he true and first inventor(s) of the invention disclosed in the complete Specification filed in pursuance of our application no. **202231032973** dated **09/06/2022** titled **“SYNTHETICALLY DEVELOPED DNA-TARGETING NAPHTHALIMIDE-ARTESUNATE DERIVATIVES AND THEIR TUMORICIDAL EFFECT AGAINST LYMPHOMA ”** is/are

**2. INVENTOR(S)**

NAME	NATIONALITY	ADDRESS
UGIR HOSSAIN SK	INDIAN	C/O Chittaranjan National Cancer Institute (CNCI), 37 S.P. Mukherjee Road, Kolkata, West Bengal, 700 026, India
PARTHA PRATIM MANNA	INDIAN	Immunobiology Laboratory, Department of Zoology Institute of Science, Banaras Hindu University, Varanasi, 221005, India
DEBAPRIYA ROYMAHAPATRA	INDIAN	C/O Chittaranjan National Cancer Institute (CNCI), 37 S.P. Mukherjee Road, Kolkata, West Bengal, 700 026, India

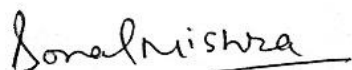
RANJEET SINGH	INDIAN	Immunobiology Laboratory, Department of Zoology Institute of Science, Banaras Hindu University, Varanasi, 221005, India
---------------	--------	---

**3. DECLARATION TO BE GIVEN WHEN THE APPLICATION IN INDIA IS FILED BY THE APPLICANT(S) IN THE CONVENTION COUNTRY: -**

I/We the applicant(s) in the convention country hereby declare that our right to apply for a patent in India is by way of assignment from the true and first inventor(s).

**4. STATEMENT (to be signed by the additional inventor(s) not mentioned in the application form)**  
**NIL**

Dated 9<sup>th</sup> day of June, 2022



**(SONAL MISHRA)**

**Reg. No. IN/PA - 3929**

**L. S. DAVAR & CO.**

**APPLICANTS' AGENT**

To,  
The Controller of Patents  
The Patent Office at Kolkata